

**Faculty of Science and Engineering**  
**Discipline of Electrical and Computer Engineering**

**Design of Degradation-Conscious Control Schemes for Energy Storage  
Systems in Grid-connected Microgrid of High PV Generation**

**Dilum Hettiarachchi**

**ORCID iD: 0000-0002-1927-1252**

This thesis is presented for the Degree of  
**Doctor of Philosophy**  
of  
**Curtin University**

**November 2023**

## **Declaration**

To the best of my knowledge, this dissertation contains my own work and material, except where specifically indicated in the text with relevant attribution statement. A part or whole of the thesis has not been previously submitted to any university for any degree or other qualification.

Dilum Hettiarachchi

Nov 2023

Signature:

Date:-29/11/2023

## **Dedication**

I would like to dedicate my PhD dissertation to my family, with deep appreciation to my father and my mother, my sister and my wife whose actions and words encourage me to survive through the hardships of this journey. They have always stood up by my side, particularly during challenging times, helping me to navigate through this challenging journey with greater perseverance.

## List of Publications

1. H. W. D. Hettiarachchi, S. Rajakaruna, S. S. Choi, and A. Ghosh, "Determination of Hybrid Energy Storage System Capacity based on Empirical Mode Decomposition for a High PV Penetrated Standalone Microgrid," in *2018 Australasian Universities Power Engineering Conference (AUPEC)*, 27-30 Nov. 2018, 2018, pp. 1-6, doi: 10.1109/AUPEC.2018.8757964.
2. D. Hettiarachchi, S. Rajakaruna, S. S. Choi, and A. Ghosh, "A new approach to identify the optimum frequency ranges of the constituent storage devices of a hybrid energy storage system using the empirical mode decomposition technique," *Journal of Energy Storage*, vol. 51, p. 104285, 2022/07/01/ 2022, doi: <https://doi.org/10.1016/j.est.2022.104285>.
3. D. Hettiarachchi, S. Shing Choi, S. Rajakaruna, and A. Ghosh, "Development of control strategy for community battery energy storage system in grid-connected microgrid of high photovoltaic penetration level," *International Journal of Electrical Power & Energy Systems*, vol. 155, p. 109527, 2024/01/01/ 2024, doi: <https://doi.org/10.1016/j.ijepes.2023.109527>.

# Attribution Statement

## Attribution Statement

The authors listed below have certified that:

- They meet the criteria for authorship in that they have participated in the conception, execution or interpretation, of at least that part of the publication in their field of expertise.
- There are NO conflicts of interest. They agree to the use of the publication in the student's thesis and its publication on the Curtin University online database.

1. CHAPTER 3 of the thesis includes some of the materials published in the following conference paper. The specific contributions of co-authors of this publication in each field are outlined in the following table.

### Conference paper:-

“Determination of hybrid energy storage system capacity based on empirical mode decomposition for a high PV penetrated standalone microgrid”

Contributors	Statement	Total Contribution
Dilum Hettiarachchi	Conceptualisation, visualisation, methodology, simulation validation, data analysis and drafting the manuscript.	76%
Sumedha Rajakaruna	Conceptualisation, supervision and critical revision of the paper.	9%
San Shing Choi (Co-Author1)	Conceptualisation, supervision and critical revision of the paper.	12%
Arindam Ghosh (Co-Author2)	Critical revision of the paper.	3%

2. CHAPTER 3 and CHAPTER 4 of the thesis include some of the materials published in the following Journal paper. CHAPTER 4 is an extended version of the main contributions made in the journal paper. The specific contributions of co-authors of this journal publication in each field are outlined in the following table.

**Journal Paper1:-**

“A new approach to identify the optimum frequency ranges of the constituent storage devices of a hybrid energy storage system using the empirical mode decomposition technique”

<b>Contributors</b>	<b>Statement</b>	<b>Total Contribution</b>
Dilum Hettiarachchi	Conceptualisation, visualisation, methodology, simulation validation, data analysis and drafting the manuscript.	73%
Sumedha Rajakaruna	Conceptualisation, supervision and critical revision of the paper.	12%
San Shing Choi (Co-Author1)	Conceptualisation, supervision and critical revision of the paper.	12%
Arindam Ghosh (Co-Author2)	Critical revision of the paper.	3%

3. The main text of the CHAPTER 6 of the thesis is same as the following published journal paper. Literature section of the chapter is extended in order to match with the context of the thesis. The specific contributions of co-authors of this journal publication in each field are outlined in the following table.

**Journal Paper2:-**

“Development of control strategy for community battery energy storage system in grid-connected microgrid of high photovoltaic penetration level”

<b>Contributors</b>	<b>Statement</b>	<b>Total Contribution</b>
Dilum Hettiarachchi	Conceptualisation, visualisation, methodology, simulation validation, data analysis and drafting the manuscript.	73%
Sumedha Rajakaruna	Conceptualisation, supervision and critical revision of the paper.	12%
San Shing Choi (Co-Author1)	Conceptualisation, supervision and critical revision of the paper.	12%
Arindam Ghosh (Co-Author2)	Critical revision of the paper.	3%

• **Candidate acknowledgement:-**

I acknowledge that these represent my contribution to the above research output.

**Dilum Hettiarachchi**

**Date**

• **Co-author1 acknowledgement:-**

I acknowledge that these represent my contribution to the above research output and I have approved the final version.

**Prof. San Shing Choi**

**Date**

• **Co-author2 acknowledgement:-**

I acknowledge that these represent my contribution to the above research output and I have approved the final version.

**Prof. Arindam Ghosh**

**Date**

• **Principle Supervisor Confirmation:-**

I have sighted email or other correspondence from the co-authors confirming their certifying authorship.

**Prof. Sumedha Rajakaruna**

**Date**

## **Abstract**

Depletion and environmental pollution of fossil fuels have led to the wide-spread installation of PV modules at the consumer end, transforming a traditional consumer of electricity into a prosumer unit and the aggregation of multiple prosumers into a microgrid. The integration of such high PV-penetrated prosumers into the distribution system is not without challenges due to the uncertain PV power. A possible remedy is to utilize the buffering actions offered by energy storage systems (ESSs) in which the ESSs are strategically placed at suitable locations within a power grid, with each ESS serving distinct power buffering purposes, and forming a hierarchical storage scheme.

This investigation examines a hierarchical hybrid ESS (HESS) scheme that incorporates both distributed and centralized energy storages. The capacity determination and energy management planning of such a hierarchical storage scheme presents significant challenges due to the diverse storage characteristics, while the design process can be highly computationally intensive. Therefore, in this thesis, the primary objective is to present a direct methodology for determining the capacities and control strategies of centralized and distributed hybrid storage scheme. Furthermore, since degradation of the ESS, particularly that in Li-ion battery, is a significant concern as it affects the service lifetime of the ESSs, the thesis proposes a degradation-conscious battery control for the HESS scheme such that grid constraints are sufficiently met concurrently.

In this work, a preliminary analysis was performed on the non-stationary net power emanating from prosumers using the empirical mode decomposition method which identifies the dominant perturbing frequency components contained in the net power. These components are accurately segregated among different storage technologies, based on the criteria of minimum cost-per-effective energy storage capacity among the constituent ESSs in the HESS. Thus, the proposed method results in the most economical design. Furthermore, it can be readily generalized to include multiple types of energy storage devices in the HESS scheme. Determining the capacity of centralized storage or community battery (CB) for a grid-connected microgrid is the focus of the next study. The CB capacity is determined by making full use of the power transfer capability of the existing grid link, with the proposed dynamic SOC referencing method that tracks the seasonal pattern of PV generation. As the degradation of Li-ion battery due to solid-electrolyte interphase (SEI) film growth is affected by the state



of charge (SOC) of the battery, this design approach leads to lower SEI film growth or else to reduced required battery capacity.

The study of CB is then extended to prioritize the independency of the microgrid from the grid link through the application of a new adaptive CB control strategy while minimizing the SEI film growth. The scheme does not require the short-term forecast of PV generation and load demand, which inevitably contains errors. Furthermore, the proposed method improves the lifetime of the CB by reducing the SEI film growth while the amount of the export-import energy via the grid link is much reduced. The proposed scheme thus leads to higher energy independency of the microgrid from the external grid system.

## **Acknowledgements**

First and foremost, I'm extremely grateful to my supervisors, Professor Sumedha Rajakaruna, Professor San Shing Choi and Professor Arindam Ghosh for their continuous guidance, supervision and encouragement throughout my PhD journey. Without their continuous support and motivation, it would not have been possible to write this doctoral thesis. Their dedication to the scientific research would continue to inspire me in my future work.

It is a great pleasure to acknowledge the rest of the thesis committee members and the staff members of Discipline of Electrical and Computer Engineering at Curtin University for their invaluable comments to improve the work during milestones. I wish to thank the staff in the Green Electric Energy Park laboratory at Curtin University for their kind assistance in accessing the lab facilities. Financial support granted by the Australian Research Council Linkage Scholarship and Curtin University is highly appreciated as it covered all tuition, living, and research costs.

Last but not least, I would like to thank my parents, wife, sister, family and friends for their continual encouragement during challenging times of this journey.

Thank you very much, everyone!

## **Copyright statement**

I have obtained permission from the copyright owners to use any third-party copyright material reproduced in the thesis, or to use any of my own published work (e.g. journal articles) in which the copyright is held by another party (e.g. publisher, co-author). Details of the copyrights obtained by publishers are mentioned under the Appendix E.

# List of Contents

<b>Declaration</b> .....	i
<b>Dedication</b> .....	iii
<b>List of Publications</b> .....	iv
<b>Attribution Statement</b> .....	v
<b>Acknowledgements</b> .....	x
<b>Copyright statement</b> .....	xi
<b>List of Contents</b> .....	xii
<b>List of Tables</b> .....	xviii
<b>List of Figures</b> .....	xix
<b>List of Abbreviations</b> .....	xxiv
<b>CHAPTER 1. Introduction</b> .....	29
<b>1.1 Background and Motivation</b> .....	29
<b>1.2 Major Contributions</b> .....	32
<b>1.3 Organization of the Thesis</b> .....	33
<b>CHAPTER 2. Literature Review</b> .....	35
<b>2.1 Introduction</b> .....	35
<b>2.2 An Overview of HESS</b> .....	35
<b>2.2.1 Different storage topologies of HESS</b> .....	35
<b>2.2.2 Applications of HESS</b> .....	37
<b>2.2.3 Capacity determination of storage components of HESS</b> .....	37

2.2.4	Frequency-based capacity determination of storage components of HESS	41
2.2.5	Research Gap	44
2.3	Frequency-based Analysis using Empirical Methods	44
2.3.1	Traditional frequency-based signal analyzing methods	45
2.3.2	EMD algorithm and applications	46
2.3.3	Theory of EMD algorithm	47
2.3.4	Salient features of EMD	48
2.3.5	Drawbacks of EMD and recent development	48
2.3.6	Research Gap	49
2.4	Li-ion Battery Degradation	49
2.4.1	Overview of different Li-ion battery degradation phenomena	50
2.4.2	Overview of Li-ion battery degradation modeling	53
2.4.3	Ageing-aware operation	53
2.4.4	Research Gap	57
2.5	Li-ion Battery SOC Control	58
2.5.1	Seasonal SOC control	59
2.5.2	Adaptive SOC control methods	59
2.5.3	Research Gap	61
2.6	Conclusions	62

<b>CHAPTER 3. Analysis of Net Power of Prosumer via Empirical Mode Decomposition</b>		
	<b>Technique</b>	64
	<b>Statement of Contribution</b>	64
3.1	<b>Introduction</b>	64
3.2	<b>System Under Study</b>	65
3.2.1	<b>The proposed Hierarchical HESS Scheme for modern power system</b>	65
3.2.2	<b>Laboratory platform for data collection</b>	65
3.2.3	<b>Data preparation and limitations of the study</b>	67
3.2.4	<b>Nonlinearity of the prosumer net power</b>	68
3.3	<b>Proposed approach to analyse <math>P_{net}(t)</math></b>	70

3.4	Results and Discussion.....	71
3.4.1	Case Study 1.....	71
3.4.2	Case Study 2.....	73
3.4.3	Comparative analysis.....	76
3.5	Conclusions.....	79
<b>CHAPTER 4. Determination of Cost-effective Frequency Band and Capacities between Constituent Storages of the Hybrid Energy Storage System.....</b>		<b>81</b>
	Statement of Contribution.....	81
4.1	Introduction.....	81
4.2	Frequency Plane Representation of ESS Devices.....	82
4.2.1	ECM of ESS.....	83
4.2.2	Selection of the ESS for the given application.....	86
4.2.3	Simplification of the ECM.....	87
4.2.4	ESS Economical Operating Frequency Range.....	88
4.2.5	Determination of cut-off frequency between the constituent storages of HESS.....	89
4.3	Hierarchical HESS Scheme.....	90
4.3.1	Introduction to hierarchical storage scheme.....	90
4.3.2	Illustrative example for community and grid scale storage technologies using Pumped Hydro Energy Storage.....	91
4.4	Validation of cut-off frequency Determination.....	95
4.4.1	Determination of cut-off frequency using existing method.....	95
4.4.2	Comparison of computation burden.....	97
4.5	Conclusion.....	97
<b>CHAPTER 5. A Statistical Approach to Estimate the Required Energy Storage Capacity of Hybrid Energy Storage System.....</b>		<b>98</b>
5.1	Introduction.....	98
5.2	System Under Study.....	99
5.3	Determination of the Buffering Power in ESS.....	100
5.3.1	Apportion of the buffering task of the boundary IMFs.....	101

5.4	A Statistical Analysis of the Stored Energy Level in an ESS .....	103
5.5	Numerical Examples .....	106
5.5.1	Segregation of IMFs .....	106
5.5.2	Buffering tasks over different seasons.....	106
5.5.3	Estimate of required energy storage capacity.....	108
5.6	Conclusions.....	112

**CHAPTER 6. Development of Control Strategy for Community Battery Energy Storage System in Grid-Connected Microgrid of High Photovoltaic Penetration Level ..... 113**

	Statement of Contribution.....	113
6.1	Introduction.....	113
6.2	Preliminaries .....	115
6.2.1	Prior Work on the Buffering of the Net Power in Prosumers.....	115
6.3	Problem Formulation .....	117
6.4	Operational Strategy .....	120
6.4.1	Development of a Rule-based Operational Strategy for the CB ....	120
6.4.2	Application of the Rule-based Operational Strategy to Alleviate the Duck Curve Phenomenon.....	123
6.5	Control Strategy for the SOC of the Centralized Battery.....	124
6.5.1	Persistent Drift in SOC .....	125
6.5.2	Daily SOC Correction .....	125
6.5.3	Dynamic Referencing Scheme of $SOC_r$ .....	128
6.5.4	A Statistical Analysis of the Impact of $SOC_r$ Setting on CB Energy Storage Capacity .....	131
6.5.5	Impact of Fixed and Dynamic Referencing of $SOC_r$ on the Rate of SEI Film Growth.....	133
6.5.6	A Summary of the Proposed Microgrid Rule-based Operational and CB SOC Control Scheme .....	134
6.6	Illustrative Examples .....	136
6.6.1	Base Case.....	137
6.6.2	Impact of the Dynamic Referencing of $SOC_r$ on the Rate of SEI Film Growth .....	138

6.6.3	Impact of the Flexible Setting of $P_G^{max,p}$ and $-P_G^{max,n}$ in Alleviating Duck-power Phenomenon .....	139
6.6.4	Impact of Dynamic Referencing of $SOC_r(t)$ and Flexible Seasonal Setting of $P_G^{max,p}$ and $-P_G^{max,n}$ on Required CB Capacity .....	140
6.6.5	Sensitivity studies .....	141
6.7	Conclusions .....	141
<b>CHAPTER 7. Development of a Degradation-Conscious Adaptive Control Strategy for the Intra-Day Operation of Community Battery .....</b>		<b>143</b>
7.1	Introduction .....	143
7.2	Preliminaries .....	144
7.2.1	Seasonal Variations of Net Power of Microgrid .....	144
7.2.2	Li-ion battery degradation due to SEI growth .....	146
7.3	Analysis .....	150
7.3.1	Energy contents in $P_{LT}(t)$ .....	150
7.3.2	Constant current charging on SEI film growth – ideal case .....	153
7.4	Development of an Adaptive Intra-day Control Strategy for CB .....	157
7.4.1	Adaptive battery SOC control ignoring – no grid constraints .....	158
7.4.2	Adaptive intra-day CB control strategy considering grid constraints 160	
7.5	Illustrative Examples and Discussion.....	163
7.5.1	SEI film growth during CB charging operations: no grid constraints applied 163	
7.5.2	SEI film growth during discharge operation in the night-time: no grid constraints applied .....	166
7.5.3	Illustrative examples on the proposed adaptive intra-day control strategies .....	168
7.5.4	Performance of CB Operating under Conventional and Proposed Adaptive Control Strategies.....	173
7.6	Conclusions .....	178
<b>CHAPTER 8. Conclusions and Recommendations .....</b>		<b>179</b>



<b>8.1 Impact of Research Findings to Industry</b> .....	179
<b>8.2 Assumptions and Limitations</b> .....	182
<b>8.3 Conclusions</b> .....	184
<b>8.4 Recommendations for Future Work</b> .....	186
<b>APPENDIX A</b> .....	187
<b>APPENDIX B</b> .....	190
<b>APPENDIX C</b> .....	196
<b>PHES costs</b> .....	196
<b>APPENDIX D</b> .....	196
<b>APPENDIX E</b> .....	199
<b>References</b> .....	201

## List of Tables

Table 2.1 Summary of advantages and disadvantages of HESS sizing methods reported in the literature.....	39
Table 2.2 Summary of comparison between FT, WT and EMD .....	46
Table 2.3 Summary of literature related to degradation-conscious SOC control .....	56
Table 3.1. $T_{j,m}$ of the IMFs.....	75
Table 3.2. Execution times of the EMD and EEMD .....	77
Table 5.1. Indices of the segregated IMFs based on the cut-off frequencies of $\omega_c = 0.0085$ Hz and $\omega_{Lc} = 1 \times 10^5$ .....	106
Table 5.2. Expected values of $E_{ESS}$ , $\rho$ : $\rho=0.5$ .....	111
Table 5.3. Required energy swing ranges for ESS over the four seasons .....	112
Table 6.1. A summary of the target $P_G(t)$ and control strategies on $P_{CB}(t)$ under the various possible scenarios of $P_{LT}(t)$ .....	122
Table 6.2. Summary of the results obtained under the Base Case and other case studies:....	138
Table 6.3. $P_G^{max,p}$ and $-P_G^{max,n}$ settings for the seasons in Studies 3-7.....	139
Table 7.1 A summary of rules incorporated in the proposed adaptive intra-day control strategy for the CB: grid link power and ramp rate constraints are complied with .....	162
Table 7.2. Parametric values used for the simulation of CB operations for the different seasons .....	168
Table A.1 Table of the characteristics of the different ESS technologies (taken from the review paper [13]).....	188
Table B.1 Parameters of PHES modelling.....	191
Table C.1 Table of PHES capacities and associated capital costs [136] .....	196
Table D.1. Parameters of degradation model of Li-ion battery .....	196
Table E.1. Details of the copyrights obtained by for the published research outputs.....	199

## List of Figures

Figure 2.1. Classification of capacity determination approaches of HESS .....	38
Figure 2.2. General algorithm used in literature to determine cut-off frequency .....	42
Figure 2.3. Degradation phenomena of the Li-ion battery and its relationship to the measurable effects (The figure is the replica of Figure 2 in [71]). .....	51
Figure 2.4. Classification of the ageing-aware scheduling methods reported in the literature. ....	54
Figure 3.1. The conceptual hierarchical HESS scheme under study for the thesis .....	66
Figure 3.2 Green Electric Energy Park at Curtin University (Image credits: Prof.Sumedha Rajakaruna, Director Green Electric Energy Park) .....	67
Figure 3.3 Samples of (a) PV power, (b) Zoomed plot of PV power (b) load power and (c) net power over a selected three-day period .....	69
Figure 3.4 The proposed approach to analyse net power .....	70
Figure 3.5 (a) IMF $P_j(t)$ and residue function $r(t)$ , (b) the corresponding energy $\Delta E_j(t)$ and (c) instantaneous frequency $f_j(t)$ of $P_{net}(t)$ - Case Study 1.....	72
Figure 3.6. CDF of IMF3 and IMF9 (a) power, (b) frequency and (c) oscillating energy in Case Study 2 .....	74
Figure 3.7 CDF of the instantaneous frequencies from $f_1(t)$ to $f_{15}(t)$ .....	75
Figure 3.8 CDF of $\Delta E_i(t)$ for IMF $P_1(t) - P_{15}(t)$ in Case study 2.....	76
Figure 3.9(a) IMF 8-10 generated by EMD (b) IMF 8-10 generated by EEMD.....	76
Figure 3.10. Comparison of the extracted frequencies between FT and HHT .....	78
Figure 3.11 Comparison of (a)Variance (b) Skewness and (c)kurtosis of the 15 IMFs in dataset1 and dataset 2 analysis .....	79
Figure 4.1. ECM of Li-ion battery given in [56] .....	83
Figure 4.2. Conversion of series ECM to the parallel branch for ESS .....	84
Figure 4.3 a) Magnitude plot of battery ECM b) Phase plot of battery ECM .....	85
Figure 4.4. Comparison of phase diagram between the 4-branch SC and equivalent series RC SC model .....	88
Figure 4.5 Effective energy capacity vs frequency profiles of battery and SC .....	88
Figure 4.6. Comparison of the capital cost per kWh capacity of battery and SC: notice at $\omega_c$ , the curves cross-over .....	89

Figure 4.7. CDF values for the frequencies from IMF1 to IMF14 ( $\Delta t=1$ sec and $T=3$ months)	90
Figure 4.8. Complete ECM of the discharging circuit of the PHES	92
Figure 4.9. Simplified ECM of discharging circuit of the PHES	92
Figure 4.10. Simulated ECM of PHES in PLECS	92
Figure 4.11. Magnitude plot of the frequency response	93
Figure 4.12. Phase plot of the frequency response	93
Figure 4.13. (a) Comparison of the ECM magnitude plot and equivalent RC (b) Comparison of the phase plots of ECM and equivalent RC	94
Figure 4.14. (a) Normalized effective capacity vs frequency for PHES and Battery (b) Cost per effective kWh curves for Battery and PHES	95
Figure 4.15. $E_{overlap}$ vs $f_g$ and the determination of $\omega_{c,e}$	96
Figure 5.1. A conceptual hierarchical energy storage scheme consisting of the hybrid energy storage system within a prosumer and an energy storage system outside of the prosumer	99
Figure 5.2 CDF of IMFs of $P_{net,i}(t)$ and the locations of the cut-off frequencies $\omega_c$ and $\omega_{Lc}$	100
Figure 5.3 Distribution of the frequencies in IMF <sub>j</sub> ; at the cut-off frequency $\omega_c$ , the CDF has the value $CDF_j(\omega_c)$ .	101
Figure 5.4. Allocation of the buffering actions for boundary IMF (a) $P_j(t)$ (b) instantaneous frequency, (c) low- and high-frequency portions of $P_j(t)$ .	102
Figure 5.5. $E_5(t)$ showing the obvious downward drift over a week	104
Figure 5.6 (a) $P_{ESS}(t)$ and (b) $E_{ESS}(t)$ over one time window of $t_s$	105
Figure 5.7. CDF of $E_{ESS}^+$ and $E_{ESS}^-$	106
Figure 5.8: (a) Selected daily $P_{SC}(t)$ in the four seasons, (b) zoomed-in plot from noon to 1 pm of the selected spring day.	107
Figure 5.9: $P_B(t)$ for (a) the selected spring day and (b) the zoomed-in plot over the noon – 1 pm period	108
Figure 5.10. CDF of the $E_B^+$ and $E_B^-$ for the seasons	109
Figure 5.11. CDF of the $E_{SC}^+$ and $E_{SC}^-$ for the seasons	110
Figure 6.1. A conceptual microgrid equipped with a community battery energy storage system to buffer the power flows between the PV-powered prosumers and the external grid interconnection	116

Figure 6.2 A sample set of results of EMD analysis of $P_{Net,i}(t)$ : IMF $c_j(t)$ and energy $E_j(t)$ for $j = 1, 10$ and $14$ .	117
Figure 6.3 $P_{LF,i}(t)$ and $P_{SC,i}(t)$ over two consecutive days in summer	119
Figure 6.4. Sample curves of $P_{LT}(t)$ , $P_G(t)$ and $P_{CB}(t)$	121
Figure 6.5 $P_{LT}(t)$ , $P_G(t)$ and $P_{CB}(t)$ for three days in summer. Power flows are expressed on a 10 MW base.	124
Figure 6.6. A sample of $P_{res}(t)$ , $P_{LT}(t)$ , $P_{G,T}(t)$ , $P_{CB,T}(t)$ and $SOC(t)$ following the application of the daily SOC restoration strategy	128
Figure 6.7 Profiles of the $SOC(t)$ under daily SOC restoration: (a) fixed- $SOC_r$ ; (b) sinusoidal dynamic referencing of $SOC_r(t)$	129
Figure 6.8 Dominant seasonal mode $SOC_s(t)$ for 2014-2015, 2016-2017, that of $P_{PV}(t)$ in 2014-2015 and the fitted dynamic SOC reference on the for 2014-2015 $SOC_s(t)$	131
Figure 6.9 (a) Probability density functions of the SOC under the fixed- $SOC_r$ and dynamic referencing of $SOC_r$ schemes. Also shown is the rate of SEI film growth vs SOC characteristic curve for $LiFePO_4$ battery; (b) Probability density functions of the rate of SEI film growth under the fixed- $SOC_r$ and dynamic referencing of $SOC_r$ schemes	132
Figure 6.10 Procedure to obtain the SOC control strategy for the community battery	136
Figure 6.11 CDF of the Li-ion battery SOC based on the fixed- $SOC_r$ (Base Case) and dynamic referencing strategies of $SOC_r$ (Case Study 2).	138
Figure 7.1. A Schematic Diagram of Grid-connected Microgrid	144
Figure 7.2. A sample of daily profile of $P_{LT}(t)$ in four seasons	145
Figure 7.3. Surface plot of SEI film growth rate verses cell current and SOC for Li-ion battery of $LiFePO_4$ cathode chemistry	147
Figure 7.4. SEI film growth rate vs SOC of Li-ion battery cell under various charging C-rates	148
Figure 7.5. SEI film growth rate vs SOC of Li-ion battery cell under various discharging C-rate	149
Figure 7.6. Demarcation of CB daily operating regimes into the daytime, nighttime and SOC restoration periods	151
Figure 7.7 Cumulative density functions of the daily $\Delta E_+$ and $\Delta E_-$ for (a) the summer and (b) the winter seasons	152
Figure 7.8 Charging current profiles of Strategies 1 and 2	155

Figure 7.9 linearized approximation of (a) $\delta$ vs SOC curves and (b) $\delta$ vs SOC curves at constant current.....	156
Figure 7.10 $P_{LT}(t)$ , $P_{CB,ref}(t)$ , $P_{CB}(t)$ , $P_G(t)$ and $SOC(t)$ of the CB during daytime and a zoomed-in plot: proposed charging strategy is applied under the presence of grid link power magnitude constraint.....	161
Figure 7.11. Sample of $P_{LT}(t)$ , $P_G(t)$ , $P_{CB}(t)$ and $P_{CB,ref}(t)$ : the proposed adaptive intra-day control strategy is applied under grid link power ramp rate constraint .....	162
Figure 7.12 a) Profiles of the assumed charging currents (b) SOC of the CB, (c) SEI film resistance of the CB .....	164
Figure 7.13 Night-time CB discharge operation: profiles of the (a) assumed $P_{LT}(t)$ , (b) assumed discharge currents $I_{CB5}$ and $I_{CB6}$ , (c) the corresponding SOC and (d) SEI film thicknesses .....	167
Figure 7.14 Application of the proposed adaptive intra-day CB SOC control strategy: summer and $SOC_{max} = 0.8$ .....	169
Figure 7.15 Application of the proposed adaptive intra-day CB control strategy: summer and $SOC_{max} = 0.5$ .....	170
Figure 7.16 Application of the proposed adaptive CB SOC control strategy: autumn and $SOC_{max} = 0.8$ .....	171
Figure 7.17 Application of the proposed adaptive CB SOC control strategy: winter and $SOC_{max} = 0.8$ .....	172
Figure 7.18 Application of the proposed adaptive CB SOC control strategy: spring and $SOC_{max} = 0.8$ .....	173
Figure 7.19 $P_{LT}(t)$ , $P_{CB}(t)$ , $P_G(t)$ and $SOC(t)$ obtained using Strategy 1: summer.....	174
Figure 7.20 $P_{LT}(t)$ , $P_{CB}(t)$ , $P_G(t)$ and $SOC(t)$ obtained using Strategy 2: summer.....	175
Figure 7.21 Resulting increase in SEI film thickness in the Li-ion battery when applying Strategies 1, 2 and 3 over a summer season .....	176
Figure 7.22 Comparison of exported energy to grid using the three methods: summer.....	176
Figure 7.23 Comparison of imported energy from grid based on the three methods: summer .....	177
Figure 8.1 Hierarchy of operations discussed in the microgrid planning problem discussed in the thesis .....	179

Figure A.1. An overview of classification of storage technologies based on the responsive time characteristics [10].....	187
Figure A.2. Overview of classification of storage technologies([12]).....	187
Figure A.3. Algorithm flow of sifting process of the EMD .....	189
Figure B.1 ECM of Li-ion battery given in [130].....	190
Figure B.2. Main components of the generalized PHES .....	192
Figure B.3. Complete ECM of the Elastic pipe .....	193
Figure B.4 ECM of the surge tank.....	194
Figure B.5 ECM of valve.....	194
Figure B.6 ECM of turbine .....	194
Figure B.7 ECM parameters of reservoir .....	195
Figure D.1 Different SEI growth rate vs SOC/I surface plots in the literature [129] [156]	198

## List of Abbreviations

ACO	Ant Colony Optimization
AEMO	Australian Energy Market Operator
ANN	Artificial Neural Network
CB	Community Battery
CDF	Cumulative Distribution Function
DOD	Depth of Discharge
DFT	Discrete Fourier Transform
DP	Dynamic Programming
ECM	Equivalent Circuit Model
EMD	Empirical Mode Decomposition
EMS	Energy Management System
EOL	End of Life
FL	Fuzzy Logic
FT	Fourier Transform
GA	Genetic Algorithm
HESS	Hybrid Energy Storage System
HHT	Hilbert-Huang Transform
HOS	Higher order statistics
IMF	Intrinsic Mode Function
ISP	Integrated System plan
LCOE	Levelized cost of energy
MILP	Mixed integer linear programming
NLP	Non-linear programming
OCP	Open Circuit Potential
OCV	Open Circuit Voltage
PDF	Probability density function
PHES	Pumped hydro energy storage



PSO	Particle Swarm Optimization
PV	Photovoltaic
RMSE	Root mean square error
SEI	Solid-electrolyte interphase
SOC	State of Charge
TOD	Time of day
VRB	Vanadium redox battery
WT	Wavelet Transform

## List of Symbols

$\tau$	Time at which CB SOC reaches the target SOC
$c$	Implicit Mode Function
$CDF_j(.)$	Cumulative Distribution value of the jth IMF value (.)
$\Delta E_i(t)/E$	Oscillating energy of the i <sup>th</sup> order IMF [kWh]
$E_{ESS}(\omega)$	Effective energy storage capacity of ESS [kWh]
$E_{ESS}(t)$	Energy fluctuation of the ESS [kWh/Wh]
$E_{ESS,\rho^+} E_{ESS,\rho^-}$	positive and negative portions of $E_{ESS}(t)$ [kWh/Wh]
$E_{overlap}$	Overlap energy between the battery and SC[Wh]
$f_i(t)$	Instantaneous frequency [Hz]
$f_c$	cut-off frequency[Hz]
$f_g$	Arbitrary cut-off frequency[Hz]
$f_{H,B}$	3dB point of the battery[Hz]
$f_i(t)$	Instantaneous frequency [Hz]
$f_{i,m}$	Mean instantaneous frequency of the i <sup>th</sup> order IMF [Hz]
$f_{L,k}, f_{H,k}$	Frequencies at boundary of the interesting frequency range[Hz]
$H(\omega)/M$	Amplitude/ in dB
$I_{sr}$	Side reactions current in battery model [A]
$I_{CB}$	Current of the CB [A]
$m, \mu$	Modulation index and initial value of sinusoidal curve fitted to the seasonal IMF mode of SOC (p.u.)
$\gamma / \lambda$	Higher threshold probability values of the CDF curve of energy
$n$	Number of prosumers
$n_1$ and $n_2$	Gradient of the $\delta$ vs SOC curve
$\zeta$	Increase in the thickness of the SEI film [n $\Omega$ ]
$P$	Power [kW]
$\dot{P}$	Power ramp rate[kW/min]
$P_{G,T}$	Total power absorbed or delivered by grid [kW]

$r$	Residue function
$R^{\pm}_1, C^{\pm}_1$	Series RC branch parameters in battery model [ $\Omega$ , F]
$R^{\pm}_2, C^{\pm}_2$	Parallel RC branch parameters in battery model [ $\Omega$ , F]
$R^{\pm}_n$	Overpotential resistance in battery model [ $\Omega$ ]
$R_e$	Sum of the resistances of the electrolyte in the electrodes and the separator in battery [ $\Omega$ ]
$R_f$	Resistance at the anode due to the formation of film at the solid-electrolyte interphase[ $\Omega$ ]
$R_{P,ESS}/C_{P,ESS}$	Equivalent parallel resistance/capacitance of the ECM of ESS [ $\Omega$ ,F]
$R_{S,ESS}/C_{S,ESS}$	Series resistance/capacitance of simplified ECM of ESS [ $\Omega$ ,F]
$SOC_{max}/SOC_{min}$	Maximum and minimum SOC limits
$SOC_{ss}$	SOC at sunset
$T$	Time span of study
$t_0$	Initial time
$T_{i,m}$	Mean oscillating time of the $i^{\text{th}}$ order IMF [s]
$t_s$	Time window of restoration
$T_{SS} T_{SR}$	Time at sunrise/sunset
$V_{r,B}$	Rated voltage of the battery[V]
$\alpha, \omega$	Magnitude and phase angle of the sinusoidal curve fitted to the seasonal IMF mode of SOC
$P_{r,CB}$	Power rating of the Li-ion community battery [kW]
$\delta_{SEI}$	SEI growth rate [ $n\Omega/m^2/s$ ]
$\Delta t$	Sampling time resolution[s]
$\rho_h$ and $\rho_l$	Higher and lower threshold probability values of the CDF curve of frequencies
$\omega_{c,p}/\omega_{c,e}$	Cut-off frequency between Li-ion battery and SC determined using the proposed/existing method [Hz]
$\omega_c _{ESS1,ESS2}$	Cut-off frequency between ESS1 and ESS2[Hz]

## Subscripts and Indices

<i>LF</i>	Lower frequency
<i>PV</i>	Photovoltaic
<i>LD</i>	Load
<i>LT</i>	Aggregated lower frequency power components of all prosumers
<i>G</i>	Grid interconnection
<i>B</i>	Li-ion battery
<i>i</i>	Index for the prosumers
<i>l</i>	Order of the implicit mode function
<i>m</i>	Mean
<i>net</i>	Net flow resulting from the generation and loads
<i>r</i>	Reference or rated value
<i>res</i>	Parameters pertaining to SOC restoration
<i>SC</i>	Supercapacitor

# CHAPTER 1. Introduction

## 1.1 Background and Motivation

As environmental concerns continue to rise due to greenhouse gas emissions, and fossil fuel reserves are expected to deplete in the next decades, recent research is increasingly focused on solutions involving new sources of energy production. With the emerging energy crisis, it is well-accepted that renewable energy is poised to play a pivotal role in electricity generation. Following this evolution in Australia, the Australian Energy Market Operator (AEMO) indicated in their recent Integrated System Plan (ISP), the current planning objective is to reach energy target with zero emission by 2050 [1]. Given the growing interest from both public and commercial sectors, this goal may even be attainable sooner than expected.

Among many other renewable energy technologies such as wind, photovoltaic (PV) has advanced sharply in the last decade since the prices of PV modules have rapidly decreased due to continuous technical advancement and the ease of installation. Thus, there is a higher tendency of increased PV generation on the consumer side, ultimately converting the conventional consumer to a prosumer [2]. This has offered the additional advantage of reducing the transmission losses encountered in conventional power grid system. In addition, the requirement of the transmission network upgrades is not necessary as the generation is distributed. Most remote communities, especially those with dispersed geographical locations, can be easily electrified through the introduction of distributed generation, avoiding the need for costly extensions of the transmission network.

Unfortunately, a high degree of power fluctuations in PV generation is unavoidable due to meteorological changes. These fluctuations can range from sudden cloud cover incidents to gradual seasonal changes, impacting PV production considerably. This intermittent nature and low inertia of PV inverters may cause severe power system instability issues in voltage, frequency and rotor angle stability [3] in the power system. Among the number of remedies to combat such stability issues, allocation of reserve generation would be a costly practice. Thus, the alternative solution is to use Energy Storage System (ESS) to smooth out PV power fluctuations and improve the dispatchability of the renewable generation. In term of such distributed generation scenario, a number of interconnected prosumers shall form a small-scale power grid. This setup encompasses local and common loads along with centralized or distributed energy storage systems, and with the

appropriate communication and control network interconnecting the prosumers. In the literature, the small-scale power grid is collectively referred to as a microgrid. Such microgrids can be operated both in grid-connected and isolated modes. Recent microgrid projects have been on the rise not only worldwide but also in Western Australia. The Onslow microgrid project by Horizon Power, Kalbarri microgrid with 5 MWh community battery by Western Power [4], Agnew renewable microgrid in Leinster with total installed capacity of 56 MW [5], and White Gum Valley project [6] are some of the examples for such recent implementations. Perenjori, Bremer Bay, and Ravensthorpe are among the locations where these renewable energy and storage combinations function as microgrids [7].

As conventional consumers increasingly shift towards becoming prosumers, the future of the modern power system will essentially be a network of interconnected microgrids. Within this networked power system, the integration of ESS can occur at various levels. The purposes of the ESS can vary widely, often reflected by their location of installation within the power system at different levels. For instance, ESS can be introduced at the prosumer level, microgrid level or at the grid scale. Primary considerations of the prosumer level storages are to resolve the power quality issues due to the short-term intermittencies and daily power buffering at the prosumer level [8]. In contrast, the microgrid level storages serve different purposes such as peak shaving (energy arbitrage), resolving duck curve phenomena, microgrid independency and smoothing grid power [9]. Even larger grid-scale storages may be intended to provide grid ancillary services or to meet seasonal storage requirements for the entire power grid.

To serve these diverse purposes, employing a single storage technology would not be a viable option. While different storage techniques are applied, these suitable ESS should be selected to serve the proposed objective based on the energy density, power density, capital cost and degradation characteristics. The question of planning a HESS with different storage technologies has been discussed over the years in a large body of reported works. However, planning such a scheme can be highly challenging as a comprehensive techno-economical assessment is required to compare the ESSs and to decide the capacity of these storages. Often, the reported works on the assessment focus on two types of ESS and are based on trial-and-error methods. These methods cannot be easily generalized for a scheme which contains a larger number of storage elements. So, it is unclear whether the generalisation of these methods is feasible for hierarchical energy storage schemes. In addition, there is a continuous argument on the centralization of the storages, as prosumer-based storage schemes are difficult to control and coordinate. In such a scenario, many studies have shown the economic perspective of centralization of the storage architecture. Some

remote microgrids in Western Australia, are often grid-connected through interconnection overhead feeder lines of considerable length. For example, the Kalbarri microgrid owned by the Western Australian Electricity Utility Corporation is connected to the South-west power grid of the state through a 140 km overhead line. The overhead line provides the only electrical link between the Kalbarri microgrid and the remaining part of the state utility network. As the PV generation and load demand in Kalbarri increases over the years, however, there will come a stage when the line needs to be upgraded in order to meet the demand. Upgrading the line can be a costly exercise. An alternative option could be to install a community battery within the Kalbarri area to provide the necessary power buffering actions in the microgrid while keeping the existing link in service. As shall be explained in CHAPTER 6 later in this thesis, there has been considerable attention in the last few years considering the installation of such similar community batteries. Notwithstanding this development, the planning of such a centralized storage facility to obtain maximum use of existing transmission link has yet to be reported in the literature.

In a contrasting scenario from the one mentioned above, if the centralized battery is community-owned and the intention of the instalment is to reduce the grid-link dependency, then the objectives of battery operation will change. Thus, the priority should be given to the battery to charge with the surplus energy in the microgrid while the stored energy is used to serve the microgrid evening peak. Under these two different scenarios, the respective objectives of the community battery operation will not be the same. Therefore, the design of community storage should align with the intended operating objectives. These two aspects must be thoroughly grasped by system planners, both during the capacity determination phase in planning and subsequently during energy storage management in real-time operation.

Moreover, for such a community-scale investment, the service lifetime of the battery would be a paramount factor. When the discussion is limited to the Li-ion battery, the degradation phenomena termed solid electrolyte interphase film growth, particularly the most dominant form of degradation, can significantly shorten the battery lifetime, if the influencing factors such as battery SOC and charging/discharging current C-rate are not properly controlled. Even though numerous recent studies have produced comprehensive battery cell models to study these degradation effects, strategization of the charging and discharging processes while taking onboard the degradation effects remains a fairly unexplored research area. This should be more vigorously addressed both in planning and controlling of the Li-ion battery management. During the capacity determination stage, the planning problem should consider long-term operation, taking into account battery SOC levels

in response to seasonal changes to determine seasonality effects on battery degradation. This will allow to adjust the storage control parameters seasonally to reduce the storage degradation. However, during the intra-day operation of the battery, more detailed storage controlling should be integrated into the battery energy management system in order to cater for the uncertainties of the weather pattern. An adaptive battery controlling is required to strategically manage storage capacity during renewable applications heuristically. Therefore, during microgrid applications battery energy management system (EMS) operations should be carefully designed with appropriate instructions to ensure the optimized operation of the ESS to reduce degradation while retaining adequate storage to withstand uncertainties. Furthermore, the storage operation should be economically feasible and sufficiently adaptive to maintain microgrid self-sufficiency. Thus, it would be a worthwhile attempt to explore the degradation conscious adaptive control of the community battery in different operating modes while incorporating power fluctuations due to load and PV. Based on above, the key objectives of the thesis can be summarized as follows.

1. To propose a method to segregate the power components of different frequencies to each constituent storage of prosumer level HESS and then determine the capacities of storages accordingly.
2. To propose a long-term SOC control method which minimizes the degradation of a grid connected community Li-ion storages.
3. To schedule intraday management of the SOC and C-rate of the Li-ion battery to minimize degradation and improved self-sufficiency.

## **1.2 Major Contributions**

Based on the aforementioned motivation, each subsequent chapter has identified a research gap in the existing studies. In striving to fill these identified gaps, this thesis intends to make the following key contributions.

### **1. Proposition of a direct method to segregate the power component for each constituent storage element of HESS based on their economic and dynamic response characteristics.**

Based on the empirical mode decomposition technique, the implicit modes existing in the net power of prosumers are extracted. The modes are then segregated into groups to be buffered by the constituent ESSs in the HESS. As an alternative to the existing cost-based optimisation methods, a new method is proposed which is based on both the dynamic response and economic characteristics



of the storage elements. The dynamics characteristics are determined using the equivalent circuit of the given storage system so that the proposed method assures that the storage element can successfully buffer the allocated power components at the lowest cost/energy storage capacity. The proposed method can be readily generalized for a hierarchical storage scheme containing any number of constituent storage elements, a design advantage which cannot be replicated using existing trial and error approaches due to their heavy computation burden.

## **2. Proposing a new method to determine the capacity of community storage for a grid-connected microgrid using dynamic seasonal SOC referencing leading to a modest SEI film growth.**

The SOC of the Li-ion battery utilized as the community storage has to be maintained such that the main degradation factor of Li-ion battery SEI growth is minimized. Existing reported works based on cycle counting methods or its variants are unsuitable for the renewable applications as the relationship between the battery SEI film growth and SOC cannot be readily incorporated in them. The proposed SOC control method allows the seasonal SOC reference to vary such that the operating SOC is kept at a range where the SEI film growth is minimum.

## **3. To develop a degradation-conscious adaptive battery SOC control for the community Li-ion battery to minimize the SEI growth.**

Since SEI film growth rate is identified as a function of not only of SOC but also that of the C-rate of the battery, the charging and discharging strategies of the Central Battery of a community microgrid are proposed to minimize the SEI growth during intra-day battery operations. The proposed method is sufficiently adaptive to the intra-day variations of the PV and load without undergoing the complexities of forecasting. Furthermore, it concurrently minimizes the power exchanged with the grid thereby increasing the energy independency of the microgrid. Moreover, it also ensures the meeting of the grid line power constraints with respect to the magnitude and ramp rate.

### **1.3 Organization of the Thesis**

The remainder of the thesis is organized as follows:

CHAPTER 2 initiates with a literature review related to the thesis. Firstly, the storage types used in HESS are examined. The HESS capacity sizing methods reported in the literature are then compared in order to identify their drawbacks. The frequency-based sizing methods reported in the literature

are closely analysed to identify areas for improvement. Then, the storage degradation modelling and aging aware methods used in controlling are discussed with the aim to identify associated challenges. Finally, adaptive battery controlling techniques reported in the literature are comprehensively examined.

CHAPTER 3 below emphasizes the need for an adaptive frequency-based decomposition method to analyse the net power variation in which Empirical Mode Decomposition is practiced. The oscillating modes of net power of a single prosumer is analysed to identify the dominant modes and their respective frequency bands. The results of this chapter pave the way for the subsequent chapters in order to determine the capacities of the constituent storages of HESS.

CHAPTER 4 aims to cover the first main contribution of this thesis. The decomposed oscillating modes should be demarcated between the constituent storages of HESS to ensure the most cost-effective HESS design. A new method to determine the cut-off frequency between the constituent ESSs is proposed to serve this purpose. The method enables the accurate segregation of power components between the ESSs, by considering both the dynamics characteristics and economics of the constituent storage elements.

With the aid of the determined cut-off frequency between the constituent storage of HESS, CHAPTER 5 employs both the EMD-based analysis and statistical approach to determine the storage capacities of the constituent storages of HESS at the prosumer level. CHAPTER 6 and CHAPTER 7 primarily focus on this community level storages. CHAPTER 6 considers a grid-connected microgrid where Li-ion battery is used as a community storage medium. The purpose of the battery design is to minimize the capacity by employing the full use of the maximum power transfer capacity of the existing grid-link. SEI film growth of the Li-ion battery degradation with respect to the SOC is also considered to define a seasonally adjusted SOC referencing method.

CHAPTER 7 further extends the community battery study when the battery is operated to enhance the microgrid independency, while reducing the amount of the grid import/export. The intra-day adaptive charging/discharging strategies are designed to align with the charging/discharging C-rate effects on the battery SEI film growth while abiding to grid constraints.

CHAPTER 8 concludes the main findings of the thesis and possible directions for future works.

# **CHAPTER 2. Literature Review**

## **2.1 Introduction**

Within the framework of microgrids, the role of the energy storage systems stands out as a critical component fostering stability, reliability and resilience. As microgrids inherently featuring the higher renewable penetration, the effective utilization of ESS is paramount for mitigating the intermittency, enhancing independence, peak shaving and supporting grid ancillary services. Since a single ESS technology cannot effectively provide the wide range of applications, different types of storages are coupled in the form of a hybrid energy storage system (HESS). The literature review chapter of this thesis begins with a broad overview of different storage schemes encompassed within the HESS. Then, the capacity determination techniques practiced in the literature are evaluated, considering their advantages and disadvantages. Subsequently, frequency-based capacity determination methods are explained while highlighting the advancements of the empirical methods compared to the classical approaches. Then, the literature analysis dwells into the battery SOC control mechanisms used in the existing studies. Subsequently, then the chapter examines closely into the issues pertaining to the degradation of the Li-ion battery and the applications of degradation-conscious control. Finally, the adaptive SOC control mechanisms in battery energy management systems used in renewable applications are extensively discussed.

This literature review chapter aims to provide significant insights into the research gaps, firstly focusing on HESS capacity determination techniques. Then, critical issues in existing literature concerning battery SOC control of Li-ion batteries are identified, particularly in degradation conscious control. Through a critical analysis of the existing methods, the shortcomings of adaptive control methods are demonstrated, and hence indicating the state of the art within the thesis domain. The primary research gaps are highlighted within each section, providing vital insights for establishing the state-of-the-art framework in subsequent chapters.

## **2.2 An Overview of HESS**

### **2.2.1 Different storage topologies of HESS**

In microgrid-based applications, relying on a single storage technology will not be sufficient as the requirement of the storage greatly varies in wide range of applications. The later analysis of the net power related to the PV and load variation shows that the net power varies over a wide

frequency bandwidth. So, it is highly unlikely that the single type of ESS can effectively respond and buffer such different modes of oscillations of a wide variety of frequencies. Therefore, the need for HESS as a suitable option for buffering these wide range of oscillating modes is clearly identified.

Variety of storage devices utilized to form the HESS is identified in the literature. Certain storage characteristics, such as energy density and power density, differ greatly from one type to another, making storage device designed for one application unsuitable for another. Classification of these diverse storage techniques can be evaluated using the discharge time as the parameter for categorization as shown in Figure A.1 in Appendix A[10].

According to the discharge characteristics shown in Figure A.1 in Appendix A, a convenient way to describe the diversity of ESSs is to categorize them under different time scales ranging from the short, medium and long term. Discharging duration of storage is an important characteristic which refers to the typical cycling time of the charging/discharging. In here, the typical discharging durations of storages can vary from seconds to years. The short-term storages have a nominal discharge duration of a few seconds to minutes, in which the supercapacitor and flywheel are considered suitable examples for this category. The mid-term storages have a typical discharge duration of minutes to hours, whereas most battery technologies generally fall into this group. The third category, long-term storage devices, includes fuel cells and flow batteries, with discharging duration ranging from a few days to year.

Another approach of ESS classification found in literature involves distinct curves on power-energy plane commonly referred as Ragone plots [11]. One such representation is shown in Figure A.2 in Appendix A taken from [12]. According to the figure, SC exhibits the highest power density. SMES, Flywheel and Li-ion batteries are other examples of storages with high power density, while Li-ion battery offers acceptable energy density. Fuel cells while having lower power density compared to Li-ion batteries, exhibit better energy density. Lead acid batteries and Vanadium redox batteries (VRB) storages are suitable candidates for applications with lower power density applications. PHES is considered to be the lowest on both power and energy densities, suiting them for long-term operations like seasonal energy buffering.

Apart from the power density and energy density, other parameters such as discharging rate C-rate, depth of discharge (DOD), cost, and lifetime are more often considered vital characteristics in the selection of storage. For example, Li-ion batteries with high discharging C-rates are swiftly replacing lead-acid batteries with low discharging rates and discharging depths. A summary of the

general characteristics of various ESS technologies are summarized in Table A.1 in Appendix A for further comparison.

### **2.2.2 Applications of HESS**

Recent review papers related to the HESS applications have clearly highlighted the advantages of combining complementary characteristics of ESS in HESS [13]. Improving the fluctuations of modern renewables like wind and solar is one such advantage [12]. These suitably integrated HESS are intended to alleviate perturbing power with varying amplitudes and frequencies, which are addressed through different low- and high-speed responses of the integrated storages in HESS.

The second advantageous characteristic of HESS is the lifespan improvement of storage. Frequent cyclic discharging has resulted the battery and fuel cell-related technologies to degrade rapidly. Therefore, the second storage device with high cycle life shall be introduced to smoothen the battery power profile to extend the battery life span. For example, battery-SC is a relatively mature HESS technology which enhances the battery lifetime by 19% as shown in [14]. Power quality improvement and stability are the third significant benefit of HESS. Key grid services like frequency regulation and harmonic mitigation are also possible with HESS in conventional power system [15]. Recent real-world scenarios of HESS implementations are also reported in the literature. Few of such well-known applications are the 1.2MW SC/Battery HESS installation in North Carolina, United States by Duke energy to handle the peak demand response and the 1MWh VR/Li-ion battery HESS developed for Monash University for Solar PV dispatching pilot studies [13].

### **2.2.3 Capacity determination of storage components of HESS**

The introduction of HESS into the power system is quite noticeable in the literature, considering both its advantages and the recent real-world applications. When different types of storage devices are integrated to form one hybrid energy storage scheme, it is vital to ensure that their characteristics complement each other well [16]. Thus, the capacity determination techniques should ensure the accurate allocation of capacities of constituent storages of HESS. Advantages and disadvantages of the existing capacity determination methods of HESS are extensively discussed in the review paper [17]. As found in the literature, the classification of capacity determination techniques for HESS

applications can be depicted as shown in Figure 2.1. These techniques are primarily divided into three categories: traditional methods, optimization methods, and methods based on software tools.

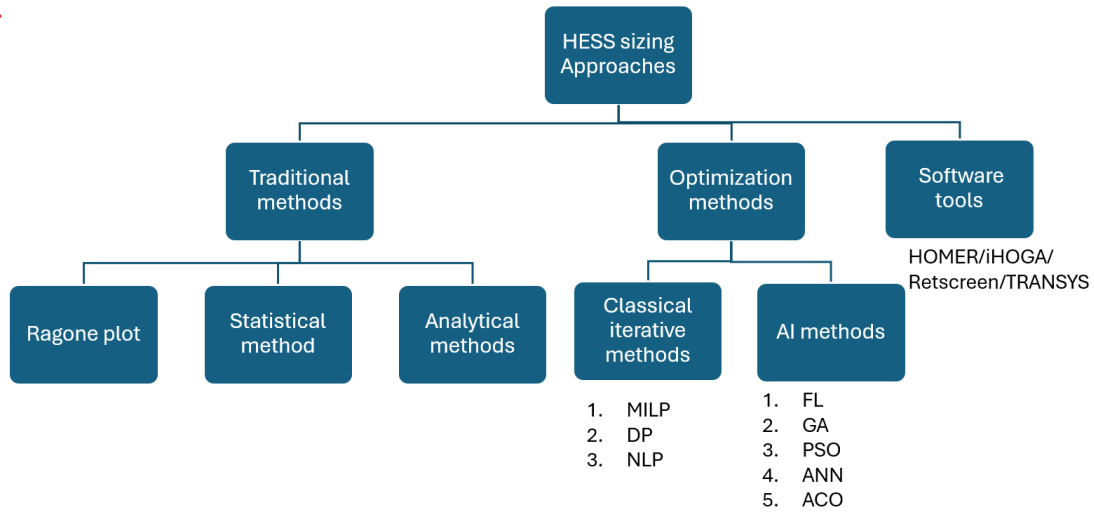


**Figure 2.1. Classification of capacity determination approaches of HESS**

Under the traditional methods of sizing, Ragone plots are used to compare the performance of the storages of HESS in energy/ power graphical space. This gives an idea of the operating constraints of the different ESS in a HESS. However, to obtain a deeper understanding of the dynamics of the storage in real-time operation, this method should be combined with other analytical methods to obtain a more exact solution [18]. Analytical methods are commonly used to size the storages based on the imbalance power of the generation and loads. Generally, the allocation of the power is performed in such a way that high energy density storage supplies low frequency components and high-power density storage provides high frequency power. Therefore, this method attends to the technical aspects of allocation, ensuring that the segregation of the power components aligns more closely with ESS dynamics. As a result, analytical methods excel in addressing the technical aspects of the HESS design compared to other methods. Frequency-based decomposition methods are such commonly practiced analytical methods [19]. Statistical methods can be readily used in real-world applications as the statistical significance of the design can be compared with the cost. However, without combining statistical method with an analytical method, the dynamics of the storage cannot be well evaluated [20]. Statistical techniques, such as Monte Carlo method, have been commonly reported in literature [21] to determine the capacities of battery and SC in HESS application.

An iterative method is an algorithm based on recursive process, which gives the end result when the optimum system design is attained. Currently, software like MATLAB integrates these traditional optimization algorithms to easily formulate the problem. As recursive calculations are

performed, these methods usually demand more computational resources compared to analytical methods. Consequently, when applied to systems combining multiple storages, the feasibility of iterative methods can become significantly challenging.

Compared with traditional optimization methods, AI algorithms can solve nonlinear and complex problems, and also deal with incomplete data and intermittent problems of solar/wind power. However, the inconvenience of this method is considerable due to the lack of transparency in solution method. In addition to the methods reported in the literature, commercial software like HOMER PRO, Transys are mostly used in the industrial applications. However, these are still not designed to formulate the problem while considering the dynamics of the storages. Mostly economic aspects are covered in the optimization, while the technical limitations are defined in the constraints of the program. For example, a user defined storage control algorithm cannot be designed using the HOMER PRO to test its optimal operation. Therefore, the flexibility and applicability of these software to the modern microgrid based systems are considerably limited. Comparative advantages of the aforementioned HESS sizing methods are summarized in Table 2.1.

**Table 2.1 Summary of advantages and disadvantages of HESS sizing methods reported in the literature.**

<b>Sizing method</b>	<b>Advantages</b>	<b>Disadvantages</b>	<b>Examples</b>
Graphical methods (Ragone plots)	Can be defined for any type of storage.	Dynamic performance of the storages is not displayed.	[18]
Probabilistic method	Simple to analyze More flexible capacity for design requirement can be chosen.	Cannot present dynamics of ESS alone	[20] [21]
Analytical method	Simple and easy to understand. Rapid and straightforward	Approximations of the system components makes it less generalized.	[22]
Classical Optimization methods (iterative methods)	Easy to formulate the problem	Require high computational resources compared to analytical method	[23],[24],[25]
AI methods	Ability to solve nonlinear and complex problems.	Inconvenience due to the complex processing	Fuzzy [26] GA [27] PSO [28]
Software tools (HOMER Pro, HYBRID, TRANSYS)	Easy to use without prior knowledge of the system components	Difficulty to apply for a generalized storage scheme. Some necessary parameters are not integrated in the problem formulation	[29]

Based on the key highlights in the aforementioned review studies on the sizing approaches, the following critical points can be summarized.

1. Optimization methods outperform the traditional sizing methods due to their notable advances, such as high performance, ability to handle complex scenarios, and support for multi-objective functions. However, a common drawback of all optimization methods is their tendency to be time-consuming and intricate. It is identified that the AI-based optimization methods are prone to fall into local optima as the complexity of the hybrid system increases.
2. A high volume of papers is reported under the category of the optimization-based storage capacity sizing methods. However, one common issue with these types of methods is their complexity in solving them in an application with multiple storages in HESS. Thus, the suitability of such methods for generalized HESS schemes is highly questionable. In addition, defining the storages dynamics is very rarely practiced in these types of capacity determination techniques. As mentioned, only the constraints are considered in the optimization process in order to ensure the dynamic ability of the storages.
3. While the statistical methods are suitable for decision making, they should be combined with the analytical approach for a better understanding of the system design. Thus, a novel method is required where both approaches are combined.
4. Existing software tools for sizing a HESS are still at the preliminary stages of development, which limits their flexibility in defining the multi-objective problem during the planning process of HESS for a modern microgrid with high renewable penetration.
5. Previous studies have highlighted that the input data for the storage capacity determination is heavily impacted by insufficient data in both load and PV variations [16]. Calculation time steps used in the existing optimization process of one year are limited to hourly. Therefore, the accuracy should be improved with smaller time steps particularly when the design consideration is to deal with short-term fluctuations. This will obviously increase the calculation burden, where optimization algorithms that require higher computation resources would not be a suitable option for designing such short-term ESS operation.
6. The suitability of the hybrid storage systems should be determined after an accurate mapping between the net-load demand and storage characteristics. The existing studies mainly focus on economic and reliability indicators. The scale of the application, degree of power fluctuations and required energy demand are factors to be considered. These factors are not sufficiently discussed in the existing techno-economic studies as such in [30]. Important dynamic such as



response time delays of storages are missed out from the constraints and objectives. Therefore, the optimisation algorithm is only aware of storages as a medium with different cost indexes and SOC constraints. However, in reality, storage chemistries are completely different from one to another, affecting their performance which was not well-awared by existing sizing optimisation methods.

7. The storage capacity optimisation research on different scale and different configurations (centralized and decentralized) needs to be improved [17] and requires more attention in depth.

#### **2.2.4 Frequency-based capacity determination of storage components of HESS**

In the literature, it is noted that frequency-domain representation can be employed within analytical methods for sizing storage to differentiate the storage devices. This presents a way of reflecting the storage response characteristics with respect to the frequency which is an alternative approach to the Ragone plots described in existing literature. In this section, these frequency-based capacity determination methods are extensively discussed to identify their existing challenges.

In order to demarcate the storages in the frequency domain, the effective frequency ranges of each storage should be determined with respect to a suitable techno-economic parameter. Then the cut-off frequency between these storages can be determined which is vital for capacity determination in frequency-based approaches. According to the literature, the most commonly reported cut-off frequency determination methods are inherited from the trial-and-error approach [19, 31-34]. Generally, for all of these studies, cut-off frequency is determined to serve the objective of optimizing the total annualized cost of HESS. The common structure of such optimization algorithm to determine cut-off frequency is depicted in Figure 2.2. It shows that initially, the net power will be decomposed based on an arbitrarily selected cut-off frequency, which will then segregate the net power into a high- and low- frequency components. As is often the case, the lower frequency component will be used to determine the capacity of a battery while the high frequency component is used to determine the energy storage capacity of a comparatively fast responsive storage like SC. Both of these power components then be evaluated using the degradation models of the respective storages to determine their lifetime. Finally, the annualized capital cost of the hybrid energy storage scheme is calculated, and the respective capital cost is estimated. By adjusting the cut-off frequency, the total capital cost will be minimized. This optimization-based method, or its variants with other associated cost indexes, was commonly used in existing literature to determine the cut-off frequency.

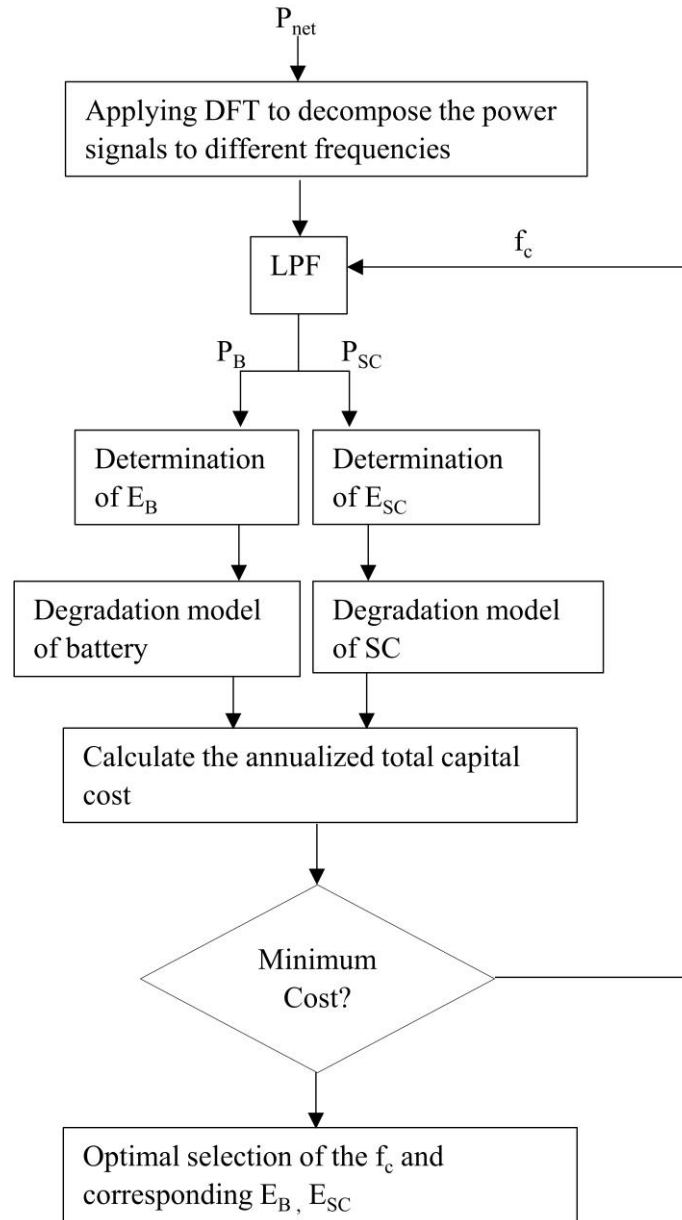


**Figure 2.2. General algorithm used in literature to determine cut-off frequency**

Many examples are reported in the literature which follows the basis of this presented algorithm. In [19], Fourier Transform is used for frequency analysis in sizing SC-battery combination to maintain the power balance of an isolated system. The objective function considers the expected lifespan cost of each storage. Here, the variations of net power resulting from wind fluctuations are divided into three components using Fourier analysis and SC is used to buffer fast power fluctuations. Authors in [35] proposed SC and Fuel Cell as components of HESS where SC power is determined by a high

pass filter. Fuel Cell and grid power are obtained by the rest of the lower frequency fluctuating components. In [22], FT is used to decompose the net power variation to realize four different fluctuating components namely very short-term, short-term, intraday and outer day components. The spectral analysis methods are used to determine the HESS capacity. Research presented in [36] also practiced the DFT-based method to separate fast cycling components like intra hour from slow cycling intraday components to design HESS. However, in both of the aforementioned works, the cut-off frequency is determined without a theoretical basis and introduced as a parameter that can be varied based on the cost parameters. Authors in [31] used a DFT-based coordinated dispatch strategy to allocate the power between the ESS and diesel generators in the frequency domain. Optimal cut-off frequency is determined using economic evaluation and gradient search procedure. In [37], DFT based method is used to obtain the frequency of the variations and cut-off frequency is numerically optimized to obtain the minimum cost of HESS configuration. In [38], adaptively cut-off frequency between the battery and SC is determined in the operation considering their SOC levels. However, this allocation does not consider the lifetime operation of the battery in the event of handling the higher frequency components of PV variations. Authors of [33] determine the cut-off frequency of low pass filter between battery and SC using PSO algorithm to obtain the minimal total cost of including battery degradation cost. In [39], PSO-NM algorithm is used for a feasible optimal solution in terms of weight, cost and battery lifetime of HESS employed for vehicular applications. Results show that the proposed algorithm outperforms GA and PSO based on computational metrics.

The cut-off frequency determination technique shown in Figure 2.2 does not ensure that the allocated frequency components would be sufficiently buffered by respective storages. This is due to the fact that the cut-off frequency is determined only based on the economic perspective. Therefore, solely economic optimization in determining cut-off frequency is not suitable for a planning study of HESS. A different optimization parameter is introduced in [40] specified as ‘minimum overlap energy’. This parameter explains the undesirable coupling between the storage devices in HESS which needs to be minimized at the design stage through an iterative method. Even though this provides some theoretical basis for determining the critical frequency, the dynamic characteristics of the ESS are not considered here. Thus, all the above iterative methods provide a lack of insights into the dynamic characteristics of the ESS in HESS design. In addition, advanced iterative process such as in [39], may lead to a heavy computation burden. Also defining an objective

function for optimization with different weights can lead to ambiguity which makes these approaches less suitable when compared to an analytical approach.

### **2.2.5 Research Gap**

Though the cut-off frequency defining methods used in the design stage consider the optimum cost of the design, the dynamic response characteristics of individual ESS are mostly ignored. Typically, ESS are treated merely as devices with different cost indices in the optimization algorithm. Therefore, it is imperative to consider both the dynamic characteristics of ESS and their associated capital costs when determining the cut-off frequency. Specifically, the dependence of ESS capacities on operating frequency should be taken into account, reflecting the unique dynamic response of each storage component to various frequency components. Secondly, the trial-and-error methods followed in the literature to determine the cut-off frequencies are computationally intensive. These computationally intensive methods are not suitable for a planning problem with a hierarchical storage scheme of three or more storage technologies in different locations of the power system. Therefore, an analytical and sufficiently generalized method is required to allocate the different frequency components of the net power to the constituent storages of the HESS. Moreover, given the intermittency of renewable applications, it is crucial to utilize statistical significance during the capacity determination design process to ensure the design confidence of the proposed system.

### **2.3 Frequency-based Analysis using Empirical Methods**

The complexity of the natural processes of daily observations arises from the composition of multiple components which makes the descriptive analysis difficult. For instance, analysis of weather-related precipitation charts is challenging due to the components related to the short-term interactions such as cyclones, heat-waves as well as more general variations like daily-hourly cycles and seasonal changes. This will give rise to the rightful desire to breakdown the complicated process into individual components and analyze each segregated component separately. This simplifies and enhances the analysis process, leading to a deeper understanding of the insights and improved forecast reliability. The analysis can be performed in either the time or the frequency domains. Time series analysis, such as that reported in [41] provides very little information on the variability of the PV power. First and foremost, this time domain analysis may struggle to capture the rapid changes in PV fluctuations as they are more susceptible to the noise of the data. On the other hand, frequency-based analysis has improved filtering and noise reduction facilitates. Analyzing raw time-series data

can be less intuitive to interpret complex variations compared to frequency domain analysis. Thus, the probabilistic approach has often been used to analyze the time series data for a long time, due to the stochastic nature of the harnessed power [41].

### **2.3.1 Traditional frequency-based signal analyzing methods**

Traditionally, extracting relevant information from the original signal, often termed as “mother signal” can be performed by the decomposition and spectral analysis techniques. One such traditional method is Fourier Transform (FT) which results in decomposition of the initial process into harmonic functions with fixed frequencies and amplitudes. Fourier methods use a series of sines and cosines as basic functions to represent the data signal. Thus, the amplitude and frequency of the resulting components are constant which means that if the nature of the initial sequence was changing over time, such changes will not be reflected in the transformation results. Therefore, the transform assumes the stationarity of the initial data. Non-stationary behaviour of dataset refers to data points that often have means, variances and covariances that change over time. This indicates the presence of trends, cycles, random variations or a combination of the above three. Therefore, non-stationary data are unsuitable for predictions, and extracting reliable results necessitates transforming them into a set of stationary data. This transformation process often requires the utilization of decomposition techniques.

Other than stationarity, linearity is also required for the Fourier Spectral analysis. Linearity is defined to be having mathematical proportionality between inputs and outputs. Nonlinear systems often exhibit the disproportionality or complex changes in the output which make them challenging to predict and analyze. It is evident that many natural phenomena have the tendency to be nonlinear even though they are approximated by linear systems. This is mainly due to the sudden variations in the phenomena which is out of the trend that we expect. As an example, the expected variation of the solar insolation can be changed due to cloud cover which is an instantaneous result of meteorological changes. This will result in the extracted solar PV power to be non-stationary and frequently non-linear.

Therefore, if such a PV power signal is analyzed by assuming the stationarity and linearity, false results usually cannot be avoided. For above reasons, Fourier spectral analysis is limited in effective use to analyze non-stationary nonlinear data signal. Such attempt is reported in [42] to show how frequency-domain analysis can be used to determine the capacity of HESS. As an alternative to the FT analysis of non-stationary signal, a wavelet transform (WT) is recommended.

Even the decomposition is similar in a fixed basis of functions as same as FT, unlike the FT this basis can be preset, i.e. a wavelet used in transform can be selected. In contrast to the FT, every component resulting from the WT has parameters that determine its scale which allows to overcome the issue of the non-stationarity of process. The major drawback of the WT is its non-adaptive nature. In spite of the drawbacks, WT has been considered as the major non-stationary analysis method which has been reported in previous power system analysis. Wavelet transform has been used in the design studies of HESS in [43, 44], as the technique is more suitable than the FT in analyzing nonlinear signals. The success of the technique depends very much on the selection of suitable mother wavelet, but it can be difficult to have such prior knowledge in practice.

Even though both Fourier and wavelet have widely recognized mathematical techniques to analyze complex signals, for practical non-linear non-stationary signals, it is desirable to use a decomposition method with an adaptive basis determined by the initial sequence. Aiming such an objective, the Empirical Mode Decomposition (EMD) technique was introduced as an alternative and powerful nonlinear signal analysis method which will be discussed in greater detail in this chapter. The basic characteristics of these three signal analysis methods are summarized in Table 2.2 according to [45] .

**Table 2.2 Summary of comparison between FT, WT and EMD**

	FT	WT	EMD
Basis	A priori	A priori	Adaptive
Output	Energy-Frequency	Energy-time-frequency	Energy-time-frequency (amplitudes of components)
Frequency	Convolution, Global, uncertainty	Convolution, Regional, uncertainty	Differentiation, Local, Certainty
Non-linear	No	No	Yes
Non-stationary	No	Yes	Yes
Basis of decomposition	Theoretical	Theoretical	Empirical

### 2.3.2 EMD algorithm and applications

The concept of EMD and the frequency transform of it named as Hilbert-Huang Transform (HHT) has been developed over the years by a wide range of applications in science and engineering since Huang, et al. [46] invented EMD. It has been used in a wide variety of fluctuating signals, including geophysical data [47] rain fall data [48] cardiovascular systems [49] solar irradiance, global temperature data, CO<sub>2</sub> concentration data [50], water flow data [51], analysis of remote sensing data [52] and shown the strengths in identifying the important insights hidden in complex mother signal.

In addition, the applications of the EMD is well established to analyze the historical data sets of in the power applications [53], in power quality assessments [54]. Moreover, forecasting methods of intermittent renewables are well benefited from the EMD according to the Literature [55]. Recently, EMD analysis is used to decompose complex wind data and then to determine the storage capacities [56].

### 2.3.3 Theory of EMD algorithm

EMD is considered to be well-suited to extract information for nonlinear and non-stationary signals in which it leads to clearer spectral analysis, more intuitive and physically meaningful results compared to that produced by FT and wavelets [57, 58]. The initial process of EMD is to decompose the signal into so-called Intrinsic mode function (IMF). The IMF can be linear or nonlinear and can be non-stationary.

IMF is a function that satisfies two conditions:

1. *In the whole dataset, the number of extrema and the number of zero crossings must either equal or differ at most by one.*
2. *At any point, the mean value of the envelope defined by the local maxima and the envelope defined by the local minima is zero.*

The decomposition algorithm utilizes a sifting process, the details of which are described in [46] depicted in Figure A.3 in Appendix A. In Brief, at the initial step of the sifting process, the maxima and minima of the given signal are located. Then, using a cubic spline or other interpolation method, the upper and lower envelopes are obtained. Next, the mean values of these envelopes are evaluated and then subtracted from the original signal to obtain the first IMF. The above process is repeated on the remainder until the extracted IMF is a monotonic function, which is termed the residue or trend. Transformation of these extracted IMFs to the frequencies is the next step. When the signal is subjected to non-stationarity where the frequency and amplitudes change over time, the notion of more flexible definitions is required for both, particularly for frequency. The concept of the instantaneous frequency has been introduced to serve this purpose, as an alternative to the cycle frequency in the theorem of HHT [59]. Through the application of Hilbert transform, the so-called instantaneous frequencies of the IMFs can be readily obtained [46].

### 2.3.4 Salient features of EMD

The salient features of the EMD can be summarized below [60].

1. Calculation of the instantaneous frequency will not include the unwanted fluctuations induced by asymmetric waveforms. According to the definition of IMF, the IMF in each cycle, defined by zero crossings involves only one mode of oscillation, no complexities are allowed.
2. An IMF is not restricted to a narrow band signal. It can be both amplitude and frequency modulated. In fact, it can be non-stationary.
3. If a signal has two or more superimposed periodic components that have periods closer than a factor of two, the extracted IMF will be the superposition of all the components within that dyadic range [61, 62].

### 2.3.5 Drawbacks of EMD and recent development

The major drawbacks of analyzing data in EMD are identified as the end-point effect and mode mixing in the literature. Both of these recognized drawbacks are caused by the uncertainty in identification of upper and lower envelopes due to (a)uncertainty in detecting maximum and minimum including end points; (b)irregular distribution of local maxima and minima. These drawbacks could be minimized by introducing improvements to maxima and minima detection algorithm and effective implementation of noise-assisted methods. A major issue of EMD reported in previous studies is the mode mixing when a single IMF contains multiple frequency components that should be separated into different IMFs. The intermittency of the composite signal exacerbates which can make the physical meaning of the IMF unclear. To overcome this inherent issue greatly, the noise-assisted EMD variants are introduced by the authors in [63]. Some recent advancements to these noise-assisted methods have resulted in introducing new variants of the EMD technique as listed below. These recent variants of the EMD transformed the algorithm into very powerful and adaptive tool suitable to the analysis in different scenarios [47].

1. Ensemble empirical mode decomposition (EEMD) [63]/ Complementary Ensemble Empirical Mode Decomposition [64, 65]
2. Compact empirical mode decomposition (CEMD) [1]
3. Complete ensemble empirical mode decomposition with adaptive noise (CEEMDAN) [66]
4. Sliding window empirical mode decomposition (SWEMD) [67]
5. Robust empirical mode decomposition (REMD) [68]



As a well-established heuristic method, inbuilt tools for EMD have also been released recently in the signal processing toolset of MATLAB [69].

### **2.3.6 Research Gap**

In this framework, the successful application of the empirical techniques was quite evident in order to obtain an accurate characterization of the non-linear, non-stationary and non-periodic signals. Particularly the EMD, when combined with HHT analysis employs a decomposition method that enables a comprehensive analysis of composite signals by providing time-varying frequency profiles. The HHT-EMD produces a balanced analysis between both empirical and mathematical which is often considered as the best match to effectively characterize the complex signal like net power resulting from renewable and load power fluctuations.

However as shown in Section 2.2.4, most of the frequency-based analysis methods used in determining the required capacities of the ESS rely heavily on the DFT and WT methods which are non-adaptive. In applications that are mostly relevant to renewables, these types of frequency-based analysis methods are not suitable as a priori basis is required. In contrast, empirical methods are helpful in extracting the dominant modes, particularly in renewable applications. The utilization of EMD-HHT based methods in PV applications, as reported in the literature, is largely negligible. Hence, there is a need for a concerted effort to incorporate the EMD-HHT based method to analyze the modes present in PV applications.

## **2.4 Li-ion Battery Degradation**

Li-ion battery technology is the benchmark energy storage technology for various applications in power system due to its combined benefits of high energy density, longevity and compactness. These features make it the most suitable battery technology showing the best economic and environmental performance in recent studies of community level batteries [70]. Nevertheless, different types of ageing phenomena continue to degrade the performance of Li-ion battery as the usable capacity of it reduces with time and usage. Li-ion battery consists of four main components such as graphite anode, cathode made with composites of lithium (commonly used lithium-iron-phosphate, lithium nickel-manganese-cobalt oxide), electrolyte and separator. During charging, at the anode, lithium ions are absorbed into the graphite layers, a process known as intercalation. Simultaneously, electrons are released from the anode and flow through the external circuit to the cathode. At the cathode, lithium ions and electrons combine with lithium cobalt oxide, forming a stable compound.

During discharging, at the anode, lithium ions leave the graphite layers and move into the electrolyte, releasing electrons in the process. These electrons flow through the external circuit, providing electric current in the opposite direction. Over time, the chemical process of intercalation and deintercalation leads to battery degradation.

### **2.4.1 Overview of different Li-ion battery degradation phenomena**

The Li-ion battery degradation phenomena can be divided into two different types based on their ageing pattern.

1. Calendar ageing: This occurs in the cell even when the battery is in an idle state (when battery is neither charging nor discharging). Calendar ageing results from ongoing side reactions that arise due to the continuous interaction among the internal materials. (Time, temperature, and SOC are the factors contributing to calendar ageing)
2. Cyclic ageing: This describes the ageing from the charging/discharging cycling of the battery. (Full equivalent cycles, temperature, C-rate, charge and discharge cut-off voltage, Depth of discharge, SOC are the factors contributing to cyclic ageing)

Figure 2.3 depicts the different types of Li-ion battery degradation phenomena, their relationships to the different root causes, and the measurable effects, as mentioned in the [71].

A wide range of studies in recent literature has explained the diverse degradation phenomena observed in batteries, including Solid Electrolyte Interphase (SEI) growth and lithium plating predominantly occurring at the anode. Additionally, the cathode material is principally impacted by phenomena such as current collector corrosion, structural disordering, particle cracking, and transitional metal dissolution [72].

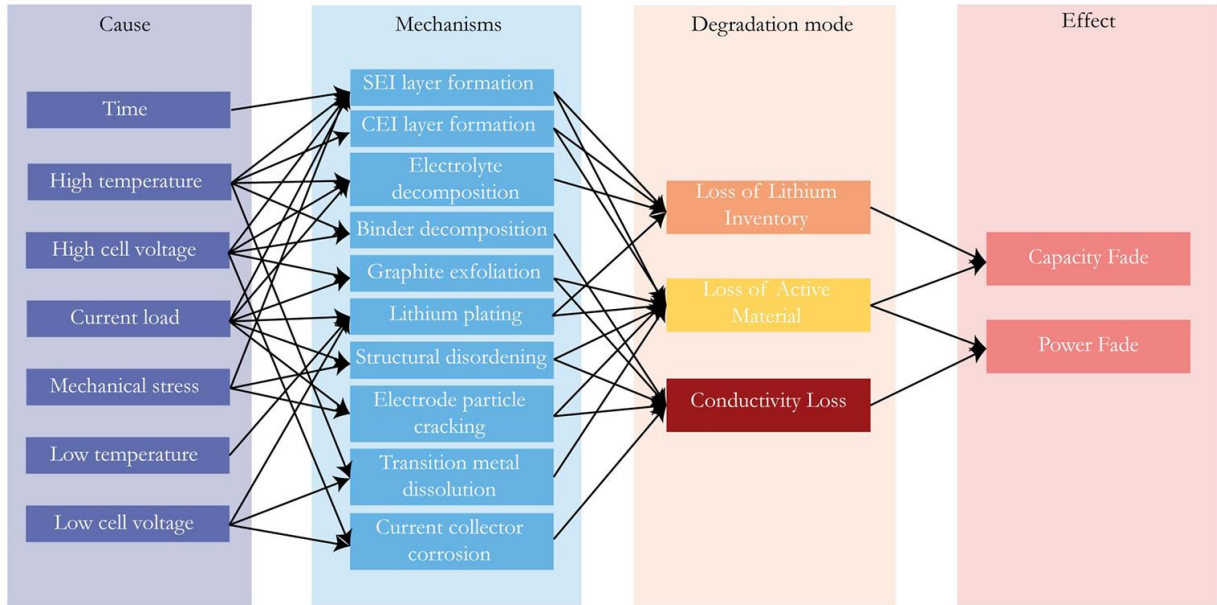


**Figure 2.3. Degradation phenomena of the Li-ion battery and its relationship to the measurable effects**  
 (The figure is the replica of Figure 2 in [71]).

These processes contribute to the depletion of active lithium-ion inventory, loss of active material, and diminished conductivity, consequently leading to capacity degradation and increased resistance within the Li-ion battery. Both capacity degradation and rising resistance significantly impair the battery's performance over time. The end-of-life (EOL) of battery is defined based on these two parameters. One way it reaches EOL is through capacity degradation, resulting in a decrease in open circuit voltage below the minimum threshold. Additionally, when resistance increases to the maximum allowable level of power fade, the battery is considered to have reached its EOL.

Among the various degradation phenomena mentioned, SEI growth and Li-plating are regarded as the most predominant ageing mechanisms. Li-plating, in particular, tends to dominate towards the EOL phase of the battery, whereas SEI growth predominantly affects the battery's performance during the majority of its operating period [73]. Consequently, this work focuses its discussion on SEI growth as the primary degradation phenomenon during Li-ion battery operation, acknowledging that other degradation mechanisms may also influence the battery's lifespan.

SEI growth occurs when graphite from the anode reacts with the electrolyte and lithium-ion at the electrode/electrolyte interface. This results in forming a thin layer of components with a permanent chemical bond. This layer consists of unreactive compounds, that prevent further intercalation of lithium ions, causing lithium ions to deposit onto the layer instead. This leads to a

loss of cycleable lithium-ion inventory, a process that is irreversible. Initially, SEI forms within the first few cycles, acting as a conductor for ions while shielding the anode from solvent molecule co-intercalation and further electrolyte decomposition. Recent studies show that SEI layer of anode consists of two layers: a compact inner layer with inorganic products and a porous outer layer with organic compounds. It is suggested that the outer layer is more unstable and the diffusion phenomena happens in this layer and continues to grow during cycling [74].

While predominantly forming during the initial charge, the formation of the SEI layer continues gradually even after the first cycle until the SEI layer is fully developed. An optimized SEI layer is expected to have low electrical conductivity and high resistance to electrolyte diffusion, as well as high selectivity and permeability to lithium ions. Once established, the SEI layer inhibits further decomposition reactions with salts and solvents by preventing electron passage, thereby increasing electronic resistance and stabilizing the surface potential of the graphite within the stability range of the electrolyte. However, in practice, the SEI layer gradually thickens over successive charge-discharge cycles due to electron exposure to the electrolyte or electrolyte diffusion onto the graphite surface. Despite this, the rate of layer thickness growth diminishes significantly after the initial cycle. The gradual thickening of the layer results in the consumption of lithium ions, solvents, and salts, consequently elevating cell resistance. This continuous growth of the SEI layer during the formation cycling process ultimately reduces cell capacity and coulombic efficiency.

Interestingly the growth of the SEI not only happens during cycling. When battery is not in use, there will be a potential drop across the electrolyte causing slow movement of lithium ions from the electrode to the electrolyte which will cause the lithium-ions to react with the electrolyte to form SEI. Therefore, the growth of the SEI also has an effect due to the calendar ageing [75]. Three direct factors that have significant effect on the growth of the SEI layer can be summarized as;

1. SOC of the battery cell
2. Current of the charging/discharging
3. Temperature.

However, previous experimental studies show that cycle life of Li-ion batteries does not significantly change with normal operating temperatures [76]. Therefore, if it is assumed that the Li-ion battery is installed inside a battery cabinet with the sufficient cooling system under minimum temperature deviation, it can be inferred that the temperature effects on the SEI growth are minimal.

## 2.4.2 Overview of Li-ion battery degradation modeling

Degradation models quantify the ageing effects of the battery concerning operating conditions and cell properties. This summary solely focuses on quantifying capacity loss through degradation modeling as documented in the literature. Empirical models, semi-empirical models, and physics-based models are utilized for this quantification. Empirical models fit cell ageing data without advanced modeling of the underlying physical mechanisms [77]. Therefore, the applications of these models are only limited to similar types of operation scenarios. Therefore, the suitability of these methods for renewable applications, where charging and discharging are intermittent, is uncertain. Semi-empirical models rely on data of cell ageing studies. However, for model fitting, these models use functions that describe the underlying ageing mechanisms. The superposition approach of calendar and cyclic losses will be used to quantify the total capacity loss in this approach [75]. For example, battery degradation-aware SOC control has been the topic of discussion in [78] whereby the battery degradation is assessed using the traditional rain-flow counting method. In renewable energy applications, however, the operations of the battery involve partial charging-discharging cycles. Therefore, it remains unclear whether the cycle counting method used in [78] would be suitable in estimating the degradation level of the battery. In contrast, physicochemical models define the cell degradation mechanism through a set of differential equations. They mostly focus on individual degradation mechanisms such as SEI growth and particle cracking. Single particle model (SPM) and P2D models are the most frequently practiced models for these physicochemical models [79]. Due to the detail modeling of the degradation phenomenon, physicochemical models are often computationally intensive compared to the empirical and semi-empirical methods which offer more accurate modelling even during partial charging/discharging of the battery [80]. However, this modelling approach has yet to be commonly employed in practical ageing-aware applications.

## 2.4.3 Ageing-aware operation

In this section, the focus will be on examining literature pertaining to strategies for operating batteries with ageing awareness. Within the literature, various terms are used to describe the process of determining charging and discharging strategies, such as energy management, scheduling, control, dispatch, or operation. Among these terms, "scheduling" is often employed in most papers, encompassing the concepts represented by the other terms. The approaches aimed at integrating battery degradation considerations into scheduling are commonly referred to as ageing-aware

scheduling methods. These ageing-aware scheduling methods can be divided into two major sections: rule-based and optimization-based methods and further classification of these methods in the literature can be presented as in Figure 2.4.

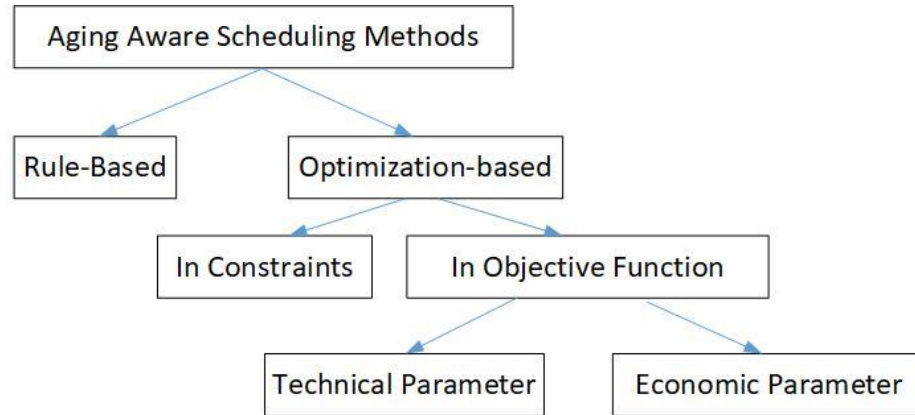


**Figure 2.4. Classification of the ageing-aware scheduling methods reported in the literature.**

1. **Rule-Based methods:** - Rule-based methods are relatively less common in battery scheduling literature. However, they are specifically targeted at improving technical or economic factors through defining a set of rules for operation. For example, as demonstrated by authors in [81] show that the 12 % decrease in the levelized cost of electricity can be achieved by rule-based and forecasting-based battery control. Nevertheless, due to the complexity of the defining rules and lack of mathematical basis for these, the implementation of the rule-based methods is less frequent. On the contrary, the computation burden far less compared to the optimization methods. Therefore, the complex degradation phenomena can be successfully integrated into these rule-based ageing-aware scheduling methods.
2. **Optimization-based methods:** - The majority of the literature is related to optimization-based methods which is targeted to minimize/ maximize the desired objective function. In these scheduling methods, ageing awareness is occasionally incorporated into the constraints, which is a simpler method of representation compared to including them directly in the objective function in a more comprehensive approach. For instance, in [82] authors introduced limits for the depth of discharge to limit the degradation. Wankmuller et al. limited the SOC range to 60% of the original battery capacity and investigated the techno-economic impact of different limits for the C-rate as part of their analysis [83]. Shi et al. limited the usable SOC range to 70% of the original battery capacity [84]. If these factors

related to the degradation are included in the objective function, they would typically be represented either within an economic function or through the utilization of technical parameters. A significantly larger set of publications have used economic optimization. This is achieved by either allocating a monetary value considering the degradation cost. In addition, multi-objective approaches allow to include technical parameters in the objective function alongside economic parameters for the profit gained in an application. For instance, authors have introduced the multi-objective optimization approach where revenue and degradation are considered using a weighting factor [85].

Based on the literature, optimization strategies can be divided into three categories of algorithms: exact solution approaches, heuristics and meta-heuristics. The most common methods of algorithms are in exact solution approaches. This group includes linear, nonlinear (NLP) [86], mixed integer linear programming (MILP) [87], and Dynamic programming(DP) [88] problems that include a linear objective function and linear constraints. In [85], an empirical model of battery degradation is considered in relation to the SOC of the battery. In addition, the authors used a multi-objective optimization using the MILP method to maximize the revenue including the degradation cost in objective function. Here, the dataset with a sufficiently lengthy time to identify seasonal effects and a higher sampling rate to identify short-term power fluctuations could not be analysed using these optimization methods due to the heavy computation burden.

The second group includes heuristics algorithms such as fuzzy logic and gradient method. Compared to exact solution approaches, heuristic methods are fast and complex non-linear relationships can be effectively performed. However, they can stick to a local optimum. Thirdly, meta-heuristics approaches such as swarm intelligence and neural network methods are considered. Hossain et al. and Li et al. applied PSO techniques in the context of microgrid communities and bidirectional electric vehicles, respectively [89, 90]. In both studies, degradation was actively incorporated into the fitness functions of the optimization method, with the degradation model implemented using a rain-flow algorithm to ascertain the energy throughput. Liu et al. utilized an electrothermal-ageing model in their optimization problem, which captures the nonlinear electrical, thermal, and degradation dynamics of lithium-ion batteries. They solved this problem using the NSGA-II algorithm [91]. Their findings revealed that the selected genetic algorithm proves to be a feasible choice for determining the optimal operation strategy, enabling the modeling of nonlinear processes and the inclusion of constraints within the optimization algorithm. Another study reported in [92] incorporates the battery ageing parameters in relation to the SOC and peak power in the

battery management system while active and reactive power management of the BESS is performed. The effect of the depth of discharge in the life cycle and the peak power constraints on the charging power are only concerned in the degradation model. As a result, the study fails to capture the varying degrees of degradation that occur with different charging rates. More literature on ageing-aware battery control can be found in [93] in which the power allocation for the battery is such that ageing is minimized. Similar in approach to many other reported works in this field, the authors have utilized the empirical model of battery charging cycles vs depth-of-discharge characteristics for the lifetime estimation. due to the high computational burdens required and is an area which remains to be explored. In [94], in the process of smoothing the PV power, the SOC reference value is determined based on the PV data of the past week and the so-called net load power reference curve. This reference curve is generated from the low-frequency components of the net load power, which are determined using a fast Fourier transform of the net load. Unfortunately, the use of the past week PV dataset will not be sufficient to detect the seasonal variation patterns in the SOC. A summary of the papers related to degradation-conscious SOC control can be presented in the tabular format in Table 2.3.

**Table 2.3 Summary of literature related to degradation-conscious SOC control**

Reference	Scheduling method	Degradation model	Included stress factors	Optimizing parameter	Remarks
Fan [93]	Rule-based control	Semi-empirical	C-rate,SOC	Ageing cost	Calendar ageing is ignored.
Li [95]	DP	Semi-empirical	SOC, temperature time	Economic optimisation	Calendar aging is linked to economic factor
Maheshwari [96]	MILP	Empirical	DOD, C-rate	Energy arbitrage	Cycle aging linked to economic factor
Abdulla [97]	DP	Empirical	DOD, C-rate, SOC	Self-consumption	Penalty factor Cumulative degradation and cost savings based on BESS
Mishra [78]	Rule-based control	Semi empirical (Arrhenisus equation and Tafel equation)	SOC, DOD temperature	Self-consumption and energy arbitrage	Battery life performance and economic benefit separately analyzed in different



					operating modes
Liu [91]	Optimization (NSGA-II)	Semi-empirical	SOC, DOD temperature	V2G energy transfer	Penalty factor based on the EOL is used
Kazemi [98]	Robust-optimization	Empirical	DOD	Aging cost	Bender's Decomposition is employed to solve the long-term scheduling problem, nonlinear

## 2.4.4 Research Gap

As pointed out in the above literature pertaining to degradation-conscious battery SOC control, the following issues are identified as the major drawbacks of the existing studies [73].

1. The first is the comparatively simple battery degradation models practiced in the existing techno-economic assessments with degradation costs that cannot provide sufficiently accurate modelling of Li-ion battery degradation. For instance, the prevalent cycle counting models for battery degradation assume that the same variation in the SOC at both high and low SOC ranges results in equivalent degradation [99]. Most of the reported literature as presented in Table 2.3 is related to the empirical degradation modelling where the physical phenomena of the degradation characteristics are not well understood.
2. The second is the existing degradation models that are used for ESS operation such as in [95] have not considered the limitations of C-rate in charge and discharge that will affect dominant ageing mechanisms of Li-ion batteries. This has been recognized as a significant limitation stemming from the inadequacy of degradation modeling, as the initial determination of Li-ion battery degradation relies on both SOC and C-rate. Even though the reported literature has presented some studies with the C-rate, their insights such as differentiation between charging and discharging are not covered in these studies.
3. Study [100], which illustrates the comparison of the different degradation models, shows the physics-based degradation models are more accurate under different C-rate and SOC conditions in comparison to the empirical battery degradation models. According to the more detailed physics-based degradation models, the degradation effects, such as SEI, differ significantly between these two scenarios. The first scenario causes more degradation than the second. These effects cannot be accurately captured using cycle counting methods. Therefore, the

appropriateness of these methods for estimating battery degradation, especially in renewable applications where charging and discharging occur in partial cycles, is highly questionable. This confirms that the physics-based degradation models closely replicate the battery dynamics in renewable applications which are not adequately studied in the recent literature.

4. The rule-based control methods are less frequently practiced in the literature and these methods are quite case intensive. So that the detailed rule-based method is required which can be readily generalized to a renewable penetrated power system. Also, the concerns like duck curve phenomena are not adequately addressed in these rules of literature.
5. Another issue incorporated with previous studies is the use of cost optimization-based studies which give very limited understanding or insights of the battery dynamics. The major drawback of a such method is in the problem formulation, as more simple representation of battery dynamics has to be used due to the intensive computation of the optimization algorithm. Thus, more accurate physics-based degradation models cannot be commonly practiced in these optimization models. Therefore, most of the optimization studies have used simplified forms in both degradation model and energy management model and then did not pay detailed attention to the operational constraints like grid constraints. For example, authors in [101] have studied the scheduling in PV system with battery storage to achieve multiple objectives of minimizing battery degradation, and grid congestion, while maximizing self-consumption. However, the method for degradation modelling was the less-accurate rain flow cycle counting method for cycle life estimation.

## **2.5 Li-ion Battery SOC Control**

The SOC of the battery bank is the prime battery parameter used to steer the control actions. The EMS of the community storage shall be tasked to control the SOC to realize these objectives comprehensively. For example, a study presented in [102] describes an integrated design of battery energy storage and its EMS, where the EMS targets to fulfill various techno-economic objectives in scheduling and operation. Alongside the primary target of maintaining the power balance between the community microgrid and the main grid, other key concerns of EMS operations include the following.

1. Peak shaving [103] and energy arbitrage [70]
2. Grid ancillary services and system stability concerns [104]
3. Increase lifetime of storages [105]

#### 4. Improve self-sufficiency of the microgrid [106]

The Li-ion battery SOC control strategies discussed here fall in two subtopics: seasonal SOC control, which pertains to long-term SOC management, and intraday SOC control, where adaptive SOC control techniques are predominantly utilized.

##### **2.5.1 Seasonal SOC control**

The seasonal variability of the net load power has been recognized by the authors of [107]. In an attempt to estimate the service lifetime of battery bank, the authors of [107] have developed a method to relate the depth of discharge of the battery with its life cycle. The authors have concluded that the deepest battery discharge occurs during the summer season whereas the deepest charging occurs during the spring season. The authors of [108] have also discussed the planning of a microgrid in different seasons, with the view to reduce the degradation cost. However, their study does not provide insights into the battery degradation when the battery operates over wide dynamic SOC ranges. Hence, there is a great need to re-examine the suitability of strategizing SOC control actions based on short-term historic PV and load data.

In particular, these existing works have proposed the reference value for the battery SOC is to be restored to pre-set value daily. In studies where the reference value is allowed to vary, such as in [94], this has been achieved using the forecasted load and PV powers. The need to provide the forecasts does complicate the design of the battery energy management and control system. Specifically, most of the cited works have attempted to keep the operating SOC within a predetermined SOC range in order to avoid extreme depth-of-discharge battery operating regimes.

##### **2.5.2 Adaptive SOC control methods**

In this subsection, the adaptive battery SOC control methods reported in the literature are analyzed. In reported EMS literature has a common framework for adaptive battery control. Firstly, PV and load forecasting algorithms are used to determine the estimated net power variation. Then, the predictive control mechanism is proposed, where the battery parameters are predicted according to the control algorithm. In most of the reported works, battery degradation model is also integrated to estimate the lifetime parameters of the battery. Thirdly, an optimization algorithm is used to ensure optimal cost of operation at the stage of scheduling of the battery.

One such integrated framework for real-time energy management of PV-battery is proposed in [109] in order to maximize peak hour savings and solar energy usage. A three-step control scheme

is proposed where the first step is the load and PV forecasting. A multi-stage stochastic optimization and a rule-based control procedure are then applied by authors. Authors of [107] discuss the optimal battery management with lifetime modelling where DOD is considered during the battery dispatch. MILP has been used and the cycling counting method is for lifetime estimation. In [110], a stochastic optimization model with Monte Carlo simulation is used to capture uncertainty and again MILP algorithm is used for solution process. Authors of [111] used day ahead forecasting method to control the battery and the cycle counting method is used for the degradation model. Cost-based optimization is used ensuring to deliver/absorb additional power while preventing reduction in expected lifetime of the battery due to overuse.

In [112], the operational objective involves the determination of the power flow limits to be placed on grid power when the microgrid PV generation and load demand are varying. So, in the real-time operational scheme for the microgrid proposed in [112], forecasts of the PV generation and load demand (typically) a day ahead are required. Based on the forecasts, the battery is to operate in accordance with a pre-defined set of rules so as to achieve the given objectives. The forecasting algorithms are integrated into the EMS of the storage to control the SOC while the optimization methods are used to optimally plan the operation of the battery.

A self-adaptive SOC control strategy based on a fuzzy logic controller and PSO optimisation model is used in [113] to determine the optimal capacity of the battery. A similar fuzzy logic controller is employed for the battery management system in [114], which relies on day-ahead forecasted renewable generation and estimated battery SOC level. The proposed battery capacity determination method guarantees the achievement of the lowest levelized cost of energy (LCOE) and the minimum CO<sub>2</sub> emissions.

A related issue is with regard to battery SOC being chosen as the parameter governing the control actions because it is then necessary to specify the reference value for the SOC for which the control actions are to target at. Accordingly, in an attempt to determine the day-ahead power dispatch for a PV-battery energy storage system, the authors in [115] have formulated the control problem to be solved using a chance-constrained stochastic optimization technique, in which a stochastic model is included to yield the predicted PV power. As witnessed in a recent study [116], the primary objective of the battery control strategy is to prevent deep discharges and overcharging of the battery cells. To address this, a double closed-loop control strategy has been proposed, incorporating operational constraints to facilitate the integration of wind power. This strategy automatically adjusts the set-point power to maintain the SOC of the ESS at its initial level.

Additionally, the MPC controller, while considering operational constraints, can effectively restrict overcharging and deep discharging. The paper claims that the proposed control strategy can improve the economic performance of both BESS and the power grid, as well as the smoothing performance of PV power.

In addition to the above shortcomings, the dependency of the studies on the forecasting-based methods is another shortcoming. Authors in [81] determine a target SOC for the battery and then the dispatch happens accordingly. However, this target SOC is determined based on the forecasting of PV and load data which contains considerable errors. It is reported that such forecasting-based methods offer limited robustness due to the higher error percentages in short-term forecasting of stochastic PV and load variations ranging RMSE from 9% to 25% [117]. Therefore, the adaptive SOC control methods abruptly failed to perform accurately during the days with extremely poor solar insolation of winter and the cloudy days of summer.

Compared to the aforementioned studies, a comprehensive adaptive battery control study with degradation reduction is reported in [118]. Here, authors have attempted degradation modelling using the physics-based model and the problem is formulated in order to result in an adaptive method to reduce the energy losses, capacity degradation losses and total operating cost using a multi-objective optimization. Auto-regressive method-based forecasting model is used to facilitate the proposed adaptive controller. It has been shown that the proposed adaptive method reduces battery degradation by 26% compared to the conventional rule-based and non-adaptive controllers. However, the computation time for the proposed method would be around two hours which is considerable for a lower sampling rate like half an hour for three month dataset. In addition, as mentioned earlier, the accuracy of the methodology is highly depending on the accuracy of the PV and load forecasting methods.

Instead, the authors of [119] have proposed a two-stage dispatch scheme which is based on predicted PV power and then dynamically adjusts the battery power flows by taking into consideration the time of sunrise in the different seasons.

### **2.5.3 Research Gap**

Firstly, the seasonal SOC fluctuation is not well understood in the storage management scheme. The research found in the literature under this topic to address this seasonal variation of SOC is quite insufficient. As the lifetime of the battery bank is greatly impacted by the DOD and SOC of the battery bank, clearly it will be prudent to allow the SOC reference value to vary over the seasons.

However, beyond maintaining the operating SOC within a predefined range to prevent extreme DOD, there is a lack of substantial literature on variable SOC referencing methods during different seasons to mitigate degradation. Achieving this would prove advantageous, especially during the long-term planning phase of the battery, particularly for larger-sized batteries.

Secondly, during the intra-day operation of the batteries, as shown in the literature, most of the aforementioned adaptive controlling methods utilized both forecasting and optimization-based approaches with degradation modelling also incorporated into the EMS. The common challenge in the cited articles is conducting a simulation that integrates both forecasting and optimization over an extended time frame with small time steps. This imposes a significant computational burden, primarily due to the tedious solution process. Additionally, uncertainties introduced into the control system are noteworthy due to inaccuracies of the forecasting algorithm, particularly for short-term planning periods such as intra-day or intra-hour. Moreover, the practical implementation of such an intricate planning method for a relatively small power distribution network is rather questionable. Furthermore, these degradation models typically do not consider the charging/ discharging C-rates in detail as the cycling counting methods are mostly practiced. Additionally, these scheduling methods fail to understand the differentiation between charging and discharging currents in degradation analysis. These, research gaps remain unanswered in the existing literature.

## **2.6 Conclusions**

After conducting a thorough review of the literature within each subsection, the following conclusions can be made as the primary gaps in existing studies.

During the HESS capacity determination, the cut-off frequency between constituent storage is not directly determined and also the dynamic characteristics of ESS are not considered. Given the limitations of optimization-based methods in HESS schemes, a direct analytical approach would offer greater generality and result in reduced computation time. A statistical approach can also aid in making design decisions. Empirical methods are not adequately practiced in the frequency-based net power analysis. This will be advantageous over frequently practiced FFT and wavelet-based methods due to their intrinsic nature.

Seasonal SOC referencing is clearly not practiced in the existing storage planning studies. This will be helpful in limiting the storage degradation. Detailed physics-based modelling of the Li-ion battery is not frequently used in renewable applications in order to accurately estimate the dominant degradation phenomena like SEI growth in Li-ion batteries. While optimization studies

commonly address economic considerations in aging-aware control, implementing this in real-time storage control poses challenges. Although short-term forecasting methods receive significant attention in research, their practical implementation for microgrid-level batteries is uncertain. Therefore, a robust adaptive storage control system based on rule-based methods is needed to mitigate degradation concerns. However, existing degradation-aware control methods lack adequate study of C-rate variations in charging and discharging currents.

Thus, a detailed discussion of the aforementioned research gaps is required to be covered in subsequent chapters.

# **CHAPTER 3. Analysis of Net Power of Prosumer via Empirical Mode Decomposition Technique**

## **Statement of Contribution**

Some of the results in this chapter are being developed for a conference paper entitled "Determination of Hybrid Energy Storage System Capacity based on Empirical Mode Decomposition for a High PV Penetrated Standalone Microgrid". The coauthors for this paper include D. Hettiarachchi, S. Shing Choi, S. Rajakaruna, and A. Ghosh <sup>1</sup>

## **3.1 Introduction**

As mentioned in the introductory chapter, unsteady PV power has raised the requirement of energy storages at suitable locations of the modern power system. However, the planning of such storage scheme would not be possible without a careful study of the unsteady variations caused by both PV and load power fluctuations. Time domain analysis often present challenges when it involves non-linear complex signals and where filtering is required. Due to the drawbacks of time domain analysis, the attempt of this chapter is to perform a comprehensive analysis of the net power using frequency-based analysis, in particular using the empirical mode decomposition technique. Therefore, this chapter highlights the important insights discovered by the EMD analysis of the net power, which will be fruitful for the next chapters in designing an appropriate HESS scheme to mitigate the power variations and to facilitate energy buffering effectively.

The chapter has been organized as follows. Section 3.2 gives an introduction to the system under study for this thesis. The proposed method to analyse the net PV power is presented in Section 3.3. Section 3.4 contains the results of the case studies along with a comparison to the existing methods. Main findings from the performed analysis are outlined in Section 3.5 for future work in following chapters.

---

<sup>1</sup> Percentage contributions of the relevant co-authors in the publication are given in the attribution statement, reviewed and signed by the each co-author.



## **3.2 System Under Study**

### **3.2.1 The proposed Hierarchical HESS Scheme for modern power system**

This section targets to provide an outline to the system under study in this thesis. It is expected that the future distribution systems shall be in the form of grid-connected or isolated entities called microgrids with a higher integration of renewable penetration particularly distributed PV. Figure 3.1 illustrates a typical configuration of a modern power system composed of microgrids, where each microgrid is comprised of prosumers, representing individual residential/commercial units. Each prosumer is considered to consist of an installed PV array and variable loads with a suitable integration of HESS. As shall be shown in a later section of the thesis, the proposed HESS consists of two constituent storage devices; one for power conditioning and the other for inter-day energy buffering. Additionally, community-level storage units serve different purposes such as night-peak shifting and enhancing grid independence. Meanwhile, storages with higher energy capacities are designated to work as grid-scaled storages assigned for seasonal storages and grid ancillary services. A real-world pilot study example of such a scheme is the White Gum Valley isolated microgrid which is under test operation in Western Australia where a centralized 670-kWh battery energy storage system has been installed [120]. There are 36 townhouses in this microgrid, and each townhouse is equipped with a 5-kW PV generator, an electric vehicle charger and a battery unit. More of the details of the research can be found in [121].

The capacity determination and energy management planning of such a hierarchical storage scheme present significant challenges due to differing characteristics and purposes of each storage component. A comprehensive analysis of the net power is the logical first step in the design process of the HESS.

In order to restrain the focus of the study to the design of the HESS scheme, the following assumptions are made to establish the boundary of the research. This investigation does not consider the reactive power needs of the prosumer/nanogrid and hence, voltage control is outside the scope of the present work. Power conversion and line losses are also ignored in order to focus on the power fluctuations due to PV array and the load.

### **3.2.2 Laboratory platform for data collection**

Since the study is aimed to facilitate the PV power fluctuations starting from shorter time length of about seconds to time length of few years, the collection of data for the study is indeed a tedious

task by itself. Test data required for this study has been obtained from the test laboratory for microgrid which is based at Curtin University premises called Green Electric Energy Park (GEEP). This has been equipped with different types of renewable sources (Solar, wind and micro-hydro unit), all power electronic interfaces, protection equipment, measurement unit and historical database server which has been used to extract historical solar data for this study [122]. Figure 3.2 shows the PV arrays of GEEP lab facility. The operating weather and power data of three different types of solar PV arrays are monitored and stored at about 1 second intervals since the end of 2012.

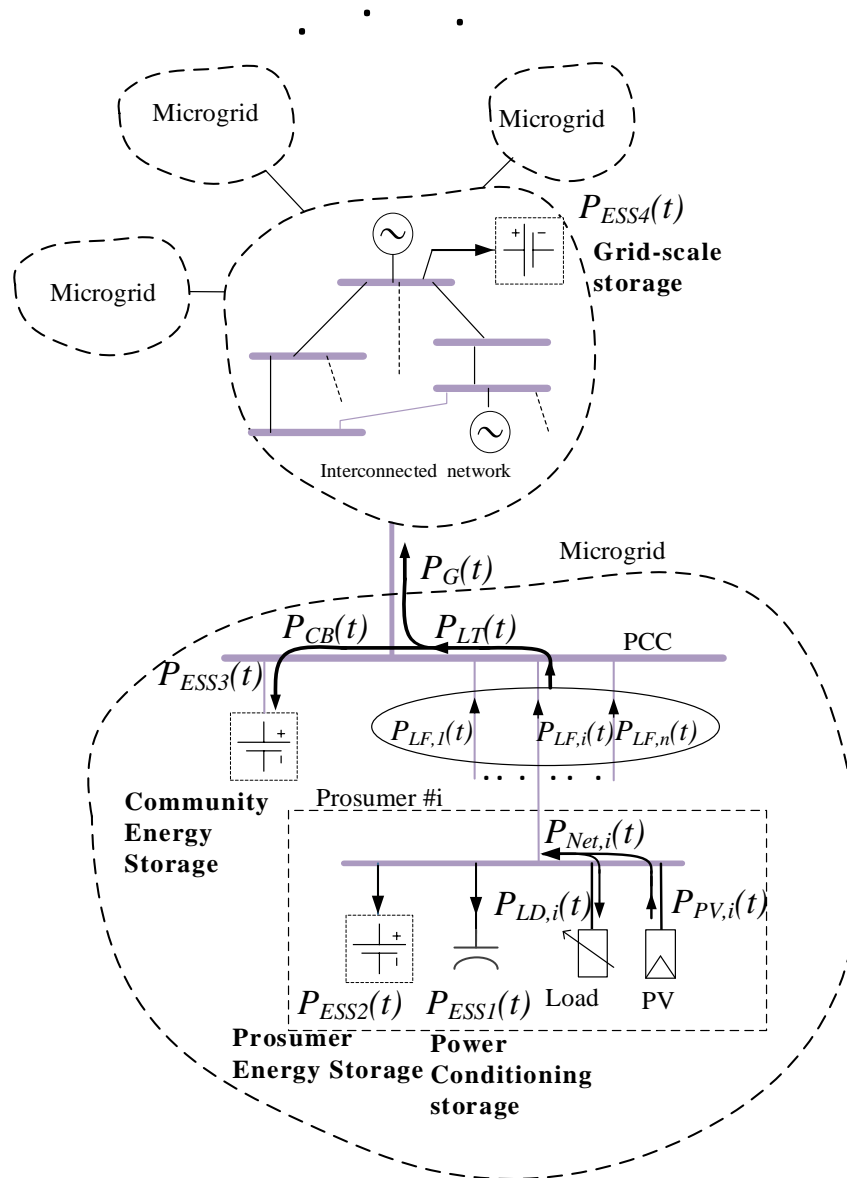


Figure 3.1. The conceptual hierarchical HESS scheme under study for the thesis



**Figure 3.2 Green Electric Energy Park at Curtin University (Image credits: Prof.Sumedha Rajakaruna, Director Green Electric Energy Park)**

Particularly, a teaching unit with Amorphous Si PV array with 6 modules, each rated at 60W 67V 0.9A is used for the measurements. The laboratory facilitates data sets of PV power ( $P_{PV}(t)$ ) of different time resolution to be obtained. Two different types of data sets are obtained with different time resolutions ( $\Delta t$ ) in order to facilitate analysis comprehensively. One is incorporated with one second sampling rate for maximum one month time span ( $\Delta t=1s$  and  $T=3$  months) to make sure that the time resolution is high enough to capture the short-term fluctuations of PV. On the other hand, long term solar input variations like seasonal changes can only be captured if the time frame of the total dataset is sufficiently large. Hence another PV power dataset of one-minute sample rate is recorded for a continuous three years' time period ( $\Delta t = 1$  min,  $T=3$  years).

### **3.2.3 Data preparation and limitations of the study**

After carefully inspecting the load power data from available sources, it has been found that the number of online databases with different data granularities are available [123]. However, due to the malfunction of sensory equipment, load usage data for many years with greater sampling rate like 1min is not readily available. Therefore, load power data collected from a single residential unit over few years with one minute sample rate is used for the study from open source database which is available at [124].

Given that the source of load power data originated from France [124], the seasonal effects to the load power curve are fundamentally different from those observed in the PV data collected in Western Australia on the same day. The significant discrepancy between these two datasets resulting from seasonality was addressed by shifting the time stamp of the data sources to ensure they share the same seasonal patterns. The temperature effects of the different location which can effect on the generation and load data are not considered in this study which is a major limitation of the study. The next challenge during the data preparation is the loss of data due to the practical interruptions like the lab sessions and maintenance of the facility. These instances are recognized at the primary data wrangling stage and the suitable replacements from the same day of another year are used to replace such missing data to ensure the continuity of the dataset with minimal effect. The third challenge is deemed with the different sampling rates of the two different datasets. The load data set with the sampling rate of 1min is unsuitable to be used with the first data set of PV which is sampled at 1 sec. Therefore, the load data is resampled using the MATLAB software with interpolation to obtain the data points in between [125]. Finally, the data from different sources of load and source need to be correctly proportionated such that the hypothetical design of the PV for the load variation matches. This has been ensured via scaling of load and PV data in order to match an average residential prosumer in Australia. Furthermore, when it is necessary, a future case with increased PV penetration is also simulated to replicate the expected future trend of zero net energy exchange with external generation.

### 3.2.4 Nonlinearity of the prosumer net power

Interesting insights into the power flows inside the prosumer unit of microgrid can be gained by examining firstly the imbalance between the generated PV power and the load demand. Accordingly, and with reference to Figure 3.1, define the net power flow  $P_{net}(t)$  as the difference between  $P_{PV}(t)$  and  $P_{LD}(t)$ ,

$$P_{net}(t) = P_{PV}(t) - P_{LD}(t) \quad (3.1)$$

A sample of  $P_{PV}(t)$  and  $P_{LD}(t)$  over a selected three day period is depicted in the Figure 3.3 in order to gain some basic insights of the variations presented.

As it is depicted in Figure 3.3(a) Day #1 and Day #2 can be identified as sunnier days compared to the Day #3 which is a rainy day. Interestingly, the PV profile of Day#1 has two distinct

types of variations. As shown in the enlarged image in Figure 3.3(b), the variations between 07.00-10.00 hours on Day #1 were predominantly due to the movements of cloud covers whereas that between 10.00 to 14.00 hours were dominated by the actions of the single axis tracker of the PV array which creates a saw tooth type of variations. Day #2 appears to have the cloud cover variation in the afternoon which makes it a different PV profile to Day #1. Day #3 appears as a vastly different PV profile with multiple peaks due to the high amount of cloud cover.

Figure 3.3(b) depicts the load profile which reflects the typical daily demand of a residential unit on Saturday, Sunday and Monday. This denotes that the lower power usage on the Monday in comparison to the weekend. Subsequently, the resulting  $P_{net}(t)$  shown in Figure 3.3(c) appears as net power with non-stationary variations obviously with no regularity in variations on an hourly or even daily basis. The apparent randomness indicated on the  $P_{net}(t)$  makes the time-domain analysis of such a stochastic process a highly challenging task.

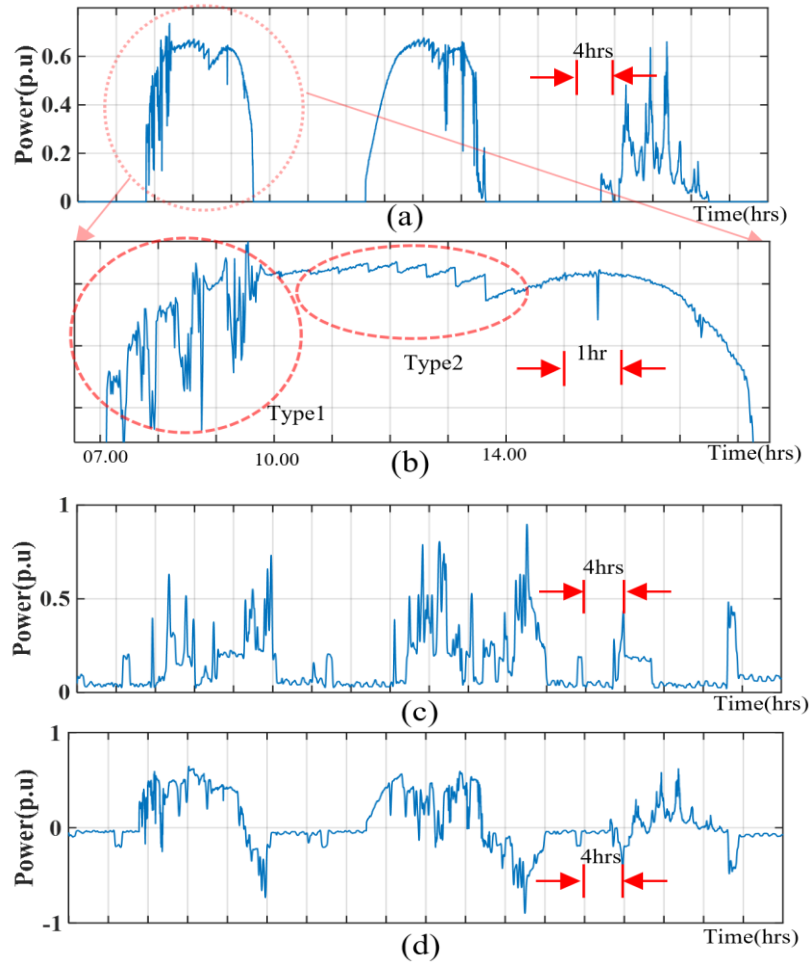


**Figure 3.3 Samples of (a) PV power, (b) Zoomed plot of PV power (b) load power and (c) net power over a selected three-day period**

### 3.3 Proposed approach to analyse $P_{net}(t)$

In this section, the proposed approach to analyse  $P_{net}(t)$  will be briefly discussed, in terms of the procedure depicted in Figure 3.4. The outcome of the analysis is to provide statistical measures to characterize  $P_{net}(t)$ .

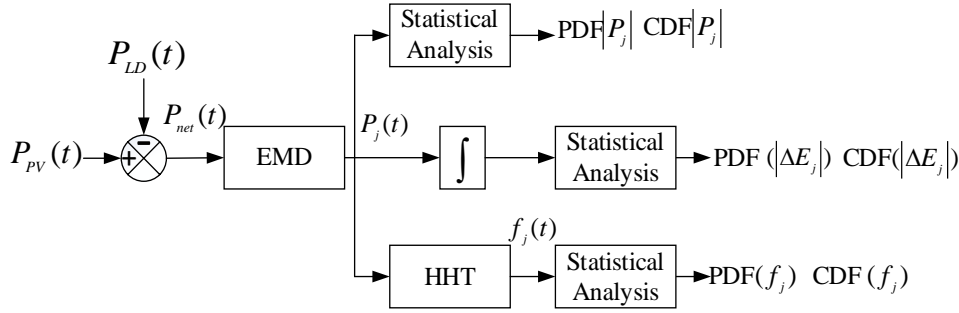


**Figure 3.4 The proposed approach to analyse net power**

In Figure 3.4, the first step of analysing  $P_{net}(t)$  is to apply EMD to it. A set of IMFs and residue functions are obtained. Mathematically,

$$P_{net}(t) = \sum_{j=1}^n P_j(t) + r(t) \quad (3.2)$$

where  $n$  is the number of IMFs,  $j$  is the order of the IMF  $P_j(t)$  and  $r(t)$  is the residue of the decomposition. One can then readily determine, by integrating  $P_j(t)$  with respect to time, the variations in the energy levels  $\Delta E_j(t)$  in  $P_j(t)$ , with respect to that at an arbitrarily chosen reference time  $t = 0$ :

$$\Delta E_j(t) = \int_{t=0}^t P_j(\tau) d\tau \quad (3.3)$$

Furthermore, HHT analysis can be performed on  $P_j(t)$  to obtain the instantaneous frequency  $f_j(t)$  of  $P_j(t)$ . Next, it is proposed to use a statistical approach to derive some useful quantitative measures of these perturbing quantities. The probability density function (pdf) and cumulative density function (cdf) of each  $P_i(t)$ , and its corresponding  $\Delta E_j(t)$  and  $f_j(t)$  can be evaluated using standard statistical technique such as that described in [23]. These transformation processes produce pdf (.) and cdf (.) of the quantity (.), as indicated in Figure 3.4. In addition, the mean value of instantaneous frequency,  $f_{i,m}$ , of  $P_i(t)$  is also an important quantity as it provides a measure of the mean period of the oscillations in  $P_i(t)$ :

$$f_{j,m} = \text{mean}(f_j(t)) \quad (3.4)$$

$$T_{j,m} = 1 / f_{j,m} \quad (3.5)$$

In order to facilitate a complete analysis of the  $P_{net}(t)$ , it is required to perform the analysis to the best available sample rate for sufficiently long period of a few years to capture all modes presented in the  $P_{net}(t)$ . Unfortunately considering the computational burden, this couldn't be effectively achieved under limited computer memory and processing resources. Therefore, the case study was performed over two different datasets of  $P_{net}(t)$  with different sampling times and total time length ( $\Delta t$  and  $T$ ). Case study 1 was performed at  $\Delta t=1\text{s}$   $T=1$  week aiming at capturing the short term power fluctuations of PV and load. Unfortunately, the long-term cycles cannot be captured in such a lower value of  $T$ . Therefore, another analysis of  $\Delta t=1\text{min}$   $T=3\text{year}$  was performed in the Case Study 2.

## 3.4 Results and Discussion

### 3.4.1 Case Study 1

In this case study, the proposed approach described in Section 3.3 to analyse  $P_{net}(t)$  is to be performed on a 1-week recorded data of  $P_{net}(t)$ , obtained at the sampling rate of 1 s/sample. The focus of the analysis is on the high to mid-frequency components of the net power. Based on this sample, one can detect frequency components of between  $1.65 \times 10^{-6}$  to 0.5Hz in  $P_{net}(t)$ . Following the EMD computational procedure described in Section 3.3, the obtained  $P_j(t)$ ,  $\Delta E_j(t)$  and  $f_j(t)$  are depicted on Figure 3.5. There are 12 IMFs and a residue function.

According to the theory of EMD, lower-order IMFs are of higher frequency than that of higher-order IMFs. It is therefore not surprising to observe that the lower-order IMFs oscillate at higher frequency than the higher-order IMFs. For example, IMF  $P_4(t)$  oscillates at higher frequency than IMF  $P_9(t)$ . Indeed, as explained in Section 3.3, one can carry out HHT on the IMFs to obtain the corresponding  $f_j(t)$ . Figure 3.5 shows that the frequency band of  $P_4(t)$  is some 500 times higher than that of  $P_9(t)$ . In Figure 3.5(b), it is observed that the energy variations corresponding to the lower order  $P_j(t)$ , such as  $\Delta E_4(t)$ , perturb over a range of  $\pm 0.6$  kWh over any given day in the selected week. On the other hand,  $\Delta E_j(t)$  corresponding to those higher order IMFs, for instance  $\Delta E_7(t)$ , have shown comparatively larger energy variations of some 2 kWh daily. In general, the low-order IMFs tend to have relatively lower oscillating energy content compared to the higher-order IMFs, although the magnitudes of these low-order IMFs can be significant. The power fluctuations due to these low-order IMFs have to be carefully smoothed,

as they can impact negatively the quality of the power supply. This topic shall be discussed in greater details in CHAPTER 4.

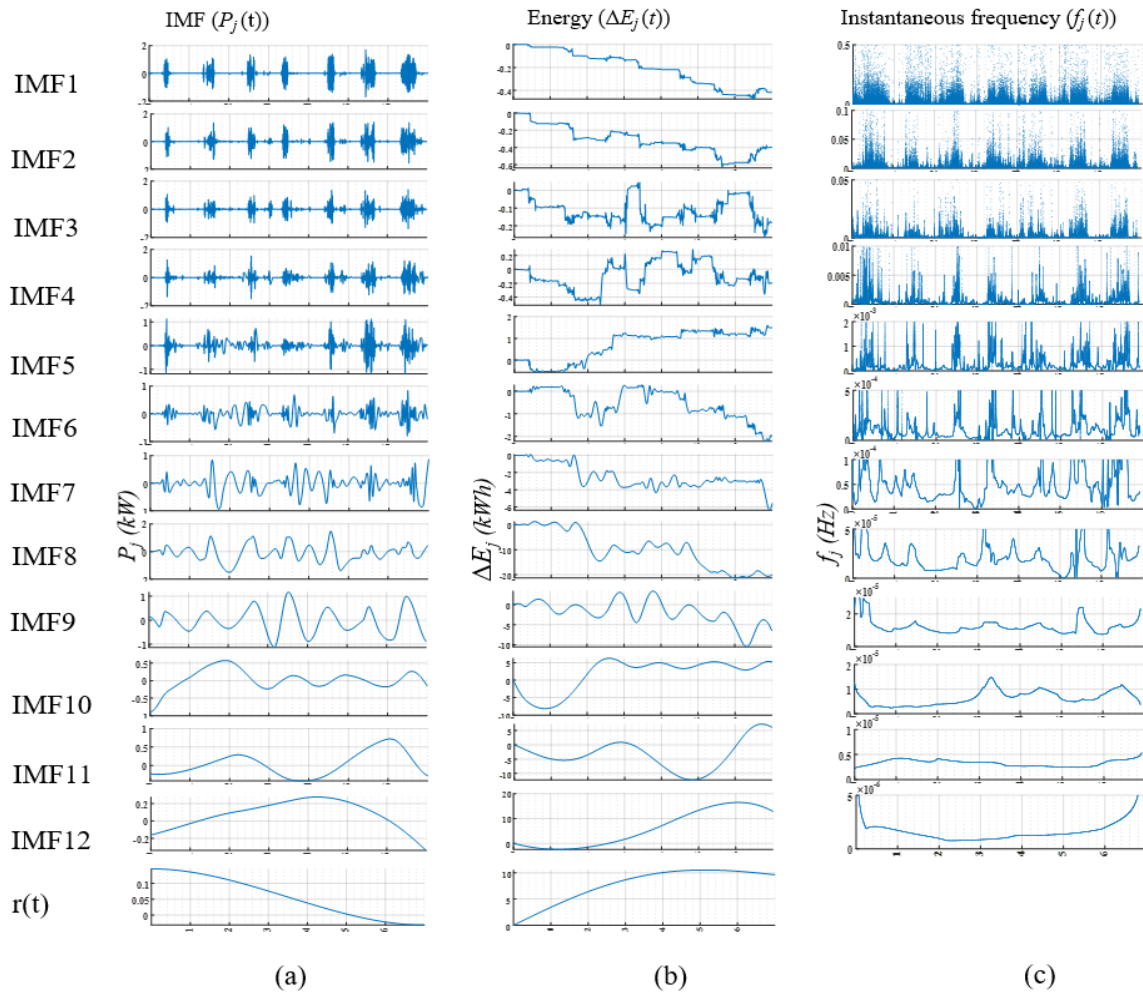


**Figure 3.5 (a) IMF  $P_j(t)$  and residue function  $r(t)$ , (b) the corresponding energy  $\Delta E_j(t)$  and (c) instantaneous frequency  $f_j(t)$  of  $P_{net}(t)$  - Case Study 1.**

Although the higher order IMFs are less significant to the power fluctuations in  $P_{net}(t)$ , they will be responsible for a large proportion of the perturbing energy exchange between the prosumer and the external microgrid system. Figure 3.5(a) shows that while  $P_j(t)$  oscillates about the 0 level, both its magnitude and period of the oscillations are time-varying. Hence,  $P_j(t)$  is both amplitude- as well as frequency-modulated. This results in the instantaneous frequency  $f_j(t)$  of  $P_j(t)$  spreading over a range, as shown in Figure 3.5(c). In addition, it can be seen that some IMFs display very clear periodical variations. As an example, the IMF  $P_9(t)$  is shown on Figure 3.5(a) in which the daily cycles are clearly displayed. This periodic mode can be attributed to the daily variations of the solar irradiance.



### 3.4.2 Case Study 2

From sampling theorem, it is clear the frequency range and the resolution on  $f_j(t)$  will depend on the sampling rate and the length of the dataset analysed. The 1-sec sampling rate used in Case Study 1 is unsuitable for the EMD analysis much beyond the 1-week study periods because of the limited memory capacity of the computer used in this investigation. Instead, in this Case Study 2, a 3-year dataset of  $P_{net}(t)$  of 1-min sampling rate has been used. At this sampling rate, one would be able to detect frequency components of  $P_{net}(t)$  of between  $10^{-8}$  Hz – 0.0083 Hz. This Case Study is used to demonstrate how interesting insights can be obtained from the outcome of the statistical analysis of  $P_j(t)$ ,  $\Delta E_j(t)$  and  $f_j(t)$ , shown as the last step of the procedure in Figure 3.4. As an example, Figure 3.6 shows the cdf of  $P_3(t)$  and  $P_9(t)$  of the  $P_{net}(t)$  and their corresponding  $f_j(t)$  and  $\Delta E_j(t)$ . The following observations can be made.

As shown on Figure 3.6(a), even though the magnitudes of  $P_3(t)$  and  $P_9(t)$  do not differ vastly, Figure 3.6(c) shows that the magnitudes of the energy perturbations  $\Delta E_9(t)$  in  $P_9(t)$  are much higher than  $\Delta E_3(t)$ , the perturbing energy level in  $P_3(t)$ . This is because the higher order IMF (i.e.  $P_9(t)$ ) occupies a lower frequency range than that of the lower order IMF (i.e.  $P_3(t)$ ), as can be readily seen in the cdf of  $f_j(t)$  in Figure 3.6(b). The lower frequencies result in longer oscillating periods which, following the integrating process in (3.3), leads to larger oscillating energy.

It can therefore be concluded that apart from the power level in  $P_j(t)$ , the frequency range of  $f_j(t)$  is also an important factor affecting the magnitude of  $\Delta E_j(t)$ . The authors of [41] have made use of the ramp rate of  $P_{PV}(t)$  to design the ESS. In contrast, CHAPTER 5 of the present work shall make use of the information on the frequency range over which the ESS is effective in buffering  $P_{net}(t)$  when determining the type of ESS to be included in the HESS.

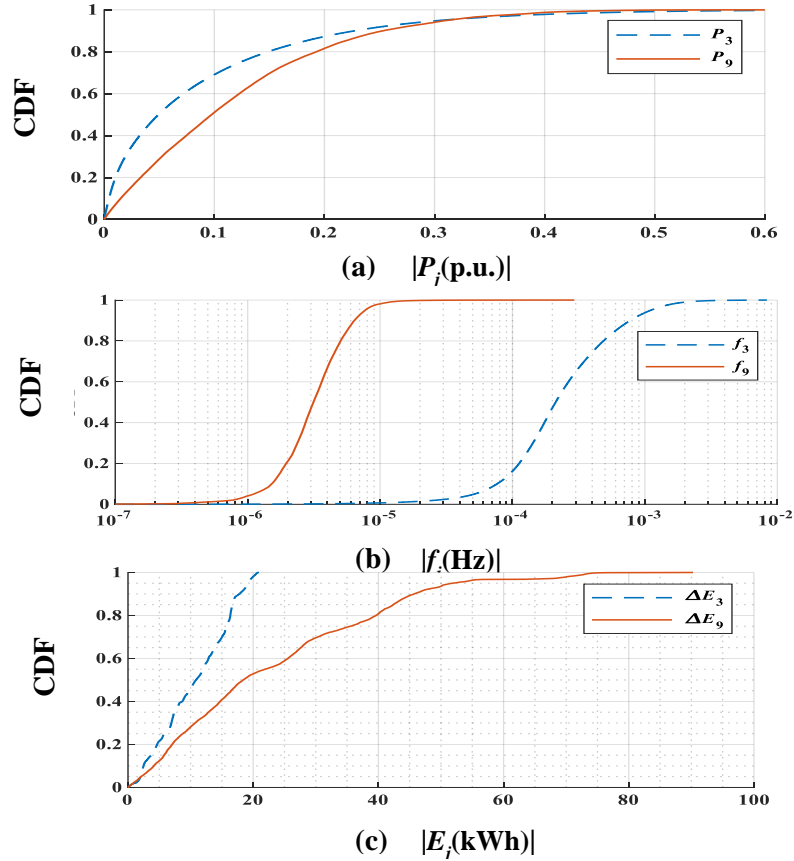


Figure 3.6. CDF of IMF3 and IMF9 (a) power, (b) frequency and (c) oscillating energy in Case Study 2

Further insights can be gained by examining more closely the full range of the IMFs of  $P_{net}(t)$  in this example. Figure 3.7 shows the cdf of  $f_j(t)$  which clearly indicates regions of overlap in the frequency range of one IMF with that of the adjacent  $P_j(t)$ . The overlaps occur because of the inherent mode mixing that occurs in the EMD analysis. Notwithstanding this,  $f_j(t)$  tends to decrease as the order of  $P_j(t)$  increases. The mean periods  $T_{j,m}$ , calculated in accordance to (3.5) and as shown on Table 3.1, ranges from 17 min to some 888 days. In most instances,  $T_{j,m}$  of a given IMF is observed to be about double that of the preceding IMF. This observation is in accord with the EMD theory: the mode decomposition process acts like a dyadic filter [126]. On a few occasions, the dyadic repetitions are not evident. This is because these IMFs contain very low power contents. For example,  $T_{14,m}$  is about 5 times of  $T_{13,m}$ .  $P_{13}(t)$  represents the two-month oscillating mode whereas  $P_{14}(t)$  is that of a year. This study appears to suggest that there is no evidence of any modes which have the mean period of between 2-month and a year.

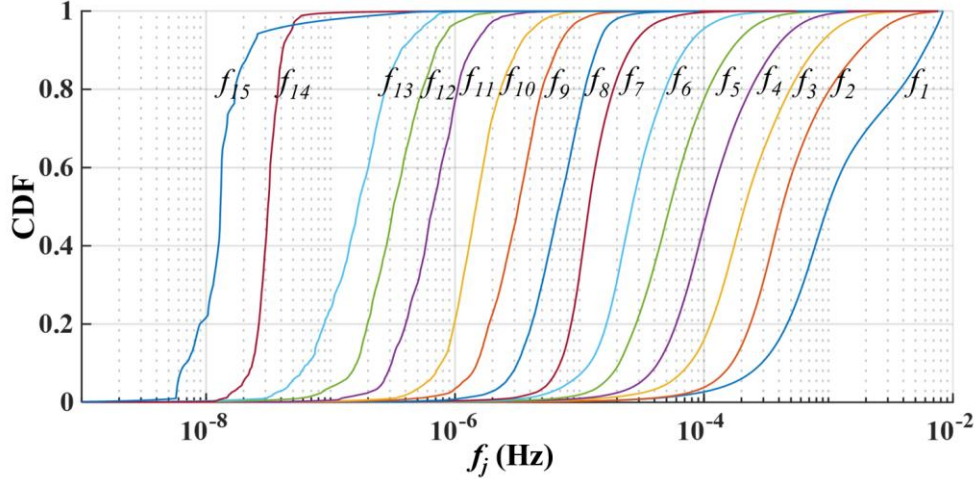


Figure 3.7 CDF of the instantaneous frequencies from  $f_1(t)$  to  $f_{15}(t)$

Table 3.1.  $T_{j,m}$  of the IMFs

IMF <sub>j</sub>	$T_{j,m}$	IMF <sub>j</sub>	$T_{j,m}$	IMF <sub>j</sub>	$T_{j,m}$
IMF1	17mins	IMF6	10.5hrs	IMF11	17days
IMF2	39mins	IMF7	23.3hrs	IMF12	36days
IMF3	1.3hrs	IMF8	1.6days	IMF13	69days
IMF4	2.5hrs	IMF9	3.5days	IMF14	368days
IMF5	5.2hrs	IMF10	7.8days	IMF15	888days

The daily and yearly cyclic modes are expected of solar power. Indeed Table 3.1 shows that IMF  $P_7(t)$  has a mean period  $T_{j,m}$  of approximately one-day while that of IMF  $P_{14}(t)$  is close to one year. Figure 3.8 presents the cdf profiles of the oscillating energy contents pertaining to IMF  $P_1(t) - P_{15}(t)$ . When comparing the IMFs, the anticipated trend is when the IMF order  $j$  increases, the mean period would increase which would in turn cause  $\Delta E_j$  to increase. This would result in a shift of its cdf profile to the right. However, according to Figure 3.8 this trend has not been observed in IMF  $P_7(t)$  and IMF  $P_{14}(t)$ . The figure shows that  $P_7(t)$  and  $P_{14}(t)$  have higher oscillating energy contents than those of  $P_8(t)$  and  $P_{15}(t)$  respectively. Thus, it reinforces the observation that in terms of energy variations, the daily and yearly cyclic modes are the two most significant components in  $P_{PV}(t)$ . The IMF components resulted from the decomposition have shown clear identification of the repetitive cycles which are presented in the  $P_{net}(t)$ . For an example,  $P_7(t)$  has reported the daily cyclic component and the  $P_{14}(t)$  has reported that of yearly. The pre-eminence of these two components would impact the selection of the type and design of HESS, the topic which is to be discussed in the next chapter of this thesis.

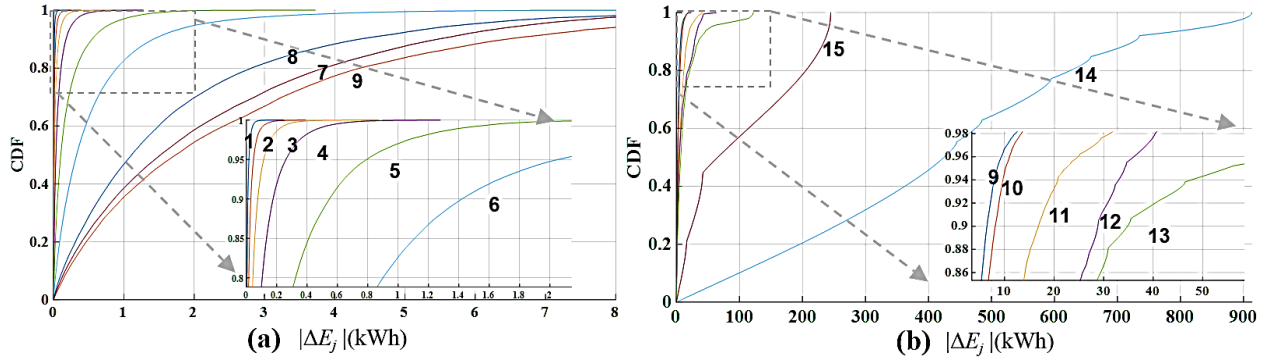


Figure 3.8 CDF of  $\Delta E_j(t)$  for IMF  $P_1(t) - P_{15}(t)$  in Case study 2.

### 3.4.3 Comparative analysis

In this section, three different comparative studies are performed on the  $P_{net}(t)$  in order to build further confidence of the proposed algorithm in analysing the stochastic net power.

#### a. Comparison of EMD and EEMD

Firstly, the need of noise-assisted method particularly in a lower data granularity such as in Case2 is shown with the comparison of EMD and EEMD. For a close inspection, three higher order IMFs obtained from the Case 2 analysis using both EMD and EEMD are compared in Figure 3.9.

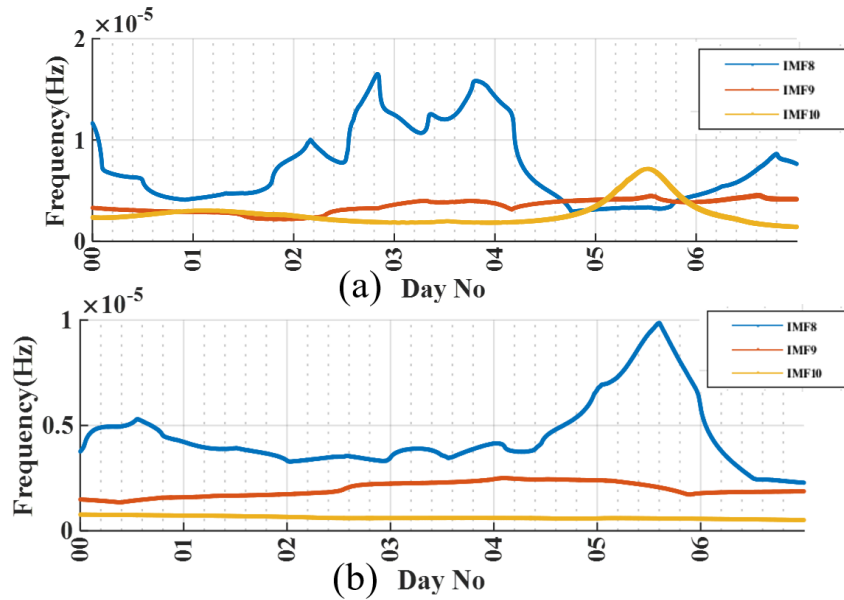


Figure 3.9(a) IMF 8-10 generated by EMD (b) IMF 8-10 generated by EEMD

The  $f_j(t)$  curves of the IMF 8,9 and 10 obtained in the Case 2 analysis (only first week is shown here) has been compared in Figure 3.9(a) and Figure 3.9(b) using EMD and EEMD respectively. In Figure 3.9(a), it is well noted that there are considerable overlaps between successive IMFs in EMD ensuring that EMD is not able to segregate the IMF such that  $f_j(t)$  are well separated due to the inherited problem of mode mixing. As a result of the de-mixing ability of EEMD with noise-assisted method, the same IMFs are well separated as depicted in Figure 3.9(b). Therefore, it is clear that improved results can be gained using EEMD particularly in Case 2 effectively reducing the mode mixing. However, the above improved results come at a cost of additional computation resources. Therefore, the computation time of the EMD and EEMD with different number of ensembles are compared in Table 3.2. According to the table, it is clear that there is a close linear relationship between the time of code execution and the number of ensembles. Usually several hundred are considered to be enough for acceptable accuracy as noted in [63].

**Table 3.2. Execution times of the EMD and EEMD**

	Number of ensembles	Execution time
EMD	1	0.315s
EEMD	10	3.464s
	20	5.54s
	50	11.9s
	100	23.68s
	500	124.73s

b. Comparative analysis of EMD with FT

As mentioned in the earlier in this chapter, FT is not a suitable option to analyse the nonlinear signal. It is necessary to determine whether the level of nonlinearity exhibited in  $P_{net}(t)$  is such that the suitability of using the FT can be called into question. In order to assess this, the proposed EMD based analysis method is compared with the FT for the same  $P_{net}(t)$  variation.

Using the FT analysis on the same dataset, a few dominant frequencies can be identified. If these frequencies were compared with the mean frequencies obtained by EMD- HHT analysis, then the results can be depicted as in Figure 3.10.

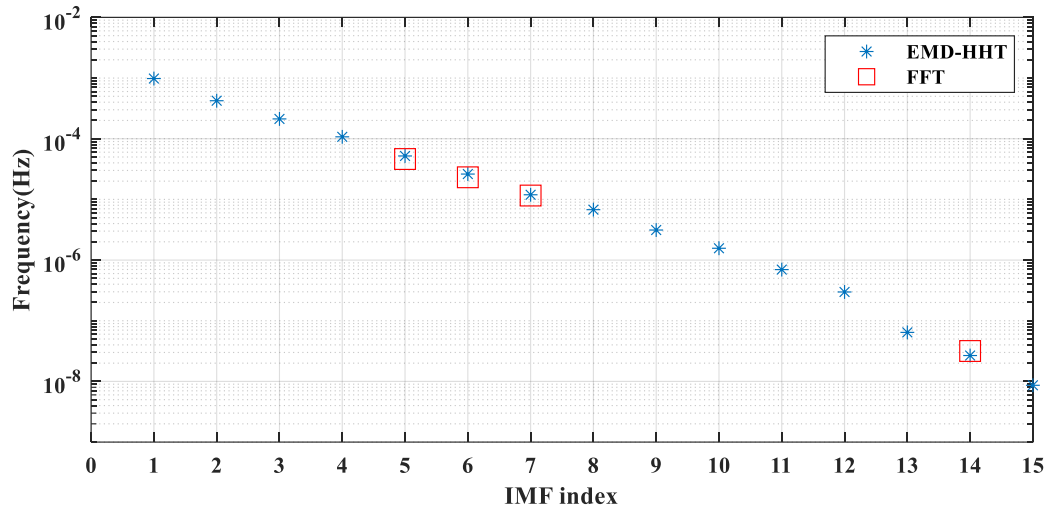


**Figure 3.10. Comparison of the extracted frequencies between FT and HHT**

According to Figure 3.10 FT appears to pick only IMF 5,6,7 and the IMF 14 successfully. In the HHT analysis, these IMFs are mostly seen as the predominant IMFs. However, the extraction of the rest of the frequencies deemed very difficult using FT since their amplitudes are very closely related to another frequency with very similar amplitude. In the process of FT, the details of the time-varying characteristic of the signal are overlooked, which is considered a very important in this analysis for identifying the oscillating energy component with respect to time. Although the higher frequency IMFs are smaller in energy contents, they have to be incorporated in the design of the HESS as these low-order IMFs can impact the power quality of the supply greatly due to short term fluctuations. Therefore, the overall performance of the FT analysis falls short of the anticipated outcome for a nonlinear analysis.

c. Comparison with second dataset

To develop enough confidence of the obtained results, the same EMD is performed on the second dataset of three years and statistical comparison is carried on the both datasets to compare them. For the statistical comparison between these two datasets, higher order statistic (HOS) is used. HOS parameters like variance, skewness and kurtosis are more commonly used parameters to obtain the level of dispersion, asymmetry and concertation around the mean of the dataset. For a perfectly symmetric distribution about mean, the skewness is zero. The kurtosis of a data with a histogram having a sharper peak and longer, fatter tails is greater than that for a distribution having a more rounded peak and shorter thinner tails. If those variance, skewness and kurtosis are compared for the dataset 1 and dataset 2, the obtained figure can be depicted as in Figure 3.11. According to the

figure, it can be observed that the at least first 12 IMFs exhibit a close relationship statistically. IMF 13, 14, and 15, on the other hand, may be due to insufficient data, are less able to accurately portray the seasonal variations as they show slight deviation of their trends.

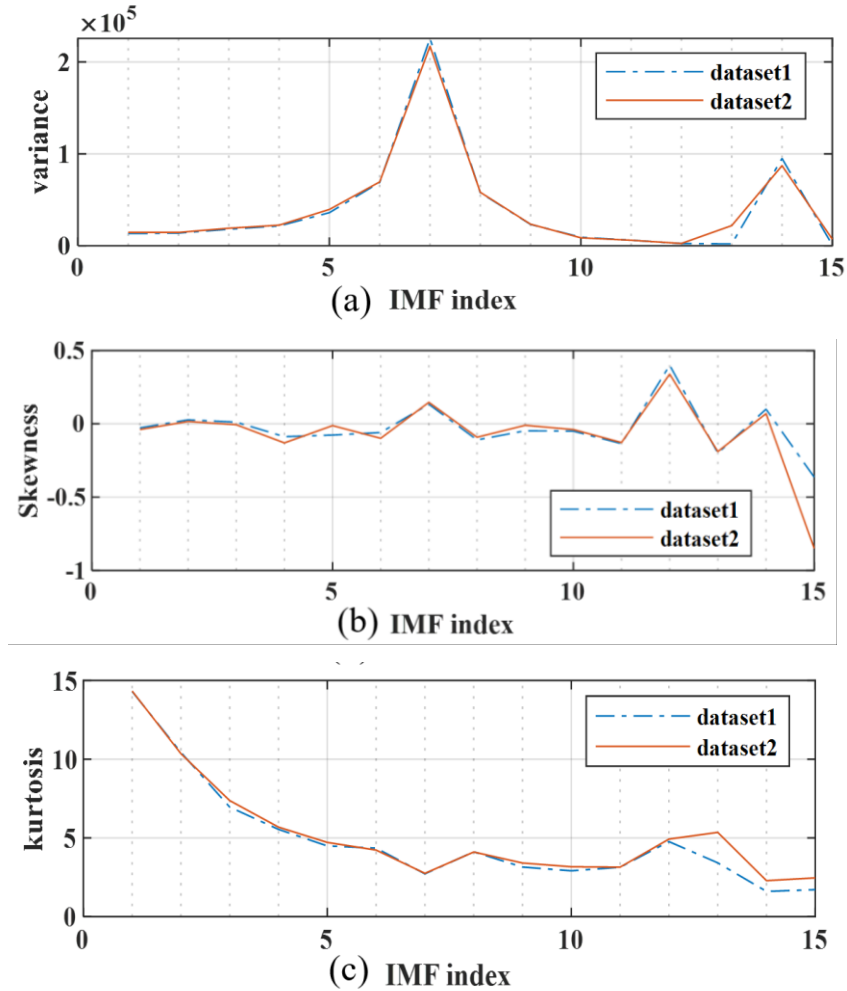


Figure 3.11 Comparison of (a) Variance (b) Skewness and (c) kurtosis of the 15 IMFs in dataset1 and dataset 2 analysis

### 3.5 Conclusions

As an opening chapter to the thesis, this chapter conducts a comprehensive analysis of the highly non-stationary net power variation. Despite the heavily practiced non-adaptive Fourier and wavelet methods, empirical mode decomposition is identified as an adaptive and intuitive technique to decompose and analyse such a non-linear variation. It is shown that the perturbing components of the net power of a PV-powered prosumer can be accurately identified through EMD analysis. This includes both higher frequency components which emphasize power quality concerns arising from

PV-load power variations and the lower frequency components associated with oscillating energy. The probabilistic distributions of the energy contents of the components indicate that the two most prominent components are those pertaining to the daily and yearly modes of variations in the solar irradiance.

The salient features of the EMD technique are well observed in the analysis of prosumer net power guaranteeing the method's consistent ability to yield reliable results. The method has statistically proven to be giving consistent results for different datasets of net power variation. Moreover, the inherent limitations of the method can be effectively mitigated through enhanced EMD variants, ensuring the necessary accuracy for further analysis in this thesis.



# **CHAPTER 4. Determination of Cost-effective Frequency Band and Capacities between Constituent Storages of the Hybrid Energy Storage System**

## **Statement of Contribution**

The work in this chapter is being developed for a publication entitled " A new approach to identify the optimum frequency ranges of the constituent storage devices of a hybrid energy storage system using the empirical mode decomposition technique," where the coauthors are D. Hettiarachchi, S. Shing Choi, S. Rajakaruna, and A. Ghosh <sup>2</sup> [127]. The sections and results of this publication are extended in this chapter as they could not be presented in the publication due to the space limitations.

## **4.1 Introduction**

As discussed in the previous chapter, non-linearity of the prosumer's net PV power variation made the decomposition of the power components a challenging task. However, the proposed EMD method has successfully facilitated the decomposition of the net load power into physically meaningful oscillating power components. Each of these oscillating power components denoted as IMFs, corresponds to a characteristic curve on the cdf vs frequency plane, resulting in a series of curves for a given net power. In a planning of HESS comprised of two or more constituent storages, it is crucial to accurately identify these oscillating power components associated with each storage. This serves the preliminary step of determining the capacities of each storage of HESS. The purpose of this chapter is to extensively discuss the HESS design problem on how to differentiate the various frequency components to the distinct constituent storage technologies.

While the research attention continues to grow on HESS in recent years, determining the design parameters of the constituent ESS in the HESS has been a widely discussed topic in the literature. However, as later discussed in the literature, the analytical method used to determine the effective frequency band of constituent storages remains mostly unknown. In view of aiming this

---

<sup>2</sup> Percentage contributions of the relevant co-authors in the publication are given in the attribution statement, reviewed and signed by the each co-author.

design problem of HESS, the following key objective is to be achieved in this chapter. Firstly, this chapter demonstrates the ESS capacities of all energy storage devices are frequency-dependent. This important characteristic is mostly ignored in the previous works. Further analysis of dynamic behavior reveals that each type of ESS has its unique cost-frequency band. This will lead to develop a methodology to analytically determine the cut-off frequency between the ESS of the HESS. Thus, the identified oscillating modes in the fluctuating net power demand of the prosumer in the previous chapter can be related to the frequency characteristics of the suitable types of energy storage devices to undertake energy buffering economically and effectively.

This chapter is organized as follows. The development of the proposed method to segregate different frequency components between the ESS components is described in Section 4.2. Section 4.3 contains the application of the proposed method for the other hierarchical storage schemes using illustrative examples. Section 4.4 contains the validation of the proposed analytical method that is compared with the existing iterative methods found in the literature. Finally, the effect of ageing of ESS on the cut-off frequency is demonstrated with respect to the equivalent circuit model of the storage.

## **4.2 Frequency Plane Representation of ESS Devices**

In order to analytically determine cut-off frequency between constituent storages, a methodology should be developed to compare the performance of the ESS in the frequency plane. Therefore, a suitable parameter should be selected in order to compare one constituent ESS to the other with respect to the operating frequency. The accurately chosen parameter should adequately reflect both the economic and dynamic performance characteristics of the ESS. Economic characteristics are quite easily understood as the cost per capacity of the storage is well-known. However, the dynamic performance in different frequencies can only be understood, if the equivalent circuit model (ECM) is known [128]. Using the ECM of the given storage, it may be easier to define a responsive frequency range for the storage. This effective frequency range is an excellent measure as it represents dynamics of the storage with respect to the frequency. Also, this measure mimics the power and energy density of the storage. As an example, the SC is usually responsive to the high frequency variations which has the higher power density but lower energy density. In contrast, batteries which are usually incapable to respond to the higher frequency variations, have lower power density but higher energy density. Therefore, the ECM-based model to determine the responsive frequency band can be used to sufficiently replicate the key diverse characteristics of

different storages. As will be shown later, according to the ECM of the storage, the effective capacity of the storage is a function of the frequency. As the cost is capacity-dependent, then a relationship can be developed to relate the frequency and cost of a given storage. In the following sections, the development of this relationship between the effective frequency and effective capacity to compare the storages will be discussed extensively.

In this section, the aim is to develop a method with the use of storage ECM to build up a relationship between the operating frequency and the effective storage capacity. The initial focus is to study the ECM of Li-ion battery storage.

### 4.2.1 ECM of ESS

Although the complete ECM of the Li-ion battery is a complex RC circuit, it can be simplified to facilitate the analysis. For instance, the comprehensive ECM of Li-ion battery presented in [56] is depicted in Figure 4.1. The figure shows that the solid phase cathode (+) and anode (-) electrodes are represented by a parallel RC branch ( $R_2^{\pm}, C_2^{\pm}$ ), the overpotential resistance ( $R_n^{\pm}$ ), the series resistance ( $R_1^{\pm}$ ) and the main capacitance ( $C_1^{\pm}$ ). In addition,  $R_f$  corresponds to the resistance due to the side-reaction induced degradation of the cell and finally,  $R_e$  relates to the resistance of the electrolyte. In the anode, there is an additional current path in which  $I_{sr}$ , the side-reaction current flows. This current accounts for the interaction between the Li ions and the solvent.  $I_{sr}$  will exist even when the battery is not in service. Furthermore, in this model, the voltages across  $C_1^{\pm}$  represent the OCP of each of the electrodes. Hence, the voltage across  $C_1^+$  and  $C_1^-$  is the open circuit voltage of the battery. Note that the OCV is a function of the state of charge of the battery.

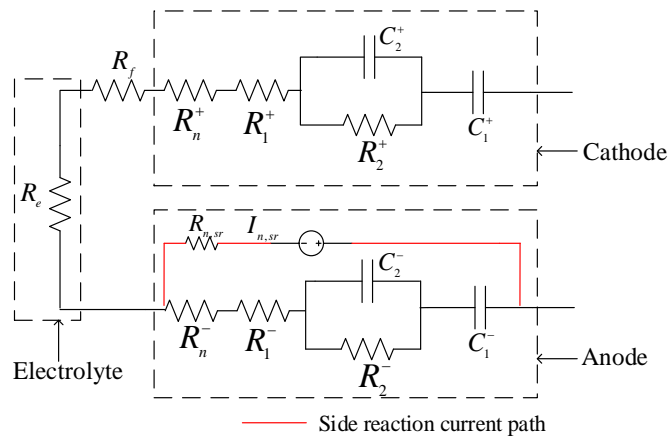
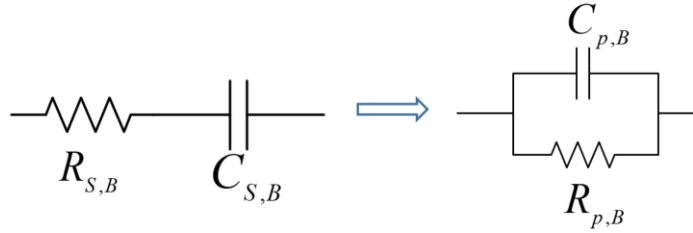


Figure 4.1. ECM of Li-ion battery given in [56]

As explained in [56], the parallel branch of the ECM is used to describe the diffusion process of the charges in the respective electrode. The capacitances in the parallel branches do not contribute significantly towards the energy storage capacity of the cell. Thus, in so far as the storage capacity of the battery is concerned, the parallel RC branches can be omitted. Furthermore, since the main focus of this work is on the selection of suitable ESS, the relatively slow degradation process shall be ignored at this stage of the study. Accordingly, the much simplified ECM of Li-ion battery becomes that of the series RC circuit shown in Figure 4.2 whereby  $R_{s,B}(\omega)$  and  $C_{s,B}(\omega)$  can be obtained using (4.1) and (4.2).

$$R_{s,B} = R_e + R_f + R_n^+ + R_n^- + R_1^+ + R_n^- \quad (4.1)$$

$$C_{s,B} = C_1^+ C_1^- / (C_1^+ + C_1^-) \quad (4.2)$$



**Figure 4.2. Conversion of series ECM to the parallel branch for ESS**

The series battery model in Figure 4.2 can be readily converted into its parallel equivalent. The parallel equivalent circuit parameters are expressed in term of the series circuit parameters as in (4.3) and (4.4). The effective terminal impedance  $H(\omega)$  of the battery is given in (4.5).

$$R_{p,B}(\omega) = R_{s,B} + \frac{1}{R_{s,B} \times \omega^2 \times C_{s,B}^2} \quad (4.3)$$

$$C_{p,B}(\omega) = \frac{C_{s,B}}{1 + R_{s,B}^2 \times \omega^2 \times C_{s,B}^2} \quad (4.4)$$

The amount of charges that can be stored within the battery is that residing in  $C_{p,B}(\omega)$ . Equation (4.4) shows that when the frequency  $\omega$  increases,  $C_{p,B}(\omega)$  decreases. Hence, the capacity for the battery to store charges, decreases with an increase in frequency. Amplitude and phase values of the impedance can be obtained from the equation (4.5) to (4.7). These are used to obtain the magnitude and phase plots for the ECM of the given Li-ion battery, as shown in Figure 4.3(a) and Figure 4.3(b). The Li-ion battery used in this example is [129].

$$H(\omega) = \frac{R_{p,B}}{1 + R_{p,B}^2 \omega^2 C_{p,B}^2} - j \frac{\omega C_{p,B} R_{p,B}^2}{1 + R_{p,B}^2 \omega^2 C_{p,B}^2} \quad (4.5)$$

$$M = 20 \log(|H(\omega)|) \quad (4.6)$$

$$\angle H(\omega) = \tan^{-1}(-\omega C_{p,B} R_{p,B}) \quad (4.7)$$

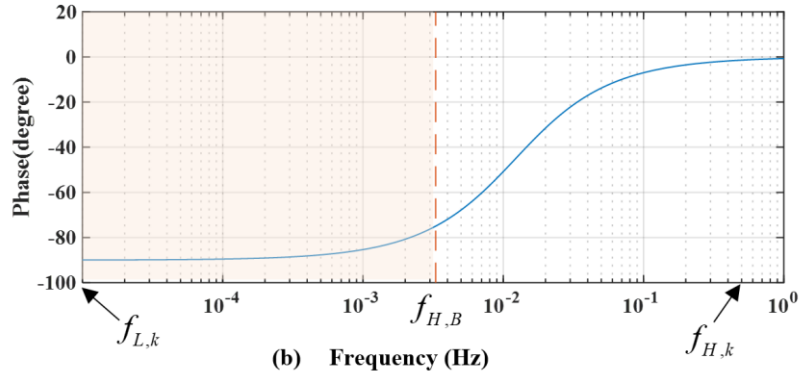
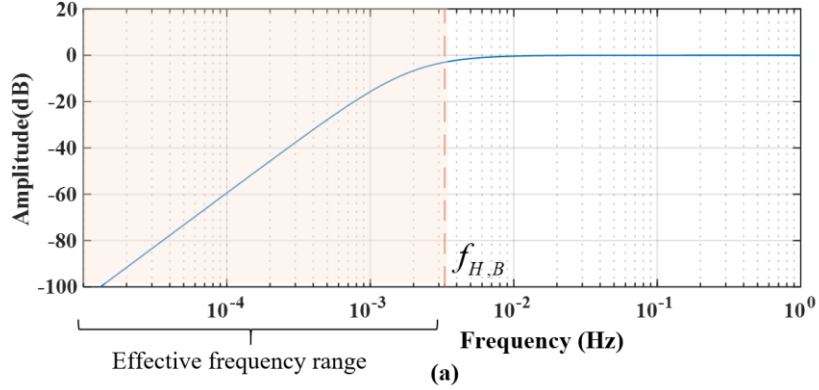


**Figure 4.3 a) Magnitude plot of battery ECM b) Phase plot of battery ECM**

In these plots, interested frequency range is denoted by the  $f_{L,k} < f < f_{H,k}$  in which the  $f_{L,k} = 10^{-6}$  Hz  $f_{H,k} = 0.5$  Hz for the considered net power of the prosumer. From the plot depicted in Figure 4.3(a), 3dB frequency of the magnitude plot for battery can be found as  $f_{H,B}$ . Considering this conventional 3dB point to define the effective bandwidth, the effective frequency range of the Li-ion battery is approximately  $f_{L,k} < f < f_{H,B}$  which is the shaded area of Figure 4.3(a) and Figure 4.3(b). According to Figure 4.3(b), within this frequency range, battery performs as an ESS device and exhibits capacitive behavior, represented by a phase lag close to -90 degrees.

Assume the terminal voltage of the battery is at its rated value  $V_{r,B}$ . When the  $C_{p,B}$  is in Farads and the unit of  $V_{r,B}$  is in Volts, the effective energy storage capacity of the battery ESS in kWh can be expressed as  $E_B(\omega)$ ,

$$E_B(\omega) = \frac{\frac{1}{2} \times C_{p,B}(\omega) \times V_{r,B}^2}{3600 \times 10^3} \quad (4.8)$$

Clearly as in the case of  $C_{p,B}(\omega)$ ,  $E_B(\omega)$  decreases with an increase in  $\omega$ .

Accordingly, the following parameters are assumed for the Li-ion battery considered in this study: the Li-ion battery rated at 1.8 Ah and  $V_{r,B} = 3.7V$  taken from [56] could be simplified in to the series circuit parameters given by  $R_{s,B} = 0.024\Omega$   $C_{s,B} = 3400F$ . Thus the  $f_{H,B} = 1.23 \times 10^{-3} Hz$  is obtained from Figure 4.3(a) for the considered Li-ion battery.

#### 4.2.2 Selection of the ESS for the given application

Denote ESS1 to indicate the device, such as a battery, and ESS2 to represent the high-frequency device, SC. When the interested frequency range is  $(f_{L,k} - f_{H,k})$  for the given application, according to the above introduction, The effective frequency range of the ESS<sub>1</sub> is  $(f_{L,k} - f_{H,ESS1})$  as shown in Figure 4.3(b) (as shown in shaded area). If  $f_{H,k} < f_{H,ESS1}$ , the selected ESS is suitable enough to serve all the frequency components of the given application. In contrary, if  $f_{H,k} > f_{H,ESS1}$ , similar to the scenario shown in Figure 4.3(b), the selected storage is only capable to handle the frequency components of the given application in the range  $f_{L,k} - f_{H,ESS1}$ . The frequencies higher than the  $f_{H,ESS1}$  cannot be met by the ESS<sub>1</sub> as the effective capacity is not sufficient enough to perform as a storage component in this frequency range.

Therefore, another storage device is required to provide the support to the first storage to cover the whole frequency range of interest. Employing another storage forms a hybrid energy storage system. The second storage device denoted by the ESS<sub>2</sub> possesses a different storage characteristic to the ESS<sub>1</sub>. Using similar process suggested in Section 3.2.2, its effective operating frequency range can be obtained denoted by the  $(f_{L,k} - f_{H,ESS2})$ . (i.e.  $f_{H,ESS2} > f_{H,ESS1}$ ). In such a situation as shown in Figure 4.3(b) the second storage should be introduced to cover the frequencies higher than the  $f_{H,ESS1}$ . Thus the combined effective frequency range of the HESS is now expanded to the  $f_{L,k} - f_{H,ESS2}$ . If the  $f_{H,k} < f_{H,ESS2}$  this arrangement is sufficient for the given application. If not, the process continues similarly for the third device. This has been the general concept of the selection of the suitable storage types for the hybrid storage scheme in order to satisfy the requirement of the

given application. Therefore, the suitability of the ESS devices of HESS for the given application can be analytically compared based on the dynamic characteristics using the proposed concept of the effective frequency range. Thus, forming a HESS for given net power discussed in this chapter primarily using the Li-ion battery-SC combination.

In a similar manner as in the construction of battery model, the behavior of supercapacitor (SC) can be studied using ECM. Complexity of these models is increased starting from a single RC branch to elevate the model accuracy. The most common equivalent circuit types are presented in literature are namely ESR and series capacitor model, constant phase element model with two RC branches and four RC branches model.

### 4.2.3 Simplification of the ECM

As it is demonstrated for Li-ion battery, simplification of ECM leads to represent the complex ECM of the battery storage using an simple series RC circuit for the given frequency range of interest. For instance, some RC branches of the comprehensive battery model are omitted in our discussion as diffusion characteristics are neglected in short term dynamics. This will guide to obtain the series RC equivalent and then the convert it to the equivalent parallel RC branch of the given storage for the given application frequency range. However, this might be tiresome practice for some storage types as the physical meaning of each component of the ECM should be well known prior to be removed from the complex ECM for the particular frequency range. Therefore, an alternative method for this simplification is introduced.

Firstly, using the EMD analysis of the given load curve, the frequency components presented in the net load curve can be readily identified and then the frequency range of interest can be determined. Considering only this interested frequency range, the complex ECM can be approximated such that a very close representation of this model can be achieved by the equivalent series RC model. Figure 4.4 compares such phase vs frequency profile obtained using the 4-branch SC ECM given in [130] with that of the equivalent series RC model. It is apparent from the figure that the series RC model produces the phase diagram which is in close agreement with that of the 4-branch SC model over the frequency range of interest in this work, viz:  $10^{-6} < f < 0.5$  Hz. Therefore, in this study where long-term diffusion effects are not considered, the simple series ECM is used to represent the SC. Once the series parameters are obtained similar to battery, effective capacity can be obtained for the SC.

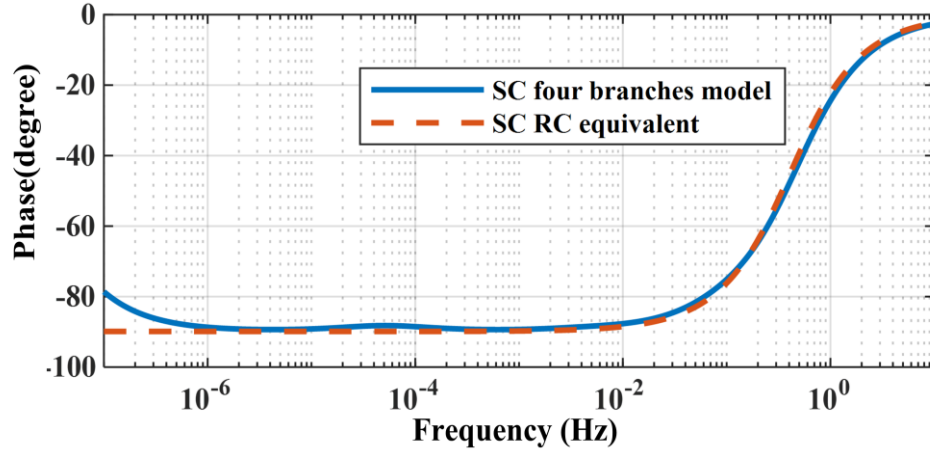


Figure 4.4. Comparison of phase diagram between the 4-branch SC and equivalent series RC SC model

#### 4.2.4 ESS Economical Operating Frequency Range

The kWh storage capacity  $E_{ESS}(\omega)$  vs frequency profiles of the selected battery and SC are given on Figure 4.5 with a p.u. base value of 6.67Wh. As expected, the figure shows that the storage capacities of both ESS decrease as frequency increases. In the operation of the HESS for the particular application, it is necessary to identify the critical frequency in which these devices are segregated. This critical frequency defined as cut-off frequency should be determined not only considering the dynamics but also the economics of the storages. Thus, each of the storages economical frequency ranges can be identified. Therefore, based on the effective storage capacity of the storage, the cost per effective kWh capacity of the storage is examined in this work to reflect both the performance and economic characteristics of the storage.

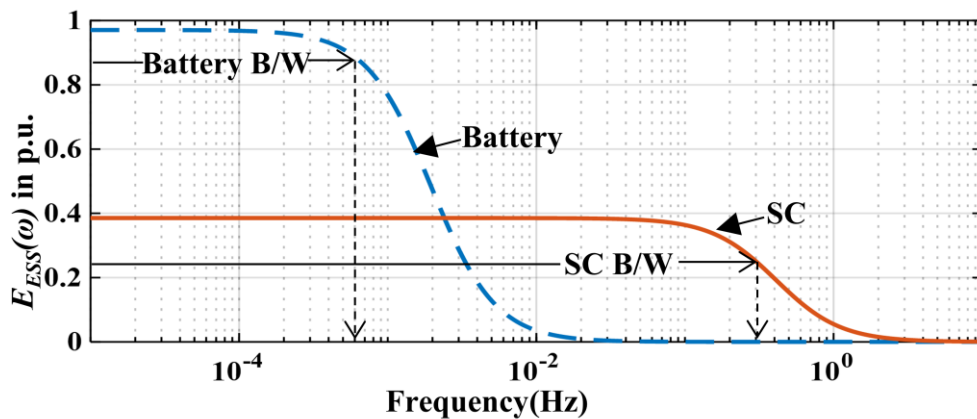


Figure 4.5 Effective energy capacity vs frequency profiles of battery and SC



## 4.2.5 Determination of cut-off frequency between the constituent storages of HESS

The variations in the battery and SC effective capacity will impact on the economic usage of the ESS. Denote the capital cost of an ESS as  $C_{ESS}$ . Therefore, the cost per kWh storage capacity of the ESS is  $C_{ESS}/E_{ESS}(\omega)$  at the frequency  $\omega$ . From the previous sub-section, it is known that  $E_{ESS}(\omega)$  decreases with the increase in  $\omega$ , therefore the capital cost per kWh storage capacity of the ESS will increase with  $\omega$ . As an illustration, Figure 4.6 shows the  $C_{ESS}/E_{ESS}(\omega)$  vs  $\omega$  curves of the SC and Li-ion battery considered earlier. The capital costs are US\$10 for the 1.8 Ah 3.7V Li-ion battery and US\$36 for the 1200F 2.7 V SC. Clearly the decrease in  $E_{ESS}(\omega)$  at elevated frequency makes the ESS increasingly expensive, in terms of the cost per kWh storage capacity of the ESS. Notice that the two curves cross-over at the frequency, which is assigned the special symbol of  $\omega_{c,p}$ . In this example,  $\omega_{c,p}$  is 0.0085 Hz. Thus, it can be concluded that in this example, in comparison with the SC, the battery will be more economical in providing the energy to buffer those perturbing power components which have frequencies below  $\omega_{c,p}$ . Conversely, the SC will be more cost effective in providing the buffering actions for those perturbing power of frequencies above  $\omega_{c,p}$ .  $\omega_{c,p}$  can be taken to be the cut-off frequency between the SC and battery, in the design of the SC-Li ion battery HESS.

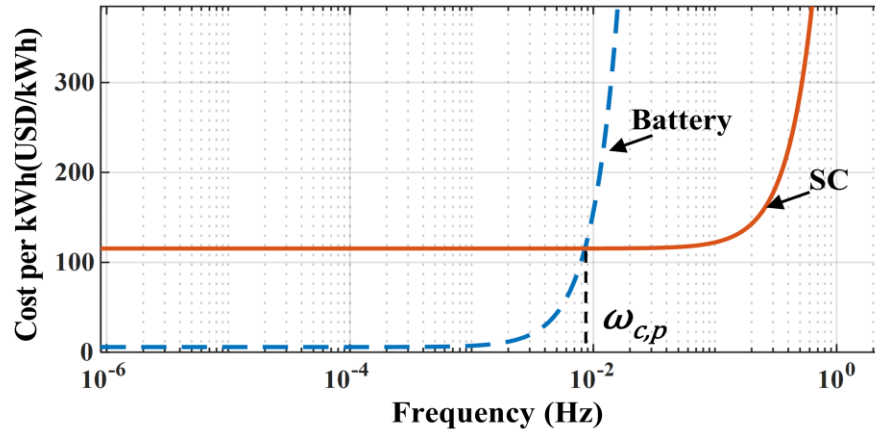


Figure 4.6. Comparison of the capital cost per kWh capacity of battery and SC: notice at  $\omega_c$ , the curves cross-over

In this investigation, the HESS is to be used to provide the buffering actions on  $P_{net}(t)$  of a prosumer. In Section 3.3, it is shown that  $P_{net}(t)$  can be decomposed into its IMFs and the associated ranges of the instantaneous frequency  $f_i(t)$ . Figure 4.7 shows the cdf plot of  $f_i(t)$

obtained from the EMD analysis of  $P_{net}(t)$  measured over a 3-month period. The figure shows that more than 50% of the instantaneous frequencies in  $P_1(t)$  and  $P_2(t)$  are above  $\omega_{c,p}$ . So, in this instance, it is considered the SC would be more cost effective in providing the buffering actions for  $P_1(t)$  and  $P_2(t)$ . Conversely, the Li-ion battery would be more cost effective in buffering  $P_3(t)$  and higher order IMFs because the probability of their frequencies at less than  $\omega_{c,p}$  is more than 50%. So in this way, the families of the IMFs which can be more cost-effectively buffered by the battery and the SC have been readily identified.

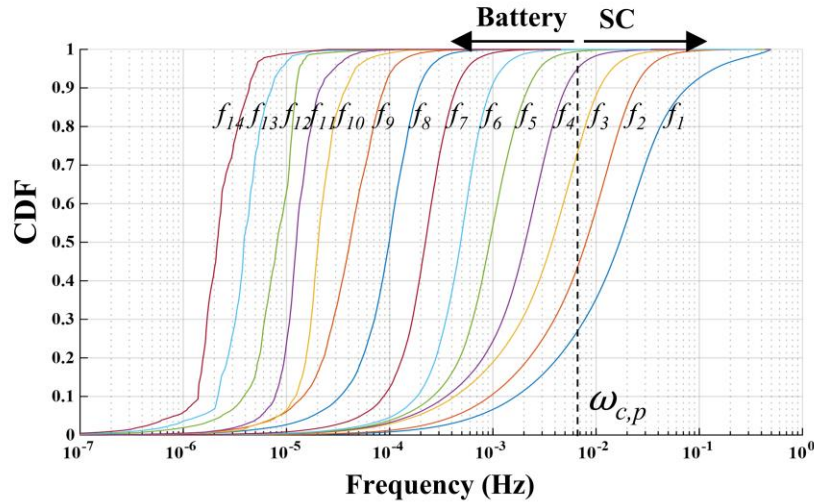


Figure 4.7. CDF values for the frequencies from IMF1 to IMF14 ( $\Delta t=1\text{sec}$  and  $T=3\text{months}$ )

### 4.3 Hierarchical HESS Scheme

#### 4.3.1 Introduction to hierarchical storage scheme

In a storage scheme presented in Section 3.2, Figure 3.1 explains the storage placement at different hierarchies of the power system. In a planning study of such a scheme, which includes multiple storages with different characteristics, the exhaustive iterative methods are unsuitable to calculate the cut-off frequencies between them. However, the proposed analytical strategy of a single prosumer can be readily extended to three or more component ESSs to plan the hierarchical storage scheme consists of community-scaled and the grid-scaled storages. Initially, the cut-off frequency between those storage can be determined comparing the cost-frequency characteristics. Then, the cdf of  $f_i(t)$  of  $P_{net}(t)$  described in Figure 4.7 can be used to identify IMFs, which can be most cost-effectively buffered by each of the respective component ESSs.

In a conceptual microgrid scheme in achieving the near-zero dependency of the grid, those community and grid scale storages play a vital role as storages for monthly and seasonal energy

variations. As shown in Section 3.4 these seasonal IMFs consist of higher oscillating energy. Thus, it is certain that these storage types should have higher storage capacities and lower cost per kWh capacity which make them suitable for such community and grid-scale applications. Therefore, even the Li-ion battery and the SC are able to handle the frequency range of the  $P_{net}(t)$  of single prosumer, it is uneconomical to accommodate such a costly storage like Li-ion battery to store these seasonal IMFs. Thus, it is worthwhile to consider a storage which has economical frequency range lower than that of a Li-ion battery which has a lower capacity cost per kWh to fit in to community and grid scaled storages. Therefore, candidate storage should result in another cost-frequency curve left to the Li-ion battery which will result in a lower cut-off frequency for battery. This will also allow to identify the IMF components related to the Li-ion battery precisely which then can be used to determine the capacity of the battery.

Such candidate storage scheme for the lower frequency oscillating components with higher energy could be Fuel Cell or Pumped hydro according to Table A.1 in Appendix A. However, the operating ranges of these storages in the frequency plane are not exactly known. Therefore, in the section, the most matured ESS technology out of these two is the PHES will be illustrated. The proposed strategy is used to accurately identify the effective frequency bandwidth of the storage first. Then this will enable to determine the lower cut off frequency when they are used with the Li-ion battery which is shown with an example next.

### **4.3.2 Illustrative example for community and grid scale storage technologies using Pumped Hydro Energy Storage**

In order to demonstrate the proposed method for the community and grid level storages, the PHES is selected for this analysis among the mentioned candidates which includes Fuel Cell and PHES. PHES is regarded to be the more matured ESS as community or grid level storage out of these, and therefore, it is considered for this illustrative example.

#### **a. Obtaining the bode plot of Equivalent circuit model (ECM)**

In most of the applications in the literature, the charging and discharging of the PHES are considered as a symmetrical operation [131, 132]. The complete integrated ECM of PHES can be depicted as in Figure 4.8. The formation of this complete ECM is described in detail in Appendix B with relevant to the literature. As mostly practiced in previous analysis, the elasticity of the pipes can be neglected [131] to simplify this complete ECM to the model presented in Figure 4.9.

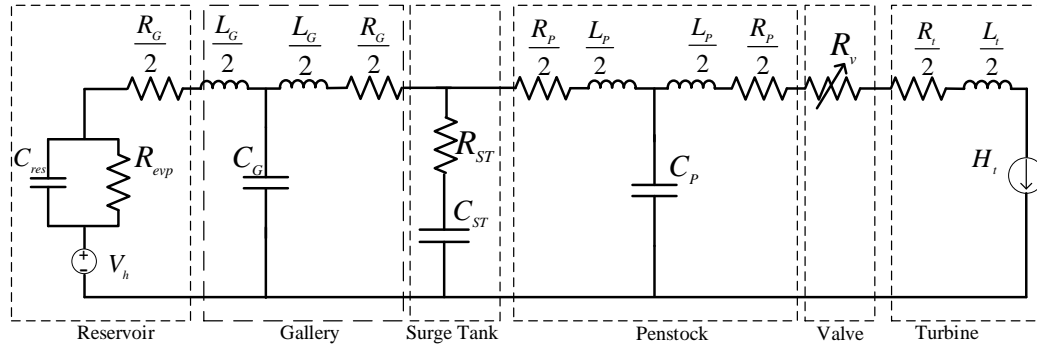


**Figure 4.8. Complete ECM of the discharging circuit of the PHES**

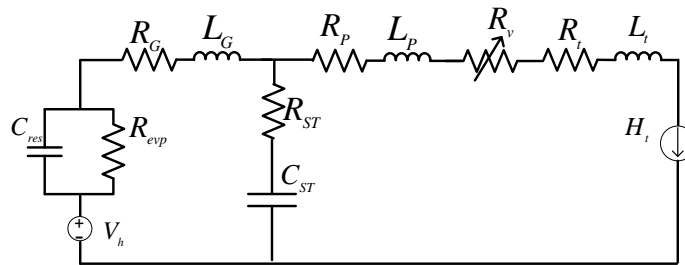


**Figure 4.9. Simplified ECM of discharging circuit of the PHES**

This reduced model is simulated using the PLECS simulator as the frequency response of such a complex circuit with variable resistances cannot be analytically simplified easily. It is assumed that the both the charging and discharging (pumping and generating) circuits follow the same ECM. Analogous to generation in PHES, ECM is simulated using the perturbation at the current source of the turbine end measuring the output voltage as shown in Figure 4.10.

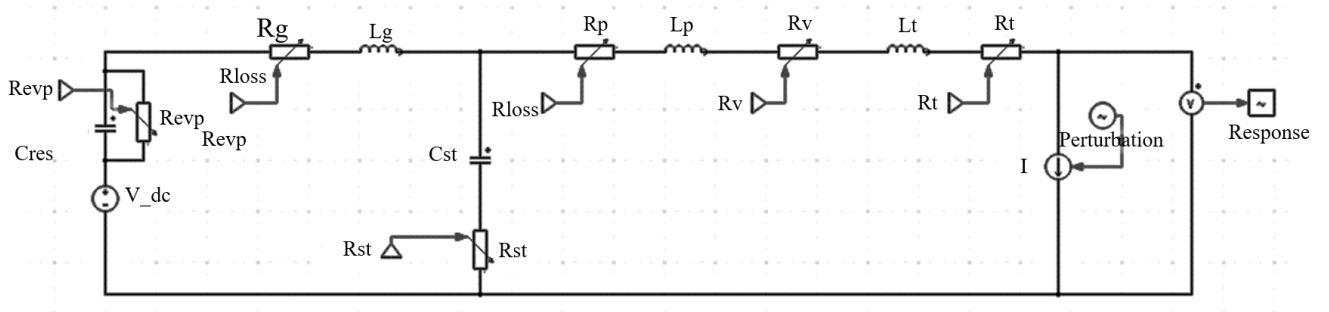


**Figure 4.10. Simulated ECM of PHES in PLECS**

**b. Obtaining the bode plot of ECM of the PHES**

Identifying the interested frequency range is the next step. Since IMFs with seasonal variations also need to be captured, at least one year of data should be analysed. To facilitate this, slower sample

rate of 1min can be selected to be analysed using the EMD. Thus, it can be determined the interested frequency range for the 1min sample rate for one year dataset is  $1 \times 10^{-8} \text{Hz}$ - $0.0083 \text{Hz}$ . Using the simulated ECM of Figure 4.10, magnitude plot shown in Figure 4.11 and phase plot shown in Figure 4.12 can be obtained for the frequency range  $1 \times 10^{-8} \text{Hz}$ - $0.0083 \text{Hz}$ . According to Figure 4.12, it is clear that the PHES shows the capacitive behavior in the frequency range  $1 \times 10^{-8} \text{Hz}$ - $1 \times 10^{-4} \text{Hz}$ . Therefore, the effective frequency range of the PHES to work as an ESS is limited to this frequency range.

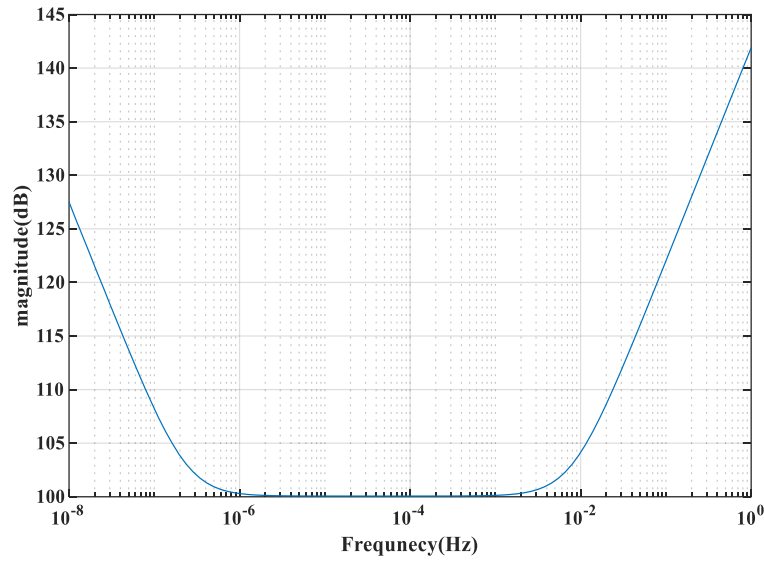


**Figure 4.11. Magnitude plot of the frequency response**

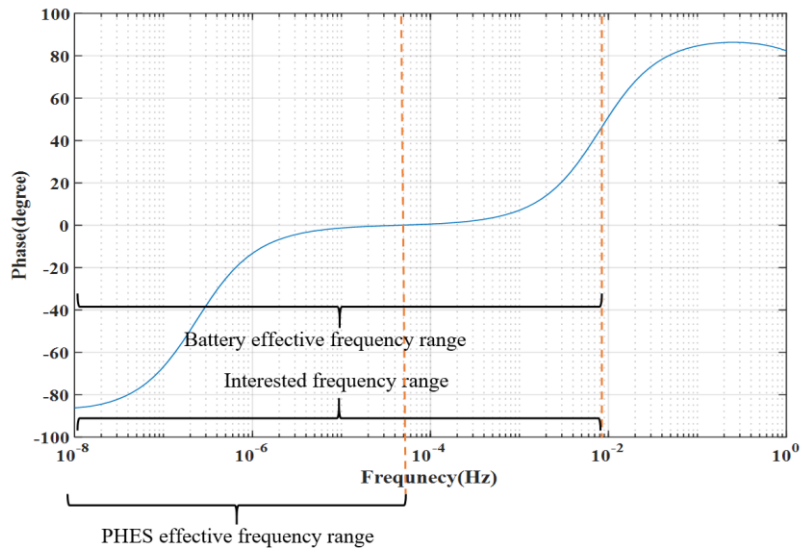


**Figure 4.12. Phase plot of the frequency response**

### c. Obtaining the simple series model parameters

If the behavior of the ECM can be represented in the interested frequency range using a simplified RC model, it is certain that simple series RC is equivalent to the behavior of the ECM in this frequency range. These R and C parameters can be estimated graphically as following.

If the equivalent series parameters are  $R_{s,PHEs}$  and  $C_{s,PHEs}$ , According to the magnitude plot of series RC circuit model  $f \rightarrow \infty$ ,  $|H(s)|_{dB} \rightarrow 20 \log |R_{s,PHEs}|$ . As shown in Figure 4.13 (a), when  $f \rightarrow \infty$ ,  $|H(s)|_{dB} \rightarrow y_1$ . Then  $R_{s,PHEs} = 10^{\frac{y_1}{20}}$ . With this estimated  $R_{s,PHEs}$ , then value of  $C_{s,PHEs}$  has to be determined such that phase response of RC equivalent is same as the phase plot of ECM. Therefore the  $C_{s,PHEs}$  will be empirically decided such that it achieves the least RMSE with the phase plot of ECM. According to the above example PHEs,  $y_1 = 100$ ,  $R_{s,PHEs} = 10^5 \text{ ohms}$ ,  $C_{s,PHEs} = 6.5F$ . Comparison of the PHEs ECM and the RC equivalent of both magnitude plot and phase plot is depicted in Figure 4.13 (a) and (b).

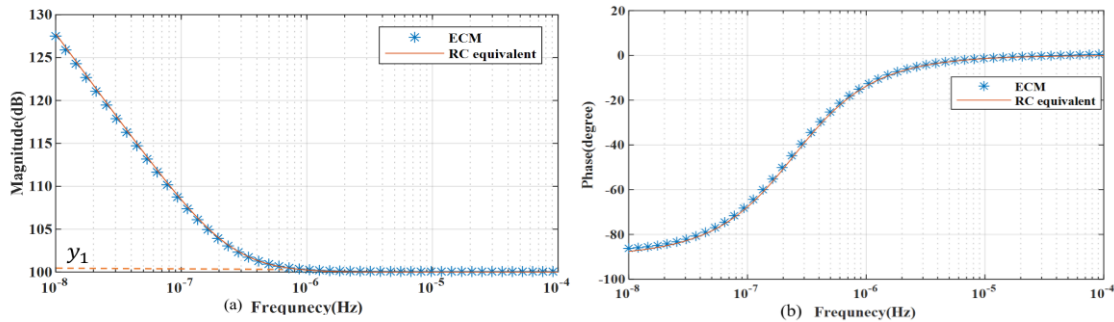


**Figure 4.13. (a) Comparison of the ECM magnitude plot and equivalent RC (b) Comparison of the phase plots of ECM and equivalent RC**

Following the same methodology performed over battery and SC, these series parameters will be converted to parallel parameters named  $R_{p,PHEs}$  and  $C_{p,PHEs}$ . Then the effective energy component of the PHEs can be calculated with respect to frequency.

### d. Determining the per kwh cost of PHEs

Cost of battery per kWh is readily available in most the recent literature as 250USD/kWh [133, 134]. However the capacity cost per kWh for pumped hydro usually varies across different scales and applications [135]. A table provided in [136] (Appendix C) offers a range of capacity costs for different PHEs units, resulting in cost per kwh between 10-60USD/kWh. For this illustrate example, a mean value of these costs is taken as 16USD/kWh.

### e. Determining the cut-off between PHES and Battery

Normalized effective capacity for PHES was obtained by normalizing the capacities of Li-ion battery and PHES as depicted as in Figure 4.14(a). Then, cost per effective capacity is obtained as depicted in Figure 4.14(b) for both Li-ion battery and PHES.

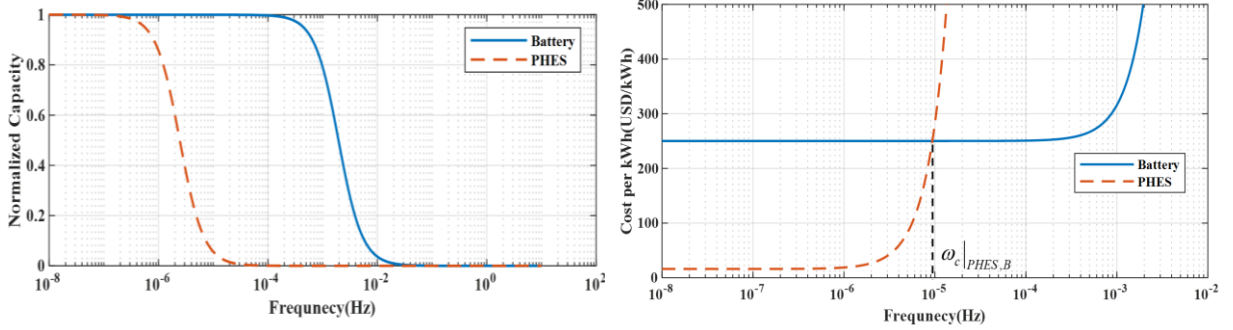


**Figure 4.14. (a) Normalized effective capacity vs frequency for PHES and Battery (b) Cost per effective kWh curves for Battery and PHES**

From Figure 4.14(b), it could be determined the cut-off frequency between the Li-ion battery and PHES denoted by  $\omega|_{PHES,B}$  is  $9.96 \times 10^{-6}$  Hz. The equivalent time of this frequency is around 1.12 days. Therefore, it is clear that the operation of the PHES is economical compared to the Li-ion battery for the frequency components which have higher oscillating time than the 1.12 days. If the cost per kWh varies in the range 10-60 USD/kWh the resulting cut-off frequencies as below.

For 60USD/kWh  $\omega|_{PHES,B} = 4.8 \times 10^{-6} = 2.37$  days

For 10USD/kWh  $\omega|_{PHES,B} = 1.2 \times 10^{-5} = 0.96$  days

Denote the cut-off frequency setting between the battery and SC as  $\omega_c|_{B,SC}$ . Then for a hierarchical HESS scheme with PHES, Battery and SC storages, the economical frequency range for Li-ion battery is  $\omega_c|_{PHES,B} < f < \omega_c|_{B,SC}$ .

## 4.4 Validation of cut-off frequency Determination

### 4.4.1 Determination of cut-off frequency using existing method

In this section, the existing cut-off frequency determination method is compared with the proposed method. In [40], an approach to determine cut-off frequency is introduced. Similar to the proposed approach, the method reported in this work is also based on EMD analysis, hence it represents the most closely comparable case with the proposed method. Authors in the [40] have introduced the

cut-off frequency determination strategy using an iterative approach to search for so-called minimum overlap energy.

Once an arbitrary cut-off frequency ( $f_g$ ) is introduced, it may cause to divide the frequency range in to two sections which are related to the respective ESS devices, say battery and SC in this case. So, the IMFs belong to these two planes can be treated as two groups related to the respective devices named as LF IMFs and HF IMFs. As explained in Section 4.2, there are regions of overlaps in the cdf of one IMF with those of the neighboring IMFs. Due to this, there can be IMFs where their frequencies accommodate in both groups, since cannot be effectively determined as HF or LF IMFs. These IMFs are henceforth named as boundary IMFs. If previous battery-SC example is considered, when a boundary IMF is attempted to be smoothened by SC, for a given cut-off frequency setting  $f_g$ , those portions of an IMF which have frequency below  $f_g$  would be buffered by the battery whereas those portions of the same IMF which have frequency above  $f_g$  would have to be buffered by the SC. Hence it is necessary to proportion the buffering actions contributed by the SC and the battery. In order to reduce the ambiguity of the segregation between the battery and SC it is targeted to reduce this amount of energy contain in the overlap region. This will minimize the amount of energy transfer between the battery and SC. In order to achieve this, the process proposed in [40] iterative search of unique value of  $\omega_c$  out of  $f_g$  values such that the overlap energy is minimized. Let  $\omega_{c,e}$  denote this cut-off frequency calculated by the existing method. Same  $P_{net}(t)$  with sample time 1sec and total timespan of 3months, is used to calculate  $E_{overlap}$  for the range of  $f_g$ . The respective graph is shown in Figure 4.15. When minimum of  $E_{overlap}$  occurs, the value of  $f_g$  is determined as  $\omega_{c,e} = 0.0114\text{Hz}$ . The value obtained from this existing method, i.e.,  $\omega_{c,e}$  is slightly higher compared to the proposed method value  $\omega_{c,p} = 0.0085\text{Hz}$ .

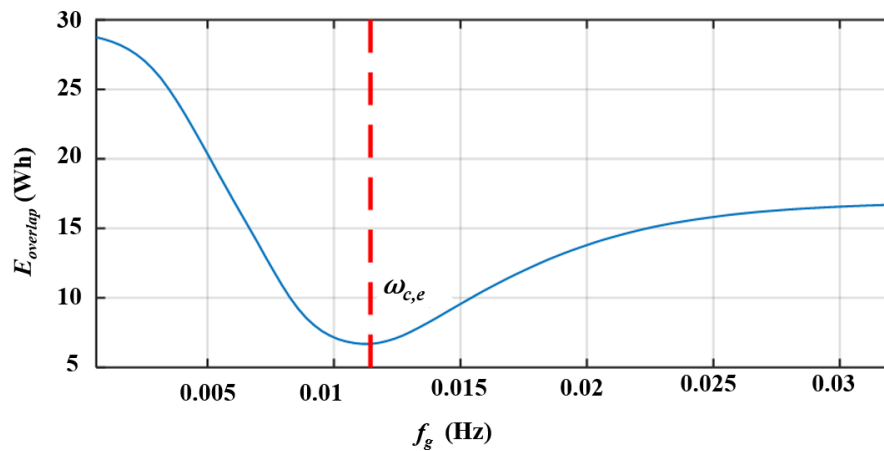


Figure 4.15.  $E_{overlap}$  vs  $f_g$  and the determination of  $\omega_{c,e}$



#### 4.4.2 Comparison of computation burden

While it is pleasing to note that the cut-off frequency determined is close to that determined earlier, i.e.,  $\omega_{c,e} = 0.0085\text{Hz}$ , it must be reported that in the course of searching for the minimum overlap energy condition, the computation had been carried out under the MATLAB environment, using a computer processor of Intel® Core™ i7-9700T CPU, 2.00 GHz, and 16-GB DDR3 RAM. The solution time is some 18.6 min. In contrast, the proposed method will yield the cut-off frequency based on the cost-effective frequency ranges of the constituent ESSs within a HESS with an execution time of some 0.34s. The proposed approach is direct, definitive and in a closed-form. Hence, it does not involve any iterative search. Furthermore, unlike the minimum overlap energy method [40], the proposed approach bears a direct relationship to the physical characteristics of the storage devices.

#### 4.5 Conclusion

This chapter identifies the primary requirement for planning study of the HESS is to determine the cut-off frequency accurately with respect to both economic and dynamic response characteristics of the storages. According to existing literature, only optimization algorithms are used to optimize the cost-based indicators in such a planning study while very limited studies have focused on the segregation of the net power components accurately considering dynamic characteristics. By utilizing the ECM of the candidate storage technology, it is identified that the effective capacity of each storage is frequency-dependent. Then the capacity cost per kWh-frequency characteristics of one storage is compared with that of the constituent storage to determine accurately the cut-off frequency between the storages of the HESS. This would ensure the most economical HESS design for prosumers. The results of the comparative analysis show the effectiveness of the proposed cut-off determination technique reaching near optimal value. The proposed method, based on device physical characteristics, results in minimum cost per kWh throughout the frequency range of interest in a deterministic way. As the proposed approach does not involve iterative search procedure, it requires least computation time. Thus, the sufficiently generalized proposed method is well-suited for a planning study onto the design of hybrid energy storage scheme consisting of a number of different types of ESS.

# **CHAPTER 5. A Statistical Approach to Estimate the Required Energy Storage Capacity of Hybrid Energy Storage System**

## **5.1 Introduction**

Once the  $P_{net,i}(t)$  variation of a prosumer is analyzed and the cut-off frequencies between the constituent energy storage components in the HESS are determined, in the manner as explained in CHAPTER 4, the next task is to evaluate the power and energy levels to be buffered by each of the constituent storage components. Therefore, this chapter delves into the segregation of the IMFs derived from the analysis presented in CHAPTER 3, based on the cut-off frequency determined in CHAPTER 4. This will enable the required capacities of the constituent ESS in the HESS to be determined. However, the existing capacity determination methods of prosumer level HESS incorporate mostly the cost-based optimization approaches as discussed in the literature in Section 2.2.5. Very few attempts were reported based on direct analytical approach which tends to require lower computational burden. Thus, in order to realize the designed levels of uncertainty during the renewable applications, it is important to incorporate the analytical method with a suitable statistical approach at the capacity determination level. This is the major contribution of this chapter.

To facilitate the discussion, the scope of the work considered in this chapter is limited to the HESS containing two constituent energy storage components at the premise of a prosumer. As seen in CHAPTER 4, the frequency band of an IMF spans over a (limited) range. So, inevitably the frequency bands of some IMFs will span over both sides of the cut-off frequency which is identified by the technique described in that chapter. These IMFs are termed the boundary IMFs. The constituent energy storage components are intended to buffer the IMFs, with the higher frequency IMFs buffered by the SC and the lower frequency IMFs dealt with by the battery. However, how to demarcate the boundary IMFs to the constituent storage components remains an unanswered question. Accordingly, the first objective of this chapter is therefore to describe a computational approach which will provide the answer to this question. Then, a statistical analysis is performed on the oscillation energy buffered by each of the constituent storage components. This is with the view to estimate the required energy capacities of the constituent storage components. In contrast to some of the existing optimization-based HESS capacity determination methods, the proposed approach is direct and can be readily extended to include HESS schemes containing more than two constituent

energy storage components, without imposing substantial increase in the computational burden.

## 5.2 System Under Study

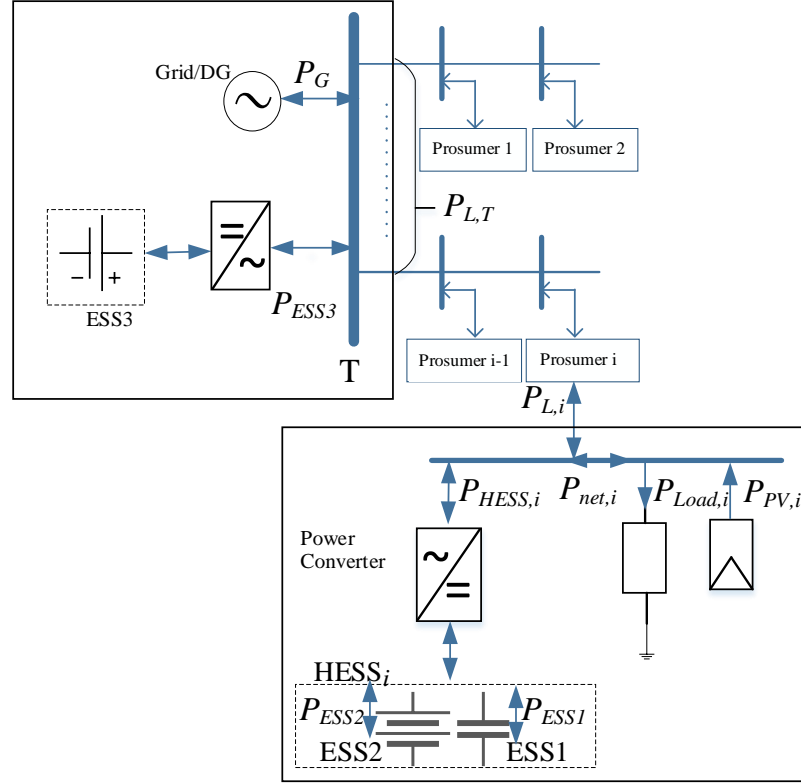


**Figure 5.1. A conceptual hierarchical energy storage scheme consisting of the hybrid energy storage system within a prosumer and an energy storage system outside of the prosumer**

CHAPTER 4 shows that the net power flow from the  $i^{th}$  prosumer ( $P_{net,i}(t)$ ) can be readily decomposed into a family of IMFs and the residue function using the EMD technique. The residue is a trend function, and therefore, in the long run, this function would indicate either a continuous energy surplus or energy deficit situation. Hence no energy storage action is to be taken to deal with the residue function. So, in the design of the HESS, attention needs to be directed only to the IMFs of  $P_{net,i}(t)$ .

Figure 5.1 depicts a conceptual hierarchical storage arrangement in which at the prosumer level, an HESS is to consist of the constituent storage components ESS1 and ESS2. Referring to the HESS example in CHAPTER 4, the prosumer ESS1 and ESS2 are selected as SC and Li-ion battery. The cut-off frequency between the battery and SC, denoted as  $\omega_c$ , can be determined using the approach proposed in CHAPTER 4. A typical example of  $\omega_c$  for the battery-SC combination is

depicted in Figure 5.2. In this figure,  $\omega_c$  is shown superimposed onto a family of cdf curves of the instantaneous frequencies of the IMFs. The determination of the cdf has also been explained in CHAPTER 4 and the cdf for IMF<sub>j</sub> shall be denoted herewith as  $f_j$ .

In Figure 5.1, another storage device ESS3 is shown located at a higher level of the hierarchical energy storage scheme. Although not discussed in the previous chapter, one could apply the same approach described there to obtain  $\omega_{L,c}$ , the cut-off frequency between ESS2 (the battery) and ESS3.  $\omega_{L,c}$  will be at a much lower frequency than  $\omega_c$ , as indicated in Figure 5.2. With known  $\omega_{L,c}$ , the approach to be described in the following sections can be equally applicable in the design of ESS3. However, since the focus of the present chapter is on the design of the HESS at the prosumer level, the design of ESS3 shall be omitted in the present study.

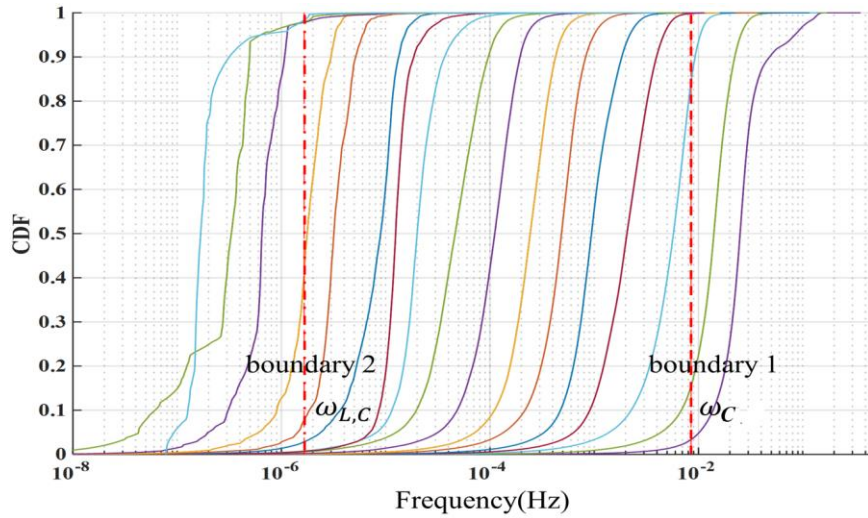


Figure 5.2 CDF of IMFs of  $P_{net,i}(t)$  and the locations of the cut-off frequencies  $\omega_c$  and  $\omega_{L,c}$

### 5.3 Determination of the Buffering Power in ESS

The previous section explains the cut-off frequency ( $\omega_c$ ) between ESS1 and ESS2 can be determined using the method proposed in CHAPTER 4. In Figure 5.3, the cdf curve of the frequencies contained in IMF<sub>j</sub> is shown as  $f_j$ . As shown, at the cut-off frequency  $\omega_c$ , the corresponding value of  $f_j$  is denoted as  $CDF_j(\omega_c)$ .

Based on the cdf, one could then readily decide whether IMF<sub>j</sub> shall be buffered by ESS1 or ESS2 in the following way. Select suitable threshold probability values  $\rho_h$  and  $\rho_l$ . Typically,  $1 > \rho_h > 0.5$  and  $0 < \rho_l < 0.5$ . Then if  $CDF_j(\omega_c) > \rho_h$ , IMF<sub>j</sub> is to be buffered exclusively by ESS2. On the other hand, if  $CDF_j(\omega_c) < \rho_l$ , IMF<sub>j</sub> is to be buffered exclusively by ESS1. In this work,  $\rho_h=0.95$  and

$\rho_l=0.05$ . In this way, the allocation of the task of buffering IMF<sub>j</sub> to either ESS1 or ESS2 becomes a straight-forward decision.

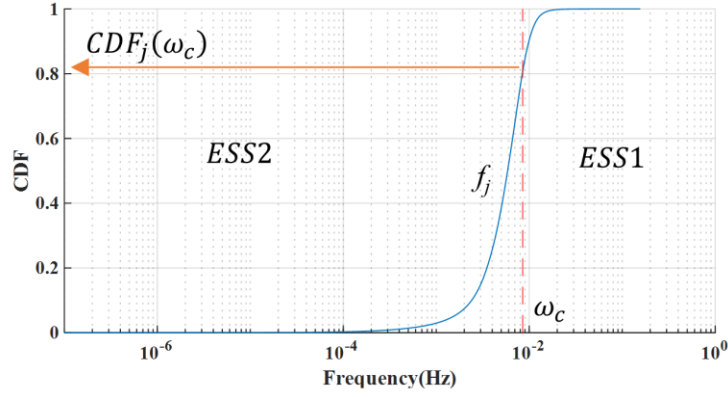


**Figure 5.3 Distribution of the frequencies in IMF<sub>j</sub>; at the cut-off frequency  $\omega_c$ , the CDF has the value  $CDF_j(\omega_c)$ .**

However, the challenge is when the value of  $CDF_j(\omega_c)$  falls within the range  $\rho_l < CDF_j(\omega_c) < \rho_h$ . In the present work, IMF<sub>j</sub> which is in this category is called a boundary IMF. The actions required for buffering the boundary IMFs would have to be shared by ESS1 and ESS2. And an approach to apportion the buffering task to the respective constituent storage components shall now be described.

### 5.3.1 Apportion of the buffering task of the boundary IMFs

The proposed method to apportion the buffering task of the boundary IMFs can be conveniently explained using Figure 5.4. Consider the boundary IMF  $P_j(t)$  in Figure 5.4(a). The corresponding instantaneous frequencies  $f_j(t)$ , obtained through the HHT analysis of  $P_j(t)$ , is as shown in Figure 5.4(b). In this figure, the cut-off frequency  $\omega_c$  has been superimposed. It can be readily seen that over the intervals a-b, c-d and e-f,  $f_j(t) < \omega_c$ . Clearly these low-frequency portions of  $P_j(t)$ , denoted herewith as  $P_{LF,j}(t)$ , should be buffered by ESS2 because the capital cost/storage capacity of ESS2 is lower than that of ESS1 at frequency below  $\omega_c$ . Conversely, the remaining portions of  $P_j(t)$  would have their instantaneous frequencies above the cut-off frequency, i.e.,  $f_j(t) > \omega_c$ . These high-frequency portions of  $P_j(t)$  denoted as  $P_{HF,j}(t)$ , shall be buffered by ESS1. This process is also straight-forward and can be readily carried out for all the boundary IMFs.

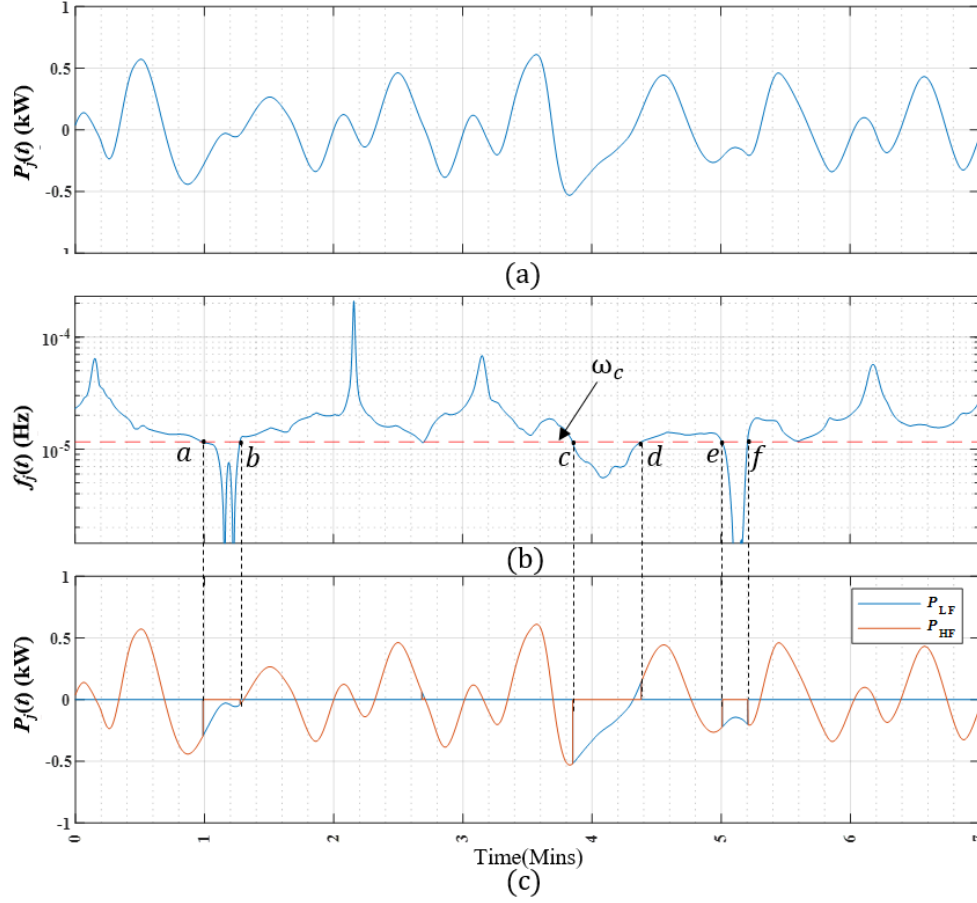


**Figure 5.4. Allocation of the buffering actions for boundary IMF (a)  $P_j(t)$  (b) instantaneous frequency, (c) low- and high-frequency portions of  $P_j(t)$ .**

As explained in the last paragraph of Section 5.2, there shall be another cut-off frequency  $\omega_{L,c}$  in the hierarchical ESS arrangement of Figure 3.1. One can follow the same procedure as outlined above and apportion the power buffering burden between ESS2 and ESS3. So, from the set of the boundary IMFs associated with  $\omega_{L,c}$ , one allocates the high- and low-frequency portions of these IMFs to the ESS2 and ESS3 respectively for the power buffering actions.

In summary, therefore, firstly there shall be those  $IMF_j$  to be exclusively buffered by ESS1 and for the convenience of discussion, the index “j” of this set of IMFs shall be given the symbol  $i_{ESS1}$  to reflect the fact that they are to be buffered exclusively by ESS1. In addition, ESS1 is to buffer the high-frequency portions  $P_{HF,j}(t)$  of those boundary  $IMF_j$  associated with the first cut-off frequency  $\omega_c$ , e.g.,  $P_{HF,j}(t)$  shown on Figure 5.4(c). The index “j” pertaining to these power components shall be denoted as  $i_{B1}$  as it is associated with the first boundary.

It follows that there shall be those low-frequency portions  $P_{LF,j}(t)$  of IMF<sub>j</sub> associated with the first cut-off frequency  $\omega_c$  which shall be buffered by ESS2. The index “j” corresponding to these power components shall also be denoted  $i_{B1}$ , since it is associated with the first set of the boundary IMFs. At even lower frequency, there shall be another set of IMFs which are to be exclusively buffered by ESS2 as the cdf of these IMFs satisfy the condition  $CDF_j(\omega_c) > \rho_h$ . The index of these IMFs are denoted as  $i_{ESS2}$ . Finally, the ESS2 is to buffer those high-frequency portions of those boundary IMFs associated with the cut-off frequency  $\omega_{L,c}$ . The index “j” for these power components is denoted as  $i_{B2}$  to indicate that it is associated with the second set of the boundary IMFs.

Let the oscillating power components to be buffered by ESS1 (SC) and ESS2 (Li-ion battery) be denoted as  $P_{SC}(t)$  and  $P_B(t)$  respectively. In accordance to the apportion procedure described above,  $P_{SC}(t)$  and  $P_B(t)$  shall be determined directly by summing the respective IMFs to be exclusively buffered by ESS1 and ESS2, and those high- and low-frequency portions of the boundary IMFs. The mathematical expressions of this determination are given in (5.1) and (5.2).

$$P_{SC}(t) = \sum_{j=i_{ESS1}} P_j(t) + \sum_{j=i_{B1}} P_{HF,j}(t) \quad (5.1)$$

$$P_B(t) = \sum_{j=i_{B1}} P_{LF,j}(t) + \sum_{j=i_{ESS2}} P_j(t) + \sum_{j=i_{B2}} P_{HF,j}(t) \quad (5.2)$$

Having determined  $P_{SC}(t)$  and  $P_B(t)$ , attention shall be directed toward the evaluation of the perturbing energies associated with the buffering actions of the two ESS.

## 5.4 A Statistical Analysis of the Stored Energy Level in an ESS

EMD analysis is a series of sifting process by which the intrinsic oscillating modes, i.e. the IMFs, of a given data-set can be identified. Again taking Figure 5.4(a) as an example, over any one of the intervals prescribed by three consecutive zero-crossing points of the IMF curve  $P_j(t)$ , one observes that the area encompassing by the positive portion of  $P_j(t)$  will not be exactly equal to that of the negative portion. The areas correspond to the energy contents  $E_j(t)$  of  $P_j(t)$ . In term of the buffering actions offered by an ESS, the energy pertaining to the positive portion of  $P_j(t)$  can be viewed as the charging energy going into the ESS. Conversely, the negative area corresponds to the discharging energy released by the ESS. In the context of the study, this leads to an interesting observation that over a sufficiently long period,  $E_j(t)$  can exhibit either a sustained upward or downward drift. An example of such an occurrence can be seen in Figure 5.5 in which the energy content of IMF<sub>5</sub> is

shown over a week. The figure shows that compared to the energy level at the beginning of the selected 7 days period, there is a sustained downward drift in the energy level in IMF<sub>5</sub>. So, if one were to use a study window of a week or longer to assess the energy storage capacity needed for an ESS to buffer IMF<sub>5</sub>, the ESS would have to be of exceedingly large capacity.

In practice, the sustained drift in  $E_j(t)$  can be prevented by allowing the transfer of energy between the ESSs within an HESS, or between the ESSs and active energy source(s) in the external grid system. The aim of the energy transfer mechanism is to restore the stored energy level in the ESS to certain pre-specified value at regular interval. So, suitable value has to be found for the restoration interval for each of the energy storage components in the HESS. In this work, the carefully selected restoration interval is denoted as  $t_s$ .

For the SC-battery HESS considered in this work, the cut-off frequency  $\omega_c$  between the battery and the SC is determined to be about 0.0085 Hz, corresponding to a period of about 2 minutes/cycle. Power fluctuations in  $P_j(t)$  at a rate faster than 2 minutes per cycle are to be buffered by the SC. Thus, a suitable setting of the restoration interval  $t_s$  for a SC would have to be longer than 2 minutes and there shall be sufficient number of cycles in  $t_s$ . In this work,  $t_s$  is set as one hour for the SC. Following similar reasoning, the restoration interval for Li-ion battery  $t_s$  is selected to be one day in the present investigation. So, in this way, one can examine the perturbing energy within the time window of  $t_s$  and assume that due to the energy transfer to/from external ESS/energy source, the amount of the stored energy in the SC or battery shall be restored to the same level as that at the beginning of the window.

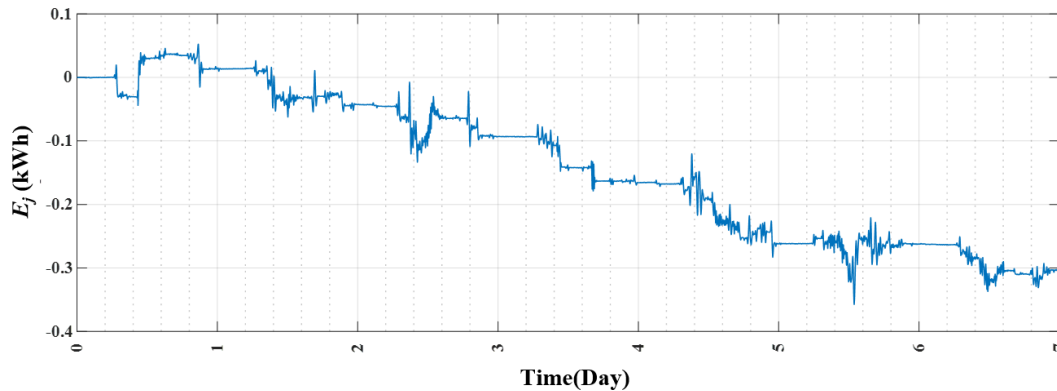


**Figure 5.5.**  $E_s(t)$  showing the obvious downward drift over a week

The variations of the stored energy in an ESS over the time window  $t_s$ , denoted as  $E_{ESS}(t)$  for a given ESS, can be expressed as,



$$E_{ESS}(t) = \int_{t_0}^{t_0+t} P_{ESS}(\tau) d\tau \quad (5.3)$$

$P_{ESS}(t)$  in (5.3) is either  $P_{SC}(t)$  or  $P_B(t)$  for the case of SC-battery HESS considered in this study.  $P_{SC}(t)$  and  $P_B(t)$  are obtained from (5.1) and (5.2) respectively. As an example, Figure 5.6(a) shows a generic  $P_{ESS}(t)$ . The respective time profile of  $E_{ESS}(t)$ , evaluated using (5.3), is depicted in Figure 5.6(b). The positive and negative portions of  $E_{ESS}(t)$ , denoted as  $E_{ESS}^+$  and  $E_{ESS}^-$ , are with reference to the stored energy level at the beginning of the  $t_s$  time period  $t_0$ .

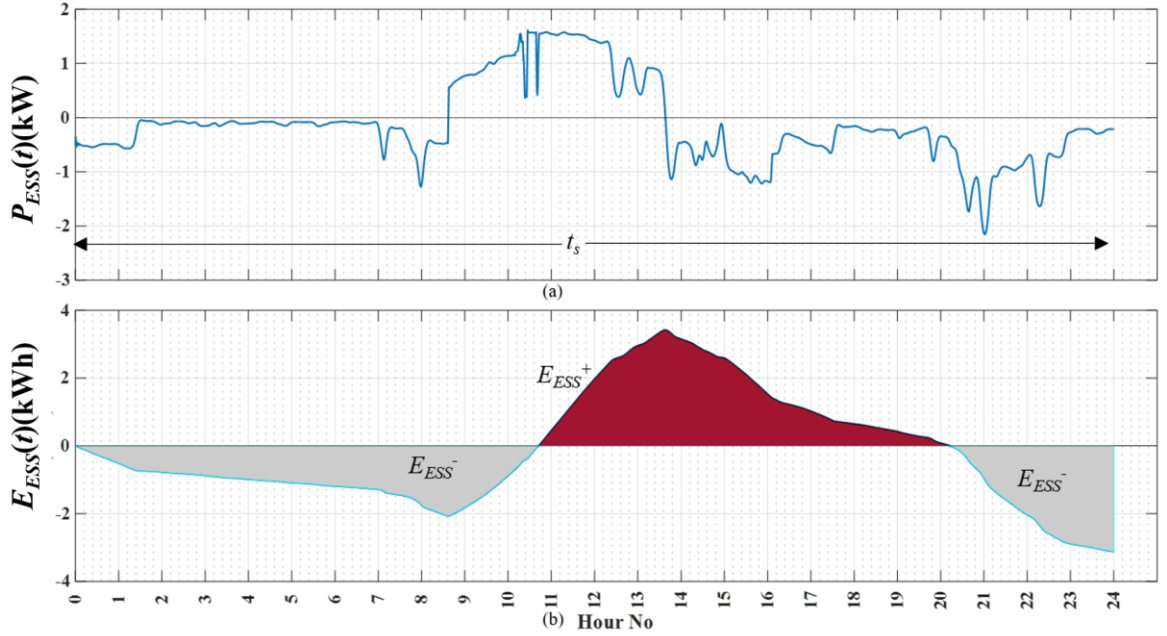


**Figure 5.6 (a)  $P_{ESS}(t)$  and (b)  $E_{ESS}(t)$  over one time window of  $t_s$**

Repeat the above calculation for a large number of time windows, each of which is of duration  $t_s$ . It is well-known that prosumer net power  $P_{net,i}(t)$  can be impacted significantly due to seasonal changes in the harnessed PV power and load demand. Hence, in the numerical example of Section 5.5, the hourly and daily statistics of  $E_{ESS}(t)$  shall be collated over each of the four seasons. From the collated statistics of  $E_{ESS}^+$  and  $E_{ESS}^-$ , generate their respective cdf curves in the usual manner. A typical example of the outcome from such an exercise is shown on Figure 5.7. The figure indicates that the increase in the amount of the stored energy in the ESS, relative to that at the beginning of the time window, will be up to  $E_{ESS,\rho}^+$  p.u. and the probability of such an occurrence is  $\rho$ . View it in another way, there is the probability of  $\rho$  the ESS has to store up to  $E_{ESS,\rho}^+$  p.u. more energy than that at the beginning of the time window. The storing up of energy in the ESS pertains to the charging operation of the ESS. Similar reasoning also applies to the discharging operation of the ESS: at the probability

level of  $\rho$ , the ESS will have to discharge up to  $E_{ESS,\rho}^-$  p.u. energy, relative to that at the beginning of the time window. This suggests that if the ESS has an energy storage swing range of  $E_{ESS,\rho}^+ + E_{ESS,\rho}^-$  p.u., there will be a probability of  $\rho$  for the successful buffering of the perturbing power  $P_{ESS}(t)$ .

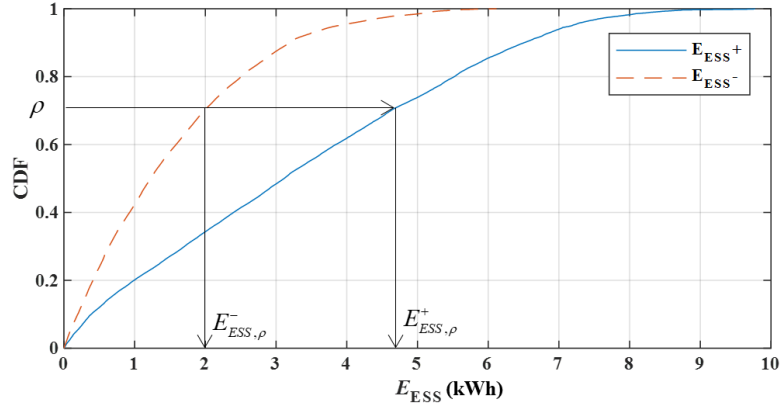


Figure 5.7. CDF of  $E_{ESS}^+$  and  $E_{ESS}^-$

## 5.5 Numerical Examples

In the following section, several numerical examples shall be included to illustrate the proposed approach in analyzing the stored energy levels in the HESS. The data pertaining to the prosumer shall be the same as the single prosumer data used in Section 3.4.

### 5.5.1 Segregation of IMFs

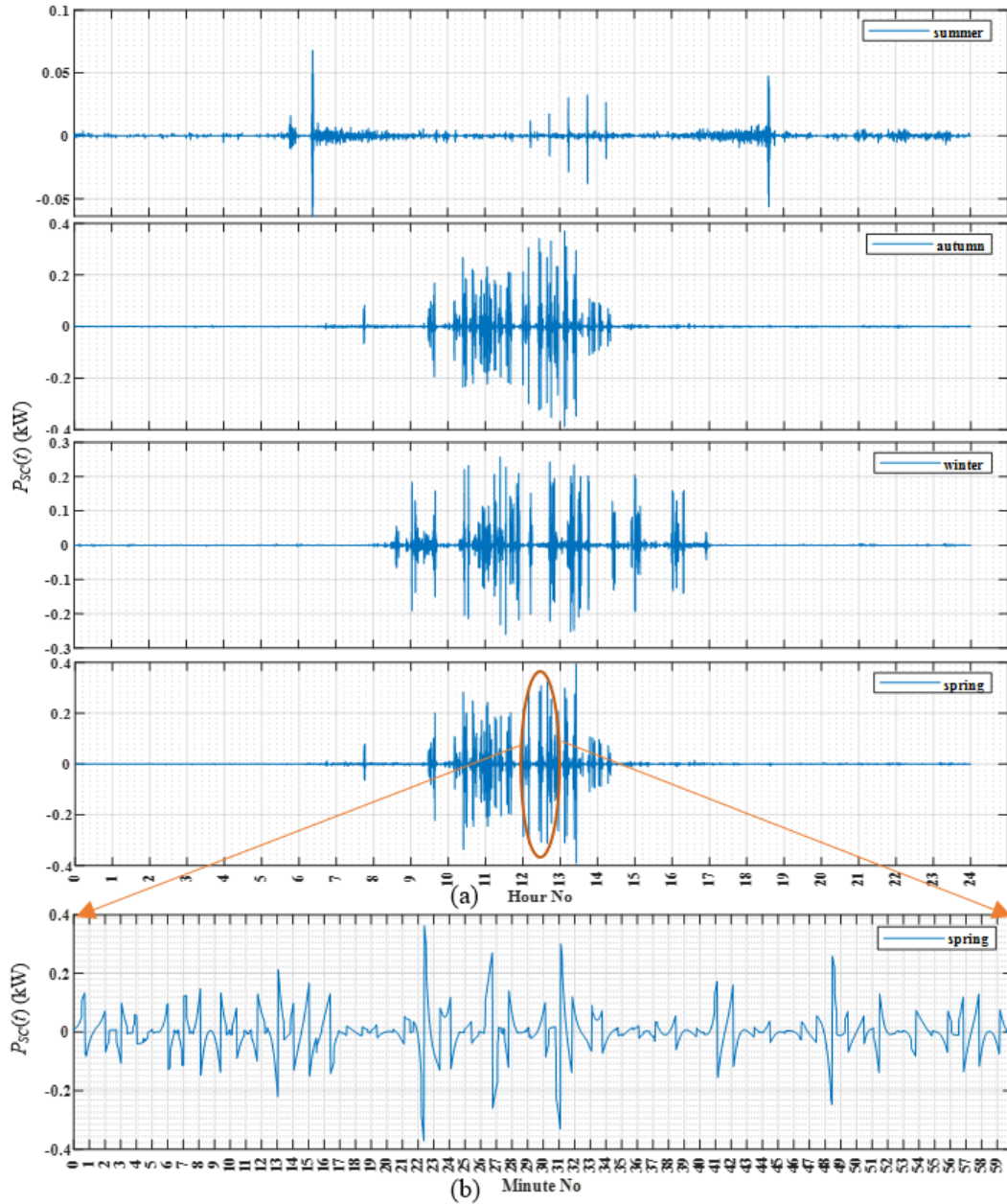
With ESS1 and ESS2 selected as SC and Li-ion battery in this example, the segregation of the IMFs based on  $\omega_c$  and  $\omega_{L,c}$  has resulted in the indices of IMF given in Table 5.1.  $\omega_c$  shall be same as the value in Section 4.2.4 and  $\omega_{L,c}$  is considered to be value taken from Section 4.3.2.

Table 5.1. Indices of the segregated IMFs based on the cut-off frequencies of  $\omega_c = 0.0085$  Hz and  $\omega_{L,c} = 1 \times 10^5$

$i_{ESS1}$	$i_{B1}$	$i_{ESS2}$	$i_{B2}$	$i_{ESS3}$
1	2, 3	4 - 12	13	14 - 17

### 5.5.2 Buffering tasks over different seasons

Daily  $P_{SC}(t)$  of four different seasons over selected 24-hours periods can be obtained using (5.1) and they are as shown in Figure 5.8(a). The zoomed-in plot for 12 noon – 1 pm of the selected spring day is shown in Figure 5.8(b).



**Figure 5.8: (a) Selected daily  $P_{sc}(t)$  in the four seasons, (b) zoomed-in plot from noon to 1 pm of the selected spring day.**

From Figure 5.8(a), it is quite evident that during the daylight hours when the solar power fluctuations are most pronounced, the energy buffering actions provided by the SC is most noticeable. In contrast, the figure shows that during the selected summer day, which has minimal cloud covers, the buffering task by the SC in the daytime is significantly diminished compared to that in other seasons. Consequently, the energy fluctuations in the SC are relatively minor during an average summer day.

Figure 5.8(b) illustrates that the SC is to buffer the higher frequency power fluctuations in the spring daytime. In contrast, the battery buffering actions have shown a much smoother power profile even during the daytime of the same spring day. An example illustrating this is shown in Figure 5.9 which shows that the largest power ramp rate in the battery is 1.63kW/min whereas that in the SC is 1.02kW/sec .This example also validates that the introduction of the SC has reduced the requirement for the Li-ion battery to buffer the more rapid changes in  $P_{net,i}(t)$ .

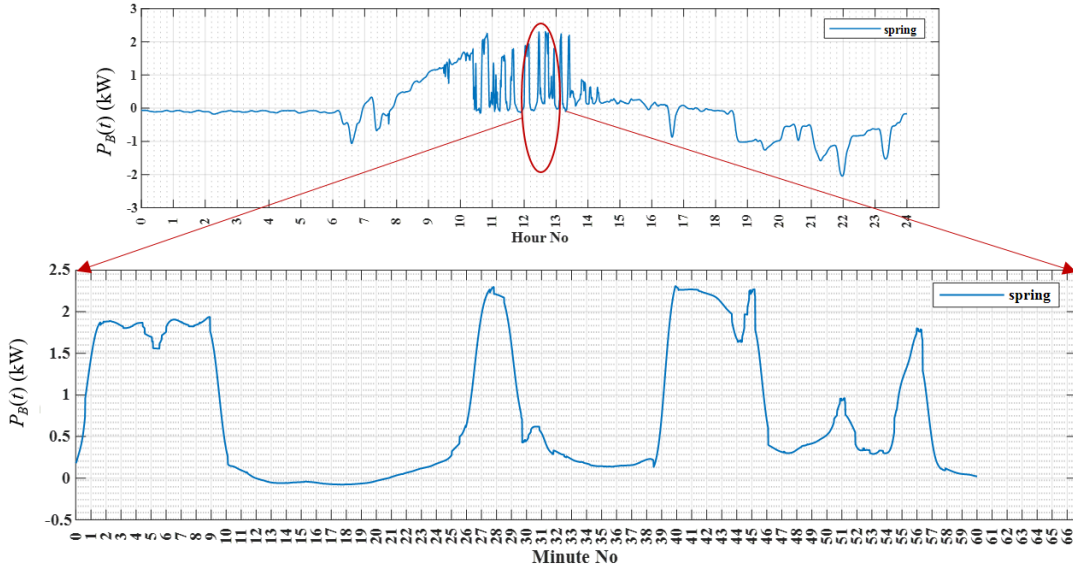
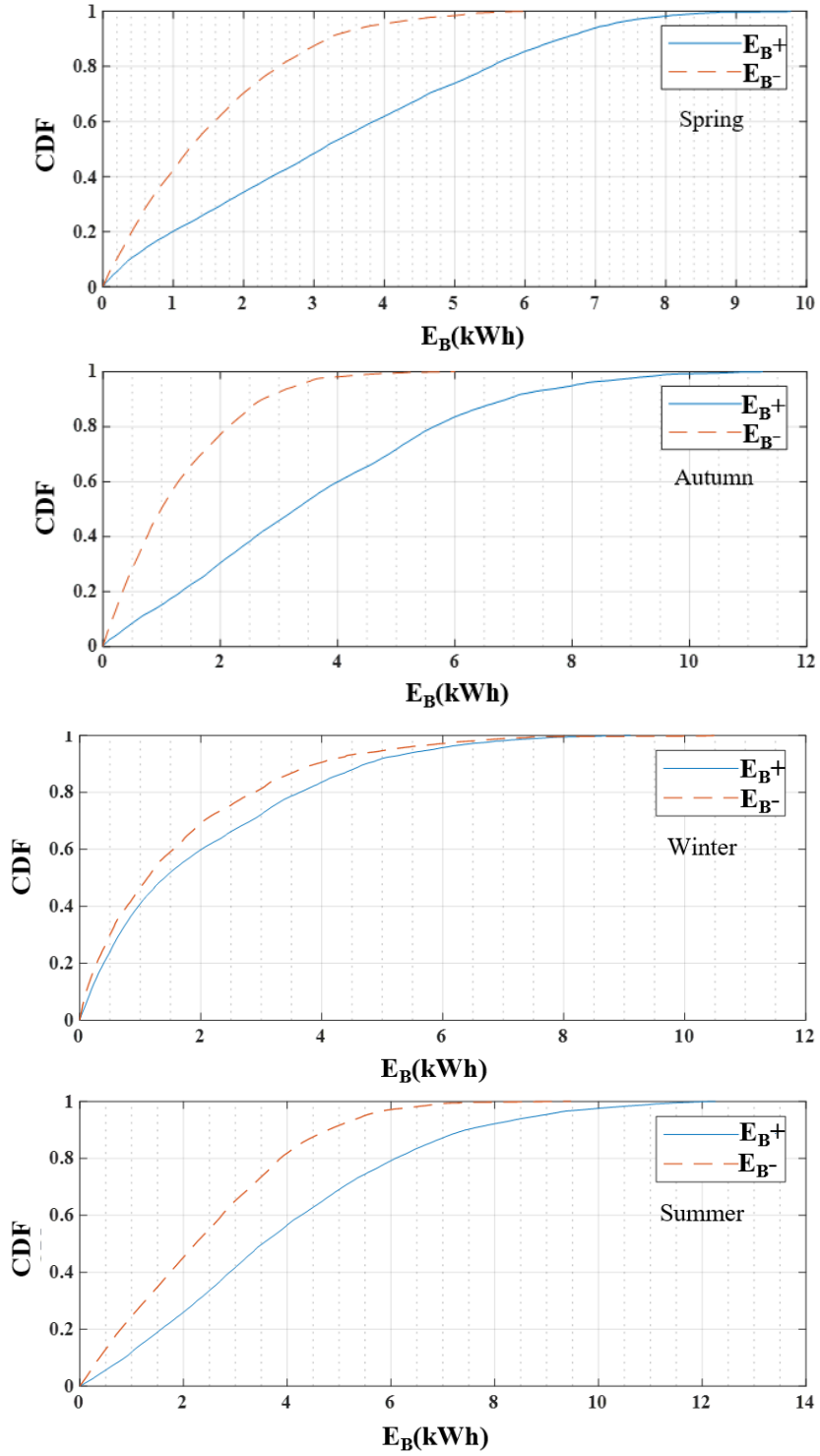


Figure 5.9:  $P_B(t)$  for (a) the selected spring day and (b) the zoomed-in plot over the noon – 1 pm period

### 5.5.3 Estimate of required energy storage capacity

The above analysis is based on the daily and hourly power variations only for a selected day in each of the four seasons. By extending the above analysis to cover all days in given season, a more accurate assessment of  $E_{ESS}^+$  and  $E_{ESS}^-$  can be obtained for the respective season. The outcome of such a study is summarised by the cdf curves shown on Figure 5.10 and Figure 5.11 for battery and SC respectively.



**Figure 5.10.** CDF of the  $E_B^+$  and  $E_B^-$  for the seasons.

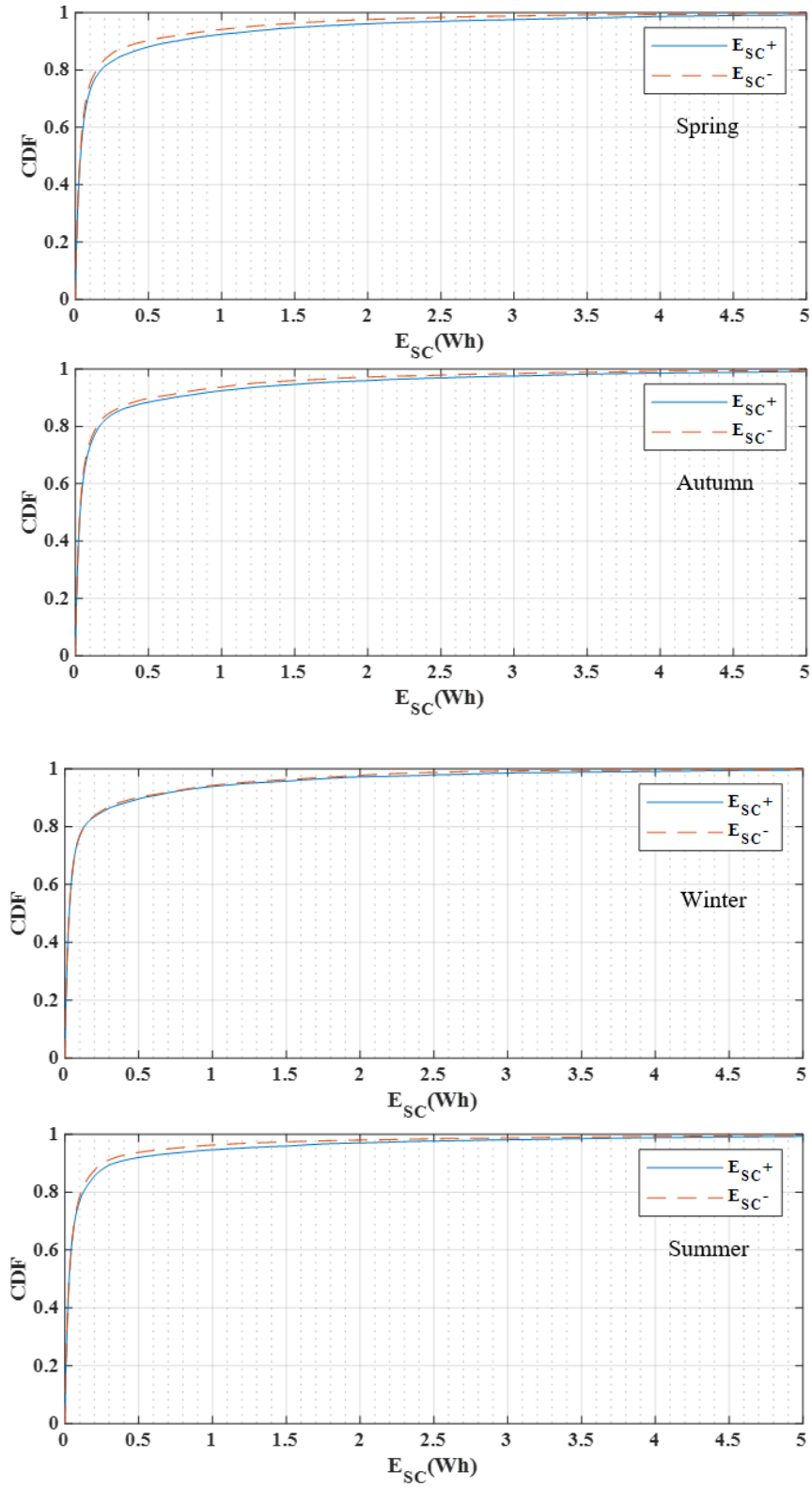


Figure 5.11. CDF of the  $E_{sc}^+$  and  $E_{sc}^-$  for the seasons.

If the overall trend of these four seasons shown in Figure 5.10 is considered, it becomes evident that the cdf for the summer season indicates the highest excess of daily surplus of energy: the cdf of  $E_B^+$  is distinctly higher than that of  $E_B^-$ . On the other hand, this gap between the two cdf curves becomes much narrower in the winter months. This appears to suggest that the allocation of the battery energy storage capacity to buffer  $E_B^+$  (charging) should be greater than that for  $E_B^-$  (discharging), particularly during the summer months. For the winter season, there shall be less of a need to allocate more storage capacity for the charging operation of the battery because the cdf curves are much closer.

Consequently, it implies that the (daily) stored energy level at the start of the time window  $t_s$  for the battery needs to be adjusted seasonally. This concept will be explored in detail in CHAPTER 6, thus enabling the storage system to have an adequate capacity for charging and discharging the expected amount of the energy in the respective season.

Similarly, the cdfs of  $E_{SC}^+$  and  $E_{SC}^-$  have also been calculated for the four seasons as depicted in Figure 5.11. From the cdf curves of Figure 5.10 and Figure 5.11, at the probability level  $\rho = 0.5$ , one can obtain the expected (mean) values of the required SC and battery charging/discharging energy levels for the given season. The results are summarized in Table 5.2.

**Table 5.2. Expected values of  $E_{ESS}$ ,  $\rho: \rho=0.5$**

	<b>Summer</b>	<b>Autumn</b>	<b>Winter</b>	<b>Spring</b>
$E_{B,0.5}^+$ (kWh)	3.521	3.284	1.402	3.112
$E_{B,0.5}^-$ (kWh)	2.229	0.992	1.121	1.224
$E_{SC,0.5}^+$ (Wh)	0.028	0.032	0.028	0.035
$E_{SC,0.5}^-$ (Wh)	0.029	0.030	0.029	0.032

As explained in the last paragraph of Section 5.5, an estimate of the energy swing ranges of SC and battery can also be obtained from the cdf curves. For this purpose,  $\rho$  should be set sufficiently large so as to ensure adequate storage capacity is available for each of the constituent ESSs to undertake the successful buffering task and at a reasonable level of likelihood. In this work,  $\rho$  is set at the 0.995 probability level. Thus, the overall swing range of the ESS is  $E_{ESS,0.995}^+ + E_{ESS,0.995}^-$ . With this  $\rho$  setting, the ESS shall have the energy storage capacity sufficient to readily meet the 0.99 probability level. The required battery and SC capacities, denoted by  $E_B$  and  $E_{SC}$ , for the four seasons are shown in Table 5.3.

**Table 5.3. Required energy swing ranges for ESS over the four seasons**

	<b>Summer</b>	<b>Autumn</b>	<b>Winter</b>	<b>Spring</b>
$E_B(\text{kWh})$	18.82	15.43	15.92	14.14
$E_{SC}(\text{Wh})$	10.49	10.99	8.33	10.10

According to the estimated energy swing range capacities obtained for the seasons, the battery ESS requires the highest capacity during the summer season, while the SC reaches its peak energy swing range during the autumn season. Note that the energy swing range is on top of the reference energy level at  $t_0$ , the beginning of the time window alluded to earlier. Consequently, in the process of determining the appropriate storage capacities, it is essential to take into account the energy requirements of both the battery and SC during these specific seasons over an extended period in order to guarantee that the designed ESS capacity can effectively meet the energy buffering task. More shall be said about this in the next chapter.

## 5.6 Conclusions

In this chapter, the focus is on developing an analytical approach to estimate the required energy storage capacity of the HESS for a prosumer. Firstly, after the cut-off frequency is determined using the proposed method described in the CHAPTER 4, the IMFs related to each constituent energy storage components of the HESS are identified. Boundary IMFs are separately treated for increased accuracy. Subsequently, a statistical method is then proposed to estimate the energy swing range over the four seasons. This is to ascertain that there is sufficient energy storage capacity for each of the constituent storage components in the HESS when the ESSs can undertake the energy buffering task successfully at reasonable probability.



# **CHAPTER 6. Development of Control Strategy for Community Battery Energy Storage System in Grid-Connected Microgrid of High Photovoltaic Penetration Level**

## **Statement of Contribution**

The main body of CHAPTER 6 of the thesis is primarily based on the content of the published journal article titled "Development of control strategy for community battery energy storage system in grid-connected microgrid of high photovoltaic penetration level," where coauthors are D. Hettiarachchi, S. Shing Choi, S. Rajakaruna, and A. Ghosh [137].<sup>3</sup> Section 5.3 to Section 5.8 of this chapter are exact replica of this journal text and other sections are included to extend the content due to space limitation of the journal paper and to maintain the flow of the overall thesis.

## **6.1 Introduction**

In view of CHAPTER 5, the capacity determination of the prosumer-level storage can be performed with a sufficiently lengthy statistical analysis. However, the planning study of the centralized battery is challenging due to the concerns of the grid constraints and the variability of the net PV power of the prosumers. Moreover, it is essential to incorporate the assessment of battery degradation into the long-term operational planning of the battery. Conducting a comprehensive long-term planning analysis can aid in accurately assessing the required battery capacity to ensure it remains sufficient for the typical yearly planning period.

The focus of this chapter is to describe the development of a control strategy for a community battery (CB) in a grid-connected microgrid which has a significant level of embedded photovoltaic generation. This will also be helpful to determine the required capacity of the community battery. In order to minimize the capacity of the community battery, the power transfer capacity of the interconnection link between the microgrid and the external grid system is utilized to safe maximum levels. Through Empirical Mode Decomposition analysis of the net power flows

---

<sup>3</sup> Percentage contributions of the relevant co-authors in the publication are given in the attribution statement, reviewed and signed by the each co-author.

of the microgrid, the daily and seasonal modes of the net power oscillations are identified as the two dominant low-frequency components. Whence a rule-based operational strategy is developed to control the power flows of the community battery via a novel dynamic referencing scheme for the state-of-charge of the battery bank. The battery control scheme counteracts the dominant daily and seasonal modes of oscillations of the net power. The numerical calculations performed for a case study shows that the proposed scheme leads to an approximately 16% decrease in the required battery capacity for particular growth rate of solid-electrolyte interphase film in the battery bank. The scheme does not require the forecasting of the net power, and thus, it has an increased degree of robustness when the community battery undertakes the power buffering task.

Firstly, a new rule-based operational strategy has been developed, which takes into account the limits imposed on the magnitude as well as the rate of change of the power flows in the interconnection link. Unlike previous works, however, the developed strategy is to make full use of the power transfer capability offered by the link, and consequently, the energy storage capacity of the CB required to buffer the perturbing power flows on the link can be kept to a modest level. On the other hand, the developed rule-based strategy is sufficiently general to be applicable in developing control actions for the CB to alleviate the duck power phenomenon. Unlike [109] and [113], the proposed control strategy does not require any optimization study process.

Secondly, a new control strategy has been developed to regulate the battery SOC reference value to counteract the two dominant modes in the net power of the microgrid. The two dominant modes, identified through the application of the Empirical Mode Decomposition technique, are pertaining to the daily and seasonal oscillating modes in the net power. The battery power flows are controlled in such a way that the SOC of the battery will be at a pre-specified SOC reference level at the end of a defined SOC restoration period daily. Furthermore, by allowing the SOC reference value to vary over the long term, this additional degree of design freedom is then taken advantage of to ensure improved utilization of the energy storage capacity of the battery bank. Moreover, based on a detailed statistical analysis of the resulting SOC profile, it is shown that the developed SOC control scheme has resulted in a reduction in the expected rate of SEI film growth in the battery cells.

Thirdly, the proposed control strategy does not require the forecasting of the microgrid load demand and PV power. This is because the proposed strategy is not intended to produce the short-term day-ahead power dispatch plan for the microgrid. Without the need for forecasts, the proposed scheme is much simpler to implement than those shown in the cited works such as [112]. The strategy assumes the seasonal variations of net power remain statistically similar to that in the historical data

analysed. It is encouraging to report that this assumption is shown to be valid in the numerical examples examined thus far in this work.

Accordingly, this chapter is organized as follows. Section 6.2 presents the findings obtained in CHAPTER 4 pertaining to the Empirical Mode Decomposition analysis of the net power of microgrid, which contains a high-level of PV penetration. The problem formulation is then presented, with particular reference to the situation of interconnection to remote microgrids such as that presented in Western Australia. The new rule-based operational strategy governing the power flows in the interconnection link, and the centralized battery bank is then developed in Section 6.3. Through a detailed analysis of the SOC profile of the CB over the long-term and the SEI-SOC characteristics of the Li-ion battery, a new SOC dynamic referencing scheme for the CB is presented in Section 6.4. Illustrative examples are included in Section 6.5 to demonstrate the efficacy of the proposed planning process for the CB. The main findings and areas for future work are included in Section 6.6.

## **6.2 Preliminaries**

As explained in the introduction of CHAPTER 1, the installation of roof-top PV panels at the premises of electricity consumers has been increasing at a rapid rate in recent years. However, the perturbing and uncertain power flows emanating from such PV-powered prosumers can bring serious challenges, e.g., the appearance of the duck curve in the daily load profile of power systems which have high penetration levels of the PV generation. The use of CB energy storage systems within the load areas has been reported extensively in the literature, as a means to perform certain power flows regulating functions so as to enhance the reliability and security of the power systems.

In this section, the main findings from the analysis of the net power flows emanating from a PV-powered prosumer shall be described. This is followed by an examination of a grid-connected microgrid in which the prosumers and a CB are the constituent elements.

### **6.2.1 Prior Work on the Buffering of the Net Power in Prosumers**

Without any loss of generality, Figure 6.1 shows a generation-transmission network interconnected to a number of microgrids. In turn, each microgrid is to encompass a number of prosumers, each with its load demand and a PV generator. Note that only the real power flows will be considered in this study. The issue of reactive power and voltage control for such a microgrid has been extensively studied (see e.g. [138]) and would not be considered herewith. The prosumers  $i$ ,  $i$

$= 1, \dots, n$ , could be residential, commercial, or industrial and would therefore exhibit their own load demand ( $P_{LD,i}(t)$ ) characteristics. Also, the PV output power ( $P_{PV,i}(t)$ ) would be weather- and season-dependent. In previous Section 5.3, the focus then is on buffering of the unsteady and uncertain net power ( $P_{Net,i}(t)$ ) from prosumer  $i$  through the actions of a hybrid energy storage system (HESS). The HESS is to consist of an aggregation of Li-ion battery and SC. One major attention of Section 5.3 is on the design of the HESS, particularly with regard to the segregation of the buffering actions between the battery and SC. This is achieved by the careful selection of the cut-off frequency ( $f_c$ ), by taking into consideration the frequency response characteristics of the battery and SC.  $f_c$  is then determined on the basis of minimizing the cost per effective energy storage capacity of the HESS.

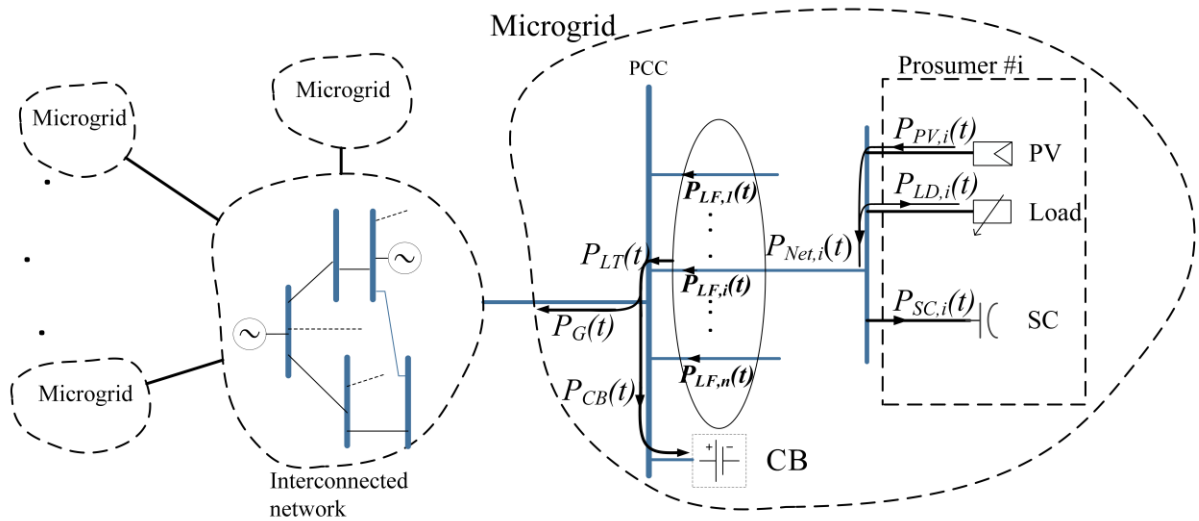


**Figure 6.1. A conceptual microgrid equipped with a community battery energy storage system to buffer the power flows between the PV-powered prosumers and the external grid interconnection**

Furthermore, the design methodology proposed in Section 3.3 is based on the decomposition of  $P_{Net,i}(t)$  using the Empirical Mode Decomposition (EMD) technique wherein a family of Implicit Mode Functions (IMF of order  $j$  is denoted as  $c_j(t)$  herewith) and a residue function ( $r(t)$ ) are obtained. The instantaneous frequency ( $f_j(t)$ ) of each of the oscillating  $c_j(t)$  spans over a frequency band, with the lower order  $c_j(t)$  occupying the higher frequency band while  $r(t)$  governs the trend of  $P_{Net,i}(t)$ . Figure 6.2 shows a sample of the outcome of the EMD analysis on  $P_{Net,i}(t)$  of a PV-powered prosumer. It shows that although the magnitudes of the selected  $c_j(t)$  are comparable, the magnitudes of the oscillating energies  $E_j(t)$  contained in  $c_{10}(t)$  and  $c_{14}(t)$  are several orders higher than that in the lowest order IMF,  $c_j(t)$ . In this example,  $c_{10}(t)$  and  $c_{14}(t)$  correspond to the daily and seasonal modes of oscillations in  $P_{Net,i}(t)$ . These modes can be readily attributed to the daily and seasonal

variation patterns in the load demand  $P_{LD,i}(t)$  and in the harnessed solar power  $P_{PV,i}(t)$ . Hence, this example illustrates the generally valid observation that the two dominant modes in  $P_{Net,i}(t)$  correspond to the daily and seasonal modes of variations. In terms of the minimum cost per effective energy storage design criteria proposed in Section 4.2.5, SC is used to buffer high frequency IMFs above the cut-off frequency  $f_c$  while the Li-ion battery would be utilized to buffer those remaining low-frequency IMFs.

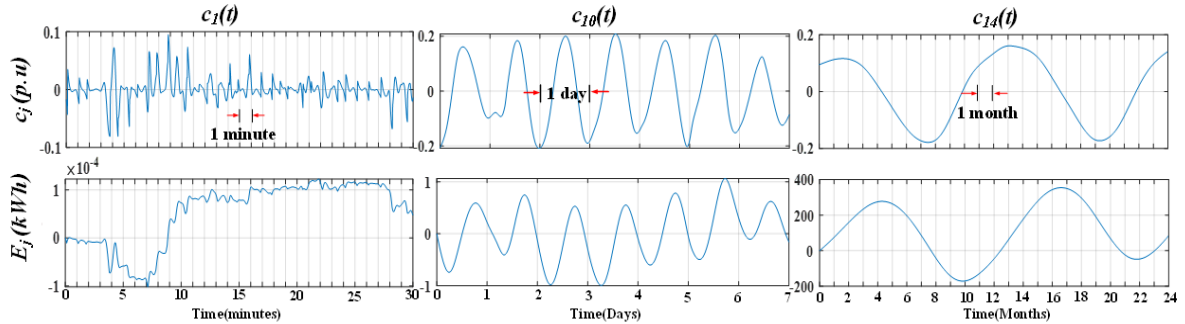


**Figure 6.2** A sample set of results of EMD analysis of  $P_{Net,i}(t)$ : IMF  $c_j(t)$  and energy  $E_j(t)$  for  $j = 1, 10$  and  $14$ .

### 6.3 Problem Formulation

Instead of the prosumers, the focus of the present work is at the microgrid level. Figure 6.1 shows that each prosumer is to be connected to an SC energy storage element instead of a battery-SC HESS considered in Section 4.2.5. In accordance with the finding of Section 4.2.5, SC would be more economical in buffering the higher frequencies  $c_j(t)$  than the Li-ion battery. In the present work, a Li-ion battery bank would be installed at the point of common coupling (denoted as PCC in Figure 6.1) between the microgrid and the external grid system. This battery bank is the centralized or community battery (CB) alluded to earlier. The SC is to buffer the higher-frequency IMFs of  $P_{Net,i}(t)$ , while the CB serves to buffer the lower-frequency IMFs and helps to regulate the power flows on the interconnected electrical link to the grid system. There is a strong economic advantage in adopting this centralized battery storage arrangement within the microgrid: due to the expected diversity between  $P_{Net,i}(t)$  among the prosumers, and if each of the prosumers in the microgrid is to be equipped with its own battery energy storage system as in the HESS considered in Section 4.2.5, then the total storage capacity of the batteries within the microgrid would be higher than that of the CB, if the objective of using the centralized and decentralized battery schemes is to achieve the same level of buffering actions seen on the electrical link to the external grid. Indeed, the use of centralized battery storage in microgrids has received much research interest in recent years, see, e.g., [139-

141] and a grid-connected microgrids, each equipped with CB, has been on trial operations in Western Australia [4, 6, 142].

Accordingly, and in the context of the conceptual microgrid shown on Figure 6.1, the PV and load demand of the  $i^{th}$  prosumer in the microgrid will result in the net power flows  $P_{Net,i}(t)$ , viz.,

$$P_{Net,i}(t) = P_{PV,i}(t) - P_{LD,i}(t) \quad (6.1)$$

Adopting a similar approach as in Section 5.3,  $P_{Net,i}(t)$  is then decomposed into its IMFs  $c_j(t)$  and the power flows  $P_{SC,i}(t)$  in the SC is controlled to buffer those  $c_j(t)$  which have frequencies above the cut-off frequency  $f_c$ . Hence, as shown in Figure 6.1, the remaining power flows  $P_{LF,i}(t)$  emanating from the  $i^{th}$  prosumer and flowing into the PCC would compose only of the lower frequency  $c_j(t)$  of  $P_{Net,i}(t)$ .  $P_{LF,i}(t)$  is given by

$$P_{LF,i}(t) = P_{Net,i}(t) - P_{SC,i}(t) \quad (6.2)$$

Figure 6.3 shows a typical profile of  $P_{LF,i}(t)$  and  $P_{SC,i}(t)$  over 2 consecutive days in summer. The figure illustrates the impacts of weather and the daily load demand on  $P_{LF,i}(t)$ : the comparatively higher level of  $P_{LF,i}(t)$  in the late morning and afternoon hours on Day 1, compared to that in Day 2, is because Day 1 is a sunnier day compared to Day 2. On the other hand, the profiles of  $P_{LF,i}(t)$  in the evening hours of the two days differ significantly. This is because Day 1 is a weekday (Friday) whereas Day 2 is in a week-end (Saturday). This figure serves to illustrate the fact that  $P_{Net,i}(t)$ , and in turn  $P_{LF,i}(t)$  and  $P_{SC,i}(t)$ , are governed by the weather and demand patterns.  $P_{Net,i}(t)$  is beyond the control of the grid operator. Hence the challenge is to develop a suitable control strategy for the microgrid in the light of the seemingly uncertain and perturbing  $P_{Net,i}(t)$ . In Figure 6.3, high-frequency buffering actions of the SC can be observed to be more prominent when there were cloud covers, and over the sunrise and sunset periods.

The sum of  $P_{LF,i}(t)$  from all the prosumers in the microgrid yields the total low-frequency power flows  $P_{LT}(t)$  into the PCC:

$$P_{LT}(t) = \sum_{i=1}^n P_{LF,i}(t) \quad (6.3)$$

Let  $P_{CB}(t)$  and  $P_G(t)$  denote the power flows in the CB and in the interconnection link between the grid and the microgrid respectively. With the assumed positive directions of power flows shown in Figure 6.1 for  $P_{LT}(t)$ ,  $P_{CB}(t)$  and  $P_G(t)$ ,  $P_{CB}(t)$  is given by

$$P_{CB}(t) = P_{LT}(t) - P_G(t) \quad (6.4)$$

Equation (6.4) clearly indicates that  $P_{CB}(t)$  would be impacted by the power flows  $P_G(t)$ . Hence, the design of power flows control actions for the microgrid has to reflect the desired outcome for

the stakeholders as follows.

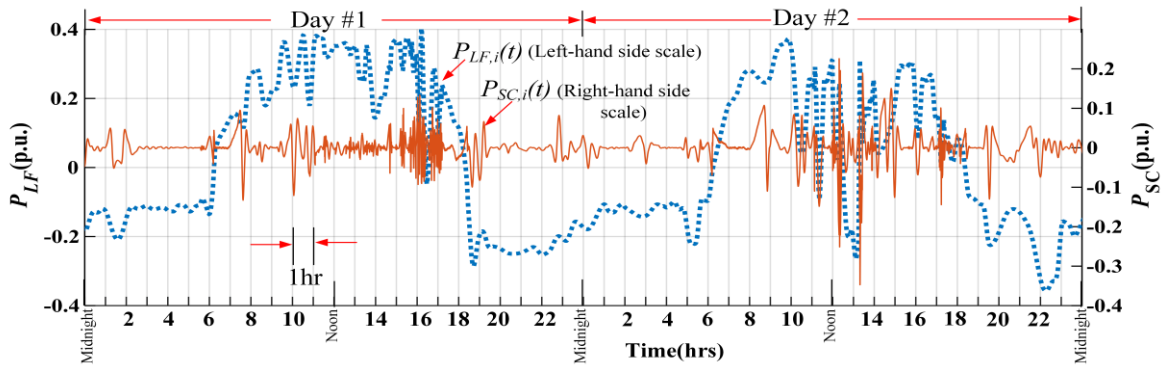


**Figure 6.3**  $P_{LF,i}(t)$  and  $P_{SC,i}(t)$  over two consecutive days in summer

Consider the common scenario when the microgrid and the interconnected system are under the purview of the same entity, for example, in the case of the Kalbarri microgrid in Western Australia [4]. This microgrid, owned by the electricity utility corporation under the state government, is in a remote part of the state, and the interconnection link consists of a 140-km overhead feeder line. The line provides the only electrical link between the Kalbarri microgrid and the remaining part of the state utility network. As the PV generation and load demand in Kalbarri increase over the years, however, there will come a stage when the line needs to be upgraded in order to meet the demand. Upgrading the line can be a costly exercise. An alternative option could be to install a CB within the Kalbarri area to provide the necessary power buffering actions in the microgrid while keeping the existing link in service. The focus of the present work is to develop a methodology to analyse this option whereby in meeting the condition (6.4), and priority is to be given in utilizing the power transfer capacity of the existing link to the fullest extent. In this way, it is anticipated that the required energy storage capacity of the CB can be kept to a modest level in order to reduce the capital cost of the CB. Short-term dispatch planning for the microgrid is not the prime consideration, unlike that considered in, e.g., [103, 115]. Therefore, it is under such a scenario that the operational rules governing  $P_{CB}(t)$  will be derived in the next section. As shall be illustrated in a latter section, in fact, the developed rules are sufficiently general to be applicable in alleviating the duck power phenomenon alluded to in Section 6.2.

A less common scenario in Western Australia is when the microgrid and the link come under the ownership of different entities, although one has to bear in mind the deepening of the deregulation of the electricity market could accelerate the development of such a commercial arrangement. Under the separate ownership scenario, it may be attractive for the microgrid stakeholders to invest in larger-capacity PV and CB in the microgrid, so that the microgrid can

become more independent of the grid. The link is to provide backup support when, for instance, there is a prolonged period of low level of PV generation. This less likely ownership scenario would be omitted in the present work, however.

## 6.4 Operational Strategy

In this study, it is assumed that  $P_G(t)$  is not directly controllable by the grid/microgrid operator. With the microgrid power flows regulated using the CB, it is envisaged that remote generation curtailment is not required in the microgrid. With the view to minimizing the capacity of the CB, it is assumed that the grid link is to have higher power transfer priority over the CB. In this section, a new rule-based operational strategy is developed to determine  $P_G(t)$  and  $P_{CB}(t)$ .

### 6.4.1 Development of a Rule-based Operational Strategy for the CB

Consider again the microgrid shown on Figure 6.1. The power flows  $P_G(t)$  on the grid link would be subject to the general constraints as follows:

$$-P_G^{\max,n} \leq P_G \leq P_G^{\max,p} ; P_G^{\max,n}, P_G^{\max,p} > 0 \quad (6.5)$$

$$\left| \frac{dP_G}{dt} \right| \leq \dot{P}_G^{\max} \quad (6.6)$$

$P_G^{\max,p}$  and  $P_G^{\max,n}$  are the maximum allowable power flows in the positive and negative directions on the link, and  $\dot{P}_G^{\max}$  is the maximum acceptable power ramp rate applicable on the link. These constraints are imposed on  $P_G(t)$  to reflect the desired outcome on  $P_G(t)$ : for example in [143], the ramp rate limit  $\dot{P}_G^{\max}$  is set to be 10% of the microgrid PV generating capacity per minute. The constraints are imposed to ensure the microgrid operates within the power transfer capability of the link, or to ensure  $P_G(t)$  complies with specific grid code requirements such as to alleviate the severity of the duck curve. This latter requirement shall be discussed further in the next subsection.

Based on the constraints (6.5)-(6.6), the following rule-based control strategy governing  $P_G(t)$  and  $P_{CB}(t)$  can be established under the possible scenarios shown in Table 6.1. An explanation of the developed strategy is facilitated by making reference to Figure 6.4.



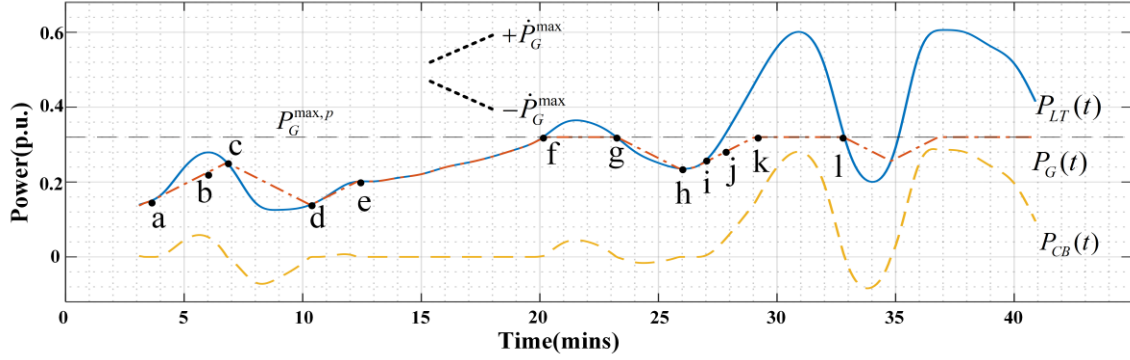


Figure 6.4. Sample curves of  $P_{LT}(t)$ ,  $P_G(t)$  and  $P_{CB}(t)$

Figure 6.4 shows a sample plot of  $P_{LT}(t)$ , the applicable power limit  $P_G^{max,p}$  and power ramp rate limits  $\pm\dot{P}_G^{max}$ . As illustrated in the figure, before “a”, since the grid link has higher priority over the CB in terms of power flows control, therefore the target is to divert all of  $P_{LT}(t)$  power flows to the link, i.e.,  $P_G(t) = P_{LT}(t)$ , because  $P_G(t)$  satisfies both constraint conditions (6.5) and (6.6). This would be the strategy (1a) shown in Table 6.1 wherein  $P_{CB}(t) = 0$ .

Upon reaching “a”, however, it is observed that while  $0 < P_{LT}(t) < P_G^{max,p}$ ,  $|dP_{LT}/dt| > \dot{P}_G^{max}$ , it would not be acceptable to continue to let  $P_G(t)$  track  $P_{LT}(t)$  as this would violate constraint (6.6).  $P_G(t)$  is therefore to increase at the maximum power ramp rate allowable on the link, i.e., in the manner as depicted under scenario (2a) in Table 6.1.  $P_{CB}(t)$  is controlled to make up the difference between  $P_{LT}(t)$  and  $P_G(t)$ , in accordance with (6.4). It is important to note that the control strategy listed in the 4<sup>th</sup> column of Table 6.1 under scenario (2a) is the only way to strategize  $P_{CB}(t)$  in order to ensure that the amount of buffering energy provided by the CB is at the minimum.

Between “a” and “b”, as  $|dP_{LT}/dt|$  continues to exceed  $\dot{P}_G^{max}$ ,  $P_G(t)$  would continue to increase at the maximum ramp rate. At the instance “b” however, it is seen that  $|dP_{LT}/dt| < \dot{P}_G^{max}$ . Although  $P_{LT}(t)$  is still less than  $P_G^{max,p}$ , it is not acceptable to set  $P_G(t) = P_{LT}(t)$  at this instance because to do so, it would result in a sudden jump in  $P_G(t)$  and constraint (6.6) would be violated. So, the prudent strategy is to continue to increase  $P_G(t)$  at the maximum ramp rate. This is the rule (1b) in Table 6.1.  $P_G(t)$  would soon intercept  $P_{LT}(t)$  at “c”. At this point,  $P_{LT}(t) < P_G^{max,p}$  but as  $|dP_{LT}/dt| > \dot{P}_G^{max}$ , and  $dP_{LT}/dt$  is negative, it is scenario (2b), and strategy (2b) in the 4<sup>th</sup> column of Table 6.1 applies to control  $P_{CB}(t)$ .  $P_G(t)$  would decrease at the maximum ramp rate until  $P_G(t)$  intercepts  $P_{LT}(t)$  at “d”. Wherein condition (1a) is satisfied and accordingly, strategy (1a) applies. From point “e” to point “f”, since  $P_{LT}(t) < P_G^{max,p}$  and  $|dP_{LT}/dt| < \dot{P}_G^{max}$ , condition (1a) applies and therefore,  $P_G(t)$  is to track  $P_{LT}(t)$  because none of the constraints (6.5) and (6.6) is violated. No buffering power is required

from the CB.

By similar reasoning, readers would be able to readily verify the remaining trajectories of  $P_{CB}(t)$  and  $P_G(t)$  shown on Figure 6.4. For example,

- at “f”, condition (3a) applies and accordingly, strategy (3a) is applicable to  $P_{CB}(t)$ . And  $P_G(t)$  is set to the maximum i.e.,  $P_G^{\max,p}$ .
- condition (4) occurs at “k” and strategy (4c) is applicable to  $P_{CB}(t)$ .

**Table 6.1. A summary of the target  $P_G(t)$  and control strategies on  $P_{CB}(t)$  under the various possible scenarios of  $P_{LT}(t)$**

Scenario	$P_{LT}(t)$	$\left  \frac{dP_{LT}}{dt} \right $	Target $P_G(t)$	Control strategy on $P_{CB}(t)$
1	$-P_G^{\max,n} \leq P_{LT}(t) \leq P_G^{\max,p}$	$\left  \frac{dP_{LT}}{dt} \right  < \dot{P}_G^{\max}$	1a) If $\left  \frac{dP_G}{dt} \right  < \dot{P}_G^{\max}$ , then $P_G(t) = P_{LT}(t)$ 1b) If $\left  \frac{dP_G}{dt} \right  > \dot{P}_G^{\max}$ and $\frac{dP_G}{dt} > 0$ , then $P_G(t) = P_G(t - \Delta t) + \dot{P}_G^{\max} \times \Delta t$ 1c) If $\left  \frac{dP_G}{dt} \right  > \dot{P}_G^{\max}$ and $\frac{dP_G}{dt} < 0$ , then $P_G(t) = P_G(t - \Delta t) - \dot{P}_G^{\max} \times \Delta t$	1a) $P_{CB}(t) = 0$ 1b) $P_{CB}(t) = P_{LT}(t) - P_G(t - \Delta t) - \dot{P}_G^{\max} \times \Delta t$ 1c) $P_{CB}(t) = P_{LT}(t) - P_G(t - \Delta t) + \dot{P}_G^{\max} \times \Delta t$
2	$-P_G^{\max,n} \leq P_{LT}(t) \leq P_G^{\max,p}$	$\left  \frac{dP_{LT}}{dt} \right  > \dot{P}_G^{\max}$	2a) If $\frac{dP_{LT}}{dt} > 0$ , then $P_G(t) = P_G(t - \Delta t) + \dot{P}_G^{\max} \times \Delta t$ 2b) If $\frac{dP_{LT}}{dt} < 0$ , then, $P_G(t) = P_G(t - \Delta t) - \dot{P}_G^{\max} \times \Delta t$	2a) $P_{CB}(t) = P_{LT}(t) - P_G(t - \Delta t) - \dot{P}_G^{\max} \times \Delta t$ 2b) $P_{CB}(t) = P_{LT}(t) - P_G(t - \Delta t) + \dot{P}_G^{\max} \times \Delta t$
3	$P_{LT}(t) < -P_G^{\max,n}$ or $P_{LT}(t) > P_G^{\max,p}$	$\left  \frac{dP_{LT}}{dt} \right  < \dot{P}_G^{\max}$	3a) If $P_{LT}(t) > 0$ , then $P_G(t) = P_G^{\max,p}$ 3b) If $P_{LT}(t) < 0$ , then $P_G(t) = -P_G^{\max,n}$	3a) $P_{CB}(t) = P_{LT}(t) - P_G^{\max,p}$ 3b) $P_{CB}(t) = P_{LT}(t) + P_G^{\max,n}$
4	$P_{LT}(t) < -P_G^{\max,n}$ or $P_{LT}(t) > P_G^{\max,p}$	$\left  \frac{dP_{LT}}{dt} \right  > \dot{P}_G^{\max}$	4a) If $P_{LT}(t) > 0$ , then $P_G(t) = P_G(t - \Delta t) + \dot{P}_G^{\max} \times \Delta t$ until $P_G(t) = P_G^{\max,p}$ 4b) If $P_{LT}(t) < 0$ , then $P_G(t) = P_G(t - 1) - \dot{P}_G^{\max} \times \Delta t$ until $P_G(t) = -P_G^{\max,n}$ 4c) If $P_{LT}(t) > 0$ , then $P_G(t) = P_G^{\max,p}$ If $P_{LT}(t) < 0$ , $P_G(t) = -P_G^{\max,n}$	4a) $P_{CB}(t) = P_{LT}(t) - P_G(t - \Delta t) - \dot{P}_G^{\max} \times \Delta t$ 4b) $P_{CB}(t) = P_{LT}(t) - P_G(t - \Delta t) + \dot{P}_G^{\max} \times \Delta t$ 4c) If $P_{LT}(t) > 0$ , then $P_{CB}(t) = P_{LT}(t) - P_G^{\max,p}$ If $P_{LT}(t) < 0$ , then $P_{CB}(t) = P_{LT}(t) + P_G^{\max,n}$

Once  $P_{CB}(t)$  has been determined based on these strategies,  $P_G(t)$  can be readily obtained to satisfy (6.4).

In applying the strategies, it must be emphasized again that the intention is to utilize fully the allowable power transfer capability of the grid link in buffering the perturbing  $P_{LT}(t)$ . The

capability is expressed in the form of constraints (6.5) and (6.6). At the same time, the CB is to provide the buffering power  $P_{CB}(t)$  required to meet the power flows condition (6.4). In this way, the required energy storage capacity on the CB would be kept to a minimum. This problem formulation is sufficiently general as to provide a possible means to alleviate the issue of the “duck-power”, as shall be discussed next.

## 6.4.2 Application of the Rule-based Operational Strategy to Alleviate the Duck Curve Phenomenon

Figure 6.5 shows the outcome of the application of the proposed rule-based control strategy to a microgrid over three summer days. Detailed information on this particular microgrid is given in Section 6.6. The total rating of the PV power generation in the studied microgrid is approximately 74% of that of the maximum load demand in the microgrid. As the main interest of this investigation is pertaining to grid-connected microgrids, hence the PV generator ratings and load demand parameters have been deliberately selected so that even with the CB, the microgrid cannot be expected to be completely independent of the external grid system. There shall be power exchanges between the microgrid and the external grid system on a daily as well as on a seasonal basis. So, subject to the assumed power transfer constraints  $P_G^{max,p}$  and  $P_G^{max,n}$  of 0.5 p.u. and 0.2 p.u., respectively, on the interconnection link, the figure shows that over the summer days, the microgrid is exporting surplus power over the day-time period and is importing power over the evening-early morning period. It shows the rapid ramping up and down of  $P_{LT}(t)$  are to occur approximately over the 6 am – 8 am and 5 pm – 7 pm periods, respectively. This, in turn, means that the conventional generators in the grid system would have to ramp down and then subsequently ramp up their generation within the 2-hour periods in order to meet the generation-demand balance. Depending on the types of conventional generators in service at the time, this can pose a serious challenge to grid operations in terms of generator unit commitments and dispatch planning of the grid network. As explained in Section 6.1, such difficulty due to the so-called “duck curve phenomenon” [144] has become very prominent and is of great concern to grid operators. One common way to obviate such difficulty is to limit the amount of the export power from PV-powered microgrids over the day-time period through the lowering of the buy-back tariff rate for the exported power from the microgrid. In this case, it may become more attractive economically for the prosumers to store the surplus energy in the CB during the daytime hours and use the stored energy to meet at least part of the evening peak in the microgrid.

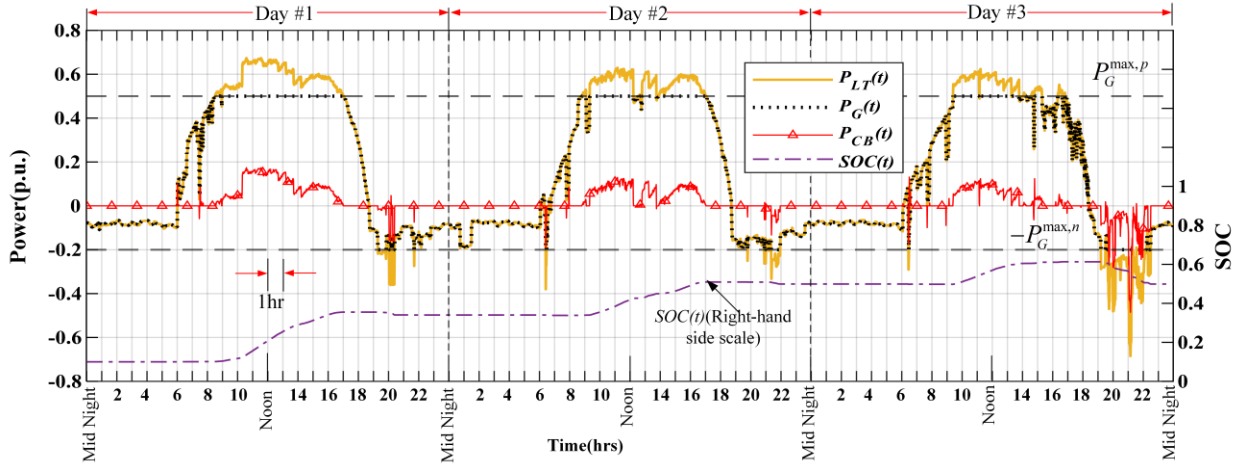


**Figure 6.5**  $P_{LT}(t)$ ,  $P_G(t)$  and  $P_{CB}(t)$  for three days in summer. Power flows are expressed on a 10 MW base.

It is toward exploring this possible way of alleviating the “duck curve phenomenon” that the present work will find ready application. This is to be achieved through the judicious setting of the power limits  $P_G^{max,p}$  and  $P_G^{max,n}$ , as follows. From Figure 6.5, it becomes obvious that by lowering of the set value of  $P_G^{max,p}$ , it will cause a decrease in the amount of energy exported to the external grid system during the summer daytime hours. Instead, the energy will be diverted and stored in the CB. Conversely, the lowering of the value of  $P_G^{max,n}$  will also reduce the amount of energy imported from the grid during the evening-early morning period. The reduction in the imported energy will be made up by the corresponding increase in the energy discharged from the CB. It is through such a load-leveilling mechanism that the duck curve phenomenon will be alleviated.

In view of the seasonal differences in  $P_{PV}(t)$ ,  $P_{LD}(t)$  and hence  $P_{net}(t)$ , one could extend the adjustments in the setting of  $P_G^{max,p}$  and  $P_G^{max,n}$  to cover the different seasons. In Section 6.6, some numerical examples shall be included to illustrate such a possibility.

## 6.5 Control Strategy for the SOC of the Centralized Battery

As alluded to in Section 6.2.1, the EMD analysis of  $P_{net,i}(t)$  shows the two most significant implicit modes are those due to the daily and seasonal variations in  $P_{PV,i}(t)$  and  $P_{LD,i}(t)$ . In this section and consistent with the observed dominant modes, a CB control scheme shall be developed in which the SOC of the CB will be adjusted on a daily and seasonal basis. The purpose of the control scheme is to eliminate the persistent drift in the SOC of the CB, a phenomenon which shall be described shortly. And it ensures an improved utilization of the energy storage capacity of the CB over the seasons. Furthermore, it will be shown that the proposed SOC control scheme will

reduce the rate of the irreversible SEI film growth, a known major contributor to battery cell degradation in the CB.

### **6.5.1 Persistent Drift in SOC**

In the above discussion pertaining to the alleviation of the “duck power phenomenon”, it is in the daily  $P_{LT}(t)$  of the microgrid which is referred to. As alluded to in the previous section, however,  $P_{LT}(t)$  does vary from one day to the next. In Figure 6.5 for example, the amount of the surplus energy harnessed in the day-time of Day #1 and stored in the CB corresponds to the area prescribed by the positive portion of the  $P_{CB}(t)$  curve of that day. This pertains to the charging of the CB. Conversely, the amount of the energy extracted from the CB over the day corresponds to the area prescribed by the negative portion of the  $P_{CB}(t)$  curve of that day, and the CB discharges in these instances. Clearly, the total amounts of the charging and discharging energies are unlikely to be equal in any given day. Hence, the amount of the energy stored in the CB at the end of the day would differ from that at the beginning of the day. In Figure 6.5, it is seen that the amounts of the charging energy is higher than that of the discharging energy in each of the three summer days: so, there is a persistent increase in the amount of energy stored in the CB at the end of one summer day to the next. This phenomenon is reflected in Figure 6.5 in the form of a persistent and upward drift in the SOC of the CB. This is obviously an untenable situation because the energy storage capacity of the CB would have to be un-acceptably large, if the CB is to accommodate the increase in the stored energy over the whole summer season. Similar reasoning will also lead to the conclusion that there would be a persistent decrease in the amount of the stored energy in the CB at the end of one winter day to the next, which is again an untenable situation.

The persistent drift in the SOC can be prevented by taking the appropriate control actions on the CB. In Section 6.2.1, it has been established that one of the two significant IMFs observed in  $P_{Net,i}(t)$  corresponds to the daily mode. With this in mind, it is therefore proposed that corrective actions be taken to restore the SOC of the CB on a daily basis.

The selection of the most suitable time window during which the daily corrective action on the SOC is to occur shall be discussed next. This SOC restoration strategy shall form one part of a new approach in the design of the CB control scheme, to be described in the subsequent sub-sections.

### **6.5.2 Daily SOC Correction**

In the previous sub-section, it is proposed that corrective action be taken on a daily basis to prevent

the persistent drift in the SOC of the CB. Changes in the weather and the variations in load demand over the daytime mean that  $P_{LT}(t)$  would vary, and often at high ramp rates at times of sun-rise and sun-set. The perturbing  $P_{LT}(t)$ , also often of large magnitudes and/or of high ramp rates, is also observed over the evening peak demand period. Therefore, the daytime and evening peak demand hours are not suitable periods for which to carry out the corrective actions on the SOC. This is because the corrective actions will require the generation of an additional power flows component in the CB, and the highly perturbing  $P_{LT}(t)$  over these periods can only make it more challenging in determining the precise amount of this power flows component. In contrast, after midnight and continuously into the early morning hours,  $P_{LT}(t)$  tends to be relatively steady and of much lower magnitude compared to that in the remaining part of the day. This observation is expected because of the absence of  $P_{PV,j}(t)$  and the usually low level of load demand in the early morning hours. Indeed, this observation has been verified to be valid in the numerical examples used in this work. Therefore, the power flows component required to correct the persistent drift in the SOC of the CB can be determined with greater accuracy and confidence over this period. Henceforth, the time interval in which the corrective action is to be effected is termed the ‘‘SOC restoration period’’ and it shall be in the early morning period of each day. The SOC restoration period is to begin at  $T_1$  and is to terminate at  $T_2$  and typically,  $T_1$  and  $T_2$  are set as mid-night and 6 am respectively, of each day.

An important assumption made in designing the daily SOC correction strategy is that the external grid system has a sufficiently large energy storage capacity to accommodate the simultaneous importing/exporting of energy from all the grid-connected microgrids over the SOC correction period. This grid-level storage can be in the form of a pumped-hydroelectric system which is well-suited for the longer-term seasonal energy storage application. As the present focus is on the energy storage requirement of microgrids, such large-scale grid-level storage is outside the scope of this work.

The control scheme to effect the daily SOC corrective action shall now be developed. The corrective action is in the form of an additional power component  $P_{res}(t)$  in the CB, over the interval  $(T_1, T_2)$ .  $P_{res}(t)$  is to be added to  $P_{CB}(t)$  which is determined based on the rule-based operational strategy described in Section 6.4.1. Therefore, the total power flows in the CB, denoted as  $P_{CB,T}(t)$ , is

$$P_{CB,T}(t) = P_{CB}(t) + P_{res}(t) \quad (6.7)$$

$P_{res}(t)$  is determined via (6.8) whereby  $E_{r,CB}$  denotes the rated energy storage capacity of the CB. Within the SOC restoration period  $T_1 < t < T_2$  and as expressed in (6.8),  $P_{res}(t)$  is the power flows

component required to restore the SOC of the CB to the pre-determined reference value  $SOC_r$  at  $T_2$ . More shall be said about the setting of  $SOC_r$  in the next sub-section. Also, within this period, the SOC of the CB at time  $t$ , denoted as  $SOC(t)$ , can be computed via (6.9) using  $P_{CB,T}(t)$  determined from (6.7) and the monitored and therefore known SOC value at  $T_1$ ,  $SOC(T_1)$ .

$$P_{res}(t) = \frac{E_{r,CB} \times (SOC_r - SOC(t))}{(T_2 - t)} \quad (6.8)$$

$$SOC(t) = \frac{\int_{t=T_1}^t P_{CB,T}(t) dt}{E_{r,CB}} + SOC(T_1) \quad (6.9)$$

Finally, the resulting power flows in the interconnection link to the grid,  $P_{G,T}(t)$ , with the daily SOC restoration action effected, is

$$P_{G,T}(t) = P_G(t) - P_{res}(t) \quad (6.10)$$

Again  $P_G(t)$  is obtained based on the rule-based strategy contained in Table 6.1.

An example of the outcome following the successive daily SOC restoration scheme is shown in Figure 6.6. The same microgrid used to produce the results of Figure 6.5 was again assumed here. It can be seen that the persistent drift in the SOC has been eliminated. The figure also confirms that over the SOC restoration period,  $P_{LT}(t)$  tends to be consistently of low level and it changes much less rapidly, compared to that seen over the daytime and evening peak demand periods. Consequently, it is observed that  $P_{res}(t)$  is fairly constant and starting at time  $T_1$ , the SOC is restored to reach the pre-determined reference value  $SOC_r$  at  $T_2$  in an almost linear manner. For a SOC restoration period of 6 hours in this example, the maximum C-rate experienced by the CB in the form of the restoration power component  $P_{res}(t)$  is only 1/6 or 0.17. Since  $P_{CB}(t)$  is also likely to be of low level over the SOC restoration period, one can therefore expect the total power loading  $P_{CB,T}(t)$  on the CB, evaluated via (6.7), would be low over the SOC restoration period. This is a desirable outcome as the low C-rate loading on the CB is helpful in ensuring longer battery cell service life. Of course,  $P_{CB,T}(t)$  and  $P_{G,T}(t)$  shall be subjected to the respective constraints of battery power rating ( $P_{r,CB}$ ) and grid link power limits  $P_G^{max,p}/P_G^{max,n}$ .

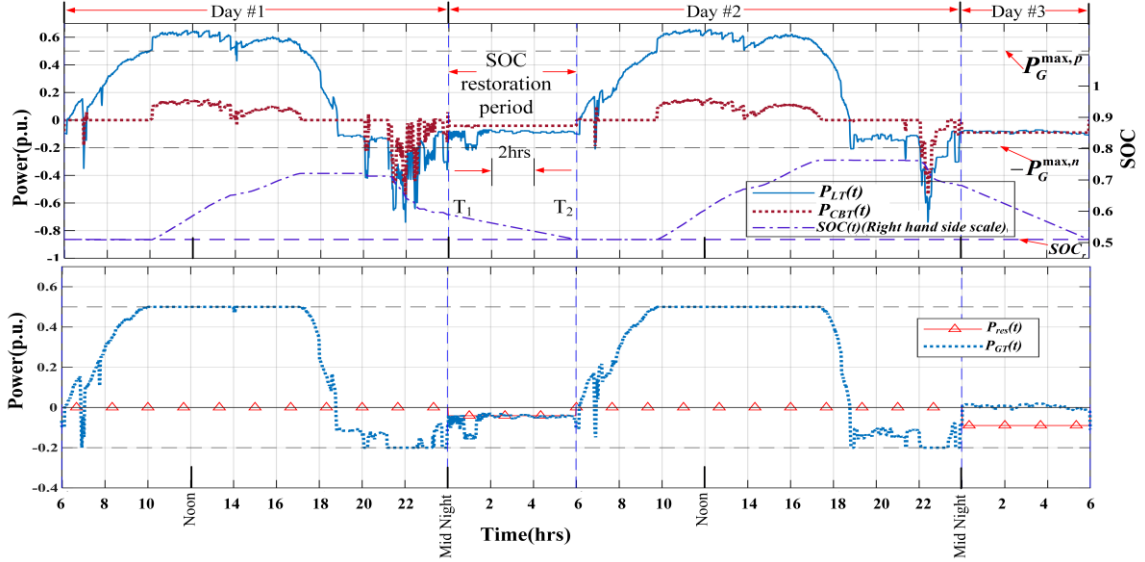


Figure 6.6. A sample of  $P_{res}(t)$ ,  $P_{LT}(t)$ ,  $P_{G,T}(t)$ ,  $P_{CB,T}(t)$  and  $SOC(t)$  following the application of the daily SOC restoration strategy

### 6.5.3 Dynamic Referencing Scheme of $SOC_r$

An augmentation to the daily SOC restoration discussed in the previous subsection pertains to the second prominent mode, that of seasonal variations in  $P_{Net,i}(t)$  alluded to in Section 6.2. The simulation study, carried out to obtain Figure 6.6, was extended to cover a 2-year operation (2014-2015) of the microgrid, and it produces the SOC profile of the CB shown on Figure 6.7(a). In this study, the reference value of the SOC for the CB ( $SOC_r$ ) had been arbitrarily fixed at 0.5: i.e., the daily SOC restoration strategy will ensure the SOC of the CB will be restored to 0.5 at  $T_2$  in each day of the two years. This is in line with the practice of restoring the CB SOC to a constant value daily, as reported in recent works [116] and [110]. The slow varying seasonal mode in  $SOC(t)$  is apparent in Figure 6.7(a), and the SOC appears to complete a full cycle in a year. Indeed, EMD analysis is performed on the  $SOC(t)$  and the IMF corresponding to this much slower dominant mode has been superimposed onto the SOC curve in Figure 6.7(a). In this microgrid example, the load demand is observed to be the highest in winter, whereas the harnessed  $P_{PV,i}(t)$  is at the highest levels in summer. So, due to the abundant sunshine and longer daylight hours in the summer months, the amount of harnessed solar energy exceeds that consumed by the prosumers on most of the summer days. This has resulted in the CB being forced to operate above the SOC reference value  $SOC_r$  in almost all summer hours. Conversely, the relatively lower amount of  $P_{PV,i}(t)$  over a typical winter day is insufficient to meet the demand of the prosumer on that day. This has resulted in the CB being



forced to operate with its SOC at below the  $SOC_r$  level in most instances over the winter months. The amount of the harnessed solar energy and the energy consumed by the prosumer each day is somewhat more balanced over the spring and autumn months: as a result, the SOC is more evenly spread about  $SOC_r$  over these two transition seasons. This explains the  $SOC(t)$  profile shown on Figure 6.7(a) and the IMF tracks the slow seasonal variation mode.

Most importantly, the above example highlights a distinct shortcoming of the daily SOC restoration scheme such as that proposed in [116] and [110], in which the  $SOC_r$  is fixed to the same value regardless of the seasons. In such a fixed- $SOC_r$  scheme and as shown in Figure 6.7(a), the CB is forced to operate predominantly in the high SOC regime in the summer months, while in winter, the CB is to operate in almost all instances at a lower SOC level. This has resulted in an undesirably wide SOC swing and uneven distribution of the SOC over the long term. As the CB energy storage capacity has to be sufficiently large to accommodate the wide range of SOC excursions over the years, it can lead to the need for an unnecessarily large-capacity, and therefore expensive, CB.

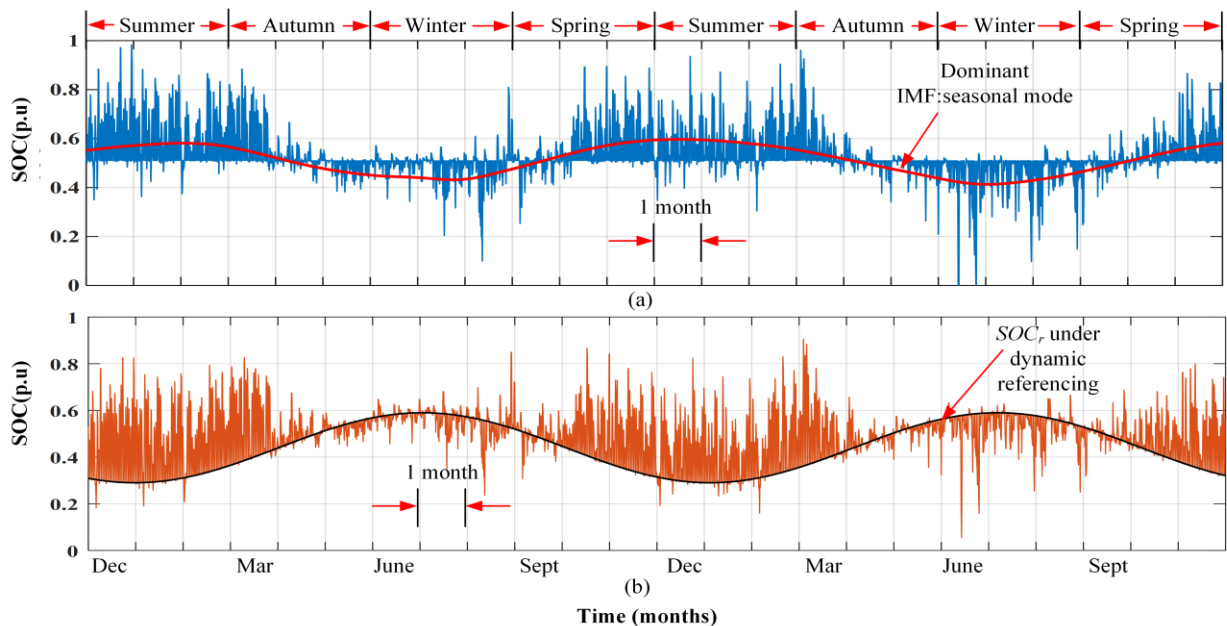


**Figure 6.7 Profiles of the  $SOC(t)$  under daily SOC restoration: (a) fixed- $SOC_r$  ; (b) sinusoidal dynamic referencing of  $SOC_r(t)$**

A dynamic referencing scheme for the SOC will now be proposed, with the view to achieving a more equitable distribution in the  $SOC(t)$  range required to support the power buffering actions. The central point of this scheme is to deliberately adjust  $SOC_r(t)$  in such a manner as to counter the seasonal mode, i.e., the proposed dynamic referencing scheme requires the  $SOC_r(t)$  to be set

deliberately at relatively lower values in summer in comparison to that in winter. This will result in the lowering of the SOC profile over the summer and the subsequent rising of the SOC profile over the winter months, relative to that under the fixed- $SOC_r$  scheme. The shifting of the SOC profiles would be less pronounced over the spring and autumn transition seasons. In Figure 6.8, the dominant seasonal mode of  $SOC(t)$  denoted as  $SOC_s(t)$ , is drawn for both 2014-2015 and for 2016-2017. The sinusoidal form of the  $SOC_s(t)$  variations over the 4 years is clearly apparent. An EMD analysis has also been carried out on  $P_{PV}(t)$  recorded over 2014-2015 and the dominant seasonal mode is included in Figure 6.7. The dominant seasonal IMF mode  $SOC_s(t)$  can be mathematically approximated by a sinusoidal function as:

$$SOC_s(t) = \alpha \text{Sin}(\omega t + \beta) \quad (6.11)$$

Then, the SOC reference signal  $SOC_r(t)$  needs to be set as a sinusoidal function in anti-phase to  $SOC_s(t)$ , as:

$$SOC_r(t) = -m \times SOC_s(t) + \mu \quad (6.12)$$

In (6.12), the modulation factor  $m$  is to be adjusted to limit the resulting SOC variations over the study period to the maximum acceptable level of depth of discharge of the battery. The dc-shift value  $\mu$  is selected to ensure the minimum SOC level during the study period is at the desired minimum SOC value of the battery,  $SOC_{min}$ . This curve-fitting process will cause the resulting  $SOC(t)$  profile over the two years to be more evenly distributed and the excursions in  $SOC(t)$  are over a narrower range. An example of  $SOC_r(t)$  obtained under such dynamic referencing scheme is shown on Figure 6.7(b): it shows the sinusoidal  $SOC_r(t)$  is in direct anti-phase to the dominant seasonal IMF shown on Figure 6.7(a).

In order to enhance the accuracy of the dynamic referencing scheme,  $SOC_r(t)$  can be updated (say) every 6 months, to accommodate the impact of other environmental changes to  $SOC_r(t)$ .

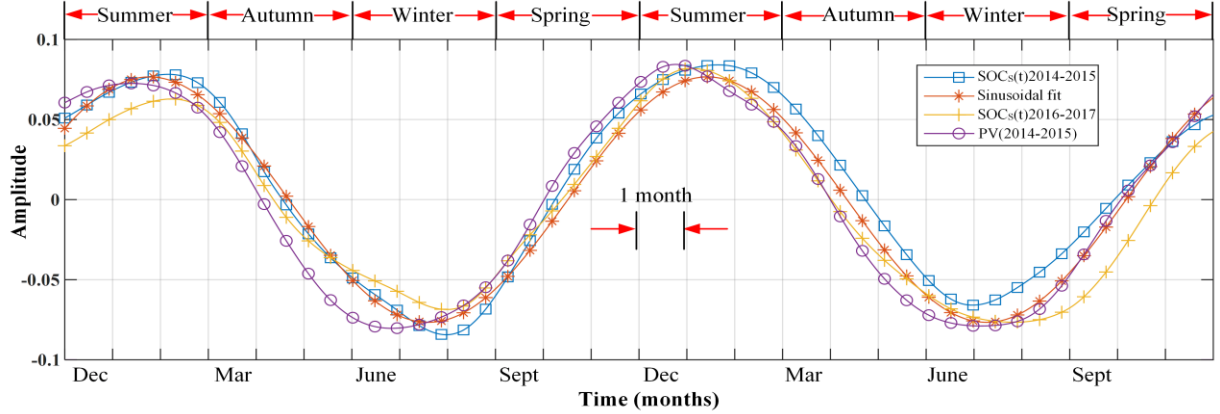


**Figure 6.8** Dominant seasonal mode  $SOC_s(t)$  for 2014-2015, 2016-2017, that of  $P_{PV}(t)$  in 2014-2015 and the fitted dynamic SOC reference on the for 2014-2015  $SOC_s(t)$

In the present work, the extra degree of design freedom offered by the dynamic referencing of  $SOC_r(t)$  shall be taken advantage of to produce the following desirable outcomes: a more effective utilization of the energy storage capacity of the CB and a reduction in the rate of the battery cell degradation. These positive outcomes shall be analysed in greater detail in the next two Sub-sections.

### 6.5.4 A Statistical Analysis of the Impact of $SOC_r$ Setting on CB Energy Storage Capacity

The profiles of the  $SOC(t)$  following the daily SOC restoration appear to be rather random. This is hardly surprising since the load demand and the harnessed PV power are stochastic in nature. Mathematically, the probability density function (pdf) of  $SOC(t)$  is one convenient way to describe quantitatively the spread of such a stochastic variable. An example of the pdfs of the  $SOC(t)$  profiles shown on Figure 6.8 are displayed on Figure 6.9. The PDFs are obtained by analysing the historical data of  $P_{LI}(t)$  over two years, sampled at 1-min interval. The results are based on the fixed-SOC referencing and the dynamic referencing approaches. Consider firstly the pdf of the SOC obtained under the fixed- $SOC_r$  scheme. The pdf can be readily evaluated to yield the mean and standard deviation of the  $SOC(t)$  as 0.53 and  $9.96 \times 10^{-2}$  respectively. Also, the CB operates at a higher SOC level than  $SOC_r$  for about 65% of the time in the two years, i.e., the CB tends to operate under the higher SOC regime than in the lower SOC regime. This is reflected by the longer “tail” in the pdf curve over the range  $SOC(t) > 0.53$ , the mean value.

Figure 6.9(a) also shows the corresponding pdf when the dynamic referencing scheme is applied to  $SOC_r(t)$ , with  $SOC_r(t)$  set in the manner shown in Figure 6.9(b). The mean and standard deviation of the  $SOC(t)$  under this dynamic referencing strategy are 0.45 and  $9.27 \times 10^{-2}$  respectively. The lower standard deviation value indicates the spread in the  $SOC(t)$  is now narrower, and the lower mean value indicates the CB operates at lower SOC range than that under the fixed- $SOC_r$  strategy over the two years.

Next, it is well-known that deep discharge of battery cells can lead to permanent damage to the cells while operating the cells at a high SOC level over an extended period can also be detrimental to battery health [145]. Thus, for example, operating a Li-FePO4 CB at SOC levels below 0.2 or higher than 0.9 should be avoided. Accordingly, in the present work, let  $SOC_{min}$  denotes the SOC level below which the CB is deemed to be operating in the undesirably deep-discharge state. And the corresponding probability of the Li-ion CB operating at or below the  $SOC_{min}$  level is denoted by the symbol  $\gamma$  herewith. So in developing the control strategy for the CB, the aim is to ensure  $\gamma$  shall be less than a (small) pre-specified value, e.g., 0.005, to reflect a negligible risk of the CB entering the undesirable deep discharge operating regime. Also, a confidence level is pre-specified, and the maximum SOC level ( $SOC_{max}$ ) the CB shall reach this confidence level can be determined from the  $Pr(SOC)$  vs  $SOC$  pdf curve: the confidence level is equal to the area under the pdf curve integrated over the SOC range  $SOC_{min} \leq SOC \leq SOC_{max}$ . The developed strategy would be deemed satisfactory when, for example,  $SOC_{max} \leq 0.9$ . In the present work, the specified confidence level is 0.99.

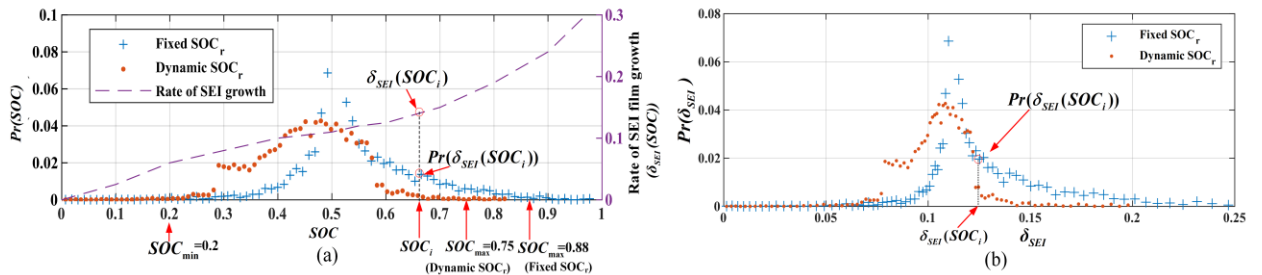


**Figure 6.9 (a) Probability density functions of the SOC under the fixed- $SOC_r$  and dynamic referencing of  $SOC_r$  schemes. Also shown is the rate of SEI film growth vs SOC characteristic curve for LiFePO<sub>4</sub> battery; (b) Probability density functions of the rate of SEI film growth under the fixed- $SOC_r$  and dynamic referencing of  $SOC_r$  schemes**

So, with respect to Figure 6.9 (a), the probability of the cells operating up to  $SOC_{min}$  of 0.2 has been evaluated to be 0.004 under either the fixed- $SOC_r$  or the dynamic referencing  $SOC_r(t)$  schemes.

Since the probability of the cells operating in the deep discharge state is below the pre-specified value of 0.005, both schemes are considered acceptable in terms of the risks of the cells operating in the deep discharge state. Also, from the respective pdf curves and at the specified 0.99 confidence level, it is seen that the  $SOC_{max}$  will reach the values of 0.88 and 0.75 under the fixed- $SOC_r$  and the dynamic referencing  $SOC_r(t)$  schemes respectively. Since  $SOC_{max}$  in both schemes is less than 0.9, it is considered the strategies are satisfactory in this regard.

However, if the CB under the dynamic referencing  $SOC_r$  scheme were to operate up to the SOC level of 0.88, the same level as under the fixed- $SOC_r$  scheme, then it can be seen from the respective pdf curve in Figure 6.9(b) that the confidence level will be almost 1. This means that the CB will be able to buffer the perturbing  $P_{LT}(t)$  successfully in almost all instances over the two years. Or view it in another way: to achieve the same confidence level of the successful buffering task under the dynamic referencing strategy for  $SOC_r$ , one would require a CB of lower energy storage capacity than that needed under the fixed- $SOC_r$  scheme.

A numerical example shall be included in Section 6.6 to illustrate the impact of  $SOC_r$  setting on the required CB energy storage capacity.

### **6.5.5 Impact of Fixed and Dynamic Referencing of $SOC_r$ on the Rate of SEI Film Growth**

Among the various factors affecting the degradation of Li-ion battery cells, the occurrence of the SEI film growth is considered to be the most dominant. It causes the loss of the cyclable Li ions which then reduces the effective storage capacity of the battery cells [72]. In addition, the SEI film growth results in an increase in the internal resistance of the cells. The development of the SEI layer is irreversible. From previous extensive research works [129, 146], it has been well established that there is a clear relationship between the rate of SEI film growth and the SOC of the cells. Although the CB operating temperature can also impact the SEI growth rate, it is most likely the CB shall be housed in a building in which the temperature shall be well-controlled. Hence, the impact of temperature variations on the SEI growth rate shall be neglected in this study. The relationship between the SEI growth rate and SOC can be expressed in term of the  $\delta_{SEI}(SOC)$  vs SOC curve, such as that shown in Figure 6.9 (a) for a  $LiFePO_4$  battery cell.  $\delta_{SEI}(SOC)$  denotes the rate of change in the thickness  $\delta_{SEI}$  of the SEI film. Although  $\delta_{SEI}$  does increase with the SOC of the cell, it can be readily seen from Figure 6.9 (a) that within the mid-SOC range, typically between 0.2 – 0.65, the rate of the film growth  $\delta_{SEI}(SOC)$  tends to be more modest compared to that at the higher SOC level.

Therefore, CB operating in the mid-SOC range would incur a slower increase in the SEI film than that when the CB operates at high SOC levels.

Figure 6.9 (a) shows that for a given  $SOC_i$ , one can readily obtain the corresponding rate of SEI film growth  $\delta_{SEI}(SOC_i)$ . Furthermore, the probability  $Pr(SOC_i)$  of the CB that operates at the level of  $SOC_i$  can also be read directly from the pdf curve of the SOC. In this way, the pdfs of  $\delta_{SEI}(SOC_i)$ , denoted as  $Pr(\delta_{SEI}(SOC_i))$ , can be constructed for the fixed- $SOC_r$  and dynamic referencing  $SOC_r$  schemes. The pdf curves are shown on battery Figure 6.9 (a). With known  $Pr(\delta_{SEI}(SOC_i))$  and  $\delta_{SEI}(SOC_i)$ , one can readily calculate the expected rate of growth of the SEI film over the long term. The expected rate of growth of the SEI film, denoted as  $E[\delta_{SEI}]$ , is given by,

$$E[\delta_{SEI}] = \sum_{\delta_{SEI}=\delta_{SEI.min}}^{\delta_{SEI}=\delta_{SEI.max}} Pr(\delta_{SEI}) \times \delta_{SEI}(SOC_i) \quad (6.13)$$

Since  $Pr(\delta_{SEI}(SOC_i))$  at the SOC level of  $SOC_i$  is precisely  $Pr(SOC_i)$ , one can rewrite (6.13) as follows.

$$E[\delta_{SEI}] = \sum_{SOC_i=SOC.min}^{SOC_i=SOC.max} Pr(SOC_i) \times \delta_{SEI}(SOC_i) \quad (6.14)$$

In (6.14),  $E[\delta_{SEI}]$  is calculated over the full range of the SOC over which the CB is to operate in, at the pre-specified confidence level. This SOC range corresponds to the full range of  $\delta_{SEI}(SOC)$  over which the CB is to operate in at the same confidence level. Using (6.14), one can readily show the extent by which the proposed dynamic referencing scheme can have another advantage over the fixed- $SOC_r$  scheme: application of the dynamic referencing of  $SOC_r(t)$  can result in reducing the rate of the film growth. This is achieved by ensuring the CB is to operate in more instances over the mid-SOC range where the rate of the SEI film growth is much lower than that at high SOC levels. Numerical examples shall also be included in Section 6.6 to illustrate this desirable outcome of using the dynamic referencing of  $SOC_r$  scheme.

### 6.5.6 A Summary of the Proposed Microgrid Rule-based Operational and CB SOC Control Scheme

The aforementioned rule-based operational and SOC control strategy for the grid-connected microgrid can now be amalgamated to produce the block diagram shown in Figure 6.10. It shows that the CB control strategy consists of three parts: Real-time rule-based control, daily SOC correction and seasonal SOC restoration according to the dynamic referencing of  $SOC_r(t)$ .

The control strategy begins with the output of the EMD analysis of  $P_{net,i}(t)$  of prosumer  $i$  and from which the low-frequency component ( $P_{LF,i}(t)$ ) of  $P_{Net,i}(t)$ , the power component of interest in the present work, shall be obtained. In “a”,  $P_{LF,i}(t)$  from all the prosumers in the microgrid is summated to produce the total low-frequency power flows  $P_{LT}(t)$  emanating from the microgrid. Whence, in “b”, the power flows on the grid-interconnection  $P_G(t)$  and in the CB  $P_{CB}(t)$  shall be determined using the rules contained in Table 6.1.

The CB control scheme governing the control of the SOC of the CB follows. Firstly, in “c”,  $P_{CB}(t)$ , determined in “b”, is added to the SOC restoration power  $P_{res}(t)$  to form the total power flows in the CB,  $P_{CB,T}(t)$ . Noting that  $P_{res}(t)$  only comes into effect over the restoration period ( $T_1, T_2$ ) of each day, a time-dependent logic switch has been included in “d” to reflect this function.

Following the determination of  $P_{CB,T}(t)$ ,  $SOC(t)$  is calculated using (6.9), and its value is compared with the SOC reference signal  $SOC_r(t)$  shown in “f”.  $SOC_r(t)$  is in turn generated from the processes shown in “e”. The SOC reference signal  $SOC_r(t)$  is there to counter the slow but dominant seasonal mode generated from the EMD analysis of the historical data of  $SOC(t)$ . So, in “e”,  $SOC_r(t)$  is generated using a sufficiently lengthy historical data of  $P_{PV,i}(t)$  and  $P_{LD,i}(t)$  in the following way. Firstly in “e”, apply the EMD method, and the same processes of “a” and “b” blocks described earlier and together with (6.9), obtain  $SOC(t)$  under the fixed-SOC referencing scheme. Through the EMD analysis, the dominant seasonal mode of  $SOC(t)$  is obtained. Via the curve fitting process described in Section 6.5.3, obtain (6.12) and whence  $SOC_r(t)$  is determined. The difference between  $SOC(t)$  and its reference  $SOC_r(t)$  is then used to calculate  $P_{res}(t)$  via (6.8). Subsequently  $P_{res}(t)$  is added to  $P_{CB}(t)$  at “c”. This completes the SOC control procedure for the CB: the SOC is manipulated on a daily basis to prevent the persistent drift in the SOC alluded to in Section 6.5.1, and the application of the dynamic referencing scheme is to adjust  $SOC_r(t)$  to counter the seasonal mode, to obtain the desirable outcomes explained in Section 6.5.3.

Unlike existing schemes pertaining to the control of grid-connected microgrid for the purpose of load shifting or in alleviating the impacts of the duck power phenomena, the proposed scheme does not require the forecasting of  $P_{LT}(t)$ . The need to forecast  $P_{LT}(t)$ , often on day-ahead basis, increases the computational burden and add complexity to the resulting control scheme. Instead of forecast, the present approach only needs to update of the dynamic referencing signal  $SOC_r(t)$ . The updating can be done off-line, as and when it is required, since the seasonal mode is slow-varying. For example,  $SOC_r(t)$  can be refreshed at regular 6-monthly interval, using updated historical  $P_{LT}(t)$ . Furthermore, the proposed scheme does not result in overshoots or undershoots due

to the feed-forward control and the power switching used in the proposed control strategy. Due to the elimination of high frequency transients by the prosumer house-based SC and the control limits applied on the rate of change of grid power, the proposed control system is deemed not to cause any instability. The proposed scheme involves relatively simple control actions and is therefore deemed to be more robust in comparison with existing schemes proposed in [147].

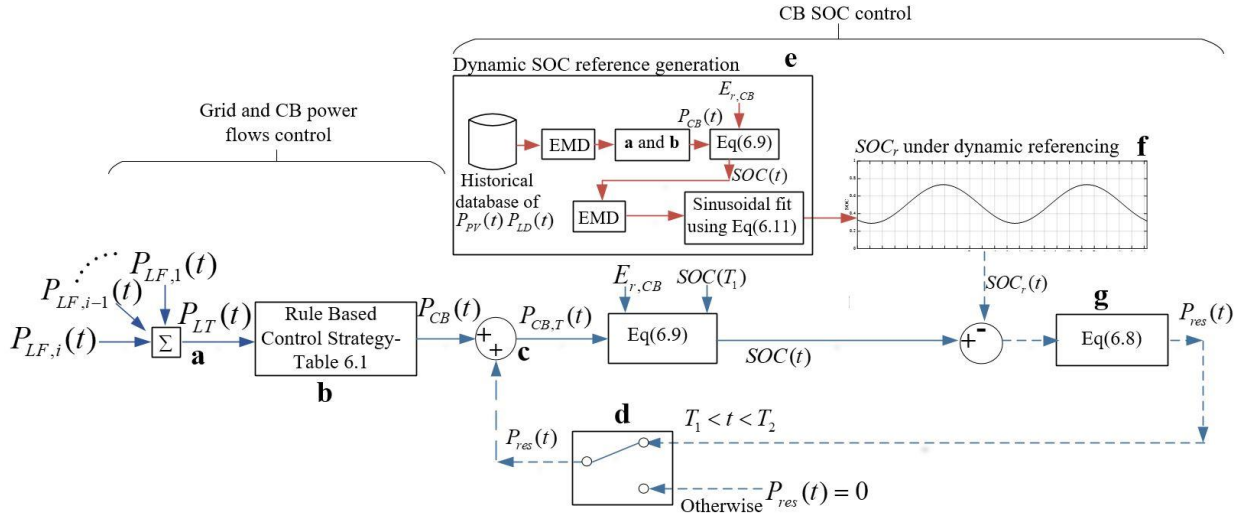


**Figure 6.10 Procedure to obtain the SOC control strategy for the community battery**

## 6.6 Illustrative Examples

The application of the proposed rule-based operational strategy on the grid-connected microgrid, the daily restoration and dynamic referencing of the SOC of the CB shall be illustrated via numerical examples. For the purpose of illustration, it is sufficient to consider a fictitious microgrid servicing three aggregated groups of residential, commercial and industrial prosumers. The electricity usage pattern for the three groups of prosumers shall be that given in [148], [149, 150] and [151, 152] respectively, and the respective power ratings of the groups are 7.2 MW, 5 MW and 1.2 MW, yielding the total rating of the loads in the microgrid as 13.4 MW. Also, the total ratings of the roof-top PV generators in the microgrid of the three prosumer groups are 4.8 MW, 4 MW and 1.2 MW respectively, giving the total PV rating in the microgrid as 10 MW. The harnessed solar power by the PV generators was obtained by scaling up the PV power measured at the authors' laboratory [122]. The laboratory allows the measured  $P_{PV}(t)$  to be downloaded at suitable sampling rates. From the re-constructed  $P_{PV,i}(t)$  and  $P_{LD,i}(t)$ , the simulation platform with the different types of prosumers is set up in the MATLAB environment where data of  $P_{PV,i}(t)$  and  $P_{LD,i}(t)$ ,  $i = 1, 2$  and  $3$ , are fed to readily obtain  $P_{Net,i}(t)$  of each prosumers. Following the application of the EMD analysis of  $P_{Net,i}(t)$ ,



the low-frequency components of  $P_{Net,i}(t)$  can be extracted to produce  $P_{LF,i}(t)$ . Summation of  $P_{LF,i}(t)$  yields  $P_{LT}(t)$ . The statistics analysis is also performed using the MATLAB simulation package. The problem formulation described in Section 6.3 is sufficiently general as to be applicable for the study of the following scenarios.

### 6.6.1 Base Case

The microgrid is assumed as connected to the grid system through an overhead line with a power rating of 5 MW. Furthermore, under the grid code, the maximum ramp rate (expressed in MW/min) on the line is 10% of the total PV generator capacity of the microgrid. Accordingly,  $P_G^{max,p} = 5$  MW,  $-P_G^{max,n} = -5$  MW and  $\dot{P}_G^{max} = 1$  MW/min. In [116] and [110], the practice of CB control is to restore the SOC of the CB daily to a fixed reference value. This existing approach of SOC management shall be included in this investigation and is denoted as the Base Case study. The outcome of this case study shall be used for comparison with that obtained based on the proposed approach described in the earlier sections. By applying the rule-based operational strategy described in Section 6.3 on  $P_{LT}(t)$ , the power flows  $P_G(t)$  and  $P_{CB}(t)$  were obtained. Whence  $SOC(t)$  of the CB can be obtained by following the procedure shown on . In fact, the pdf curve of the  $SOC(t)$  over a 2-year period is that shown on Figure 6.8(a) under the fixed- $SOC_r$  strategy whereby the reference value  $SOC_r$  had been arbitrarily set as 0.5. The corresponding cdf curve had been generated from the pdf curve and it is as shown on Figure 6.10. In this case study, the same practice as in Section 6.5.4 is adopted, i.e.,  $SOC_{min}$  of 0.2 and the confidence level of 0.99. From the zoomed-in plot of the cdf curve, it can be seen that  $\gamma$ , the probability of  $SOC(t)$  is within the range  $0 < SOC(t) < SOC_{min}$ , is 0.0043 and is below the set-threshold value 0.005. Hence the risk of the CB operating under the deep discharge state is considered acceptable. At the 0.99 confidence level, the zoomed-in plot of the cdf curve shows that at the cdf value of 0.99+0.0043 or 0.9943, the CB reaches the SOC value of 0.8538, i.e.,  $SOC_{max} = 0.8538$ : the probability of the CB operating within the range  $0.2 \leq SOC(t) \leq 0.8538$  is 0.99. This set of results was obtained when the energy storage capacity  $E_{r,CB}$  of the CB was set at 31 MWh.

Next, based on the corresponding pdf of the rate of SEI film growth shown on Figure 6.8(b) and by applying (6.14), it was determined that the expected rate of SEI film growth,  $E[\delta_{SEI}]$ , is 0.1377  $\mu\Omega/m^2/sec$ . The column under the “Base Case” in Table 6.2 summarizes the set of results explained above.

## 6.6.2 Impact of the Dynamic Referencing of $SOC_r$ on the Rate of SEI Film Growth

The dynamic referencing of  $SOC_r(t)$  can be effected in the manner as explained in Section 6.5.3. So, with  $P_G^{max,p}$  and  $-P_G^{max,n}$  kept at the same levels as in the Base Case, the intention of Study 2 is to assess the impact of the dynamic referencing of  $SOC_r(t)$  on the rate of the SEI film growth in the CB. The outcome of the study is summarized under the column “Study 2” in Table 6.2 whereby  $SOC_r(t)$  is automatically adjusted to track the seasonal dynamic referencing curve shown on Figure 6.6(b). From the pdf obtained from the resulting  $SOC(t)$  of the CB, the respective cdf curve for this case was also generated and it is included on Figure 6.10. From this figure, it is seen that compared to the Base Case, the dynamic referencing strategy has resulted in a lower mean value of the SOC and the left-shifting of the cdf curve also signifies that the CB is now operating over a  $SOC(t)$  range where the rate of the SEI film growth is more modest.

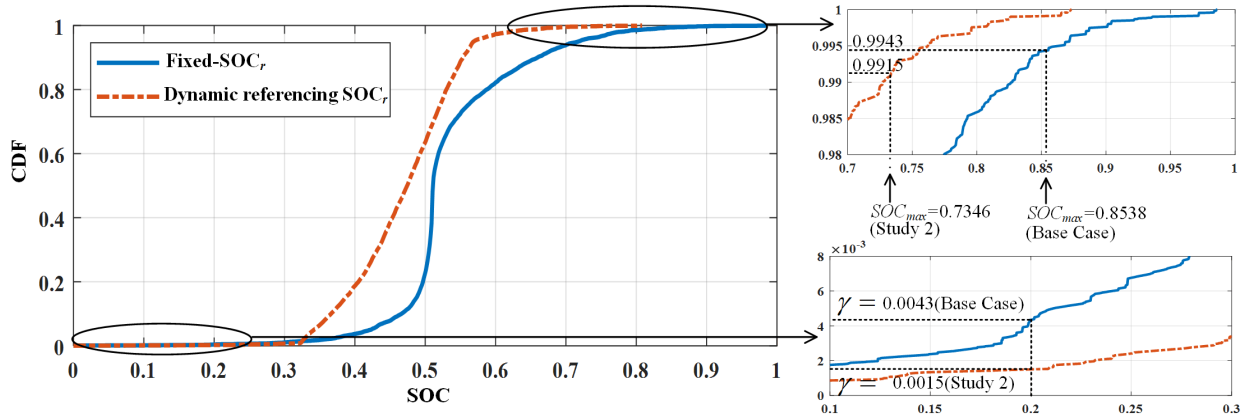


Figure 6.11 CDF of the Li-ion battery SOC based on the fixed- $SOC_r$  (Base Case) and dynamic referencing strategies of  $SOC_r$  (Case Study 2).

Table 6.2. Summary of the results obtained under the Base Case and other case studies:

	Base Case (Fixed $SOC_r$ )	Study 2 (Dynamic $SOC_r$ )*	Study 3	Study 4	Study 5	Study 6	Study 7
<b>PV generator rating</b>	10 MW	10 MW	10 MW	10 MW	10 MW	11 MW	11 MW
<b>Settings for <math>P_G^{max,p}</math> and <math>P_G^{max,n}</math></b>	5 MW fixed	5 MW fixed	Variable (Table 6.3)	Variable (Table 6.3)	Variable (Table 6.3)	Variable (Table 6.3)	Variable (Table 6.3)
<b>SOC reference <math>SOC_r</math></b>	0.5 (Fixed)	Dynamic	0.5 (Fixed)	Dynamic	Dynamic	Dynamic	Dynamic
<b><math>\gamma</math></b>	0.0043	0.0015	0.0043	0.0029	0.0047	0.0031	0.0042
<b><math>SOC_{max}</math></b>	0.8538	0.7346	0.8782	0.7592	0.8292	0.8754	0.9050
<b>CB Rated Capacity (MWh)</b>	31	31	31	31	26	32	30
<b>Expected rate of growth of SEI(<math>\mu\Omega/m^2/sec</math>)</b>	0.1377	0.1169	0.1181	0.1129	0.1166	0.1140	0.1168
<b>Expected rate of SEI film growth relative to that of the Base Case</b>	-	0.84	0.85	0.82	0.85	0.83	0.85

\*The term “Dynamic” denotes  $SOC_r$  is automatically adjusted to track the seasonal dynamic referencing curve  $SOC_r(t)$  shown on Figure 6.7 (b)

As a result, the dynamic referencing scheme has produced a much reduced expected rate of SEI film growth at  $0.1169 \mu\Omega/\text{m}^2/\text{sec}$ . This is some 16% reduction in the rate of film growth as compared to that obtained in the Base Case for the same CB rated storage capacity of 31 MWh. Also, at the same 0.99 confidence level as in the Base Case,  $SOC_{max}$  is seen to reduce to 0.7346, as indicated in Table 6.2. The reduction in the rate of SEI film growth is an encouraging development as a consequence of applying the seasonal dynamic referencing scheme: the CB can be envisaged to sustain for longer service life.

### 6.6.3 Impact of the Flexible Setting of $P_G^{max,p}$ and $-P_G^{max,n}$ in Alleviating Duck-power Phenomenon

The impact of the settings of  $P_G^{max,p}$  and  $-P_G^{max,n}$  on the CB will now be illustrated. As explained in Section 6.3, one could institute a more flexible adjustment in  $P_G^{max,p}$  and  $-P_G^{max,n}$  in accordance with the seasons in order to achieve certain grid export/import objectives. For the same fictitious microgrid with the 5 MW capacity limit applicable on the overhead line, it is assumed as necessary to alleviate the duck-power phenomenon alluded to in Section 6.2. This objective can be achieved by discharging more of the stored energy in the CB to meet (at least partially) the evening peak demand in summer. So in Study 3, a lowering of the value of  $-P_G^{max,n}$  from - 5 MW to (say) -2 MW was attempted in the summer months. Furthermore, since the harnessed  $P_{PV}(t)$  would be expected to be lower in the daytime in winter than that in summer, it is desired to direct more of the harnessed  $P_{PV}(t)$  to the CB during the winter daylight hours. Accordingly, it is proposed to lower  $P_G^{max,p}$  from 5 MW to 3 MW over the winter months. By similar reasoning,  $P_G^{max,p}$  and  $-P_G^{max,n}$  were adjusted to some intermediate values for the transition seasons of spring and autumn in this study. The final adjusted  $P_G^{max,p}$  and  $-P_G^{max,n}$  for the seasons are summarized in Table 6.3. The detailed plots of the various power flows, seasonal dynamic referencing curve for  $SOC_r(t)$  and the pdf curve of  $SOC(t)$  corresponding to Study 3 are as shown in Figure 6.5, Figure 6.6(a) and Figure 6.8 respectively. Since  $SOC_r$  has been fixed at 0.5 in the Base Case, so the impact of the flexible setting of  $P_G^{max,p}$  and  $-P_G^{max,n}$  can be made by comparing the results of the Base Case with that of this study.

**Table 6.3.  $P_G^{max,p}$  and  $-P_G^{max,n}$  settings for the seasons in Studies 3-7**

	Summer	Autumn	Winter	Spring
$P_G^{max,p}(MW)$	5	4.8	3	4.5
$-P_G^{max,n}(MW)$	-2	-4	- 5	- 4

Based on the outcome of the simulation, the expected rate of SEI film growth,  $E[\delta_{SEI}]$ , was determined to be  $0.1181 \mu\Omega/\text{m}^2/\text{sec}$ . Compared to the Base Case, this is an almost 15% reduction in the rate of the SEI film growth. Further evaluation has shown that, compared to the Base Case, the flexible setting of  $P_G^{max,p}$  and  $-P_G^{max,n}$  has resulted in an annual reduction of some 176 MWh in the grid exported energy and some 225 MWh in grid imported energy. This means that a higher amount of the stored energy obtained from harnessed  $P_{PV}(t)$  in the microgrid has been used to meet the microgrid evening peak demand. In turn, it shows that there is an increased level of independency of the microgrid from the interconnection. Thus, this study serves to illustrate that the duck power phenomenon can be alleviated through this approach of judicious adjustments of  $P_G^{max,p}$  and  $-P_G^{max,n}$  over the seasons.

From the results of Section 6.5.5, it is known that the rate of the SEI film growth can be reduced by using the dynamic SOC referencing of  $SOC_r(t)$ . So, Study 4 was carried out by combining the strategy of varying  $P_G^{max,p}$  and  $-P_G^{max,n}$  settings in the manner shown in Table 6.3 and the dynamic referencing of  $SOC_r(t)$ , as was done in Study 2. The detailed plots of the various seasonal dynamic referencing curve for  $SOC_r(t)$  and the pdf curve of  $SOC(t)$  corresponding to the Study 4 are shown Figure 6.6(b) and Figure 6.8 respectively. The expected rate of SEI film growth  $E[\delta_{SEI}]$  is seen to reduce further to  $0.1129 \mu\Omega/\text{m}^2/\text{sec}$ , which is some 18% less than that obtained in the Base Case.

#### **6.6.4 Impact of Dynamic Referencing of $SOC_r(t)$ and Flexible Seasonal Setting of $P_G^{max,p}$ and $-P_G^{max,n}$ on Required CB Capacity**

In view of the above encouraging developments, the next attempt was to explore the possibility of reducing the energy storage rating of the CB required to undertake the power buffering task. With the same seasonal settings of  $P_G^{max,p}$  and  $-P_G^{max,n}$  and the seasonal dynamic referencing of  $SOC_r(t)$  as in Study 4, the column under Study 5 of Table 6.2 shows that a reduction of the energy storage rating of the CB to 26 MWh has resulted in the expected rate of SEI film growth to  $0.1166 \mu\Omega/\text{m}^2/\text{sec}$ . This storage capacity is needed to meet the same confidence level of 0.99, and it yields  $SOC_{max}$  of 0.8292. As indicated in Figure 6.7(b), the proposed dynamic SOC referencing method has led to the narrowing of the SOC swing range and in Study 5, the CB of lower storage capacity of 26 MWh can still be able to provide the buffering actions with the same confidence level as in Study 4. Comparing the outcomes of study 3 and study 5, it can be concluded that with the seasonally adjusted  $P_G^{max,p}$  and  $-P_G^{max,n}$ , some 16% reduction in the required CB rated capacity is possible when the proposed dynamic referencing of  $SOC_r(t)$  is applied, instead of adopting the fixed-

$SOC_r$  strategy described in [116] and [110], and still be able to achieve similar expected rate of SEI film growth.

Hence, Studies 3-5 serve to demonstrate that there is considerable advantage in adopting flexible setting of  $P_G^{max,p}$  and  $P_G^{max,n}$  in accordance to the seasons, in terms of slowing down the SEI film growth through the dynamic referencing of  $SOC_r$ , and the possibility to arrive at a more modest CB energy storage capacity design.

### 6.6.5 Sensitivity studies

The purpose of Studies 6 and 7 in Table 6.2 is to assess the sensitivity of the CB design to increases in PV generation. For this purpose, the total PV generation rating in the microgrid is increased by 10%, without any corresponding increase in the rating of the loads. Study 6 shows that if the CB storage capacity is increased to 32 MWh, the expected rate of SEI film growth is  $0.1140 \mu\Omega/\text{m}^2/\text{sec}$ , a level which is below that of Study 5. To arrive at a similar rate of SEI film growth as in Study 5, the CB storage capacity can be reduced to 30 MWh, as shown in Study 7. Therefore, it is observed that the 10% increase in the PV generator-rated capacity requires some 15% percentage increase in the rated CB storage capacity, in order to produce the same rate of SEI film growth.

All the studies in Table 6.2 were carried out using the recorded data of  $P_{PV}(t)$ , scaled from the harnessed PV power measured in the authors' laboratory in 2014-2015. An additional sensitivity study had also been carried out based on  $P_{PV}(t)$  recorded in 2016-2017. The intent of this study is to assess the sensitivity of the designed CB to differences in the  $P_{PV}(t)$  data-set. The results of this additional study can be compared to that of Study 5, in the form of the cdf of the SOC of the CB for the two different 2-year periods. Although the detailed results have not been included in this manuscript due to space consideration, it can be reported that the cdf of the SOC of the CB for 2016-2017 is almost identical to that of 2014-2015. Therefore it can be concluded that the designed CB operating under the proposed control strategies will be able to provide the same confidence level in the successful buffering of the power flows at the PCC between the microgrid and the external grid connection.

## 6.7 Conclusions

A new SOC control scheme for centralized battery in a microgrid of high PV penetration level has been developed in this chapter. The intention is to reduce the rate of the SEI film growth in the Li-ion battery cells while avoiding deep discharge and therefore, to enhance the service lifetime of the

battery bank. The proposed seasonal dynamic referencing of the  $SOC_r(t)$  scheme, based on the identified predominant daily and seasonal implicit modes of oscillations, has been shown to be effective in reducing the rate of the SEI film growth, thus alleviating a major contributor to the degradation of the battery cells. Moreover, the proposed scheme has been able to reduce by a considerable percentage the required storage capacity of CB compared to the fixed- $SOC_r$  referencing scheme contained in many existing CB control schemes. Furthermore, by allowing the flexible setting of  $P_G^{max,p}$  and  $-P_G^{max,n}$  in accordance with the seasons, more effective utilization of the CB energy storage capability is shown to be readily achievable. As the focus of this work is not on the short-term dispatch planning of the microgrid, the proposed rule-based operational strategy does not require forecasts of the PV generation and load demand. Hence the proposed control scheme is comparatively simpler and more robust. Numerical examples show that with the proposed rule-based approach, the grid power import/export can be controlled such that the proposed CB control scheme can assist in achieving a higher level of independency in term of meeting the energy demand of the microgrid, and it can alleviate potential problems such as the duck power phenomenon observed in the daily operation of the microgrid.

Notwithstanding the above encouraging outcomes, further work is needed to investigate the inclusion of other potential cell degradation factors e.g., the impacts of the magnitudes of charging/discharging currents on the service lifetime of the CB.

# **CHAPTER 7. Development of a Degradation-Conscious Adaptive Control Strategy for the Intra-Day Operation of Community Battery**

## **7.1 Introduction**

In the previous chapter, the study was when the buffering action of the existing grid link is prioritized over that of the CB. The aim is to fully utilize the power flow capacity of the grid link, and the CB is to supplement the link in buffering the fluctuating  $P_{LT}(t)$ . In this way, the required capacity of the CB can be reduced. The significant increase in solar installations in recent years, encourages to re-examine the role of the grid link. Indeed, to reduce transmission losses and to exclude the requirement of costly upgrades of transmission lines to remote communities, the modern microgrid with distributed generation has become increasingly independent from the existing conventional power system, i.e., in making the microgrid less dependent on the grid link when meeting the electricity demand of the prosumers in the microgrids [153]. In view of the above, the focus of this chapter is to re-examine the role of the CB, and to develop the appropriate control strategy. The chapter assumes the primary role of CB is to buffer  $P_{LT}(t)$  while the grid link is to supplement the actions of the CB in the intra-day operations of the microgrid.

Furthermore, the previous planning study has considered the SEI growth of Li-ion battery only with respect to the SOC of the CB. The magnitudes of the charging/discharging current are assumed to be relatively low and hence, the impact of the battery currents on the SEI growth has been neglected. In this chapter, the effect of the C-rate of the CB shall be included in defining the charging and discharging strategies for more precise evaluation of the SEI growth. Using this comprehensive ageing model, it is aimed to operate CB to attain lowest SEI growth.

## 7.2 Preliminaries

### 7.2.1 Seasonal Variations of Net Power of Microgrid

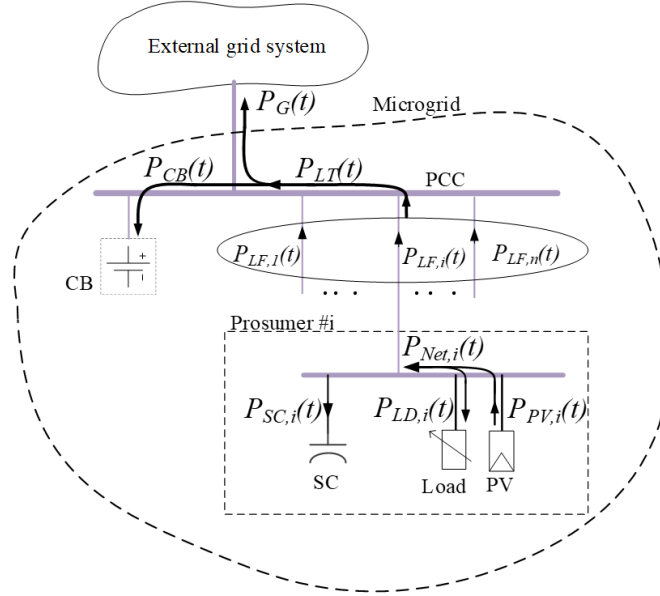


**Figure 7.1. A Schematic Diagram of Grid-connected Microgrid**

As explained in CHAPTER 4 to 6 and re-introduced in the schematic diagram Figure 7.1, the net power flows  $P_{net,i}(t)$  from the  $i^{th}$  prosumer in the microgrid is a highly stochastic quantity due to the perturbing  $P_{PV,i}(t)$  and  $P_{LD,i}(t)$ . It is also clear from these chapters that the highest levels of the perturbing energy in  $P_{net,i}(t)$  reside in the lower frequency components, i.e., in the higher order IMFs, of  $P_{net,i}(t)$ . Also, it was shown that the high- and low- frequency perturbations in  $P_{net,i}(t)$  can be more economically buffered by the SC and electrochemical battery respectively. The cut-off frequency segregating the low- and high-frequency bands is of the order of  $10^{-2}$  Hz.

As the focus is on the intra-day power flows control of the microgrid, it is these lower frequency power perturbations in  $P_{net,i}(t)$  which are of interest in this chapter. The low frequency perturbing power flows from the  $i^{th}$  prosumer is denoted as  $P_{LF,i}(t)$  and the summation of all  $P_{LF,i}(t)$  in the microgrid produces the net power flows  $P_{LT}(t)$  shown in Figure 7.1.

$P_{LT}(t)$  is the addition of two power flows components: that in the grid link ( $P_G(t)$ ) and that in the CB ( $P_{CB}(t)$ ). As explained in the Introduction, the primary aim of the present study is to successfully buffer  $P_{LT}(t)$  by placing higher priority on  $P_{CB}(t)$ , while  $P_G(t)$  is to provide the supplementary buffering actions. Through this prioritization of the CB buffering actions over that



of the grid link, the objective is to reduce the amount of grid daily import/export power flows through the grid link, and thus realize a higher level of grid-independency of the microgrid, in comparison to the strategy developed in the previous chapter.

Figure 7.2 shows a typical daily profile of  $P_{LT}(t)$  over the four seasons. According to the figure, there is no readily identifiable trend of  $P_{LT}(t)$  across four seasons. Over the daylight hours,  $P_{LT}(t)$  is considerably smoother in the summer day compared to that in the transitional seasons of spring and autumn. In the literature [154], it has been reported that there is a tendency to have more cloud movements during spring and autumn and hence,  $P_{PV,i}(t)$  would be accounted with more non-deterministic variations over these transitional seasons. These relatively fast variations in  $P_{PV,i}(t)$  are reflected in  $P_{LT}(t)$  in the daytime hours over the four seasons, as evidenced in Figure 7.2. This observation is in line with the outcome of the statistical analysis of the seasonal  $P_{LT}(t)$  contained in CHAPTER 5. As given in Section 5.4, there are considerably lower levels of power perturbations in summer, as compared to the other seasons.

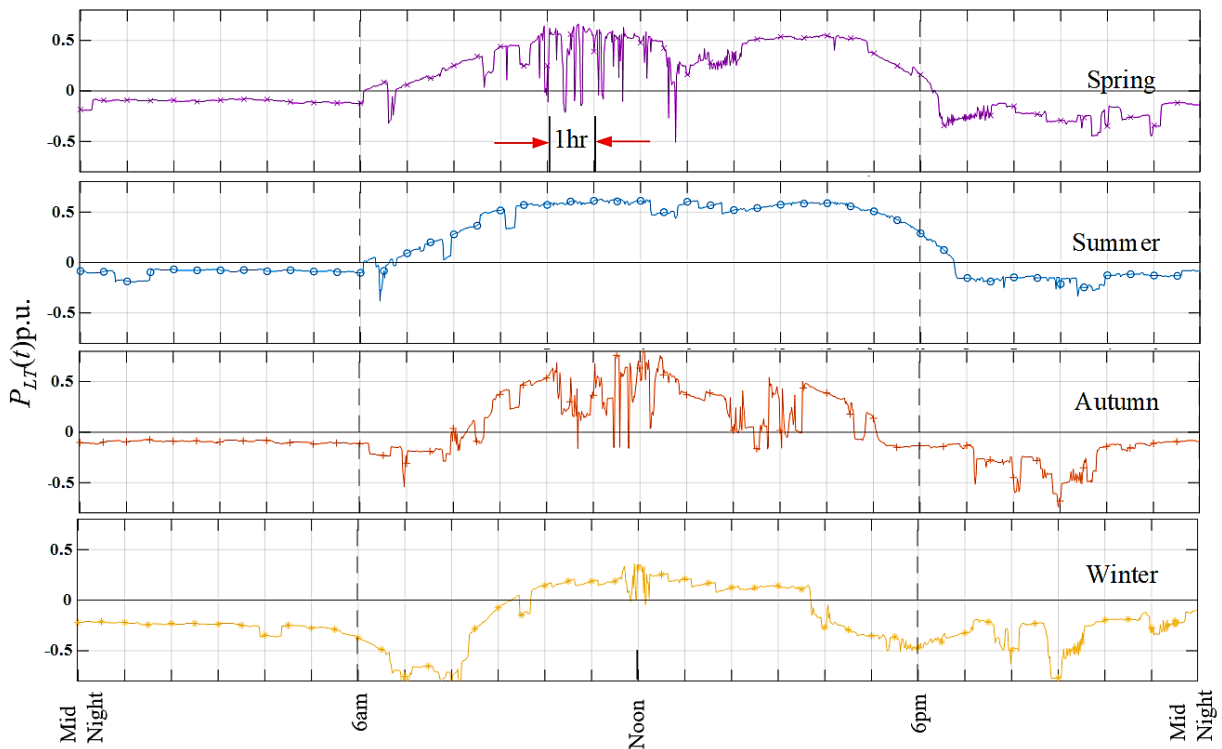


Figure 7.2. A sample of daily profile of  $P_{LT}(t)$  in four seasons

In addition, the time duration of positive  $P_{LT}(t)$  varies across different seasons. During summer, this is 6.30am-6.00pm while during the winter this is 9.30am to 3.30pm. Positive  $P_{LT}(t)$  can only start a short while after the sunrise and it can only end a short while before the sunset,

depending on the relative magnitudes of the PV generation and the prosumer loads at the time. Hence, the 6.30 am and 6 pm time tags correspond to the approximate instances of the sun-rise and sun-set hours of the particular summer day. Similar reasoning applies to the other seasons. Since the sun-set and sun-rise hours are readily available a day ahead, it will be shown in latter sections that this information shall be made use of when designing the adaptive CB control strategy.

Another noteworthy observation from Figure 7.2 is daily positive and negative areas of  $P_{LT}(t)$  are unequal during four seasons. In summer, there is a surplus of energy, whereas in winter, there is an expected deficit of energy. It therefore signifies that the microgrid is a net energy exporter for this summer day. Conversely, it can be readily seen that in the particular winter day shown in Figure 7.2, the microgrid is a net energy importer for the day.

In the absence of the CB, if this variable  $P_{LT}(t)$  of the microgrid is fed to the grid which will raise certain control issues for the system operator. Particularly during summer, daytime grid export would be problematic raising the duck power issue. Even during the autumn and spring, as can be seen from Figure 7.2 the highly fluctuating daytime  $P_{LT}(t)$  would not be acceptable to serve grid ramp rate constraints. In addition to these grid requirements, from the perspective of the microgrid it is economically viable to store this daytime surplus energy of  $P_{LT}(t)$  as much as possible to serve the night time energy including peak demand. This makes the microgrid more independent from the main grid. Therefore, real time control of the  $P_{CB}(t)$  to meet such successful buffering of  $P_{LT}(t)$  is required. If the forecasting is to be used for this task as in [81] and [118], it will add unavoidable complexity to the control and energy management of the CB.

In view of the above considerations there may be strategic as well as economic advantages to store as much as possible the surplus daytime energy in the CB and use the stored energy to meet part, or all, of the electrical energy needs in the microgrid during the night/early morning interval, including that of the evening peak demand. This will result in the microgrid being made less dependent on the grid link. Towards meeting this objective, proposing a simple adaptive control of the  $P_{CB}(t)$  is to be developed in this chapter. This will further enable to meet successful buffing of stochastic and uncertain  $P_{LT}(t)$  while respecting grid constraints while resulting in a modest SEI growth of CB.

### **7.2.2 Li-ion battery degradation due to SEI growth**

Different types of ageing phenomena continue to degrade the performance of Li-ion battery as the usable capacity reduces with time and usage. As discussed in the literature, among the wide range

of degradation phenomena, it is considered the SEI growth and Li-plating are the most dominant aging mechanisms. Li-plating is mostly dominant towards the end of life of the battery while SEI growth dominates the rest of the methods during most of the operating period of the Li-ion battery [73]. Therefore, in this work, discussion is limited to the SEI growth as the predominant degradation phenomenon during Li-ion battery operation, bearing in mind that other degradation factors can also affect to the lifetime of the battery.

In CHAPTER 6, the rate of the SEI film growth ( $\delta$ ) has been considered as being impacted by the SOC of the battery cells. In the present investigation, this relationship has been extended to include the impact of the cell current on the rate of SEI film growth as well. The relationship between the SEI growth vs SOC and cell current is shown in Figure 7.3 for LiFePO<sub>4</sub> cathode chemistry. This is developed based on the literature that detailed in [155]. The detailed mathematical expressions pertaining to the relationship are given in Appendix D. Similar surface plots have also been observed in [146] and [156], thus assuring that the general trends of the curve would be similar even the parameters of the considered Li-ion battery vary for the other chemistries like LiNiCoMnO<sub>2</sub> [157].

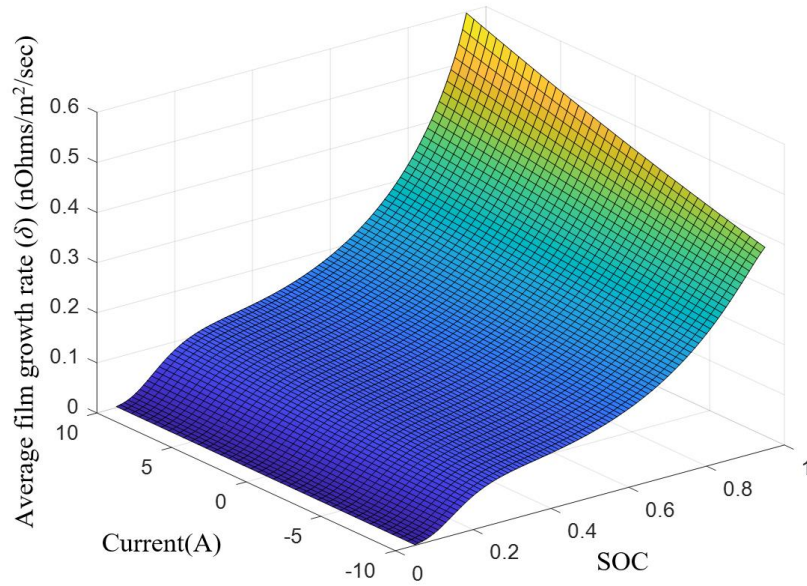


**Figure 7.3. Surface plot of SEI film growth rate versus cell current and SOC for Li-ion battery of LiFePO<sub>4</sub> cathode chemistry**

The surface plot of Figure 7.3, indicates that the positive direction of the current corresponds to the charging current of CB. The depicted surface plot generally demonstrates a convex relationship between the SEI growth rate and the SOC particularly in the SOC range from 0.5 to 1 suggesting that the higher SOC ranges are associated with higher SEI growth rates. The salient features of above

surface plot can further be described using the series of plots shown in Figure 7.4 and Figure 7.5 at various charging and discharging C-rates, respectively. In Figure 7.4, the direction of the arrow indicates the increase in the charging current while the zero-charging current denotes the state in which the battery is in the resting stage. As the charging current increases, the SEI layer grows faster with higher growth rate. This behaviour is very significant particularly in the higher SOC range. In contrast, during the operation in the lower SOC range, the effects of the charging current magnitude (C-rate) on the SEI growth becomes rather less significant as SEI growth curves are quite close to each other in Figure 7.4. Notably, even with zero charging current, the corresponding non-zero  $\delta$  indicates that even in the resting state, the SEI film layer continues to grow. This occurs because the neutral lithium (i.e. lithium ion with an electron) in the electrode reacts with the electrolyte at the electrode-electrolyte interface, and this leads to the presence of the side-reactions current.

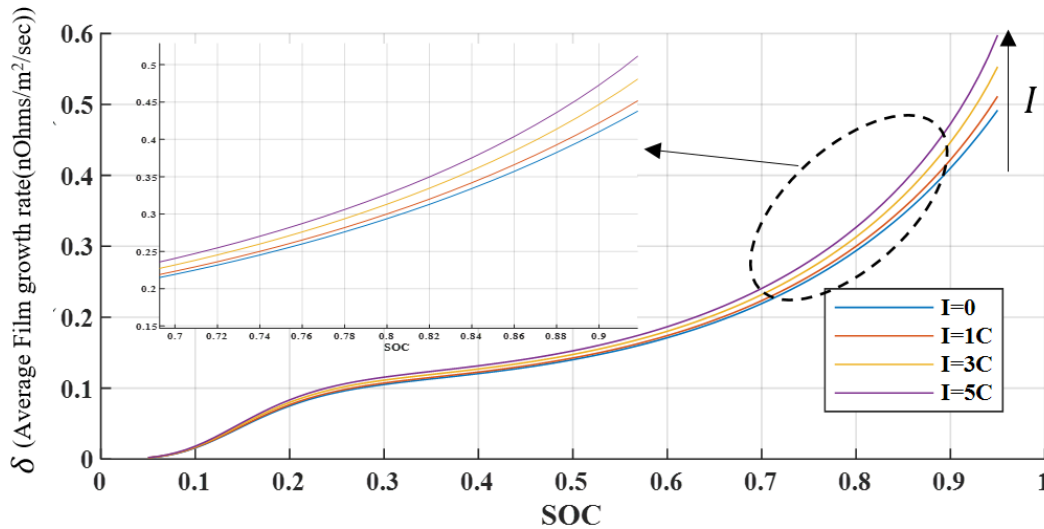
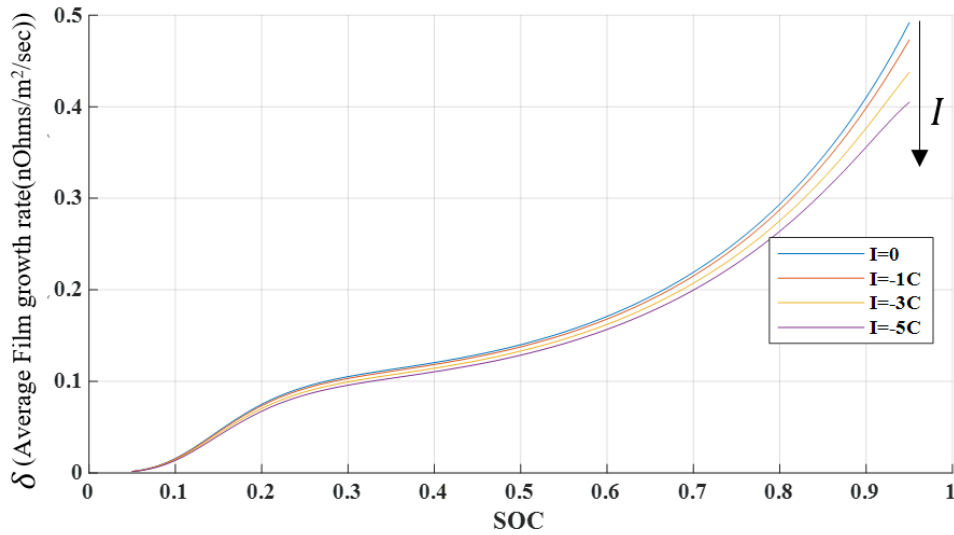


Figure 7.4. SEI film growth rate vs SOC of Li-ion battery cell under various charging C-rates



**Figure 7.5. SEI film growth rate vs SOC of Li-ion battery cell under various discharging C-rate**

Interestingly, in contrast to the increase in charging current, as shown in Figure 7.5 during discharging operation, when the discharge current C-rate increases,  $\delta$  becomes lower. In other words, discharging with higher C-rate decelerates the SEI film growth. This observation in the asymmetry in the charging and discharging operations is in accord with the results reported in the recent experimental study [74]. Further explanation of this asymmetrical behaviour is given in [158]. The higher charging currents increase the potential of the negative electrode. This elevated negative potential facilitates the Li-ion intercalation which will then increase the interaction with electrolyte leading to increasing the SEI growth. However, during discharging, the potential of the negative electrode decreases as lithium ions move from the negative electrode to the positive electrode. The loss of Li-ion inventory in negative electrode leads to decelerate the formation of SEI growth. This asymmetry in SEI growth between charging and discharging currents can be useful to define the appropriate charging/discharging strategies of the CB to minimise the degradation effect. In summary of the above discussion of SEI growth of Li-ion battery, the following key points are highlighted.

1. During CB charging operation, the rate of the SEI film growth increases with the charging current C-rate;
2. During CB discharging operation, the rate of the SEI film growth rate decreases with the increase in the discharging current C-rate.

A more detailed analysis of this charging/discharging approach shall be presented in Section 7.3.2 based on these observations.

## 7.3 Analysis

The last section has highlighted the several distinct characteristics of  $P_{LT}(t)$  over the seasons and the highly nonlinear relationship between the rate of the SEI film growth in the Li-ion CB with that of the SOC and magnitudes of the CB current. The focus of this section is to analyse in greater detail these phenomena.

### 7.3.1 Energy contents in $P_{LT}(t)$

Consider the daily profile of  $P_{LT}(t)$  shown in Figure 7.6. Since PV generation is the only source of power generation within the microgrid,  $P_{LT}(t)$  can be positive only during sunrise ( $T_{SR}$ ) and sunset ( $T_{SS}$ ). During this period too,  $P_{LT}(t)$  can be negative whenever, the total generation falls below the total consumption, ignoring the minor of high frequency components. The first instance the  $P_{LT}(t)$  becomes positive during the daytime is a short time after  $T_{SS}$ . Similarly, the last instance  $P_{LT}(t)$  is positive during the daytime is another short time before  $T_{SS}$ . In developing the adaptive charging control strategy, these small-time differences are ignored. Hence  $T_{SR}$  is taken as the time  $P_{LT}(t)$  becomes positive for the first time in the day and  $T_{SS}$  is taken as the time  $P_{LT}(t)$  becomes positive for the last time in the day. The motivation behind the assumption is  $T_{SR}$  and  $T_{SS}$  are readily known a priori. Therefore, without any forecasting the times can be readily calculated using known equations.

Also shown in the figure are  $T_1$  and  $T_2$  which govern, as in CHAPTER 6, the starting and end time of the SOC restoration period for the CB. Also, from CHAPTER 6, it has been concluded that a suitable SOC restoration period for the CB is generally from close to midnight to  $T_{SR}$  of the next day. This is because over this period, variations in  $P_{LT}(t)$  tend to be small and therefore, there is more certainty the restoration actions can be more accurately calculated. So,  $T_1$  and  $T_2$  are treated as settable design parameters in the present study. To be able to do so will allow an extra degree of freedom when strategizing the CB operations. For convenience, in the rest of this study, the interval between  $T_{SR}$  to  $T_{SS}$  is denoted as the daytime, and that between  $T_{SS}$  and  $T_1$  is denoted as nighttime.

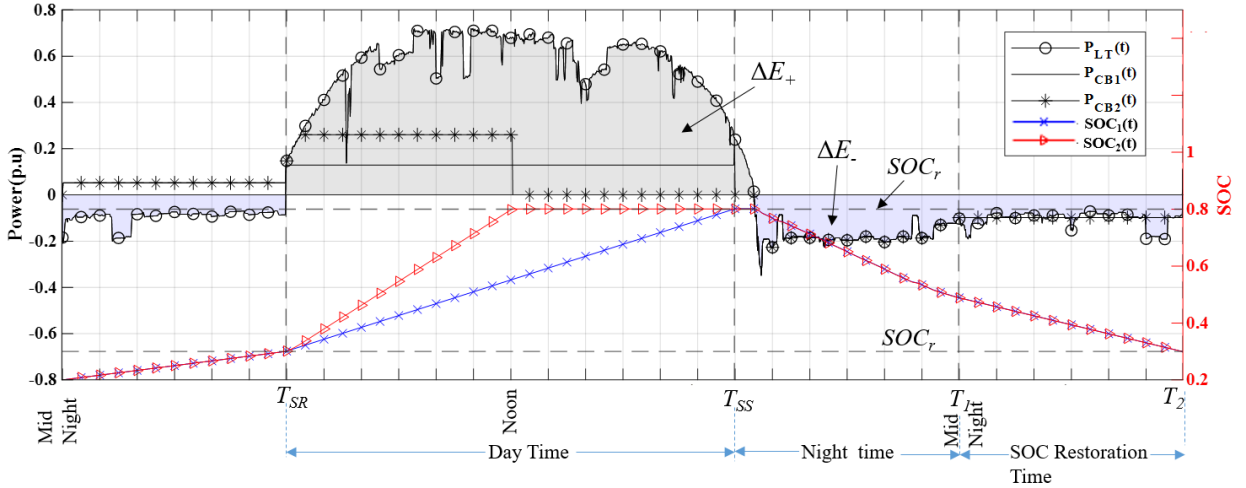


**Figure 7.6. Demarcation of CB daily operating regimes into the daytime, nighttime and SOC restoration periods**

As presented in CHAPTER 6, the “duck power” phenomenon is one of the most critical operating conditions for the grid system as the daytime oversupply of excess PV power to the grid causes system stability issues. Therefore, one possible way to alleviate the duck power would be to divert as much as possible the surplus power from the microgrid to the CB. The stored energy in the CB can in turn be used to meet the demand in the night-time hours. Thus, in this manner, it also decreases the level of dependency of the microgrid on the grid link. To achieve the energy independency for the microgrid, it would be most desirable to have sufficient stored energy in the CB to support the microgrid power demand in the evening hours between  $T_1$  and  $T_2$ .

Since the objective is on developing control strategy for the intra-day operation of the CB, the following analysis is therefore on the daily behavior of the microgrid. Consider once again the daily  $P_{LT}(t)$  depicted in Figure 7.6. The shaded area prescribed by the positive portion of the  $P_{LT}(t)$  curve, detected approximately between  $T_{SR}$  and  $T_{SS}$ , corresponds to the total amount of the surplus energy originated from the microgrid. This surplus energy is denoted as  $\Delta E_+$  in the figure. Conversely, the amount of the deficit energy (denoted by shaded area  $\Delta E_-$  in the figure) has to be provided by the grid and/or from the CB, in order to meet the energy demand of the microgrid from  $T_{SS}$  to  $T_2$ . So, the CB will be discharging to supply some of its stored energy over the interval  $T_{SS}$  and  $T_2$ . The daily historical  $P_{LT}(t)$  can be integrated with respect to time  $t_0$  obtain a set of the daily  $\Delta E_+$  and  $\Delta E_-$ . A statistical approach is used to quantify the variations in the daily  $\Delta E_+$  and  $\Delta E_-$ . So, the daily  $\Delta E_+$  and  $\Delta E_-$  for a given seasonal and their cdfs can be readily generated as illustrated in

Figure 7.7(a) which is the cdf of such for summer season. The figure presents the numerical values of  $\Delta E_+$  and  $\Delta E_-$  are expressed in p.u., on the base of the energy rating of the CB.

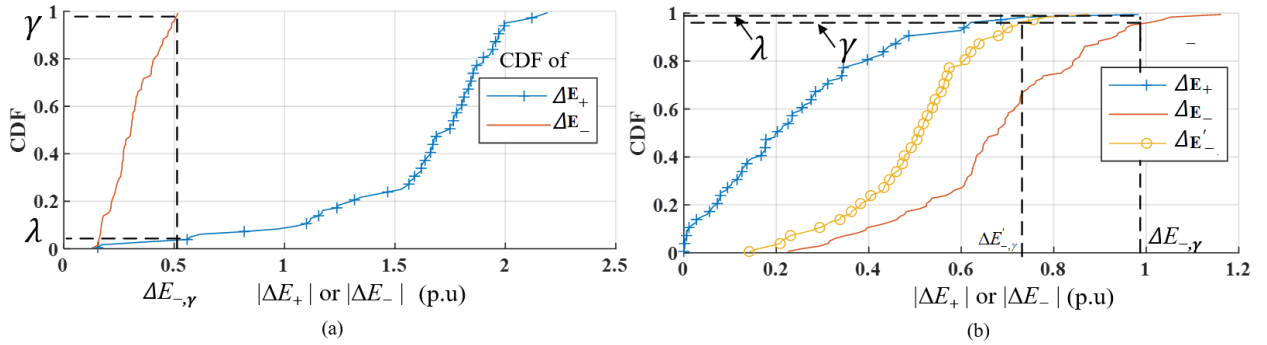


**Figure 7.7** Cumulative density functions of the daily  $\Delta E_+$  and  $\Delta E_-$  for (a) the summer and (b) the winter seasons

Based on the cdf curve of the daily  $\Delta E$  in Figure 7.7(a), one can determine the probability of the daily  $\Delta E_-$  to be at or below the level of  $\Delta E_{-, \gamma}$  p.u. in a summer day as  $\gamma$ . Correspondingly, based on the cdf curve of the daily  $\Delta E_+$ , one can also conclude that the probability of the daily  $\Delta E_+$  to be at or below the level of  $\Delta E_{-, \gamma}$  p.u. in a summer day as  $\lambda$ . This in turn means that the probability of the daily  $\Delta E_+$  to be more than  $\Delta E_{-, \gamma}$  p.u. is  $1 - \lambda$ . In Figure 7.7(a), the cdf curve of the daily  $\Delta E_-$  is positioned to the left of the cdf curve of the daily  $\Delta E_+$  which leads to the following interesting observation. For example, the probability of the daily  $\Delta E_{-, \gamma}$  to be less than or equal to 0.51 p.u. is 0.99, i.e.,  $\gamma = 0.99$ , reading from the cdf curve of the daily  $\Delta E_-$ . From the cdf curve of  $\Delta E_+$ , the probability of the daily  $\Delta E_+$  equal and up to the level of 0.51 p.u. is  $\lambda = 0.035$ , i.e., the probability of  $\Delta E_+$  exceeding the 0.51 p.u. level is  $1 - 0.035$  or 0.965. Therefore, since  $\gamma$  and  $1 - \lambda$  are close to 1, it can be concluded that it is with almost certainty one can expect that in a summer day, the amount of the daily surplus energy  $\Delta E_+$  shall be equal to or more than that of the deficit energy  $\Delta E_-$ . This shows that the microgrid is easily self-sustained with its stored daytime energy in the CB during summer. Indeed, the further the cdf curve of  $\Delta E_-$  is to the left of that of  $\Delta E_+$ , the higher it would be to achieve the intra-day independency.

Unfortunately, this level of energy independency in summer cannot be valid for all other seasons. Converse to the previous example, Figure 7.7(b) shows the cdf of the daily  $\Delta E_+$  and  $\Delta E_-$  for a winter season wherein it is seen that the cdf curve for  $\Delta E_+$  is now appearing to the left of that of  $\Delta E_-$ . To achieve  $\gamma$  of 0.99,  $\Delta E_{-, \gamma}$  is approximately 1.05 p.u. This in turn leads to  $\lambda$  of almost 1, i.e., the probability of the microgrid having sufficient surplus energy to meet the deficit energy daily is close to 0 in winter. Another scenario with an earlier SOC restoration (i.e.  $T_1$  starts two hours before



midnight) gives the curve  $\Delta E'$  in the Figure 7.7(b). This new alternation of the time  $T_l$  results in a left shifted curve  $\Delta E'$  compared to the previous one giving a value of  $\Delta E'_{\rightarrow,\gamma}$  which is much lower than the  $\Delta E_{\rightarrow,\gamma}$ . This indicates that this alternation of the SOC restoration would be much more desirable during the winter season where the daytime stored energy is less.

Although details are not included in this chapter, similar analysis for the transitional seasons of spring and autumn had been carried out. For the same probability level  $\gamma$  of 0.99, the corresponding probability of having sufficient surplus energy to meet the deficit energy daily are 0.67 and 0.42 in spring and autumn, respectively.

Even though the above outcome is well expected across different seasons, the seasonal analysis provides a qualitative analysis of the impact of the seasons in terms of energy independency of the microgrid. Also, it indicated that the control parameters of the CB should vary across different seasons. During the summer, even the microgrid independency can be easily obtained as shown above, the primary target of the control of the CB should be to reduce the SEI film growth rate. Thus the charging/discharging strategies during daytime and nighttime should be aligned with this objective. This will be the attention of the next section.

### 7.3.2 Constant current charging on SEI film growth – ideal case

Firstly, to simplify the discussion, consider an ideal situation whereby power flows constraints imposed on the grid link are ignored. Also, the commonly-adopted constant current charging strategy is assumed in this case due to the valid reasons related to battery degradation for using such charging method in the literature [155].

With reference to Figure 7.6 , it was earlier mentioned that the sunrise hour  $T_{SR}$  and sunset hour  $T_{SS}$  are known quantities. As the CB is intended to be charged at a constant C-rate, the SOC of the CB would increase linearly with time. From CHAPTER 6, the dynamic referencing scheme sets a reference value of the SOC, denoted as  $SOC_r$ , and at the end of the SOC restoration period. Therefore, the SOC of the CB will reach  $SOC_r$  at  $T_{SR}$ . Hence, the  $SOC(T_{SR})$  would be known. The exact value of the SOC at  $T_{SS}$  would depend on the charging C-rate. As the discharging of the CB persists after  $T_{SS}$ , it will be prudent to set the target value for the SOC at  $T_{SS}$  as as high a value as possible. This will also allow the maximum allowable amount of the daily surplus energy  $\Delta E_+$  diverted to the CB. In this way, the issue of the duck power phenomena can be mitigated to a certain degree and also degree of the independency of the microgrid from the grid system can be maximized.

However, Figure 7.3 shows that the rate of the SEI film growth would increase with the SOC. Hence, it is necessary to impose an upper limit on the target value for the SOC at  $T_{SS}$ , denoted as  $SOC_{max}$ . Also, it is well-known that in order to avoid deep-discharge a lower limit on the SOC should be set up, denoted as  $SOC_{min}$ .

Accordingly, the battery terminal voltage is assumed as constant. Let  $E_r$  be the rated energy storage capacity of the CB. Thus, in order to reach the battery target SOC limit of  $SOC_{max}$  at  $T_{SS}$ , the required constant charging current  $I_1$ , or correspondingly, the constant charging power  $P_{CB,1}$ , shall be applied from  $T_{SR}$  to  $T_{SS}$ , where  $P_{CB,1}$  is given as

$$P_{CB,1} = (SOC_{max} - SOC(T_{SR})) \times E_r / (T_{SR} - T_{SS}) \quad (7.1)$$

In the subsequent discussion, this strategy is denoted as Strategy 1.

Therefore, under Strategy 1, CB is intended to charge with this target power  $P_{CB,1}$ .  $I_1$  is the minimum charging current which will guarantee  $SOC(T_{SS}) = SOC_{max}$ . In Figure 7.6,  $P_{CB,1}$  has been indicated and as expected, the constant charging power (i.e., the constant charging current  $I_1$ ) has resulted in the SOC of the CB increases at a linear manner. As this is an ideal case, it is assumed that the PV generation during summer despite interruptions like clouds, rain, etc., is adequate to maintain this minimum charging current. More practical scenario incorporating those weather interruptions will be subsequently discussed in latter sections based upon this ideal case. In this example,  $SOC_{max}$  is set as 0.8 and this SOC target value is reached at  $T_{SS}$ .

Theoretically, there are infinite number of constant current strategies which can be used to achieve the same objective. One could apply a higher constant charging current than  $I_1$  from the start of the daytime hour  $T_{SR}$  and once the SOC reaches the target value of  $SOC_{max}$ , the charging process is stopped, and the battery is placed in the rest state until  $T_{SS}$ . This alternative charging strategy, labelled as Strategy 2, is shown as  $P_{CB,2}$  in Figure 7.6. The profiles of Strategy 2 charging current is denoted as  $I_2$  in Figure 7.8 where that of Strategy 1 (i.e.,  $I_1$ ) is also shown. With Strategy 2, the SOC of the CB is reached at  $\tau$ , following which the charging process is stopped. Clearly over the interval before the charging process is stopped,  $I_2 > I_1$ .

In Section 7.2.2, it has been concluded that the rate of the SEI film growth increases with the magnitude of the charging current. However, since Strategy 2 keeps the battery cell at rest, where the side-reactions still exist, it is not directly obvious the impact to the SEI film growth using those two strategies. A detailed analysis of the two charging strategies is required in order to analyse this further.

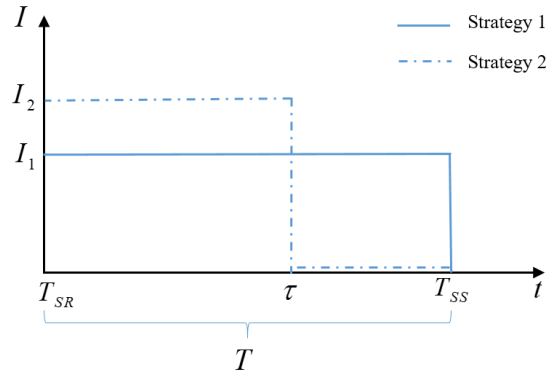


**Figure 7.8 Charging current profiles of Strategies 1 and 2**

Figure 7.3 shows that the functional relationships between the rate of the SEI film growth  $\delta$ , the SOC and the battery charging current C-rate are highly non-linear. Over the daytime hours, the charging operation is to achieve a change in the SOC, denoted as  $\Delta SOC$ , and over a time interval  $T$ . In the context of the present investigation,  $\Delta SOC = SOC_{max} - SOC(T_{SR})$  and  $T = T_{SS} - T_{SR}$ . The analysis to follow is based on the linear approximation of the non-linear functions, as shown on Figure 7.9(a) and Figure 7.9(b) whereby:

$$d\delta/dSOC|_{I1} = n_1, \quad n_1 = (\delta_3 - \delta_1) / \Delta SOC \quad (7.2 \text{ (a)})$$

$$d\delta/dSOC|_{I2} = n_2, \quad n_2 = (\delta_4 - \delta_2) / \Delta SOC \quad (7.2 \text{ (b)})$$

$$d\delta/dI = k, \quad k > 0 \quad (7.2 \text{ (c)})$$

Equations (7.2 (a)) and (7.2 (a)) govern the relationship between  $\delta$  and SOC at the constant charging current levels (C-rates)  $I_1$  and  $I_2$ , the currents under Strategy 1 and Strategy 2 alluded to in earlier section whereby  $I_1 < I_2$ .  $I_1$  is the minimum current level under Strategy 1 which will ensure that  $SOC(T_{SS})$  reaches the charging SOC target level of  $SOC_{max}$ . See Figure 7.9(a).

The initial values of  $\delta$  at the start of the charging processes are denoted as  $\delta_1$  and  $\delta_2$  respectively, and  $n_1$  and  $n_2$  denote the gradients of the  $\delta$  vs SOC linear curves at the respective currents. From Figure 7.3, it is obvious that  $n_1$  and  $n_2$  are positive. So, with the linear approximation, as the SOC increases,  $\delta$  is seen to increase linearly with the SOC but since  $I_1 < I_2$  and from the observation made in Section 7.2.2, therefore  $n_1 < n_2$ . Accordingly, when the SOC under each of the two charging processes reaches the target level of  $SOC_{max}$ ,  $\delta$  will have increased to the values of  $\delta_3$  and  $\delta_4$  respectively, as shown in Figure 7.9(a).

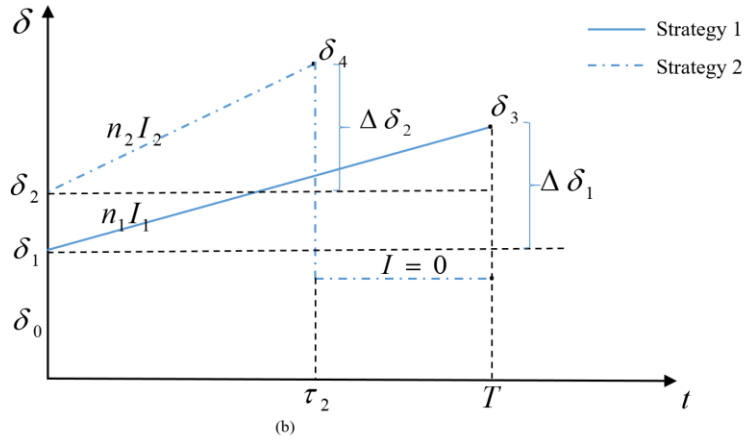
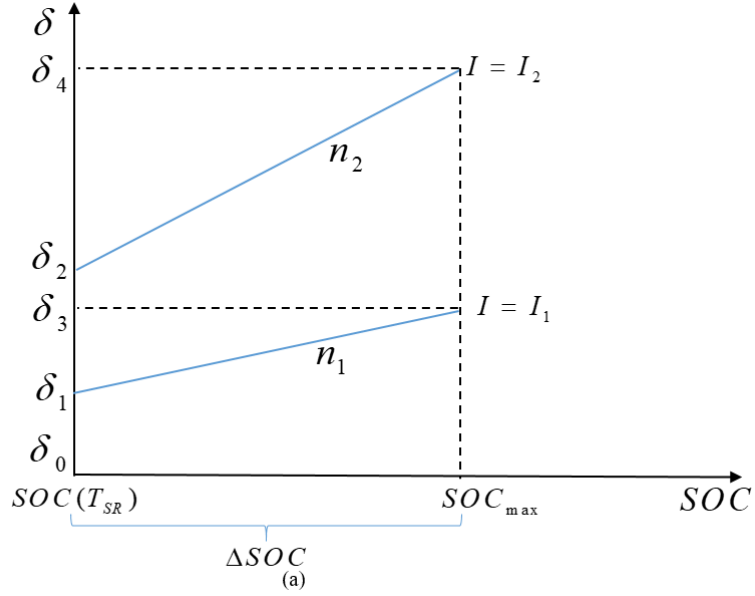


**Figure 7.9 linearized approximation of (a)  $\delta$  vs SOC curves and (b)  $\delta$  vs SOC curves at constant current**

Expressed in mathematical form, at sun-rise,  $SOC = SOC(T_{SR})$  and based on (7.2 (a)),

$$\delta_1 = \delta_0 + kI_1 \quad (7.3)$$

$$\delta_2 = \delta_0 + kI_2 \quad (7.4)$$

When the SOC reaches  $SOC_{max}$ , under Strategy 1 and based on (7.2 (a)),

$$\delta_3 = \delta_0 + kI_1 + n_1\Delta SOC \quad (7.5)$$

and under Strategy 2 and based on (7.2 (a)),

$$\delta_4 = \delta_0 + kI_2 + n_2\Delta SOC \quad (7.6)$$

In (7.3)-(7.6),  $\delta_0$  represents the rate of the SEI film growth at zero charging current.

Denote

$$\Delta\delta_1 = \delta_3 - \delta_1 = n_1\Delta SOC \quad (7.7)$$

$$\Delta\delta_2 = \delta_4 - \delta_2 = n_2\Delta\text{SOC} \quad (7.8)$$

The increase in the thickness of the SEI film, denoted as  $\zeta$  in this analysis, corresponds to the area under the  $\delta$  vs time curves shown on Figure 7.9(b). Thus, under the two constant charging current strategies,

$$\zeta_1 = \delta_1 T + \Delta\delta_1 T/2 \quad (7.9)$$

$$\zeta_2 = \delta_2 \tau_2 + \Delta\delta_2 \tau_2/2 + \delta_0(T - \tau_2) \quad (7.10)$$

The terms  $\delta_1 T$  and  $\delta_2 \tau_2 + \delta_0(T - \tau_2)$  on the RHS of (7.9) and (7.10) correspond to the increases in the thicknesses of the SEI film when  $d\delta/d\text{SOC} = 0$ , i.e., when  $\delta$  is independent of the state of the SOC. It can be readily shown that  $\delta_1 T = \delta_2 \tau_2 + \delta_0(T - \tau_2)$ . Taking the difference between  $\zeta_2$  and  $\zeta_1$ ,

$$\zeta_2 - \zeta_1 = \Delta\delta_2 \tau_2/2 - \Delta\delta_1 T/2 \quad (7.11)$$

Substituting (7.7), (7.8) into (7.11) and noting that  $\Delta\text{SOC} = I_1 T = I_2 \tau_2$ , one can show that

$$\zeta_2 - \zeta_1 = (\Delta\text{SOC})^2 [n_2/I_2 - n_1/I_1] / 2 \quad (7.12)$$

Hence, for  $\zeta_2 > \zeta_1$ , the condition is  $n_2/I_2 > n_1/I_1$  or

$$n_2/n_1 > I_2/I_1 \quad (7.13)$$

Equation (7.13) indicates that the increase in the thickness of the SEI film will be larger under Strategy 2 than that under Strategy 1 if the gradient of the  $\delta$  vs SOC curve increases at a higher rate than the corresponding increase of the charging current level. Since  $I_1$  corresponds to the minimum constant charging current strategy,  $n_1 < n_2$  will be satisfied which means that according to (7.13)  $\zeta_2 > \zeta_1$  is always satisfied. Therefore, it can be concluded that the minimum constant charging current strategy will lead to the minimum amount of the SEI film growth. Numerical examples shall be included in Section 7.6 to validate this conclusion. The above analysis has provided a firm theoretical base on which one can develop the appropriate charging strategy wherein the degradation of CB due to the SEI film growth can be minimized. This is focused on the next section.

## 7.4 Development of an Adaptive Intra-day Control Strategy for CB

There is now sufficient information needed for the development of an adaptive intra-day control strategy for the CB during the daytime, night-time and the SOC restoration periods. Grid constraints are ignored first to facilitate the development.

## 7.4.1 Adaptive battery SOC control ignoring – no grid constraints

### a. Daytime

As explained in Section 7.3.1,  $P_{LT}(t)$  can be positive or negative during the daytime hours. As a remedy to the duck power phenomena, the power export to the grid from the microgrid in the daytime hours should be reduced as much as possible. In another words, the energy contents  $\Delta E_+$  in the positive portion of  $P_{LT}(t)$  should be used to charge the CB to the maximum acceptable level. The stored energy in the CB can in turn be used to meet the night-time electricity need, especially the evening-peak demand of the microgrid. In this way, the objective of the intra-day peak-logging is realized. As has been shown in Section 7.3.2, the charging of the CB should be done at the minimum current level in order to foster the lowest rate of SEI film growth. The corresponding minimum charging power level is governed by (7.1) which will guarantee the SOC of the CB will reach the pre-specified value of  $SOC_{max}$  at  $T_{SS}$ .

The negative  $P_{LT}(t)$  during daytime on the other hand encourages the import from the grid and thereby effectively reduces the duck curve problem. Therefore, in ideal conditions, no CB discharging is expected during daytime. At sunrise,  $SOC(T_{SR}) = SOC_r$  where  $SOC_r$  is determined from the dynamic referencing scheme described in CHAPTER 6. As the CB is being charged for  $T_{SR}$  to  $T_{SS}$ , the SOC of the CB increases. In line with the aim to maximize the energy-independency of the microgrid alluded to earlier,  $SOC(T_{SS})$  is set to be the maximum allowable SOC level ( $SOC_{max}$ ) as the charging does not occur after  $T_{SS}$ . Hence, to reach the targeted operating state of  $SOC_{max}$  at  $T_{SS}$ , and since the SOC can be readily measured at regular time intervals, one can generalize (7.1) and derive the following reference charging power ( $P_{CB,ref}(t)$ ) at any given time  $t$  as

$$P_{CB,ref}(t) = \frac{SOC_{max} - SOC(t)}{T_{ss} - t} \times E_r, P_{LT}(t) > 0, T_{SR} < t < T_{SS} \quad (7.14(a))$$

$$P_{CB,ref}(t) = 0, P_{LT}(t) \leq 0, T_{SR} < t < T_{SS} \quad (7.14(b))$$

In (7.14(a)),  $E_r$  is the rated energy storage capacity of the CB. Accordingly,  $P_{CB,ref}(t)$  can be regularly updated based on (7.14(a)) and the CB is to be charged with the reference value of  $P_{CB,ref}(t)$ . While the CB is set to absorb this target power, the grid should maintain the balance of power given by;

$$P_G(t) = P_{LT}(t) - P_{CB}(t), \text{ when } P_{LT}(t) > P_{CB,ref}(t) \quad (7.15(a))$$

However, there can be instances that  $P_{LT}(t)$  is less than  $P_{CB,ref}(t)$ . When this occurs, all of  $P_{LT}(t)$  shall be directed to the CB:

$$P_{CB}(t) = P_{LT}(t), \quad \text{when } P_{LT}(t) < P_{CB,ref}(t) \quad (7.15(b))$$

In the latter case, the CB shall be charged at a level lower than the reference power  $P_{CB,ref}(t)$ . At this charging power level, the SOC will be below  $SOC_{max}$  at  $T_{SS}$ . So, in order to compensate for the shortfall, a new  $P_{CB,ref}(t)$  shall be generated at the regular interval and is updated. In this way,  $P_{CB,ref}(t)$  is adaptive to the changing  $P_{LT}(t)$ .

At the end of the charging period at  $t = T_{SS}$ ,  $P_{CB}(t)$  is to ramp down at a rate complying with the power ramp rate constraint of the grid link. The power ramp rate constraints are discussed in Section 7.4.2.

### **b. Night-time**

According to the observation reported in Section 7.2.2, during discharging, it is advisable to use the maximum discharging current during discharging to limit the SEI growth. Therefore, CB will be discharged following  $P_{LT}(t)$  during nighttime. As the night peak is most likely to occur early in the evening, this event should be covered by the CB.

Therefore, after  $T_{SS}$  and before the start time of the SOC restoration period  $T_I$ , the CB shall discharge at the level of  $P_{LT}(t)$  viz.

$$P_{CB}(t) = P_{LT}(t), \quad T_{SS} < t < T_I \text{ and } SOC > SOC_{min} \quad (7.16(a))$$

$$P_G(t) = 0 \quad (7.16 (b))$$

The discharging strategy (7.16(a)) is valid when the SOC of the CB is above the pre-specified minimum limit  $SOC_{min}$ . In the event the SOC has reached  $SOC_{min}$  before  $T_I$ , the CB is to stop discharging. The CB is switched to the SOC restoration period.

As this discharging operation happens with less than 0.5C discharging current rates, it is expected that the effects of the other discharging mechanism due to higher C-rates, do not affect to the current study. Moreover, the proposed strategy assumes the Time of the Day Tariff (TOD) allowing CB to discharge during the evening peak in which the unit cost is maximum and then restoring the CB SOC during the off-peak time where unit cost is minimum. In this way, the proposed strategy is also deemed to be economical for the microgrid users.

### **c. SOC restoration Period**

The CB operation during this time period is the same as that we proposed in CHAPTER 6. At the end of  $T_2$ , grid power would be able to restore the SOC of the CB to the reference SOC specified by  $SOC_r$ , which is generated by the dynamic reference scheme described in that chapter.

## 7.4.2 Adaptive intra-day CB control strategy considering grid constraints

The aforementioned adaptive battery control strategy is to control the CB power flow for very ideal conditions where the grid constraints are not yet considered. However, in a more realistic operation of the CB, grid constraints must be taken into account. To simplify the understanding, first, these constraints are separately studied and later combined in this section with the adaptive SOC control described in Section 7.4.1 to form the integrated CB control strategy.

### a. Inclusion of grid link power constraint

If the grid export power constraint is  $P_G^{max,p}$ , when  $P_G(t) > P_G^{max,p}$  during the above buffering, then it is required to set  $P_G(t) = P_G^{max,p}$ . One such scenario is illustrated in Figure 7.10. During the time  $6 < t < 8$  it is clear that the  $P_{CB}(t)$  follows the target  $P_{CB,ref}(t)$  which varies fairly constantly as  $P_G(t) < P_G^{max,p}$ . However, at the time around  $t=9.4$ hrs as shown in the Figure 7.10,  $P_{LT}(t) - P_{CB,ref}(t) > P_G^{max,p}$  where it is required to limit  $P_G(t)$  such that  $P_G(t) = P_G^{max,p}$ . By setting  $P_G(t)$  to this constraint, the  $P_{CB}(t)$  is forced to buffer the  $P_{LT}(t) - P_G^{max,p}$ .

$$\begin{aligned} P_G(t) &= P_G^{max,p} && \text{when } P_G(t) > P_G^{max,p} \\ P_{CB}(t) &= P_{LT}(t) - P_G^{max,p} \end{aligned} \quad (7.17)$$

As shown in the zoomed plot, the resulting  $P_{CB}(t)$  would be higher than the target power  $P_{CB,ref}(t)$  when this happens. Therefore, the next instance target power  $P_{CB,ref}(t+1)$  will be slightly lower than the  $P_{CB,ref}(t)$ . As a result of this,  $P_{CB,ref}(t)$  steadily decreases as shown on the zoomed plot from 0.129 at 9hrs to 0.116 at 11hrs. As can be seen from the SOC curve of the first graph, it also loses its linearity when these instances occur. Since this is a sunny day, during most of the instances after time  $t=9.4$ hrs, it often violates the  $P_G^{max,p}$  therefore the  $P_{CB}(t) > P_{CB,ref}(t)$ . So that  $P_{CB,ref}(t)$  gets lower as time progresses. Due to this additional energy flows to the CB, SOC gets close to the  $SOC_{max}$  around  $t=17$  hrs. Form this example, it is evident that the reference power is responsive to the magnitude constraint of the grid export. Therefore, it can be concluded that the proposed method is adaptive enough to abided to such grid magnitude constraint.

During the night-time,  $T_{SS} < t < T_I$ , according to (7.16(a))  $P_G(t) = 0$  and so, grid link power constraint is not applicable. Finally, during the SOC restoration period  $T_I < t < T_{SR}$ , by similar reasoning, one can readily show that (7.17) is applicable although there is the possibility of grid link importing power from the microgrid during this period. Accordingly, an added control condition is



$$P_G(t) = P_G^{max,n} \quad \text{when } P_G(t) < P_G^{max,n} \quad (7.18)$$

where  $P_G^{max,n}$  denotes the grid link import power limit.

This example serves to show that the adaptive intra-day CB control strategy is responsive to the grid link power constraint. More examples are included in Section 7.5 to further illustrate other pertinent features of the proposed strategy.

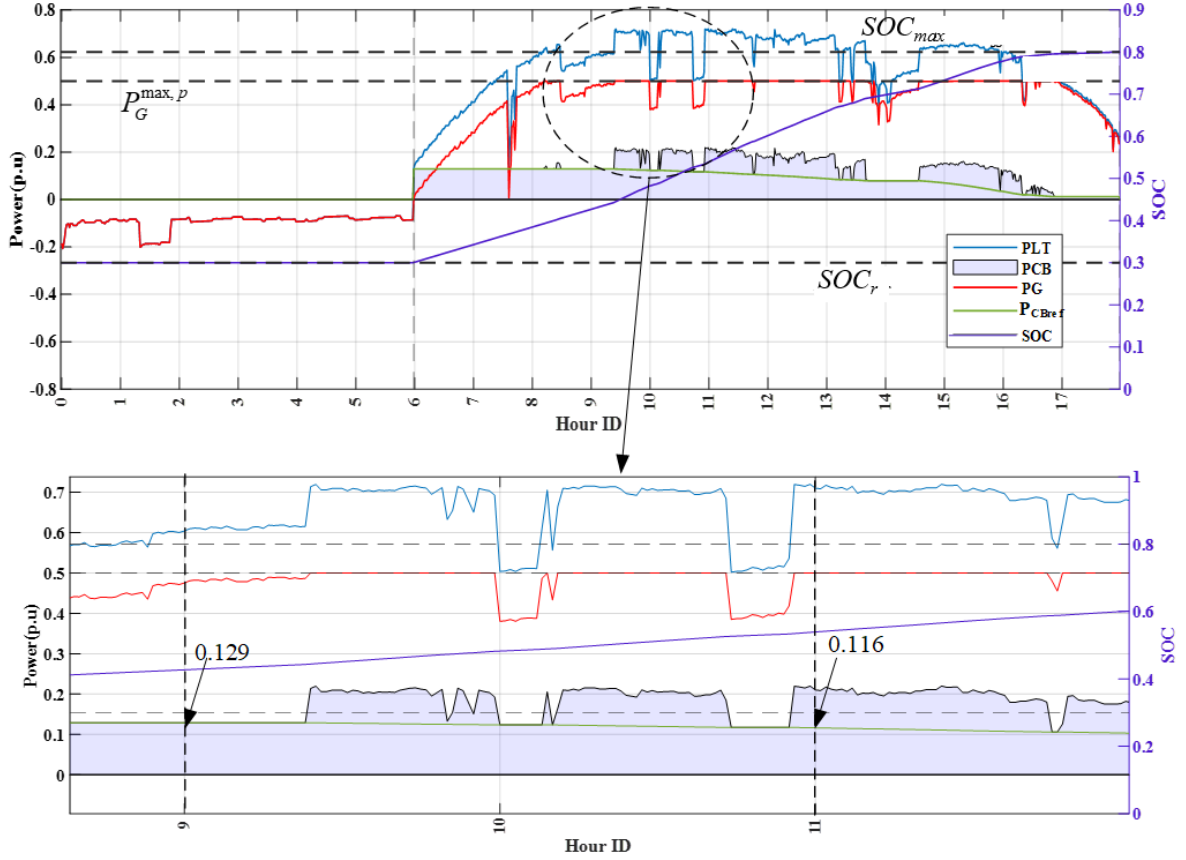


**Figure 7.10**  $P_{LT}(t)$ ,  $P_{CB,ref}(t)$ ,  $P_{CB}(t)$ ,  $P_G(t)$  and  $SOC(t)$  of the CB during daytime and a zoomed-in plot: proposed charging strategy is applied under the presence of grid link power magnitude constraint

### b. Inclusion of grid link power ramp rate constraint

The adaptive intra-day control strategy described above for the CB operation is further studied in the scenario whereby the grid link ramp rate constraint is considered. To facilitate the discussion, Figure 7.11 shows a sample plot of  $P_{LT}(t)$  and the applicable power ramp rate limit  $\dot{P}_G^{max}, P_{CB,ref}(t)$ . It is clear that from point a to b,  $0 < P_{LT}(t) < P_{CB,ref}(t)$  and since the CB has higher priority over grid link over the charging period, since the CB has higher

priority over grid, all the  $P_{LT}(t)$  is diverted to charge the CB. This operation is summarized as Scenario 1 in Table 7.1.

For the interval “b” to “c”, as  $P_{LT}(t) > P_{CB,ref}(t)$ , the CB is charged at the reference power level and so,  $P_{CB}(t) = P_{CB,ref}(t)$ .  $P_G(t)$  is obtained via (7.15(a)). Also, it is seen that the power ramp rate  $dP_G(t)/dt < \dot{P}_G^{max}$ . This is Scenario 2 in Table 7.1. For the interval “c” to “d”, if  $P_{CB}(t)$  is set to track  $P_{CB,ref}(t)$ , then the anticipated power flows in the grid link  $P_B(t)$ , i.e.,  $P_{LT}(t) = P_{CB}(t)$ , is seen to exhibit a ramp rate higher than  $\dot{P}_G^{max}$ . This is Scenario 3 of Table 7.1:  $|d(P_{LT} - P_{CB})/dt| > \dot{P}_G^{max}$ . Therefore, the power flows  $P_G(t)$  is modified in the manner as shown in the 5<sup>th</sup> column of the table under this scenario whereby  $P_G(t)$  is ramp down at the maximum allowable value  $\dot{P}_G^{max}$ . As a result, that shall be a subsequent increase in  $P_{CB,ref}(t)$ . From d to e and e to f the same scenario 1 and scenario 2 will be repeated respectively. When the CB acts to maintain the  $\dot{P}_G^{max}$  constraint by lowering its charging during the time c to d, this makes its target charging power at the next instance to rise up. This is visible as a slow inclination of the  $P_{CB,ref}(t)$  from time c to d. Again, from d to e, as  $P_{CB}(t)$  is unable to meet  $P_{CB,ref}(t)$  with given  $P_{LT}(t)$ , the  $P_{CB,ref}(t)$  continues to rise and then be constant during e to f.

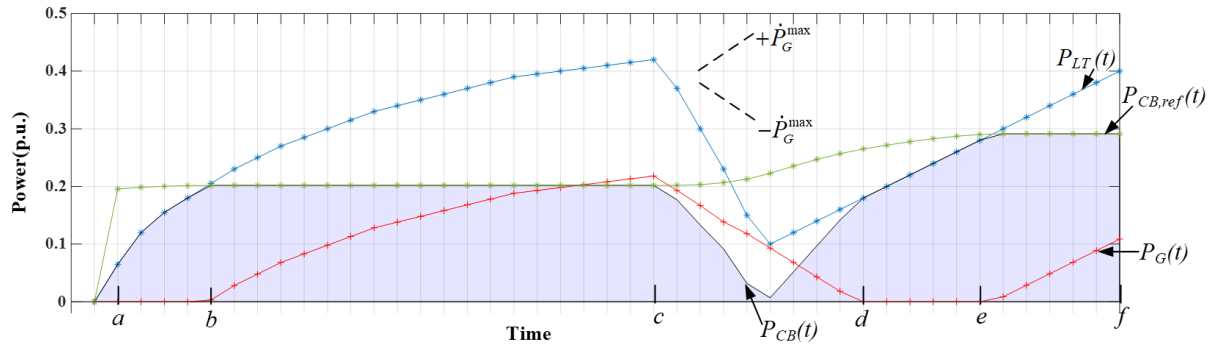


**Figure 7.11. Sample of  $P_{LT}(t)$ ,  $P_G(t)$ ,  $P_{CB}(t)$  and  $P_{CB,ref}(t)$ : the proposed adaptive intra-day control strategy is applied under grid link power ramp rate constraint**

**Table 7.1 A summary of rules incorporated in the proposed adaptive intra-day control strategy for the CB: grid link power and ramp rate constraints are complied with**

Scenario	$P_{LT}(t)$	$\left  \frac{d(P_{LT} - P_{CB})}{dt} \right $	Control strategy on $P_{CB}(t)$	Target $P_G(t)$
1	$0 \leq P_{LT}(t) \leq P_{CB,ref}(t)$	$\left  \frac{d(P_{LT} - P_{CB})}{dt} \right  < \dot{P}_G^{max}$	$P_{CB}(t) = P_{LT}(t)$	$P_G(t) = 0$
2	$P_{LT}(t) > P_{CB,ref}(t)$	$\left  \frac{d(P_{LT} - P_{CB})}{dt} \right  < \dot{P}_G^{max}$	$P_{CB}(t) = P_{CB,ref}(t)$	$P_G(t) = P_{LT}(t) - P_{CB,ref}(t)$

3	$P_{LT}(t) > P_{CB,ref}(t)$	$\left  \frac{d(P_{LT} - P_{CB})}{dt} \right  > \dot{P}_G^{\max}$	<p>3a) If <math>\frac{dP_{L,T}}{dt} &gt; 0</math> then  <math>P_{CB}(t) = P_{LT}(t) - P_G(t - \Delta t) - \dot{P}_G^{\max} \times \Delta t</math></p> <p>3b) If <math>\frac{dP_{L,T}}{dt} &lt; 0</math> then  <math>P_{CB}(t) = P_{LT}(t) - P_G(t - \Delta t) + \dot{P}_G^{\max} \times \Delta t</math></p>	<p>3a)  <math>P_G(t) = P_G(t - \Delta t) + \dot{P}_G^{\max} \times \Delta t</math></p> <p>3b)  <math>P_G(t) = P_G(t - \Delta t) - \dot{P}_G^{\max} \times \Delta t</math></p>
4	$P_{LT}(t) < P_{CB,ref}(t)$	$\left  \frac{d(P_{LT} - P_{CB})}{dt} \right  > \dot{P}_G^{\max}$	<p>4a) If <math>\frac{dP_{L,T}}{dt} &gt; 0</math> then  <math>P_{CB}(t) = P_{LT}(t) - P_G(t - \Delta t) - \dot{P}_G^{\max} \times \Delta t</math></p> <p>4b) If <math>\frac{dP_{L,T}}{dt} &lt; 0</math> then  <math>P_{CB}(t) = P_{LT}(t) - P_G(t - \Delta t) + \dot{P}_G^{\max} \times \Delta t</math></p>	<p>4a)  <math>P_G(t) = P_G(t - \Delta t) + \dot{P}_G^{\max} \times \Delta t</math></p> <p>4b)  <math>P_G(t) = P_G(t - \Delta t) - \dot{P}_G^{\max} \times \Delta t</math></p>

## 7.5 Illustrative Examples and Discussion

In this section, the results obtained from an extensive series of simulation studies are presented. The aim is to use the results to illustrate the application of the developed adaptive intra-day control strategy for the CB.

### 7.5.1 SEI film growth during CB charging operations: no grid constraints applied

Based on the preliminary study of the SEI growth rate, the adaptive charging strategy was introduced in the previous section. The proposed approach aims to charge the battery with the lowest possible charging current to minimize the SEI growth. However, a counter-argument may arise as the time required to complete the charging operation is higher in the lower charging current approach. Hence, it is not straightforward to say that lower charging current to complete constant SOC changing results in lower SEI growth. Therefore, in this sub-section, the attempt is to compare the charging operation with different magnitudes of current profiles to further understand its effect on the SEI growth.

For these validation studies,  $P_{LT}(t)$  shown on Figure 7.6 was used and the profiles of the charging currents  $I_{CB1}$ ,  $I_{CB2}$  and  $I_{CB3}$  are considered as shown on Figure 7.12(a). No grid constraints are considered in these studies. The  $I_{CB1}$  in Figure 7.12(a) refers to the strategy of applying the minimum constant charging current starting at  $T_{SR}$ .  $I_{CB1}$  corresponds to the case of charging the CB to track the constant reference charging power level  $P_{CB,ref}(t)$  given by (7.1) from  $T_{SR}$  to  $T_{SS}$ , a duration of 12 hours. This charging strategy will allow the SOC of the CB to increase from  $SOC_{SR} = 0.3$  to the target maximum SOC level of  $SOC_{max} = 0.8$  at  $T_{SS}$ . Thus,  $I_{CB1}$  is pertaining to C-rate of

C/24 (i.e. (0.8-0.3) C/12). Assuming every battery cell of 1.8Ah capacity is equivalent, the charging current of the battery cell is 0.075A. The constant charging current of the  $I_{CB2}$  profile is twice that of  $I_{CB1}$  and the constant charging current of the  $I_{CB3}$  profile is three times that of  $I_{CB1}$ . The comparison of these different charging currents yields the results of SOC and SEI growth shown in and Figure 7.12(b) and Figure 7.12(c) respectively.

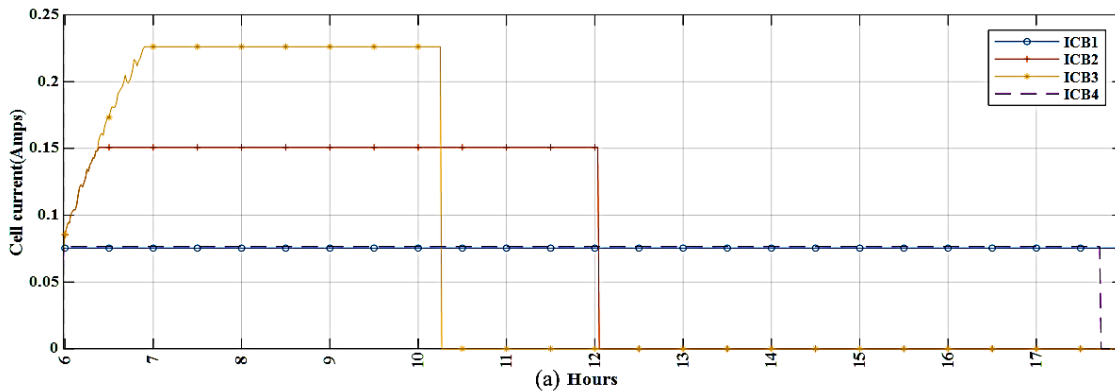
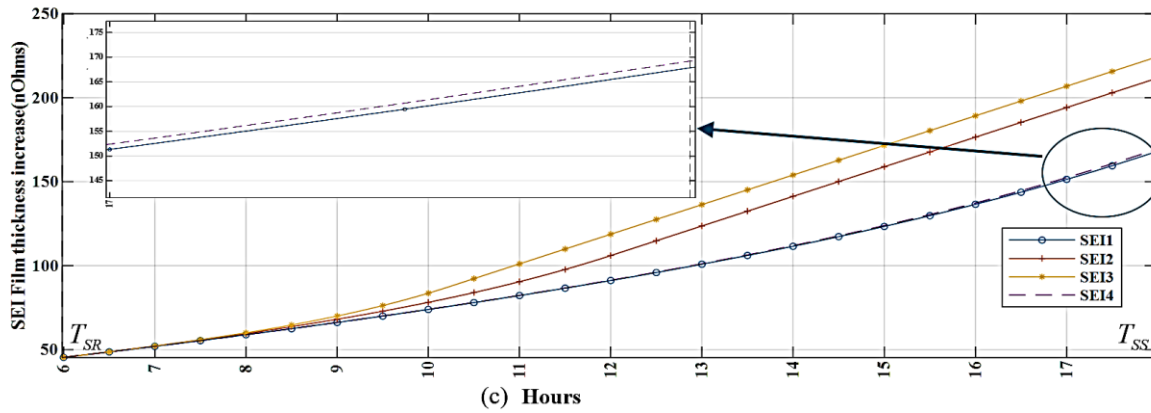
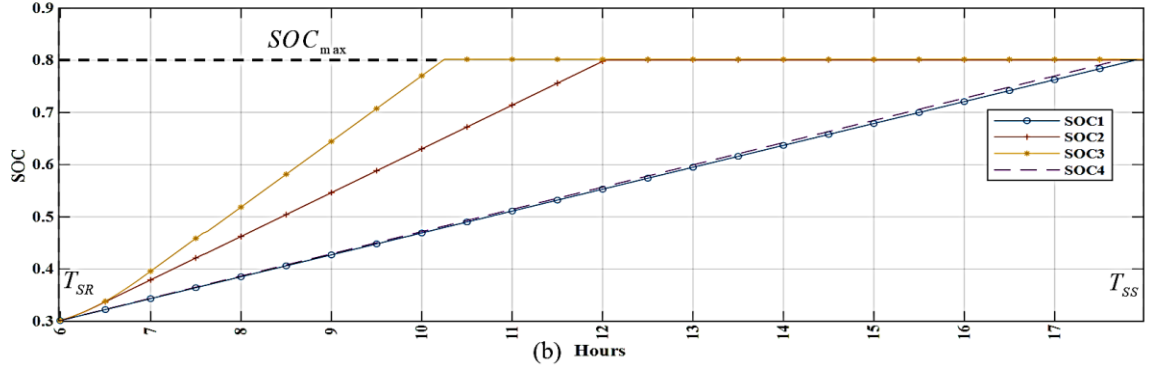


**Figure 7.12 a) Profiles of the assumed charging currents (b) SOC of the CB, (c) SEI film resistance of the CB**

According to Figure 7.12(b), the SOC profile associated with charging current  $I_{CB1}$  reaches the target SOC at  $T_{SS}$ , which in this case is 1800 hrs. With twice the current, charging current  $I_{CB2}$

can reach the target SOC in around 1200 hours. For the  $I_{CB3}$  charging profile, the target SOC is achieved around 1000 hrs. The area under the three curves in Figure 7.12(b) is the same because the energy required to reach  $SOC_{max}$  from the  $SOC_{SR}$  is the same. However, the triple current of  $I_{CB1}$  i.e.  $I_{CB3}$ , will not result in exactly one-third of charging time due to the ramp of the current at  $T_{SS}$ . This is because in the initial hour or so of the charging process,  $P_{LT}(t)$  is too low to provide the full charging current  $I_{CB3}$  of  $C/8$ . So,  $I_{CB3}$  is shown to ramp up before it reaches the final constant level of  $C/8$  at around 0700 hours. Hence  $SOC_{max}$  is only reached at about 1027 hours in this case.

Another notable observation that can be derived from profiles pertains to the gradients seen in Figure 7.12(c), which represents the SEI growth rate. Upon reaching 08.30hrs, from the Figure 7.12(c), both SEI 2 and SEI 3 curves display an increasing positive gradient, with SEI 3 showing an even steeper gradient. This is in line with the observation made in surface plot on Figure 7.3, which reveals that the higher C-rate and higher SOC levels lead to high SEI growth rate. Hence, SEI 3 curve corresponding to a comparatively higher C-rate and higher SOC leads to steeper gradient in SEI thickness growth. However, after reaching target SOC around 10.15am, the  $I_{CB3}$  becomes zero as charging ceases. Due to zero current and constant SOC, SEI growth rate then becomes constant. Therefore, SEI 3 curve in Figure 7.12(c) displays as a straight line after 10.15am. Similarly,  $I_{CB2}$  reaches the target SOC at 1200 hours. Thus, after 1200hrs both profile 2 and 3 have same zero current and same target SOC which lead to same SEI growth rate. This is clearly noticeable in Figure 7.12(c) after 1200 hrs, where both profiles SEI 2 and SEI 3 exhibit same gradient parallel lines.

Meanwhile, SEI 1 shown in Figure 7.12(c) continues to charge the CB at a lower charging current while slowly increasing SOC, resulting in a slower SEI growth rate. The corresponding SEI thickness given by SEI 1 in Figure 7.12(c) deviates significantly from the other two SEI thickness curves after 1200 hrs. This is due to the lower gradient of SEI 1 curve, which is influenced by the lower SOC levels leading to reduced SEI growth rate. While  $SOC_I$  reaches the target SOC at set time  $T_{ss}$ , it results in the lowest SEI growth compared to other two profiles.

However, due to the non-linearity of the relationship between the SEI growth rate and SOC vs I according to the surface plot on Figure 7.3, one may speculate a different scenario to the above. Due to the higher charging current the charging time taken to raise the SOC between constant SOC range would decrease. The decrease in the time taken for charging can develop lower SEI growth which is detrimental effect to the above effect. Therefore, an additional current profile, with slightly higher current  $I_{CB1}$ , denoted by  $I_{CB4}$  as shown in Figure 7.12(a) is also considered. SEI growth results of SEI 4 on the zoomed plot of Figure 7.12(c) ensures that the slightly higher current result in slightly

higher SEI thickness compared to that of  $I_{CB1}$ . On the contrary, it should be noted that even lower current than  $I_{CB1}$  would result in even less SEI growth. However, this would not achieve the desired SOC at  $T_{SS}$ . Thus, it can be concluded that the proposed approach follows the minimal charging current required to charge the battery to reach SOC to target SOC at sunset. Therefore, this is the optimal charging current to yield minimal SEI growth in this ideal situation with no grid constraints applied. Thus, this example has demonstrated that the minimum constant charging current required to charge the CB to reach the targeted SOC level at sunset will yield the lowest SEI film growth.

### **7.5.2 SEI film growth during discharge operation in the night-time: no grid constraints applied**

Again, to confirm the 2<sup>nd</sup> outcome of Section 7.2.2 related to discharging of the CB, two different discharging profiles during the nighttime shall be compared in terms of their SEI growth rates. To facilitate this comparison, a sample  $P_{LT}(t)$  curve during nighttime obtained from Figure 7.6 is used as shown in Figure 7.13(a). The discharging profile shown in Figure 7.13(b) with  $I_{CB5}$  is related to the 0.075 A discharging C-rate which is similar to the charging C-rate of  $I_{CB1}$ . In comparison, the  $I_{CB6}$  is pertaining to the proposed discharging strategy whereas  $P_{CB}(t) = P_{LT}(t)$  during nighttime.

According to Figure 7.13(c), the two different discharging currents resulting in two SOC profiles will lead to different SOC at the midnight. As explained in Section 7.2.2 higher discharging current and lower SOC levels lead to lower SEI growth. Similarly,  $I_{CB6}$  and SOC<sub>6</sub> represent the higher discharging current and lower SOC levels, which contribute to lower SEI growth. Thus, the SEI thickness of the discharging current  $I_{CB6}$  is less than that of the  $I_{CB5}$ , as shown in Figure 7.13(d).

Figure 7.13(d) shows the increase in the SEI film growth over the evening period under the two discharging cases. A comparison of the two SEI film growth profiles confirms that the observation made in Section 7.2.2: that higher discharge current ( $I_{CB6}$ ) has indeed resulted in the lower SEI film growth. In fact, in this example,  $I_{CB6}$  has resulted in some 15% lower SEI growth than the case with  $I_{CB5}$  over a 6-hour period.

This example shows that if there is sufficient stored energy in the CB, it will be desirable to allow the CB to discharge and meet all the evening peak demand, as a means of peak-lopping strategy. The strategy has the added advantage in that it leads to lower level of the SEI film growth, in comparison to that resulted under a lower discharge current level.

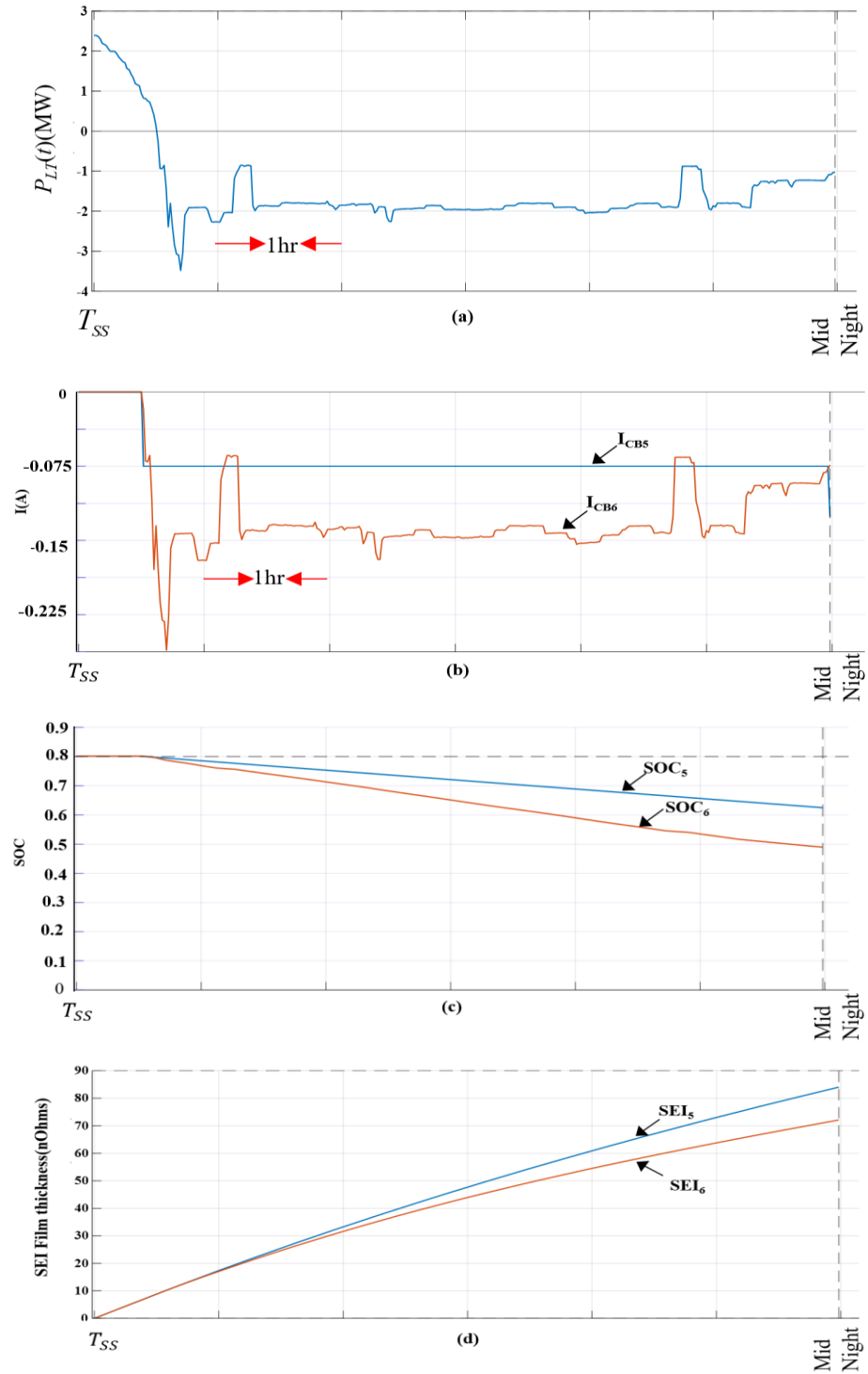


**Figure 7.13 Night-time CB discharge operation: profiles of the (a) assumed  $P_{LT}(t)$ , (b) assumed discharge currents  $I_{CB5}$  and  $I_{CB6}$ , (c) the corresponding SOC and (d) SEI film thicknesses**

### 7.5.3 Illustrative examples on the proposed adaptive intra-day control strategies

In this sub section, the main aim is to demonstrate the effectiveness of the proposed method in different seasons including the extreme weather events. The proposed strategy was implemented on MATLAB R2022a platform, and the simulation study was carried out based on the parametric settings shown in Table 7.2. The reference value  $SOC_r$  for the SOC in the respective season is that determined from the dynamic referencing scheme described in CHAPTER 6, and  $SOC_r$  is the SOC value seen at  $T_{SR}$ . The target value of the SOC at  $T_{SS}$ , i.e.,  $SOC_{max}$ , is assumed to be 0.8 in all the cases discussed in this section, except for one case. Accordingly, the rules developed in Sections a are applied in the simulation studies.

**Table 7.2. Parametric values used for the simulation of CB operations for the different seasons**

	Summer	Autumn	Winter	Spring
$SOC_{max}=SOC_{SS}$	(1) 0.8 (2) 0.5	0.8	0.8	0.8
$SOC_{min}$	0.24	0.24	0.24	0.24
$SOC_r = SOC_{SR}$	0.3	0.47	0.55	0.4
$P_G^{max,p}$	0.5	0.3	0.1	0.45
$P_G^{max,n}$	-0.2	-0.4	-0.5	-0.4
$\dot{P}_G$	1MW/min			

#### a. Summer

Figure 7.14 depicts the simulation result for a two-day time period for the summer season where the  $SOC_r$  is set to 0.3 and  $SOC_{max}$  is set to 0.8.  $T_{SR}$  and  $T_{SS}$  estimation were set to 0600 and 1800 for this summer case respectively. Even though these estimated times are not so accurate in this case, they have been in place to showcase the worst case of not having accurate  $T_{SR}$  and  $T_{SS}$  estimations. Also, the grid link power flows constraint is activated more often in Day #1 than in Day #2, particularly after about 0900 hours. Due to the  $P_G^{max,p}$  constraint, the additional energy flows into the battery during the day time of day #1. As a result, after 0900 hours in Day #1, the proposed adaptive intra-day CB control scheme is seen to respond with much active downward adjustment in  $P_{CB,ref}(t)$ . This is in order to ensure the SOC reaches the target value of  $SOC_{max}$  at  $T_{SS}$ . However, in Day #2 since the daily surplus energy  $\Delta E_+$  is comparatively lower and  $P_G^{max,p}$  constraint is activated less often than in Day #1,  $P_{CB,ref}(t)$  remains almost constant at approximately 0.125p.u. The figure shows that the proposed method successfully achieves the target SOC in both days. As depicted, during day



#1 which is sunny day of these two, target SOC is achieved bit earlier compared to the day #2 as expected.

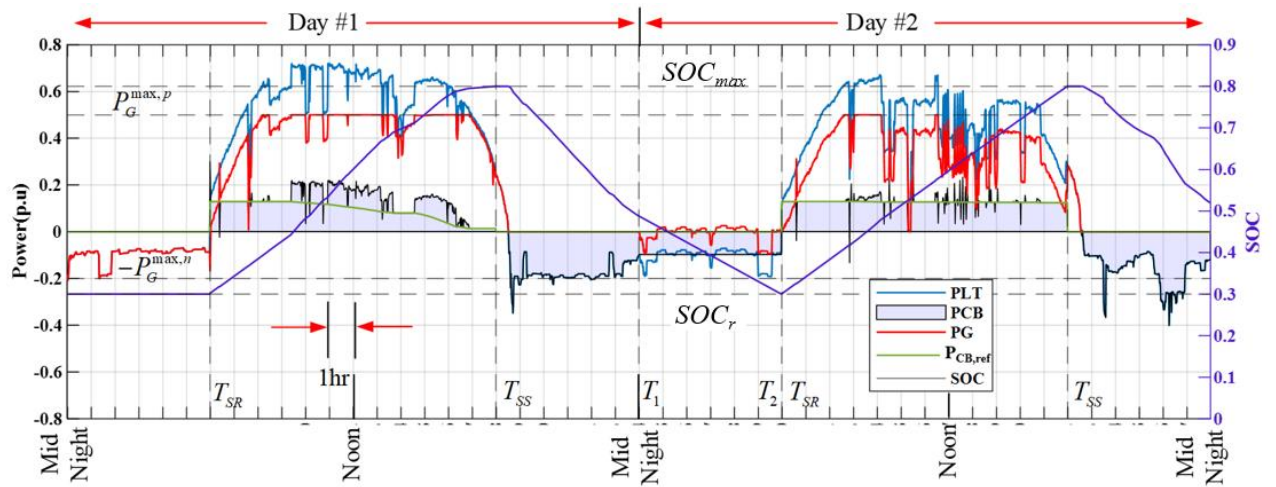


**Figure 7.14 Application of the proposed adaptive intra-day CB SOC control strategy: summer and  $SOC_{max} = 0.8$**

The discharging of the CB follows the same principle described in Section 7.5.2, i.e., the discharge power of the CB is set to track  $P_{LT}(t)$  in the nighttime until  $T_1$ , after which the SOC restoration period commences. The restoration strategy is that described in CHAPTER 6. It can be readily seen from Figure 7.14 that with the proposed CB discharge and SOC restoration strategy, the SOC is maintained within the allowable SOC range, while none of the grid power flows and ramp rate constraints is violated. In summary, one can observe from Figure 7.14 that the proposed adaptive intra-day CB control strategy is able to accommodate the grid constraints most satisfactorily for the summer days. Meanwhile successful peak shaving is also achieved, and the CB is able to operate within the stipulated SOC range, even under considerable wide variations in the daily  $P_{LT}(t)$ .

The Figure 7.15 repeats the same simulation in which the target SOC setting  $SOC_{max}$  is arbitrarily set as 0.5. However, results show that this target SOC is achieved in the day #1 even before the noon. This scenario may then force to violate the  $P_G^{max,p}$  constraint as the battery charging has to be stopped after reaching target SOC. As an alternative this scenario, if charging continues, the battery will have a higher SOC than the target SOC. This is, of course, not a desirable outcome. The violation of the grid code is somewhat less severe on Day #2. Nevertheless, this example clearly demonstrates the unsatisfactory state of operation of the power system is due to the fact that  $SOC_{max}$  has been set at too low a value for the summer days.

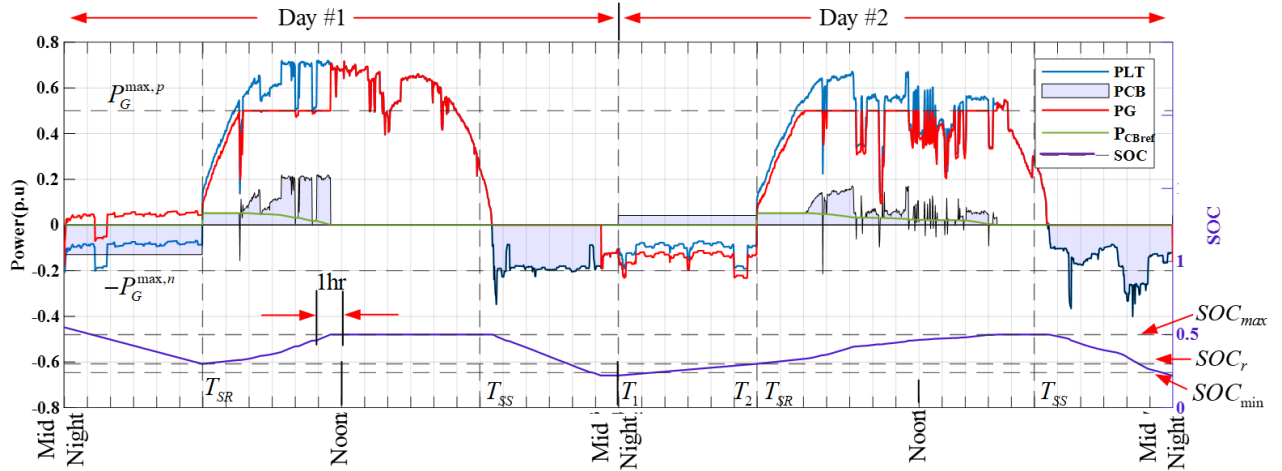


**Figure 7.15 Application of the proposed adaptive intra-day CB control strategy: summer and  $SOC_{max} = 0.5$**

### b. Autumn

During the autumn season  $SOC_{max}$  is set to 0.8. As shown in Figure 7.16, at the beginning of the daytime, SOC is set to the 0.47 which is the daily SOC restoration for the particular day in autumn.  $T_{SR}$  and  $T_{SS}$  are considered as 0700 and 1700 during these days of autumn for this example. Adaptive  $P_{CB,ref}(t)$  is rapidly increasing as it approaches  $T_{SS}$ . At  $T_{SS}$ , it can only reach to a SOC=0.62 as the day #1 is one of the worst days of the autumn season in terms of insolation. This stored energy is adequate to serve the night peak of the day #1 until 2300hrs as CB reaches the set lower limit  $SOC_{min}$  of 0.24. From this situation onwards, grid will import the power to serve  $P_{LT}(t)$  until the restoration starts. Grid restoration happens from  $T_1$  to  $T_2$  to raise SOC level to the 0.47 value.

Similarly, Day #2 allows the SOC to reach a higher value of 0.78 at  $T_{SS}$ , and before the charging process has to stop because  $P_{LT}(t)$  becomes negative. Even with the SOC level below the target level of 0.8, there is sufficient stored energy in the CB for the CB to support the night-time demand until mid-night before the grid link needs to come in to assist the SOC restoration process, and the SOC is still above the 0.24 minimum SOC limit setting.

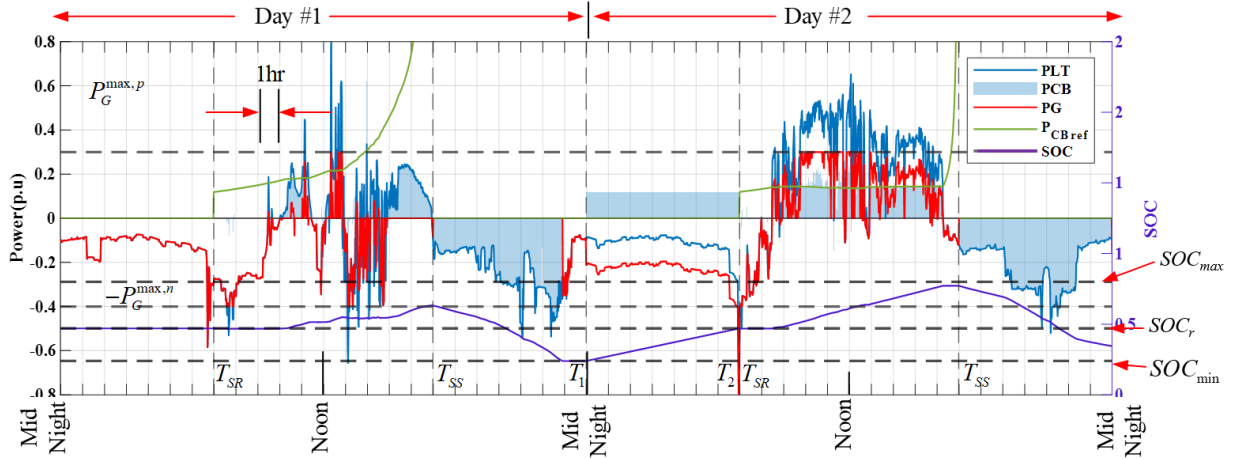


**Figure 7.16 Application of the proposed adaptive CB SOC control strategy: autumn and  $SOC_{max} = 0.8$**

### c. Winter

Winter presents an even more challenging situation as shown in Figure 7.17 to test the proposed method. At the beginning of the daytime SOC is set to the 0.55 which is the daily SOC restoration for winter season.  $SOC_{max}$  is set to 0.8 as in the other seasons.  $T_{SR}$  and  $T_{SS}$  are considered as 0700 and 1700 during these days of winter for this example. Adaptive  $P_{CB,ref}(t)$  is rapidly increasing as time gets closer to the  $T_{SS}$ . At  $T_{SS}$ , SOC can only reach 0.58 as the day #1 is one of the worst insolation days of the winter season. This stored energy is only adequate to serve the night peak of the day #1 until around 2030hrs. At this time, battery SOC reaches close to its minimum SOC level. Then, the grid will import the power to handle until restoration starts. As from the previous analysis of  $SOC_{ss}$ , it is suggested to start the grid restoration during the winter season much earlier to midnight. In this simulation, start of the restoration happens at 2200hrs. Grid restoration happens from  $T_{SS}$  to  $T_{SS}$  to raise SOC level to the 0.55 value.

Day #2 is another worst day of the winter which has an extremely high night time power demand. During the daytime SOC reaches up to 0.62 SOC level. Then battery discharges by delivering peak load until 8.30pm, at which time  $SOC_{min}$  is reached. Then CB stops its discharging allowing grid to take initiative in supplying the load power. However, the power demand exceeds the grid import limit which forces CB to involve in discharging until it reaches the  $SOC_{min}$ . In fact, few instances occur that SOC falls less than the  $SOC_{min}$ , which has happened due to extreme conditions of higher night loads and lower daytime surplus power. Therefore, it demonstrates that  $SOC_{min}$  needs to be set with a certain tolerance margin to allow for extreme weather occurrences.

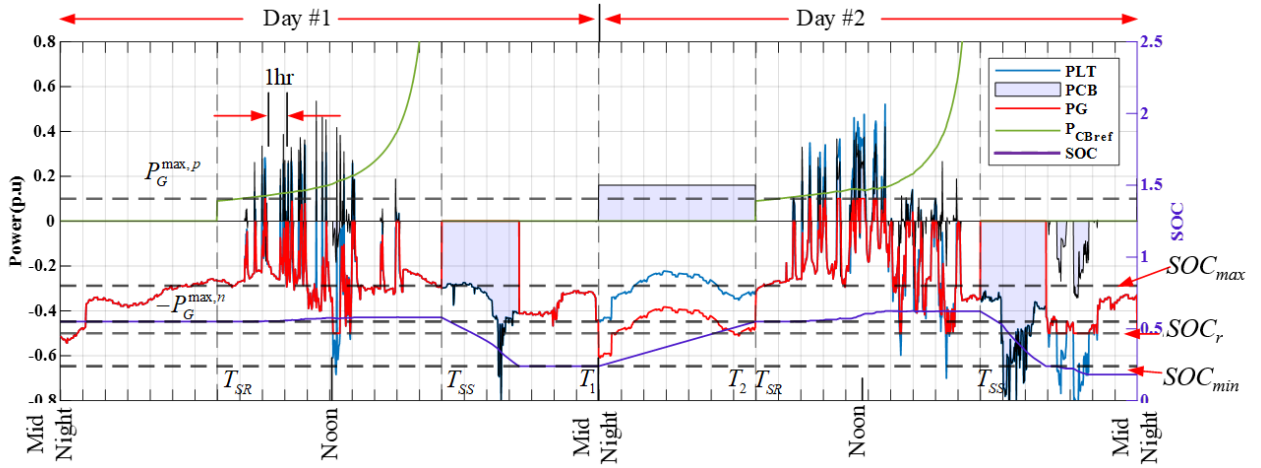


**Figure 7.17 Application of the proposed adaptive CB SOC control strategy: winter and  $SOC_{max} = 0.8$**

#### d. Spring

For the completeness, similar study has been performed for spring as well, as illustrated in Figure 7.18. The results show a similar trend to that of summer described in section 6.6.3.1. The imbalance in  $\Delta E_+$  and  $\Delta E_-$  becomes lesser in spring compares to that in winter. This can be deduced from the results shown on Figure 7.18. Although the target  $SOC_{max}$  is not reached in either of the two days, there is still sufficient stored energy in the CB for it to support the night-time load while maintaining the SOC level above  $SOC_{min}$ .

According to the dynamic simulation study shown above for the four seasons, the proposed adaptive intra-day CB control strategy appears to be able to maintain the SOC of the CB within stipulated range. Even under adverse weather conditions, the CB operating under the proposed strategy has managed to buffer  $P_{LT}(t)$  while adhering to the grid codes. Adaptive reference power leads to control the SOC and C-rate in order to reduce the SEI growth with response to the changes in different PV and load power conditions. Even during the extreme weather events of the year, the proposed method has managed to buffer the battery, adhering to the grid constraints resulting in very minimal SOC limit violations. It is demonstrated that the adjustable settings such as the  $SOC_{max}$  could be used to improve the performance of the proposed method in terms of several factors such as lowering SEI growth and alleviating duck curve phenomena. The effects of adjustable settings could be analysed statistically using probabilistic analysis ensuring the stochastic optimal planning of the proposed method.

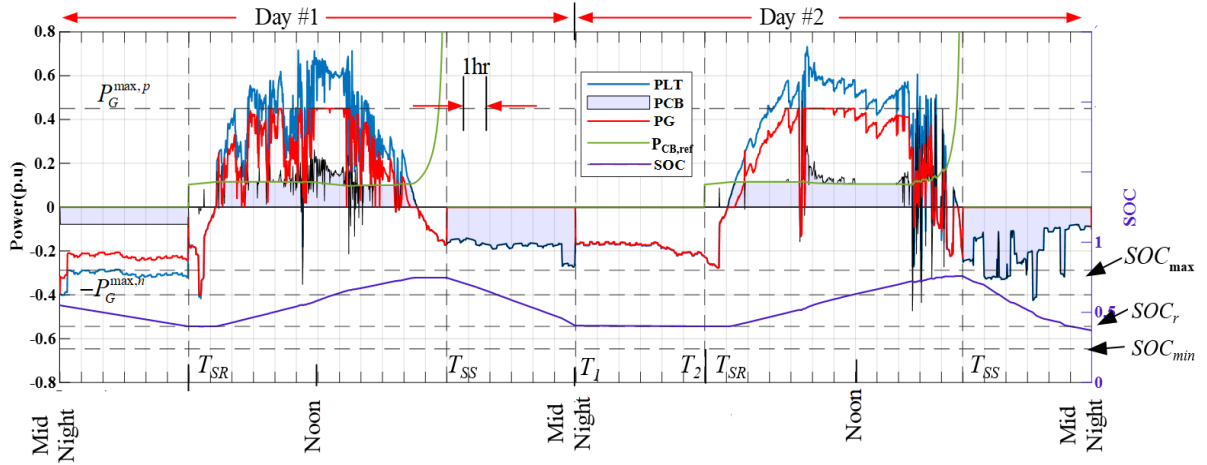


Figure 7.18 Application of the proposed adaptive CB SOC control strategy: spring and  $SOC_{max} = 0.8$

### 7.5.4 Performance of CB Operating under Conventional and Proposed Adaptive Control Strategies

In this section, the performance of the CB operating under two conventional and proposed adaptive CB control strategies is compared. The two conventional strategies are denoted as Strategies 1 and 2 in this investigation.

#### a. Strategy 1

Strategy 1 has been introduced in [81] to maximize the self-consumption of PV power. The battery is charged here using the maximum available surplus power until it reaches its maximum SOC. When CB reaches its maximum SOC, the charging process must be stopped, forcing the grid to absorb all excess PV power. As a result, in this approach, there could be instances that grid power exceeds  $P_G^{max,p}$  and  $\dot{P}_G^{max}$  limits, particularly after battery reaches its maximum SOC. This is demonstrated in Figure 7.19 which displays the results of the simulation study based on Strategy 1. As shown, the CB is charged to its maximum SOC using the maximum available surplus  $P_{LT}(t)$ . Then charging stops at around 0915 hours, and all the  $P_{LT}(t)$  is then exported to the grid until 1830 hours. The grid power constraint has been violated, almost to the end of this period.

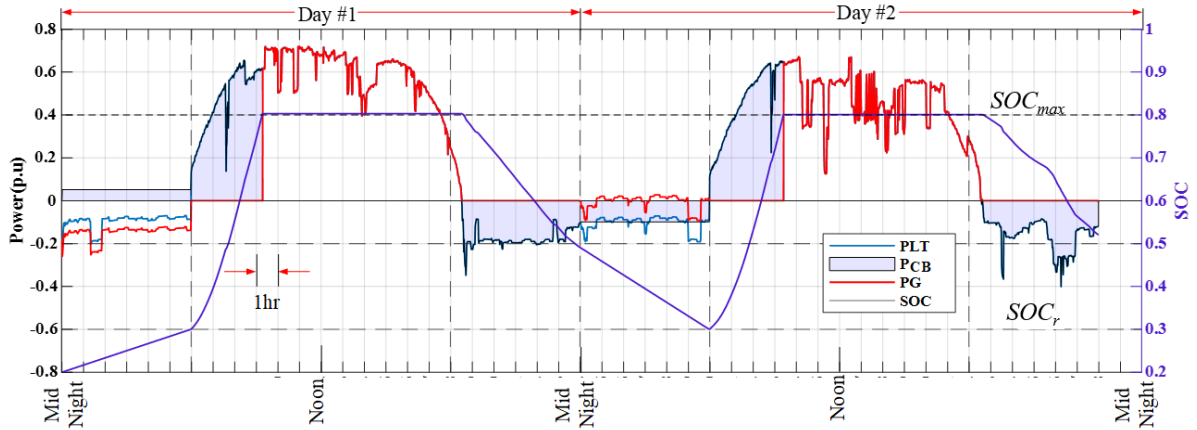


**Figure 7.19**  $P_{LT}(t)$ ,  $P_{CB}(t)$ ,  $P_G(t)$  and  $SOC(t)$  obtained using Strategy 1: summer

### b. Strategy 2

This strategy adopts the conventional battery control approach whereby constant charging and discharging powers are used in the intra-day operations of the CB. Detailed discussion of the general constant charging/discharging approach is also presented in [81]. Translating this approach for the CB considered in the present work, the constant charging power is applied in order for the SOC of the CB to reach the pre-specified maximum SOC level at  $T_{SS}$ . During nighttime, the CB shall discharge at a certain pre-set constant power level if  $P_{LT}(t)$  is less than this pre-set level. Otherwise, the discharge power flows is controlled to be equal to  $P_{LT}(t)$ . Unlike the adaptive intra-day CB control strategy proposed in the present work, there is no continuous adjustments in the charging/discharging power level in respond to the changing  $P_{LT}(t)$ . Again this method does not consider the  $P_G^{max,p}$  and  $\dot{P}_G^{max}$  limits. The main aim of this method is to minimize the effect of the C-rate fluctuations on battery degradation.

Example curve for this strategy is displayed in Figure 7.20. It can be seen that battery is charged and then discharged with the constant power, resulting in a linear variation in SOC as expected. It should be noted that in carrying out the simulation studies for Strategies 1 and 2, the SOC restoration strategy becomes effective between  $T_I$  and  $T_{SR}$ . In the examples shown on Figure 7.19 and Figure 7.20,  $SOC_r = 0.3$ .

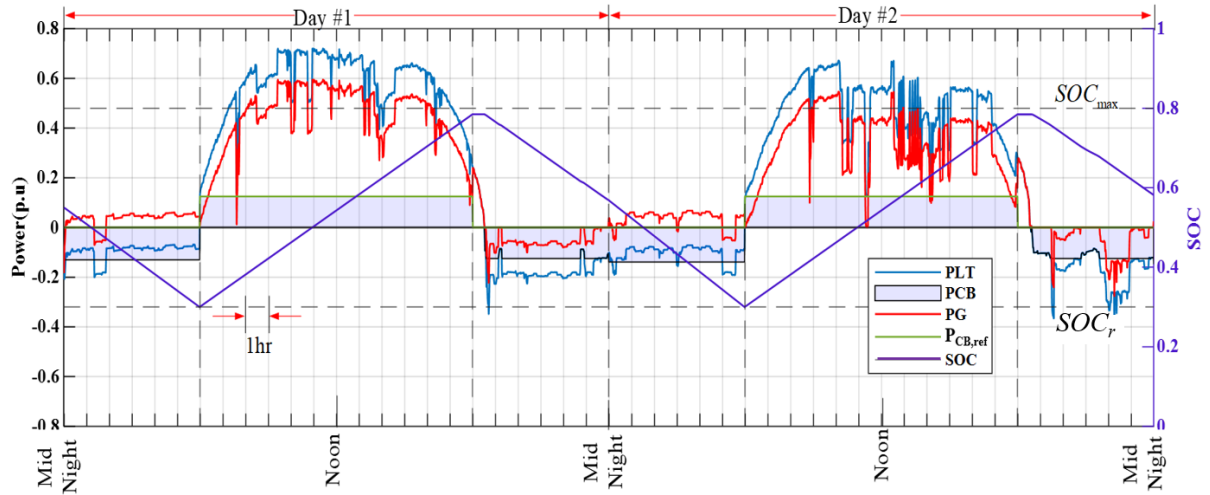


**Figure 7.20**  $P_{LT}(t)$ ,  $P_{CB}(t)$ ,  $P_G(t)$  and  $SOC(t)$  obtained using Strategy 2: summer

### c. Strategy 3

Strategy 3 denotes the proposed adaptive charging approach as shown in Figure 7.6. Here the seasonal SOC reference is followed, and the proposed adaptive power reference is utilized. The grid export and import constraints are also applicable in this method.

The outcomes of applying the three aforementioned strategies can be compared in greater detailed in term of the resulting SEI film growth, the amount of energy import/export on the grid link and the extent of the grid link constraint violation.

#### 6.6.3.1 Comparison of SEI film growth

From the simulation studies performed under each of the three strategies described earlier. The respective SOC and the charging/discharging powers lead to a SEI thickness that can be determined using the expressions shown in Appendix D. This increase in the thickness of the SEI film ( $\delta$ ) of the Li-ion CB battery is compared across the three strategies over the course of 90 days in summer. As shown in Figure 7.21, the proposed adaptive intra-day CB control strategy has resulted in some 24% lower increase in the SEI film thickness when compared with those based on the two conventional CB control strategies. The lower level in the SEI film growth indicates less degradation of the battery cells and therefore, one can expect a longer service lifetime when applying the adaptive intra-day CB control strategy to the CB. Even though it is not shown here due to the repetition of results, the other seasons also show a similar trend of encouraging results.

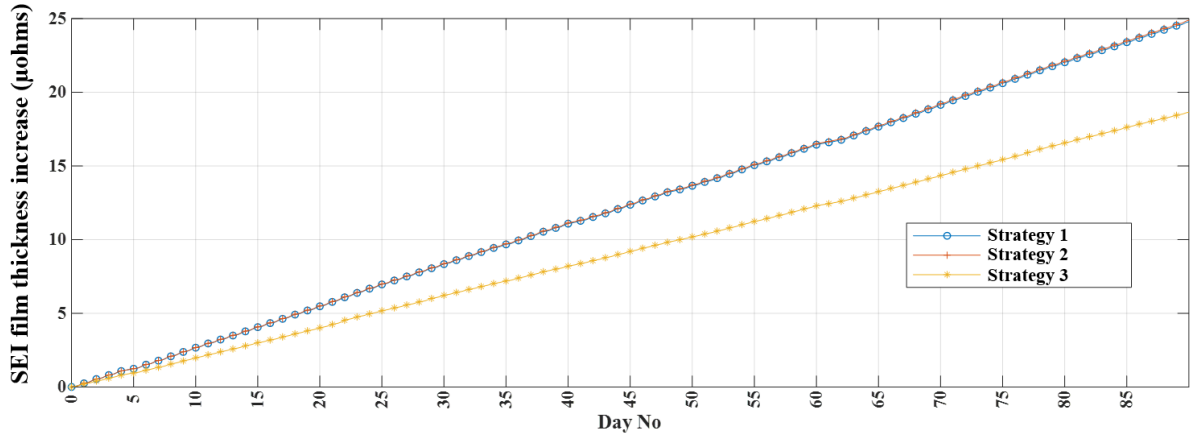


**Figure 7.21 Resulting increase in SEI film thickness in the Li-ion battery when applying Strategies 1, 2 and 3 over a summer season**

### 6.6.4.2 Comparison of the amounts of export/import energy on grid link

As Strategy 1 is designed to promote self-consumption, it is not surprising to note that there will have the lowest amount of energy export to the grid using this strategy among the three strategies considered. As shown in Figure 7.22, some 8-9% lower amount of the additional energy export using Strategy 2 and Strategy 3 can be seen in this example.

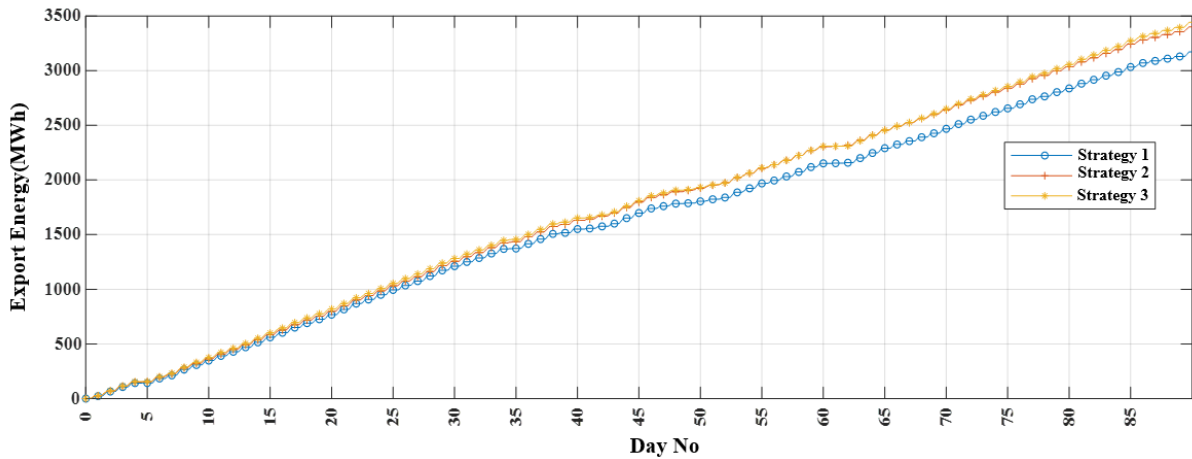


**Figure 7.22 Comparison of exported energy to grid using the three methods: summer**

Next, the import energy for each of the three strategies is computed and a comparison of the imported energies is shown on Figure 7.23. It can be seen that the amount of the imported energy from the grid using the proposed strategy is slightly lower than that obtained under Strategy 1. This outcome appears to suggest that in term of energy-independency of the microgrid from the grid link, the proposed strategy performs as well as Strategy 1. Most encouragingly, the proposed adaptive



control strategy has resulted in some 60% reduction in the import energy when compared to that using Strategy 2. This set of results certainly shows that the proposed adaptive control strategy has indeed resulted in great improvement in term of energy-independence in comparison to the commonly used Strategy 2, i.e., that based on constant charging/discharging currents.

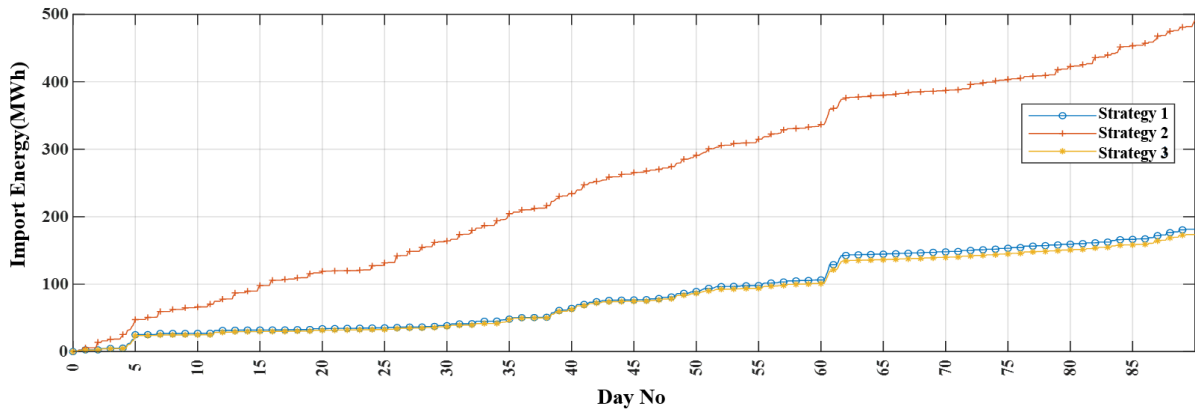


Figure 7.23 Comparison of imported energy from grid based on the three methods: summer

#### 6.6.4.3 Comparison of the grid link constraint violations

In order to understand the frequency of grid constraint violations across these three methods, this test is performed over one year time period of analysis. First, the instances of grid maximum power limit violations are considered and then probability of these occurrences are calculated. The probability of strategy 1 of not meeting the grid requirements is 0.18 while in strategy 2 this is 0.08. The proposed method (strategy 3) adhered to grid requirements at all times as it follows the rule-based control continuously.

According to the above comparison under three factors between existing methods and proposed method, following important remarks can be made. It can be concluded that the proposed method has shown improved performance of battery lifetime causing for lesser SEI growth in each season. Even though the strategy1 shows the best performance in terms of the grid export energy, this comes under more often violations of the grid export constraints. It is certain that these grid code violations are only acceptable to certain limits. They usually account for grid code breaching penalty costs which is an economically undesirable outcome for the microgrid. In contrast, the proposed method has greatly abided to those grid constraints while resulting in acceptable grid export/ import energy while accounting for the lowest SEI growth of the Li-ion battery.

## 7.6 Conclusions

A new degradation-conscious adaptive intra-day control scheme for centralized battery in a microgrid with high PV penetration has been developed. The primary objective is to operate the microgrid as independent as possible while the SEI growth rate is maintained at an optimal level.

The proposed adaptive power referencing method is sufficiently adaptive to the grid magnitude and ramp rate constraints. In addition, the proposed method is proven to be effective during the different seasons. As the proposed method does not require forecasting methods, it can avoid the computational complexities. Furthermore, it assures improved performance in SEI growth reduction, grid independency and maintaining grid power constraints.

Despite these encouraging outcomes, there is scope to improve further on the strategy. As shown in the comparison with the existing methods, adjustable settings of the proposed method could be fine-tuned in order to obtain the optimal outcomes of CB operation. This could only be investigated considering the economic factors such as grid tariff, battery costs, grid penalties for code violations etc. Only an aggregated cost due to all the related factors can then be utilized for an overall economic evaluation of the system. Further work is required to develop such economic evaluation where the aggregated cost could be minimized using the adjustable settings.

# CHAPTER 8. Conclusions and Recommendations

## 8.1 Impact of Research Findings to Industry

The theoretical concept outlined in this thesis can be applied to real-world situations, given that specific concerns not extensively covered within the thesis, are adequately addressed. Thus, it will be fruitful to establish a connection between the outcomes of the study and the practical needs of the industry to apply the proposed research work for the real-world applications. In order to bridge the gap between the proposed approach and real-world implementation, this section identifies the challenges and offers solutions for such issues. Figure 8.1 depicts the hierarchy of operations that are covered in this thesis for a real-world planning problem of HESS for microgrid.

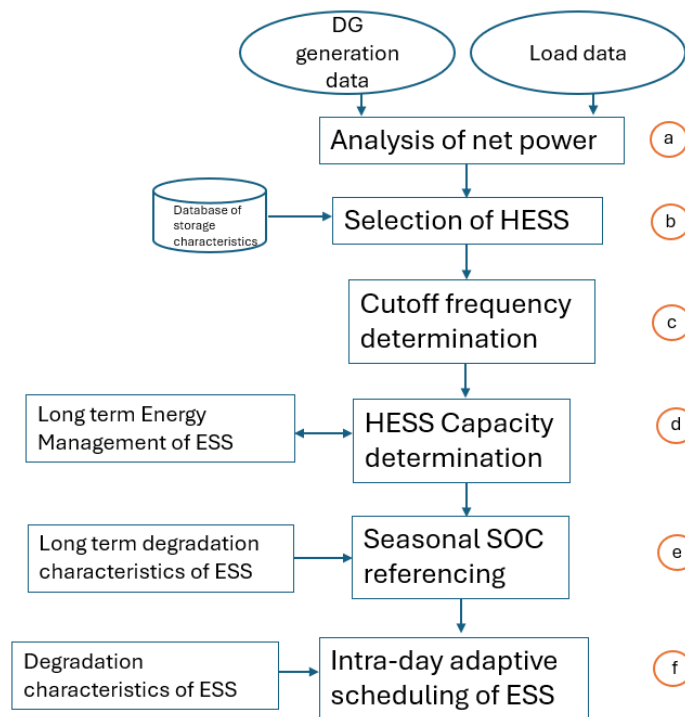


**Figure 8.1 Hierarchy of operations discussed in the microgrid planning problem discussed in the thesis**

(a) Usually, a planning problem starts with the analysis of the historical data of PV and load variation of the given site. In CHAPTER 3, the distributed generation data and load data are used to analyse the net power variation of the prosumers. This will help to identify the different loading and generation characteristics of the given application. For an example, the microgrid

in Kalbarri is operating as a self-sufficient unit during non-tourist seasons, whereas during tourist seasons, the increase load demand is met through the grid intervention. These net load variations should be considered at the planning stage of the ESS extensively. In a real-world scenario, the main challenging task would be dealing with heavy volumes of data from different sources for many years. For an example, the White Gum Valley project discussed in [121] incorporates heavy volumes of data from the dataloggers from prosumers for designing individual storage and shared storage. Employing EMD proves beneficial in handling such heavy data loads achieving the desired levels of accuracy. Intrinsic nature of the algorithm would be helpful to realize the dominant modes presented in the load and generation profiles without prior knowledge.

- (b) After a proper analysis of the data, the required constituent ESS can be determined. In Section 4.2, the selection of the HESS according to the appropriate application is described. This will ensure that the selected ESS technology is techno-economically feasible for the given application. It is important to note that in some storage techniques, ECM can be complex for some non-battery storage techniques. For instance, renewable projects utilizing Fuel Cells and electrolyzers are becoming increasingly prevalent in the industry nowadays [159]. However, simplifying the ECM would not be as direct as in the case for batteries in such instances. This may require additional understanding about the components of the ECM to simplify the network or empirical fitting method may need to be employed. In addition, other practical factors, such as site availability, geographical location, maintenance, maturity of technology and material availability should also be taken into consideration when selecting the appropriate ESS.
- (c) In order to determine the required storage capacity, as shown in the frequency-based attempts, the cut-off frequency should be determined first. In Section 4.2.5, the cut-off frequency determination between the selected ESS technologies is discussed. This will be helpful for the next stage of the HESS capacity determination. Various combinations of Energy Storage Systems (ESS) are commonly utilized in modern microgrids. Additionally, system planners are investigating different storage configurations, including distributed and centralized hierarchy, in microgrid studies [12]. Therefore, planning such a scheme using existing optimization-based methods would require significant resources. In contrast, the proposed method offers a much-generalized and direct way to the solution avoiding repetitive trial and error calculations. Several example ESS configurations are provided to assist system planners in understanding the implementation of the proposed method to various storage combinations.

- (d) Next, it is essential to ascertain the necessary capacity of the storage systems, taking into account the uncertainty of renewable generation and load variation. As in CHAPTER 5, HESS capacity of a prosumer can be determined based on the determined cut-off frequency and statistical analysis of the data. Usually, system planners should be able to assess the designed system by evaluating the loss of load probability through risk assessment, aiming to minimize this probability while maintaining an acceptable design cost. The proposed statistical analysis facilitates the determined capacity that can be validated as adequate during different seasonal variations.
- (e) However, in a hierarchy where a community storage is involved, the storage planning problem should be considered with respect to the power flows of the other prosumer types and grid power flow constraints. These power flow constraints are very commonly practiced due to the thermal heating limitations of the long transmission lines connecting the rural communities in Australia [7]. To respect these power flow constraints, a rule-based design methodology with a long-term ESS management is discussed in CHAPTER 6. The proposed method seasonally adjusts the SOC reference of the storage with respect to PV and load data of the site location. Thus, the setting for SOC reference clearly reflects the seasonal variations of both PV and load characteristics. This might be helpful in situations like the Kalbarri microgrid where load patterns change according to tourist seasons. The proposed method also acknowledges the long-term degradation characteristics of the ESS. Thus, the determined ESS capacity has considered the degradation modelling of the battery. In addition, the duck curve phenomenon is a major concern in the electricity market where AEMO implements different pricing approaches to mitigate the effects of it [160]. The proposed rule-based approach effectively address this issue resulting as maximum self-sufficiency of the microgrid using effective management of community storage capacity.
- (f) Using the above determined seasonal SOC reference, it is important to determine the control strategy for intraday operation. This has been the discussed topic in CHAPTER 7. Operational planning of microgrids with storages is a widely discussed topic these days [161]. For the online control of scheme of batteries at distribution level, it is not practical to use controllers with complex optimization and short-term forecasting. In contrast to this, the proposed rule-based adaptive method supports direct approach with minimum computation. The consideration of the control takes into account the uncertainty of the PV, load, degradation asymmetry during charging and discharging currents, degradation effects due to SOC variation of the battery and

self-consumption of the microgrid. To address additional degradation factors, the model must be further enhanced, especially regarding installations where temperature fluctuations significantly affect storage performance across different seasons. Consequently, storage management must also incorporate temperature effects into the degradation modeling process. The proposed method should be economically optimized to be able to be applied in the real-world scenario using the cost indexes. It is important to note that these economic aspects are not covered in this thesis.

In addition to the charging and discharging strategies mentioned in the microgrid based community storage, it is important to note that the proposed degradation conscious charging control method can be incorporated to any of battery management scheme to minimize the SEI growth of the Li-ion battery.

If the proposed methodology is going to be installed in the real time control of the storages, this would encounter challenges and additional costs of installation. The major concern is the filter design for the different constituent components to generate power reference. Also, during the real time control, the communication is required between the multi agent based coordinated control of the microgrid while the delays of this communication should be further considered in the control of the microgrid particularly with the fast-acting storage devices. Also, the stability concerns such voltage stability should be studied at the feeders. Reactive power support of inverter-based controllers should further be studied at the stage of power system planning.

## **8.2 Assumptions and Limitations**

The following concerns are identified as assumptions and limitations of the proposed methodology, and the mitigation techniques are also discussed in brief.

1. The first main point of the concern is during the analysis of net power using proposed EMD method in CHAPTER 3, where inherent issues such as mode mixing may be encountered. Nonetheless, it has been observed that advanced EMD techniques like EEMD might offer a solution to this issue, at the cost of additional computation resources. As a result of mode mixing, there will be an ambiguity in demarcation of some IMFs named as boundary IMFs here. This can be addressed using the additional step in the calculation introduced as apportion of boundary IMFs as introduced in CHAPTER 4.
2. During the proposed method in capacity determination, it is required to convert the ECM of the proposed storage technology to equivalent parallel RC representation in CHAPTER 4. However,

some storage mechanism would need to be carefully considered as RC elements hold distinct interpretations [131]. Thus, the simplification of the model would pose difficulty for certain storage technologies like Fuel Cell. In such situations, instead of mathematical simplification, simplified RC parameters for the interested frequency range can be calculated using empirical curve-fitting technique.

3. In addition to the gaps mentioned in steps related to real-world application, the most important assumptions in this thesis are related to the line losses that are neglected in the calculations. Charging and discharging efficiencies of the storages are also neglected. Charging and discharging efficiencies of the Li-ion batteries are typically around 0.95-0.97 [162]. Therefore, the calculation instances of the charging and discharging power in the expressions of (eq (6.8)-(6.9)) should be included with these efficiency factors for the completeness of the proposed method.
4. Due to the simplicity and unavailability of the data for the long term, only three different load profiles are considered in the microgrid considered. In real world scenario, the data should be available for different consumers for sufficiently long of at least 4-5 years. Processing this data would be challenging task. However, as the optimization is avoided, the computing efficacy is improved compared to other methods. Furthermore, when designing community-level storage, the complexity of data management is reduced, as data loggers are positioned at the aggregator level of the PCC within the microgrid. Therefore, this is unlikely to be a significant issue in such community storage design practices.
5. In the research outlined in CHAPTER 6, it is assumed that the seasonal reference will exhibit similar behavior in subsequent years. This is a common assumption made by long-term system planners. However, considering environmental concerns, future trends in solar insolation levels can be factored in to refine the proposed method.
6. The proposed methods of seasonal SOC referencing, and the intraday operation are only applicable to microgrids dominated by PV sources. This level of benefits cannot be guaranteed when the microgrid is dominated by other types of renewables such as wind.
7. In real-time control of such systems, it is presumed that the primary control parameter, SOC can be precisely estimated from battery parameters. This control scheme necessitates an accurate SOC measurement unit, which incurs associated costs. However, many battery management systems nowadays include such measurement units, so it is reasonable to assume that these costs would also apply to similar other methods.

8. A practical EMS for isolated microgrid should consider the operational constraints of reactive power balance, unbalanced system configuration and loading, and voltage dependent loads, protection criteria and required short-circuit ratio levels of voltage stability. These aspects are not covered in this discussion as the study is limited to the active power balance of the system. A fruitful future study should cover these topics prior to the implementation of the proposed method.

### 8.3 Conclusions

This thesis has extensively investigated the designing and control of energy storage systems at both the prosumer and community levels within a grid-connected microgrid, with a particular focus on the application of Li-ion battery in the schemes and taking into consideration the degradation of the battery cells due to the SEI film growth.

In the context of a grid-connected microgrid, CHAPTER 3 provides the preliminary analysis on the net power flows emanating from a prosumer. The unsteadiness in the net power is due to the time-varying and uncertain harnessed power from the PV generation and load demand fluctuations of the prosumer makes it unsuitable to analyse using the classical FT and wavelet-based methods. The objective is to assess the applicability of EMD-based analysis in decomposing various oscillating frequency components of the net power. In contrast to the classical methods, the adaptive EMD method has proven its effectiveness in extracting all the relevant frequency components in the form of the implicit mode functions (IMFs). The examination of power magnitudes of the IMFs has shown that high-frequency IMFs, despite their relatively low energy content, can play an important role in impacting power quality in the network. Thus, it is essential to have a highly responsive energy storage system to effectively buffer these high-frequency IMFs. The statistical analysis of the oscillation energy contained in the IMFs has identified that the dominating IMF components are those pertaining to the daily and seasonal fluctuations.

In view of the above, CHAPTER 4 proposes a new method to determine the cut-off frequency between the constituent ESSs of a HESS installed in a prosumer. The method takes into account both the frequency response characteristics and the capital cost of the ESSs. The cost per effective capacity of each of the ESSs is examined, expressed as a function of frequency. The optimum operating frequency range of the ESS corresponds to that which has the lowest cost per unit of energy storage capacity among the constituent ESSs. The cut-off frequency demarcates the optimum frequency ranges between the ESSs.



In CHAPTER 5, a statistical approach to estimate the required energy storage capacity of the HESS is discussed. Firstly, based on the method to determine the cut-off frequency described in CHAPTER 4, IMFs related to each constituent ESS of the HESS are identified. Boundary IMFs are separately treated to improve the accuracy of the determination. Subsequently, a statistical method is then proposed to estimate the energy variation for which the ESS would handle. The energy fluctuation is shown to vary over the seasons. A sufficient energy storage capacity is warranted using the statistics over different seasons for each of the constituent ESSs so that the ESSs can undertake the energy buffering task successfully and at reasonable probability level.

Building on the outcomes of the investigation obtained in the preceding chapters, attention is then directed toward the design of centralized battery-based ESS. CHAPTER 6 examines the scenario whereby the centralized battery (CB) shall be operated to make full use of the power capacity of the grid link. So, the capacity of the CB can be minimized while flexible grid import/export can be achieved. A rule-based operational strategy is proposed which does not require the forecasting of the PV and load demand. The proposed scheme of seasonal dynamic referencing of the SOC of the CB reduces the rate of the SEI film growth in the CB, the SEI film growth being the dominating degradation factor impacting the service lifetime of Li-ion battery. Moreover, the proposed scheme is able to reduce the required capacity by a considerable margin, compared to the fixed-SOC referencing scheme used in many existing CB control methods. Also, numerical examples show that with the proposed rule-based approach, the grid power import/export can be controlled such that the proposed CB control scheme can assist in achieving a higher level of independency of the microgrid in terms of alleviating the duck power phenomenon observed in the daily operation of the microgrid.

The attention of CHAPTER 7 is to consider the alternate scenario when the CB is placed to minimize the intra-day grid import/export, and thus improve the independency of the microgrid from the grid link. In addition, the effect of asymmetry in charging and discharging C-rate on the SEI growth rate is taken advantage of in the design of new charging and discharging strategies for the intra-day operation of the CB. Numerical examples have shown significantly lower SEI film growth when the proposed strategy is implemented, while the import/export constraints imposed on the grid link are not violated. Finally, the proposed CB control method is adaptive to seasonal changes in the PV power and load variations, and to do so without the need of forecasting.

## 8.4 Recommendations for Future Work

Notwithstanding the progress made thus far, the following studies are suggested for further investigations.

1. The inclusion of a grid-scaled ESS by expanding the system under study to grid level can be fruitful. In such a study, there is a need to coordinate the actions of the different ESS at different power levels. The evaluation of the economics of the storage scheme has to include the aging of the ESS. Some of the findings from CHAPTER 6 and 7 in this thesis could become very useful in the evaluation of Li-ion CB.
2. There are a number of other degradation factors such as that due to thermal effect that should be included into the ESS degradation analysis. The effect of SOC and the C-rate has been considered in the present study pertaining to the SEI film growth rate in Li-ion battery, however, other degradation factors such as Li-plating can be studied to more accurately determine the lifetime of the battery.
3. Optimization of the adaptive control of the community battery by considering economic factors. Though the operational strategies are adequately considered when developing the rules, the rules could be optimized by considering their economic impact on several factors. The factors can include the cost of grid export/import energy, annual degradation cost and penalty cost due to the violation of grid code. These costs are to be directly considered in developing an optimization-based method for the adaptive control scheme.
4. The stability analysis of the adaptive control scheme.  
Prior to developing a real-time controller for the degradation-aware adaptive control scheme proposed in CHAPTER 6 and 7, an in-depth stability analysis of such scheme can be fruitful. This is to ensure the proposed scheme is robust and resilient operating under an increasingly uncertain and volatile grid environment.

## Appendix A

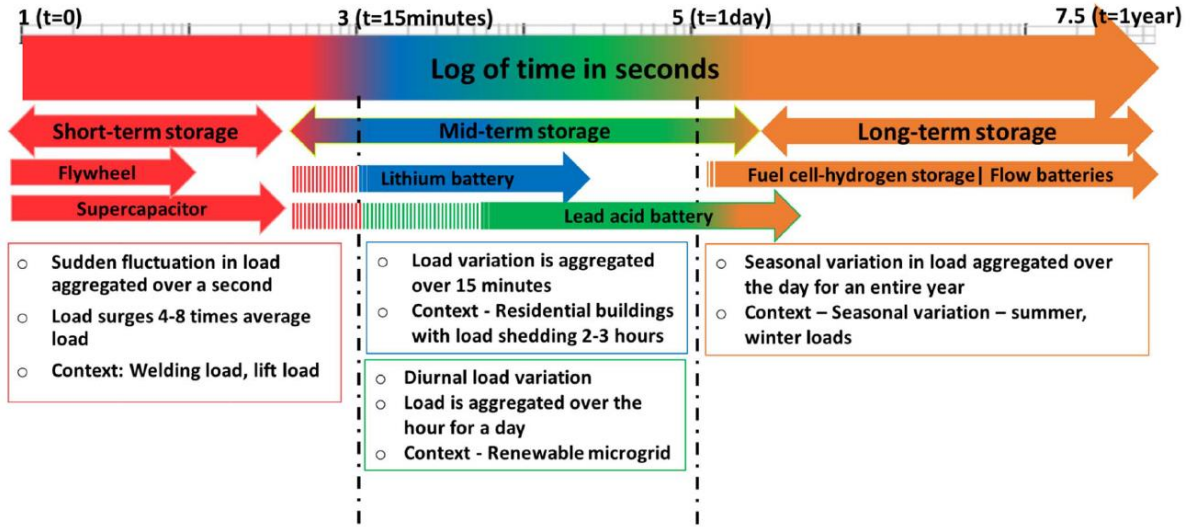


Figure A.1. An overview of classification of storage technologies based on the responsive time characteristics [10]

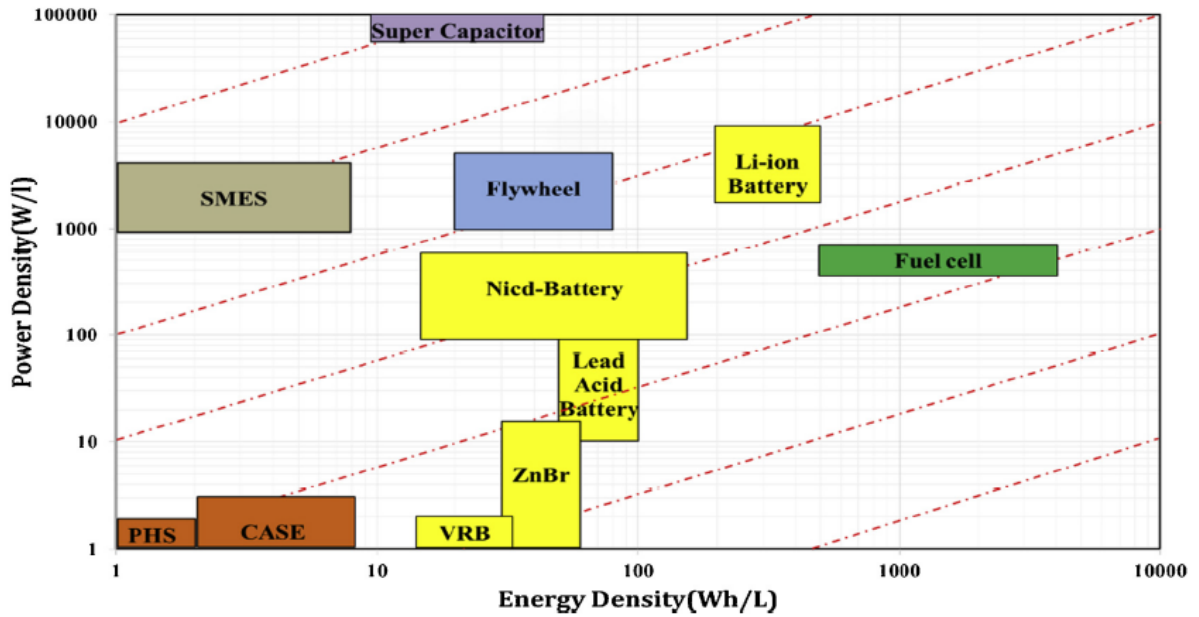


Figure A.2. Overview of classification of storage technologies([12])

**Table A.1 Table of the characteristics of the different ESS technologies (taken from the review paper [13])**

Type of Storage device	Energy density in $Wh/l$	Installation costs in $\text{€}/kW$	Installation cost in $\text{€}/kWh$	Reaction time	Self-discharge rate	Lifetime in years	System efficiency in %	Technology maturity	Application
SC	2-10	150-200	10000-20000	< 10ms	Up to 25 % in 1 <sup>st</sup> 48 h	15	77-83	Demonstration	Distributed generation and microgrid
SMES	0, 5-10	High	High	1-10 ms	10-15 %/day	20	80-90	Demonstration	Power quality, system stability, LF oscillation
Flywheel	80-200	300	1000	>10 ms	5-15 %/h	15	80-95	Commercial	FR, auxiliary service, PQ, enterprise UPS
Lead-acid	50-100	150-200	100-250	3-5 ms	0, 1-0, 4 %/day	5-15	70-75	Commercial, Demonstration	Peak load shifting, transportation, communication, national defense, reserve power supply, etc.,
Lithium-ion	200-350	150-200	300-800	3-5 ms	5 %/month	5-20	80-85	Demonstration, Commercial	All aspects of generation, transmission, distribution use.
Nas	150-250	150-200	500-700	3-5ms	10 %/day	15-20	68-75	Commercial	LR, peak load shifting, PQ, large-scale grid-connected RES etc.,
Redox-flow	20-70	1000-1500	300-500	> 1 s	0,1-0,4 %/day	10-15	70-80	Demonstration	Peak LR, large-scale grid-connected RES, UPS, emergency power supply, etc.,
Hydrogen	750/250 bar 2400/liquid	1500-2000	0,3-0,6	10 min	0,003-0,003 %/day	20	34-40	Commercial	Peak LR
Pumped hydro	0,27-1,5	500-1000	5-20	>3 min	0,005-0,02 %/day	80	75-82	Commercial	FR, peak LR, black start, phase shift.
CAES	3-6	700-1000	40-80	3-10 min	0,5-1 %/day	Ca. 25	60-70	Commercial, Demonstration	Peak LR, grid connected RES

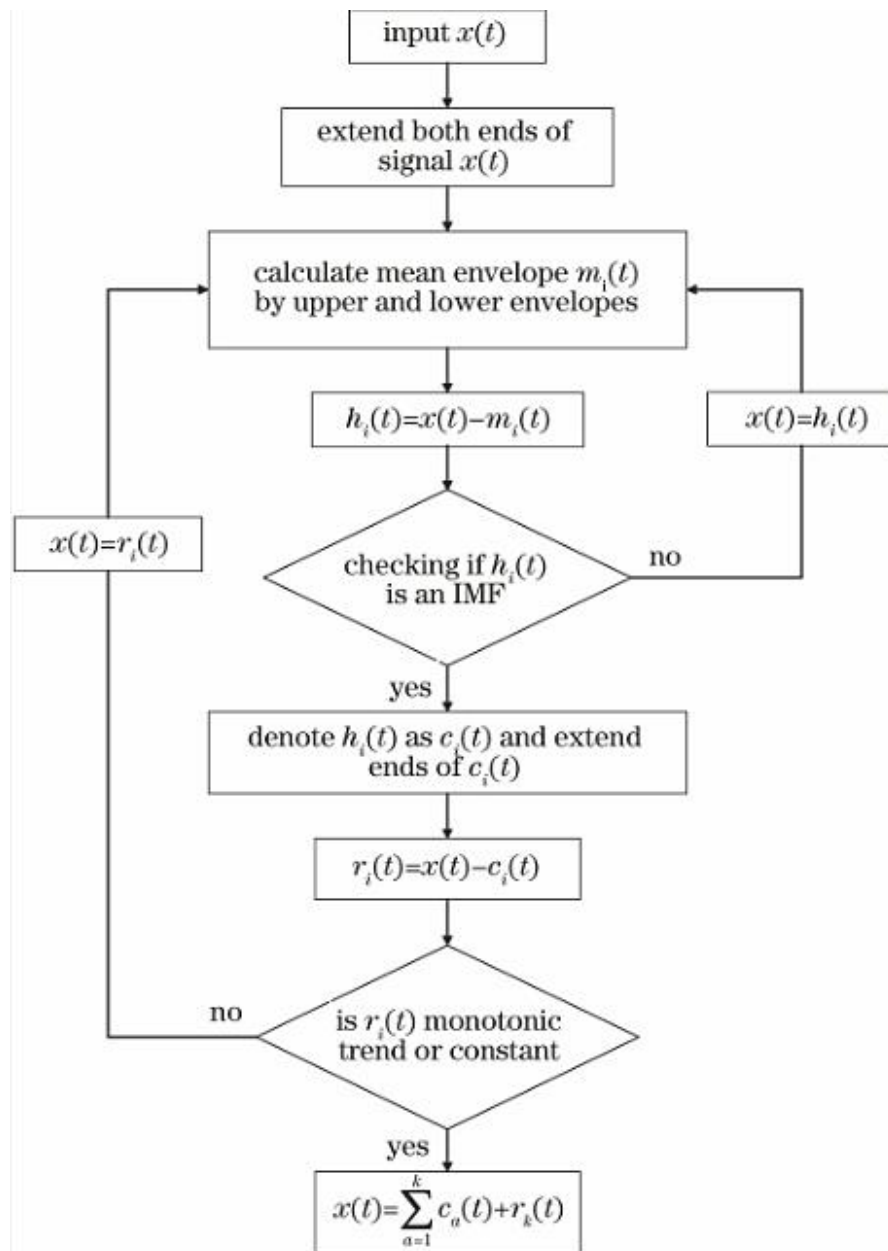


Figure A.3. Algorithm flow of sifting process of the EMD

## Appendix B

### a. ECM of SC

The simplest representation of the supercapacitor involves an equivalent series resistor (ESR) connected with capacitor of the SCs as presented in [163]. This is further improved by integrating a parallel resistor to the model in [164]. The primary aim of these RC branches is to simulate the time response of the supercapacitor during both charging and discharging processes. In addition, many such models include leakage resistance as the self-discharging component [165]. Subsequently, the complexity of the model is increased by introducing multiple RC branches to establish a close match to the measured characteristics of SC [126]. First RC branch is related to fastest charging/discharging process while subsequent branches represent progressively slower charging/discharging processes as their indices increase. Recently a more complex 4-branch SC model has been reported in [130] introducing four diffusion time constants.

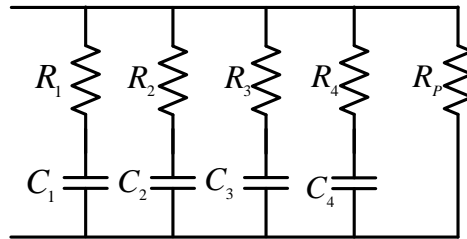


Figure B.1 ECM of Li-ion battery given in [130]

The parameters for the four branches model are as follows:

$$R_1=0.33 \times 10^{-3}, R_2=0.0124, R_3=1.3173, R_4=45.91, R_p=6323$$

$$C_1=1035, C_2=129.8, C_3=25.76, C_4=69.84$$

### b. ECM of PHES

Detailed modelling of the equivalent circuits of the PHES is presented and the values for the PHES are taken from the reference [166].

**Table B.1 Parameters of PHES modelling**

Symbol	Description	Value
<b>Water Hammer</b>		
$h$	Water head	
$a$	Wave speed	
$A$	Area of the pipe	
$D$	Internal diameter of the pipe	
$\lambda$	Loss coefficient	
$Q$	Volumetric discharge per second	
$\varepsilon / D$	Relative roughness of the pipe	0.0000049 [167]
$\mu$	Dynamic viscosity of water	$8.9 \times 10^{-4}$ [167]
$v$	Velocity of the water flow	
$\rho$	Density of water	1000kgm <sup>-3</sup>
<b>Gallery</b>		
$R_G$	Equivalent resistance of gallery	
$L_G$	Equivalent inductance of gallery	
$l_G$	Length of gallery	70m
$D_G$	Internal diameter of gallery	0.3m
<b>Penstock</b>		
$R_p$	Equivalent resistance of turbine	
$L_p$	Equivalent inductance of turbine	
$D_p$	Internal diameter of penstock	0.3m[166]
$l_p$	Length of penstock	70m[166]
<b>Surge Tank</b>		
$A_{st}$	Cross area of the surge tank	38.48m <sup>2</sup> [167]
$K_d$	Loss coefficient of surge tank	1.5 [166]
$C_{st}$	Equivalent capacitance of surge tank	
<b>Valve</b>		
$R_v$	Equivalent resistance of valve	
$K_v$	Loss coefficient of valve	1 [166]
<b>Turbine</b>		
$R_t$	Equivalent resistance of turbine	
$L_t$	Equivalent inductance of turbine	
$l_{equ}$	Equivalent length of turbine case	30m
$A_{equ}$	Equivalent area of turbine case	0.3m
$h_{loss}$	Head loss of the turbine	10% of total head
<b>Reservoir</b>		
$h_s$	Static head of upper reservoir	63m
$h_{res}$	Water height of the upper reservoir	7m
$V_{res}$	Volume of the upper reservoir water	4000m <sup>3</sup>
$A_r$	Area of the reservoir	571.42m <sup>2</sup>
$V_h$	potential gain due to the height of the upper reservoir	
$E_0$	Evaporation in mm day <sup>-1</sup>	
$T$	Air temperature in C	25°C
$I_s$	Solar radiance in Wm <sup>-2</sup>	600W
$z$	Local altitude	63m
$u$	Local wind speed	6ms <sup>-1</sup>
$R_h$	Relative humidity	52%

## 1. Main components of the PHES

Prior to developing of the complete ECM of the PHES, the main components need to be separately studied in order to denote the characteristics using appropriate equivalent electrical circuit parameters. The generalized main components of the PHES could be identified as in Figure B.2.

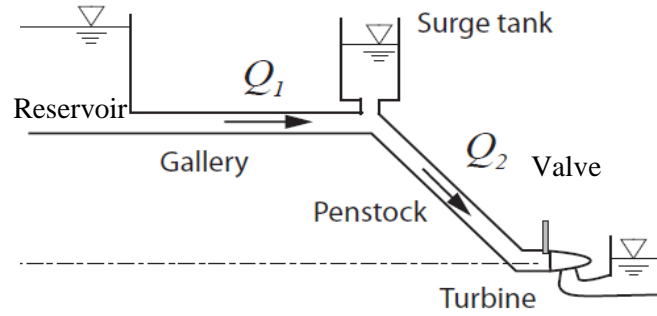


Figure B.2. Main components of the generalized PHES

## 2. ECM of the Water Hammer

As mentioned in the [168], the behavior of the water hammer of  $\Delta x$  could be mathematically explained using the following set of partial differential equations.

Continuous Equation: -

$$\frac{\partial h}{\partial t} + \frac{a^2}{gA} \cdot \frac{\partial Q}{\partial x} = 0 \quad (\text{B.1})$$

Momentum Equation: -

$$\frac{\partial h}{\partial x} + \frac{1}{gA} \cdot \frac{\partial Q}{\partial t} + \frac{\lambda|Q|}{2gDA^2} \cdot Q = 0 \quad (\text{B.2})$$

Similarly, the study of electrical wave propagation in conductors leads to the establishment of the set of equations expressed as follows, referred to as the telegraphist's equation: [169]

$$\begin{cases} \frac{\partial U}{\partial x} + L'_e \frac{\partial i}{\partial t} + R'_e i = 0 \\ \frac{\partial U}{\partial t} + \frac{1}{C'_e} \frac{\partial i}{\partial x} = 0 \end{cases} \quad (\text{B.3})$$

Where:

- $i$ : electrical current [A]
- $U$ : electrical potential [V]
- $R'_e$ : lineic electrical resistance [ $\Omega/m$ ]
- $L'_e$ : lineic electrical inductance [ $H/m$ ]
- $C'_e$ : lineic electrical capacitance [ $F/m$ ]



Considering the analogy between the hydraulic and electrical systems, the equations of the (B.1), (B.2) and (B.3) can be rewritten considering the lineic hydraulic resistance  $R'$ , a lineic hydraulic inductance  $L'$  and a lineic hydraulic capacitance  $C'$  as in (B.4).  $R'$  represents the head losses through the pipe, while  $L'$  is associated with the inertia of fluid, and the  $C'$  relates to the storage effect caused by pressure increase due to both compressibility of the fluid and due to pipe wall deflection.

$$\begin{cases} \frac{\partial h}{\partial x} + L' \frac{\partial Q}{\partial t} + R'(Q)Q = 0 \\ \frac{\partial h}{\partial t} + \frac{1}{C'} \frac{\partial Q}{\partial x} = 0 \end{cases} \quad (\text{B.4})$$

Where the lineic hydroacoustic parameters are defined as:

- lineic hydroacoustic capacitance  $C' = \frac{g \cdot A}{a^2} [m]$ ;
- lineic hydroacoustic inductance  $L' = \frac{1}{g \cdot A} [s^2/m^3]$ ;
- lineic hydroacoustic resistance  $R' = \frac{\lambda \cdot |Q|}{2 \cdot g \cdot D \cdot A^2} [s/m^3]$ .

As a result of the aforementioned equivalence the elastic pipe could be represented as in Figure B.3.

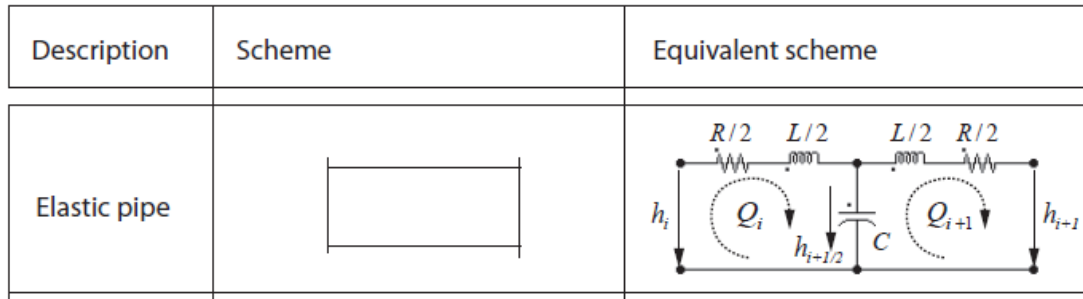


**Figure B.3.** Complete ECM of the Elastic pipe

Equivalent electrical parameters of the circuit shown on would be as follows.

$$R = R' \cdot l \cdot p \cdot g \quad (\text{B.5})$$

$$L = L' \cdot l \cdot p \cdot g \quad (\text{B.6})$$

$$C = C' \cdot l / (p \cdot g) \quad (\text{B.7})$$

The more important parameter in the (B.4) is the friction factor ( $\lambda$ ) which can be approximated by the (B.8) that shows the relationship between friction factor ( $\lambda$ ), Reynolds number ( $R_e$ ), and the relative roughness of the pipe ( $\varepsilon / D$ ). Reynolds number can be calculated using the (B.10) where  $\mu$  dynamic viscosity of the fluid and  $v$  is the velocity of the water flow which can be calculated by (B.9).

$$\lambda = \left[ 1.8 \log \left( \frac{6.9}{R_e} + \left( \frac{\varepsilon / D_p}{3.7} \right)^{1.11} \right) \right]^{-2} \quad (\text{B.8})$$

$$v = \frac{Q}{A} \quad (\text{B.9})$$

$$R_e = \frac{\rho v D_p}{\mu} \quad (\text{B.10})$$

Following the same analogy, the ECM for the surge tank, valve and the turbine can be electrically modeled as below.

### 3. ECM of the surge tank

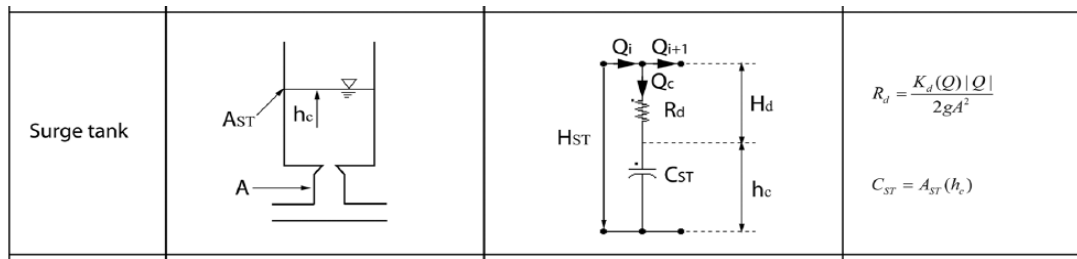


Figure B.4 ECM of the surge tank

### 4. ECM of the Valve

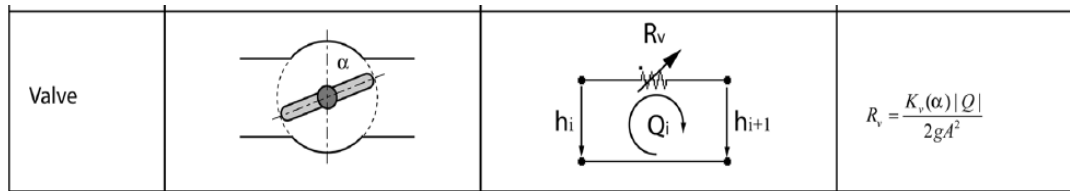


Figure B.5 ECM of valve

### 5. ECM of the Turbine

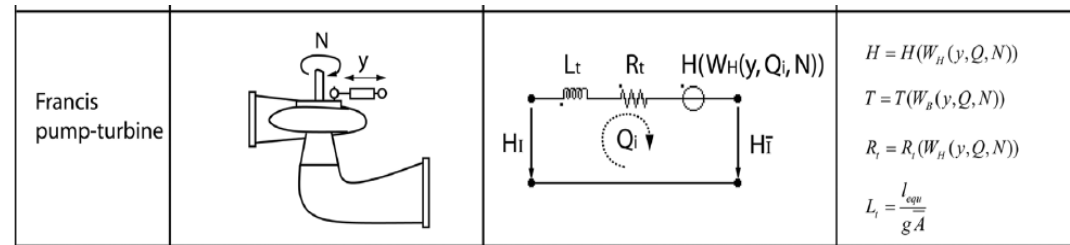


Figure B.6 ECM of turbine

## 6. ECM of the Reservoir

ECM for the reservoir is adopted from the reference [170] which are described by the (B.11)-(B.14).  $C_{res}$  represents the storing capacity of the reservoir which is determined by the (B.11). Voltage source  $V_h$  represents the equivalent potential increase due to the height of the water level.

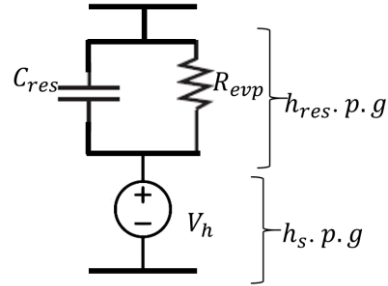


Figure B.7 ECM parameters of reservoir

$$C_{res} = A_r / (p \cdot g) \quad (B.11)$$

$$V_h = h_s \cdot p \cdot g \quad (B.12)$$

$$R_{evp} = h_{res} \cdot p \cdot g / Q_{evp} \quad (B.13)$$

$$Q_{evp} = 8.64 \times 10^{-7} A_r E_0 \quad (B.14)$$

$$E_0 = (0.015 + 0.00042T + 10^{-6}z) \cdot [0.8Is - 40 + 2.5Fu(T - T_d)]$$

$$F = 1 - 8.7 \times 10^{-5}z$$

$$T_d = \frac{c\gamma}{b - \gamma}, \quad \gamma = \ln\left(\frac{R_h}{100}\right) + \frac{bT}{c + T}$$

where  $b = 18.678$ ,  $c = 257.14^\circ\text{C}$

## Appendix C

### PHES costs

**Table C.1 Table of PHES capacities and associated capital costs [136]**

Payback period and lifetime benefit of the proposed storage system.

Storage capacity (kWh)	Turbine Price (AUD)	BOS (AUD)	Capital cost (AUD)
4.2	276	200	476
6.9	292	220	512
10	301	220	521
14	344	250	594
21	346	300	646
28	350	300	650
42	430	300	730
69	803	300	1103
139	3410	500	3910
208	3740	500	4240
278	8130	700	8830
417	9100	700	9800
556	9750	1000	10,750

## Appendix D

### SOC /I vs SEI growth of Li-ion Battery

Prior to establishing the relationship, SOC and current ( $I$ ) are considered as the known parameters of the Li-ion battery. The remaining known parameters of the Li-ion battery are displayed in Table D.1 which are obtained from the studies in [56, 124]. Using the equations from (D.1)-(D.10), resistance growth rate and the rate of the capacity loss of the Li-ion battery can be quantified due to the SEI growth in relation to the SOC and current( $I$ ) [171].

**Table D.1. Parameters of degradation model of Li-ion battery**

Parameter	Unit	Value
Maximum concentration in solid phase $C_{s,n,max}$	(mol·m <sup>-3</sup> )	30555
Concentration of Lithium-ion in the electrolyte $C_e$	(mol·m <sup>-3</sup> )	1200
Electrode plate area $A_n$	m <sup>2</sup>	0.358
Specific surface are $a_n$	m <sup>-1</sup>	7.236*1e5
Reaction rate constant $k_n$	A·m <sup>2.5</sup> ·mol <sup>-1.5</sup>	5.031*1e-11
Length of the electrode $L_n$	m	8.8*1e-5
$R$	J/(K·mol)	8.314
$T$	(K)	298.15
$F$	s·A/mol	96487
Side reaction potential $U_{s,ref}$	V	0.4
SEI molar mass $M_p$	kg mol <sup>-1</sup>	0.162
SEI layer density $\rho_p$	kg m <sup>-3</sup>	1690
Conductivity of the SEI $\kappa_p$	1/(m·Ω)	17.5*1e-5
Charge transfer coefficient $\alpha_n$		0.5

1. Surface SOC of the negative electrode is the ratio between the surface concentration ( $C_{s,n,surf}$ ) and maximum concentration ( $C_{s,n,max}$ ).

$$SOC = C_{s,n,surf}/C_{s,n,max} \quad (D.1)$$

Since the  $C_{s,n,max}$  is known parameter, knowing the SOC,  $C_{s,n,surf}$  could be determined.

2. The main reaction exchange current density can be found by following, where  $C_e$  is the concentration of Lithium-ion in the electrolyte.

$$i_{o,n}(t) = \alpha_n k_n (C_{s,n,max} - C_{s,n,surf})^{\alpha_a} (C_{s,n,surf})^{\alpha_c} (C_e)^{\alpha_a} \quad (D.2)$$

3. Current density can be determined when the current is known,

$$j_n = I/(A_n L_n) \quad (D.3)$$

4. Solving butler and volmer equation, the main reaction over potential of the negative electrode ( $\eta_n$ ) can be found

$$\eta_n = \frac{RT}{\alpha_n F} \sinh^{-1} \left( \frac{j_n^{Li}}{2a_s^n i_0^n} \right), \quad (D.4)$$

5. Side reaction over potential can be found by

$$\eta_s(t) = \eta_n(t) + U_{n,ref} - U_{s,ref} \quad (D.5)$$

Where Side reaction potential ( $U_{s,ref}$ ) is known as given in table and  $U_{s,ref}$  is the equilibrium potential of negative electrode which is a function of SOC.

Where  $U_n = 0.722 + 0.1387 \times x + 0.029 \times \text{power}(x, 0.5) - 0.0172 \times \text{power}(x, -1) + 0.0019 \times \text{power}(x, -1.5) + 0.2808 \times \exp(0.9 - 15 \times x) - 0.7984 \times \exp(0.4465 \times x - 0.4108)$  for  $x = \text{SOC}$

6. Side reaction current density can be found by Tafel equation,

$$j_{side}(t) = -i_o a_n \exp \left( \frac{\alpha F}{RT} \eta_s(t) \right) \quad (D.6)$$

7.  $\frac{\partial \delta_{film}(t)}{\partial t}$  is the SEI film growth rate which can be found by,

$$\frac{\partial \delta_{film}(t)}{\partial t} = -\frac{M_p}{a_n \rho_p F} j_{side}(t) \quad (D.7)$$

8.  $R_{film}(t)$  represents the SEI resistance which is assumed to grow in proportion to its thickness,

$$R_{film}(t) = R_{SEI} + \frac{\delta_{film}(t)}{\kappa_p} \quad (D.8)$$

9. Capacity fade rate due to the side reaction can be determined by,

$$\frac{\partial Q_{loss}(t)}{\partial t} = - \int_0^{L_n} J_{side}(t) A_n dx \quad (D.9)$$

10. Capacity fade rate in Ah/sec can be expressed as

$$\frac{\partial Q_{loss}(t)}{\partial t} = \frac{-j_{side}(t) \times A_n \times L_n}{3600} \quad (D.10)$$

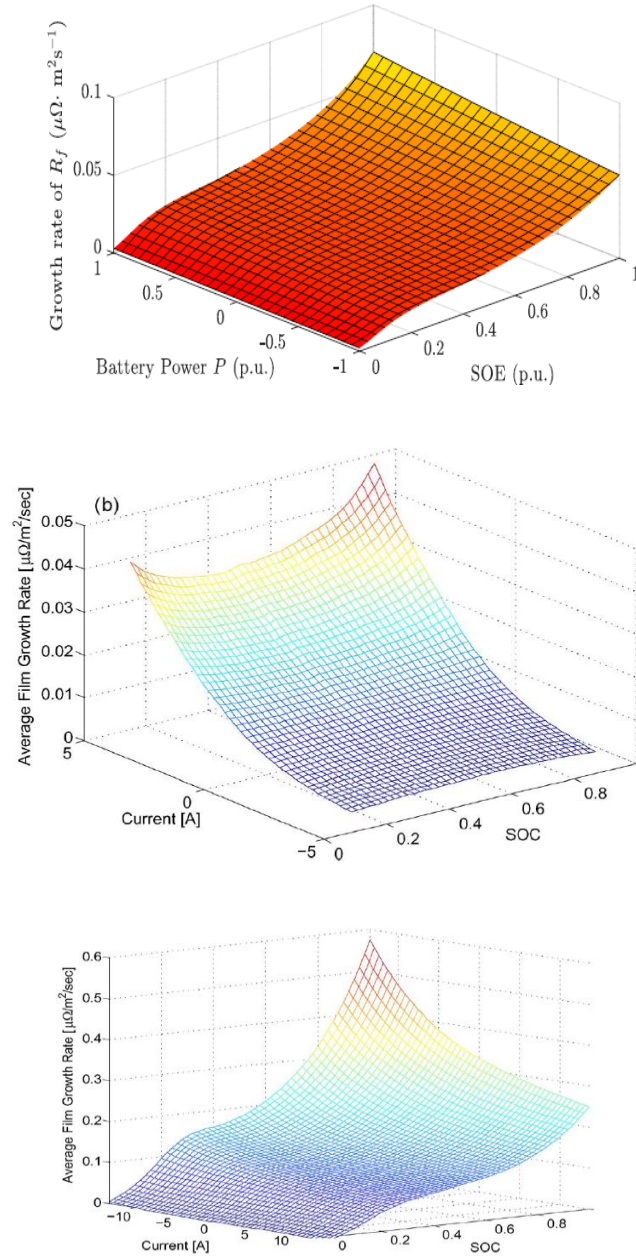


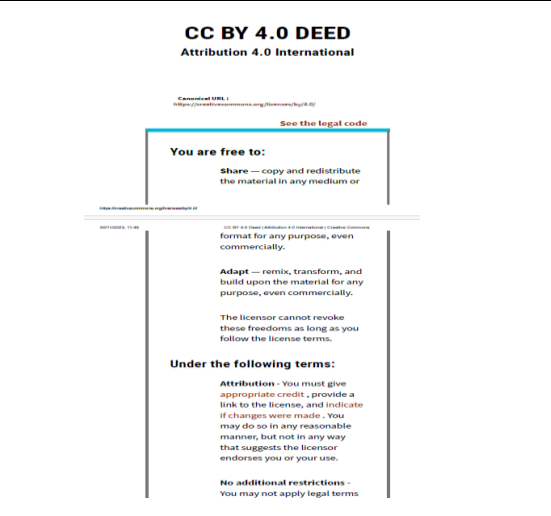
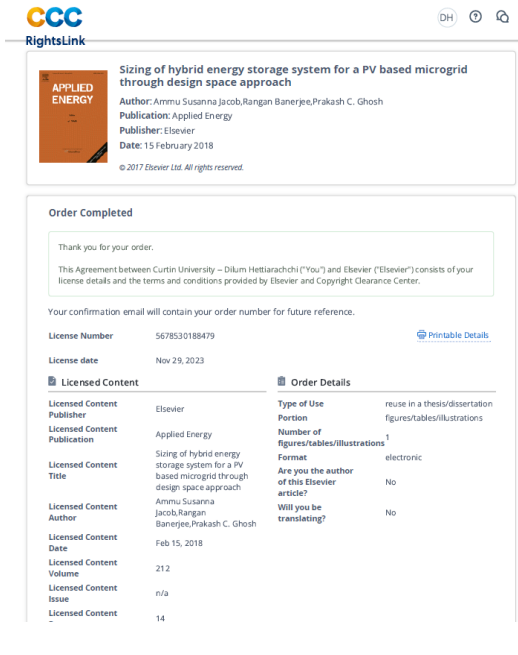
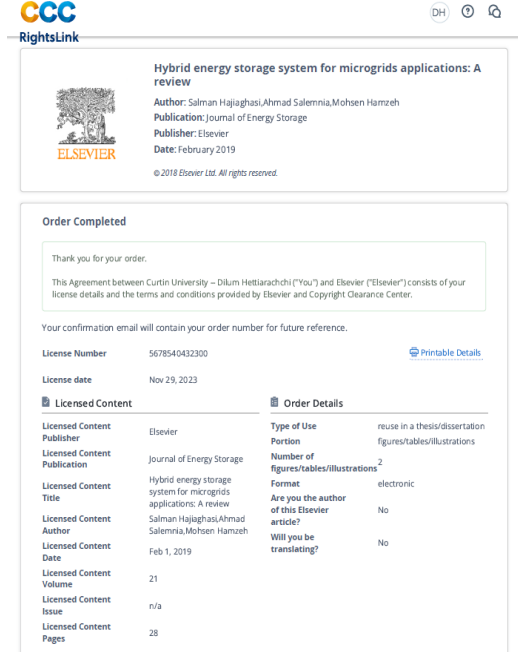


Figure D.1 Different SEI growth rate vs SOC/I surface plots in the literature [129] [156]

## Appendix E

Table E.1. Details of the copyrights obtained by for the published research outputs

Content in the thesis (Chapter/Figure name)	Article Name/Publisher	Copyrights owner	Copyright license
CHAPTER 4 text and figures	A new approach to identify the optimum frequency ranges of the constituent storage devices of a hybrid energy storage system using the empirical mode decomposition technique	Elsevier	 <p>The screenshot shows the RightsLink interface for an Elsevier article. It includes the article title, author information (Dilum Hettiarachchi, Sumedha Rajakanuna, San Shing Choi, Arindam Ghosh), publication details (Journal of Energy Storage, Elsevier, July 2022), and a 'Journal Author Rights' section. The rights section states that the author retains the right to include the work in a thesis or dissertation, provided it is not published commercially. It also provides a link to the Elsevier copyright policy.</p>
CHAPTER 6 text	Development of control strategy for community battery energy storage system in grid-connected microgrid of high photovoltaic penetration level	Open Access (Creative Commons)	 <p>The screenshot shows the RightsLink interface for an Elsevier article. It includes the article title, author information (Dilum Hettiarachchi, San Shing Choi, Sumedha Rajakanuna, Arindam Ghosh), publication details (International Journal of Electrical Power &amp; Energy Systems, Elsevier, January 2024), and a 'Creative Commons' section. The rights section states that the article is distributed under the terms of the Creative Commons CC-BY license, which permits unrestricted use, distribution, and reproduction in any medium, provided the original work is properly cited. It also provides a link to the Elsevier Global Rights Department.</p>
Figure 2.3	A comprehensive review on the characteristics and modeling of lithium-ion battery aging	Open Access (Creative Commons)	 <p>The screenshot shows the CC BY 4.0 Deed page. It includes the title 'CC BY 4.0 DEED Attribution 4.0 International', the Creative Commons logo, and the text 'You are free to: Share — copy and redistribute the material in any medium or format for any purpose, even commercially. Adapt — remix, transform, and build upon the material for any purpose, even commercially. The licensor cannot revoke these freedoms as long as you follow the license terms. Under the following terms: Attribution - You must give appropriate credit, provide a link to the license, and indicate if changes were made. You may do so in any reasonable manner, but not in any way that suggests the licensor endorses you or your use. No additional restrictions - You may not apply legal terms'.</p>

<p>Figure A.1</p>	<p>Sizing of hybrid energy storage system for a PV based microgrid through design space approach</p>	<p>Elsevier</p>	 <p>The screenshot shows the 'Order Completed' page for a license. It includes a thank you message, a confirmation of the agreement between Curtin University and Elsevier, and a confirmation email reference. The license details are as follows:</p> <table border="1"> <thead> <tr> <th colspan="2">Licensed Content</th> <th colspan="2">Order Details</th> </tr> </thead> <tbody> <tr> <td>Licensed Content Publisher</td> <td>Elsevier</td> <td>Type of Use Portion</td> <td>reuse in a thesis/dissertation figures/tables/illustrations</td> </tr> <tr> <td>Licensed Content Publication</td> <td>Applied Energy</td> <td>Number of figures/tables/illustrations</td> <td>1</td> </tr> <tr> <td>Licensed Content Title</td> <td>Sizing of hybrid energy storage system for a PV based microgrid through design space approach</td> <td>Format</td> <td>electronic</td> </tr> <tr> <td>Licensed Content Author</td> <td>Ammu Susanna Jacob,Rangan Banerjee,Prakash C. Ghosh</td> <td>Are you the author of this Elsevier article?</td> <td>No</td> </tr> <tr> <td>Licensed Content Date</td> <td>Feb 15, 2018</td> <td>Will you be translating?</td> <td>No</td> </tr> <tr> <td>Licensed Content Volume</td> <td>212</td> <td></td> <td></td> </tr> <tr> <td>Licensed Content Issue</td> <td>n/a</td> <td></td> <td></td> </tr> <tr> <td>Licensed Content</td> <td>14</td> <td></td> <td></td> </tr> </tbody> </table>	Licensed Content		Order Details		Licensed Content Publisher	Elsevier	Type of Use Portion	reuse in a thesis/dissertation figures/tables/illustrations	Licensed Content Publication	Applied Energy	Number of figures/tables/illustrations	1	Licensed Content Title	Sizing of hybrid energy storage system for a PV based microgrid through design space approach	Format	electronic	Licensed Content Author	Ammu Susanna Jacob,Rangan Banerjee,Prakash C. Ghosh	Are you the author of this Elsevier article?	No	Licensed Content Date	Feb 15, 2018	Will you be translating?	No	Licensed Content Volume	212			Licensed Content Issue	n/a			Licensed Content	14		
Licensed Content		Order Details																																					
Licensed Content Publisher	Elsevier	Type of Use Portion	reuse in a thesis/dissertation figures/tables/illustrations																																				
Licensed Content Publication	Applied Energy	Number of figures/tables/illustrations	1																																				
Licensed Content Title	Sizing of hybrid energy storage system for a PV based microgrid through design space approach	Format	electronic																																				
Licensed Content Author	Ammu Susanna Jacob,Rangan Banerjee,Prakash C. Ghosh	Are you the author of this Elsevier article?	No																																				
Licensed Content Date	Feb 15, 2018	Will you be translating?	No																																				
Licensed Content Volume	212																																						
Licensed Content Issue	n/a																																						
Licensed Content	14																																						
<p>Figure A.2</p>	<p>Hybrid energy storage system for microgrids applications: A review</p>	<p>Elsevier</p>	 <p>The screenshot shows the 'Order Completed' page for a license. It includes a thank you message, a confirmation of the agreement between Curtin University and Elsevier, and a confirmation email reference. The license details are as follows:</p> <table border="1"> <thead> <tr> <th colspan="2">Licensed Content</th> <th colspan="2">Order Details</th> </tr> </thead> <tbody> <tr> <td>Licensed Content Publisher</td> <td>Elsevier</td> <td>Type of Use Portion</td> <td>reuse in a thesis/dissertation figures/tables/illustrations</td> </tr> <tr> <td>Licensed Content Publication</td> <td>Journal of Energy Storage</td> <td>Number of figures/tables/illustrations</td> <td>2</td> </tr> <tr> <td>Licensed Content Title</td> <td>Hybrid energy storage system for microgrids applications: A review</td> <td>Format</td> <td>electronic</td> </tr> <tr> <td>Licensed Content Author</td> <td>Salman Hajiaghahi,Ahmad Saleemnia,Mohsen Hamzeh</td> <td>Are you the author of this Elsevier article?</td> <td>No</td> </tr> <tr> <td>Licensed Content Date</td> <td>Feb 1, 2019</td> <td>Will you be translating?</td> <td>No</td> </tr> <tr> <td>Licensed Content Volume</td> <td>21</td> <td></td> <td></td> </tr> <tr> <td>Licensed Content Issue</td> <td>n/a</td> <td></td> <td></td> </tr> <tr> <td>Licensed Content Pages</td> <td>28</td> <td></td> <td></td> </tr> </tbody> </table>	Licensed Content		Order Details		Licensed Content Publisher	Elsevier	Type of Use Portion	reuse in a thesis/dissertation figures/tables/illustrations	Licensed Content Publication	Journal of Energy Storage	Number of figures/tables/illustrations	2	Licensed Content Title	Hybrid energy storage system for microgrids applications: A review	Format	electronic	Licensed Content Author	Salman Hajiaghahi,Ahmad Saleemnia,Mohsen Hamzeh	Are you the author of this Elsevier article?	No	Licensed Content Date	Feb 1, 2019	Will you be translating?	No	Licensed Content Volume	21			Licensed Content Issue	n/a			Licensed Content Pages	28		
Licensed Content		Order Details																																					
Licensed Content Publisher	Elsevier	Type of Use Portion	reuse in a thesis/dissertation figures/tables/illustrations																																				
Licensed Content Publication	Journal of Energy Storage	Number of figures/tables/illustrations	2																																				
Licensed Content Title	Hybrid energy storage system for microgrids applications: A review	Format	electronic																																				
Licensed Content Author	Salman Hajiaghahi,Ahmad Saleemnia,Mohsen Hamzeh	Are you the author of this Elsevier article?	No																																				
Licensed Content Date	Feb 1, 2019	Will you be translating?	No																																				
Licensed Content Volume	21																																						
Licensed Content Issue	n/a																																						
Licensed Content Pages	28																																						



## References

- [1] P. C. Chu, C. Fan, and N. Huang, "Compact empirical mode decomposition: an algorithm to reduce mode mixing, end effect, and detrend uncertainty," *Advances in Adaptive Data Analysis*, vol. 4, no. 03, p. 1250017, 2012.
- [2] M. Abbasi, E. Abbasi, L. Li, R. P. Aguilera, D. Lu, and F. Wang, "Review on the Microgrid Concept, Structures, Components, Communication Systems, and Control Methods," *Energies*, vol. 16, no. 1, p. 484, 2023. [Online]. Available: <https://www.mdpi.com/1996-1073/16/1/484>.
- [3] D. Sampath Kumar, O. Gandhi, C. D. Rodríguez-Gallegos, and D. Srinivasan, "Review of power system impacts at high PV penetration Part II: Potential solutions and the way forward," *Solar Energy*, vol. 210, pp. 202-221, 2020/11/01/ 2020, doi: <https://doi.org/10.1016/j.solener.2020.08.047>.
- [4] B. P. Koirala, E. van Oost, and H. van der Windt, "Community energy storage: A responsible innovation towards a sustainable energy system?," *Applied Energy*, vol. 231, pp. 570-585, 2018, doi: 10.1016/j.apenergy.2018.09.163.
- [5] A. Bartolini, F. Carducci, C. B. Muñoz, and G. Comodi, "Energy storage and multi energy systems in local energy communities with high renewable energy penetration," *Renewable Energy*, vol. 159, pp. 595-609, 2020, doi: 10.1016/j.renene.2020.05.131.
- [6] S. Cui, Y.-W. Wang, Y. Shi, and J.-W. Xiao, "Community Energy Cooperation With the Presence of Cheating Behaviors," *IEEE Transactions on Smart Grid*, vol. 12, no. 1, pp. 561-573, 2021, doi: 10.1109/tsg.2020.3022792.
- [7] S. Rizvi and A. Abu-Siada, "A Review on Active-Power-Sharing Techniques for Microgrids," *Energies*, vol. 16, no. 13, p. 5175, 2023. [Online]. Available: <https://www.mdpi.com/1996-1073/16/13/5175>.
- [8] C. K. Das, O. Bass, G. Kothapalli, T. S. Mahmoud, and D. Habibi, "Overview of energy storage systems in distribution networks: Placement, sizing, operation, and power quality," *Renewable and Sustainable Energy Reviews*, vol. 91, pp. 1205-1230, 2018/08/01/ 2018, doi: <https://doi.org/10.1016/j.rser.2018.03.068>.
- [9] M. Uddin, M. F. Romlie, M. F. Abdullah, C. Tan, G. M. Shafiullah, and A. H. A. Bakar, "A novel peak shaving algorithm for islanded microgrid using battery energy storage system," *Energy*, vol. 196, p. 117084, 2020/04/01/ 2020, doi: <https://doi.org/10.1016/j.energy.2020.117084>.
- [10] A. S. Jacob, R. Banerjee, and P. C. Ghosh, "Sizing of hybrid energy storage system for a PV based microgrid through design space approach," *Applied Energy*, vol. 212, pp. 640-653, 2018/02/15/ 2018, doi: <https://doi.org/10.1016/j.apenergy.2017.12.040>.
- [11] T. Christen and M. W. Carlen, "Theory of Ragone plots," *Journal of Power Sources*, vol. 91, no. 2, pp. 210-216, 2000/12/01/ 2000, doi: [https://doi.org/10.1016/S0378-7753\(00\)00474-2](https://doi.org/10.1016/S0378-7753(00)00474-2).
- [12] S. Hajiaghahi, A. Salemnia, and M. Hamzeh, "Hybrid energy storage system for microgrids applications: A review," *Journal of Energy Storage*, vol. 21, pp. 543-570, 2019/02/01/ 2019, doi: <https://doi.org/10.1016/j.est.2018.12.017>.

- [13] T. S. Babu, K. R. Vasudevan, V. K. Ramachandaramurthy, S. B. Sani, S. Chemud, and R. M. Lajim, "A Comprehensive Review of Hybrid Energy Storage Systems: Converter Topologies, Control Strategies and Future Prospects," *IEEE Access*, vol. 8, pp. 148702-148721, 2020, doi: 10.1109/ACCESS.2020.3015919.
- [14] A. M. Gee, F. V. P. Robinson, and R. W. Dunn, "Analysis of Battery Lifetime Extension in a Small-Scale Wind-Energy System Using Supercapacitors," *IEEE Transactions on Energy Conversion*, vol. 28, no. 1, pp. 24-33, 2013, doi: 10.1109/TEC.2012.2228195.
- [15] Z. Yixin, Z. Fang, and W. Feng, "Coordination control of lithium battery-supercapacitor hybrid energy storage system in a microgrid under unbalanced load condition," in *2014 16th European Conference on Power Electronics and Applications*, 26-28 Aug. 2014 2014, pp. 1-10, doi: 10.1109/EPE.2014.6910727.
- [16] C. Ammari, D. Belatrache, B. Touhami, and S. Makhloufi, "Sizing, optimization, control and energy management of hybrid renewable energy system—A review," *Energy and Built Environment*, vol. 3, no. 4, pp. 399-411, 2022/10/01/ 2022, doi: <https://doi.org/10.1016/j.enbenv.2021.04.002>.
- [17] J. Lian, Y. Zhang, C. Ma, Y. Yang, and E. Chaima, "A review on recent sizing methodologies of hybrid renewable energy systems," *Energy Conversion and Management*, vol. 199, p. 112027, 2019/11/01/ 2019, doi: <https://doi.org/10.1016/j.enconman.2019.112027>.
- [18] Y. Zhang, X. Tang, Z. Qi, and Z. Liu, "The Ragone plots guided sizing of hybrid storage system for taming the wind power," *International Journal of Electrical Power & Energy Systems*, vol. 65, pp. 246-253, 2015/02/01/ 2015, doi: <https://doi.org/10.1016/j.ijepes.2014.10.006>.
- [19] Y. Liu, W. Du, L. Xiao, H. Wang, S. Bu, and J. Cao, "Sizing a Hybrid Energy Storage System for Maintaining Power Balance of an Isolated System With High Penetration of Wind Generation," *IEEE Transactions on Power Systems*, vol. 31, no. 4, pp. 3267-3275, 2016, doi: 10.1109/TPWRS.2015.2482983.
- [20] A. Abbassi, M. A. Dami, and M. Jemli, "A statistical approach for hybrid energy storage system sizing based on capacity distributions in an autonomous PV/Wind power generation system," *Renewable Energy*, vol. 103, pp. 81-93, 2017/04/01/ 2017, doi: <https://doi.org/10.1016/j.renene.2016.11.024>.
- [21] H. Jia, Y. Mu, and Y. Qi, "A statistical model to determine the capacity of battery-supercapacitor hybrid energy storage system in autonomous microgrid," *International Journal of Electrical Power & Energy Systems*, vol. 54, pp. 516-524, 2014/01/01/ 2014, doi: <https://doi.org/10.1016/j.ijepes.2013.07.025>.
- [22] P. Zhao, J. Wang, and Y. Dai, "Capacity allocation of a hybrid energy storage system for power system peak shaving at high wind power penetration level," *Renewable Energy*, vol. 75, pp. 541-549, 2015/03/01/ 2015, doi: <https://doi.org/10.1016/j.renene.2014.10.040>.
- [23] R. Atia and N. Yamada, "Sizing and Analysis of Renewable Energy and Battery Systems in Residential Microgrids," *IEEE Transactions on Smart Grid*, vol. 7, no. 3, pp. 1204-1213, 2016, doi: 10.1109/TSG.2016.2519541.
- [24] P. Yang and A. Nehorai, "Joint Optimization of Hybrid Energy Storage and Generation Capacity With Renewable Energy," *IEEE Transactions on Smart Grid*, vol. 5, no. 4, pp. 1566-1574, 2014, doi: 10.1109/TSG.2014.2313724.

- [25] S. Bahramirad, W. Reder, and A. Khodaei, "Reliability-Constrained Optimal Sizing of Energy Storage System in a Microgrid," *IEEE Transactions on Smart Grid*, vol. 3, no. 4, pp. 2056-2062, 2012, doi: 10.1109/TSG.2012.2217991.
- [26] J. Cao, W. Du, H. Wang, and M. McCulloch, "Optimal Sizing and Control Strategies for Hybrid Storage System as Limited by Grid Frequency Deviations," *IEEE Transactions on Power Systems*, vol. 33, no. 5, pp. 5486-5495, 2018, doi: 10.1109/TPWRS.2018.2805380.
- [27] M. Masih-Tehrani, M.-R. Ha'iri-Yazdi, V. Esfahanian, and A. Safaei, "Optimum sizing and optimum energy management of a hybrid energy storage system for lithium battery life improvement," *Journal of Power Sources*, vol. 244, pp. 2-10, 2013/12/15/ 2013, doi: <https://doi.org/10.1016/j.jpowsour.2013.04.154>.
- [28] T. Zhou and W. Sun, "Optimization of Battery-Supercapacitor Hybrid Energy Storage Station in Wind/Solar Generation System," *IEEE Transactions on Sustainable Energy*, vol. 5, no. 2, pp. 408-415, 2014, doi: 10.1109/TSSTE.2013.2288804.
- [29] A. Chauhan and R. P. Saini, "A review on Integrated Renewable Energy System based power generation for stand-alone applications: Configurations, storage options, sizing methodologies and control," *Renewable and Sustainable Energy Reviews*, vol. 38, pp. 99-120, 2014/10/01/ 2014, doi: <https://doi.org/10.1016/j.rser.2014.05.079>.
- [30] M. H. Athari and M. M. Ardehali, "Operational performance of energy storage as function of electricity prices for on-grid hybrid renewable energy system by optimized fuzzy logic controller," *Renewable Energy*, vol. 85, pp. 890-902, 2016/01/01/ 2016, doi: <https://doi.org/10.1016/j.renene.2015.07.055>.
- [31] J. Xiao, L. Bai, F. Li, H. Liang, and C. Wang, "Sizing of Energy Storage and Diesel Generators in an Isolated Microgrid Using Discrete Fourier Transform (DFT)," *IEEE Transactions on Sustainable Energy*, vol. 5, no. 3, pp. 907-916, 2014, doi: 10.1109/TSSTE.2014.2312328.
- [32] L. Bai, F. Li, Q. Hu, H. Cui, and X. Fang, "Application of battery-supercapacitor energy storage system for smoothing wind power output: An optimal coordinated control strategy," in *2016 IEEE Power and Energy Society General Meeting (PESGM)*, 2016: IEEE, pp. 1-5.
- [33] Q. Zhang, W. Deng, and G. Li, "Stochastic Control of Predictive Power Management for Battery/Supercapacitor Hybrid Energy Storage Systems of Electric Vehicles," *IEEE Transactions on Industrial Informatics*, vol. 14, no. 7, pp. 3023-3030, 2018, doi: 10.1109/TII.2017.2766095.
- [34] S. Majumder, S. A. Khaparde, A. P. Agalgaonkar, P. Ciufu, S. Perera, and S. V. Kulkarni, "DFT-based sizing of battery storage devices to determine day-ahead minimum variability injection dispatch with renewable energy resources," in *2018 IEEE Power & Energy Society General Meeting (PESGM)*, 5-10 Aug. 2018 2018, pp. 1-1, doi: 10.1109/PESGM.2018.8586029.
- [35] I. San Martín, A. Ursúa, and P. Sanchis, "Integration of fuel cells and supercapacitors in electrical microgrids: Analysis, modelling and experimental validation," *International Journal of Hydrogen Energy*, vol. 38, no. 27, pp. 11655-11671, 2013/09/10/ 2013, doi: <https://doi.org/10.1016/j.ijhydene.2013.06.098>.

- [36] Y. V. Makarov, P. Du, M. C. W. Kintner-Meyer, C. Jin, and H. F. Illian, "Sizing Energy Storage to Accommodate High Penetration of Variable Energy Resources," *IEEE Transactions on Sustainable Energy*, vol. 3, no. 1, pp. 34-40, 2012, doi: 10.1109/TSTE.2011.2164101.
- [37] S. Majumder, S. A. Khaparde, A. P. Agalgaonkar, P. Ciufu, S. Perera, and S. V. Kulkarni, "DFT-Based Sizing of Battery Storage Devices to Determine Day-Ahead Minimum Variability Injection Dispatch With Renewable Energy Resources," *IEEE Transactions on Smart Grid*, vol. 10, no. 1, pp. 626-638, 2019, doi: 10.1109/TSG.2017.2749406.
- [38] Y. Zhou, Z. Huang, H. Liao, H. Li, Y. Jiao, and J. Peng, "A Predictive Set-Point Modulation Energy Management Strategy for Hybrid Energy Storage Systems," *IEEE Transactions on Industry Applications*, vol. 55, no. 6, pp. 6266-6277, 2019, doi: 10.1109/TIA.2019.2933386.
- [39] T. Mesbahi, F. Khenfri, N. Rizoug, P. Bartholomeüs, and P. L. Moigne, "Combined Optimal Sizing and Control of Li-Ion Battery/Supercapacitor Embedded Power Supply Using Hybrid Particle Swarm–Nelder–Mead Algorithm," *IEEE Transactions on Sustainable Energy*, vol. 8, no. 1, pp. 59-73, 2017, doi: 10.1109/TSTE.2016.2582927.
- [40] Y. Yuan, C. Sun, M. Li, S. S. Choi, and Q. Li, "Determination of optimal supercapacitor-lead-acid battery energy storage capacity for smoothing wind power using empirical mode decomposition and neural network," *Electric Power Systems Research*, vol. 127, pp. 323-331, 2015/10/01/ 2015, doi: <https://doi.org/10.1016/j.epsr.2015.06.015>.
- [41] J. Marcos, O. Storköl, L. Marroyo, M. Garcia, and E. Lorenzo, "Storage requirements for PV power ramp-rate control," *Solar Energy*, vol. 99, pp. 28-35, 2014.
- [42] Y. V. Makarov, P. Du, M. C. Kintner-Meyer, C. Jin, and H. F. Illian, "Sizing energy storage to accommodate high penetration of variable energy resources," *IEEE Transactions on sustainable Energy*, vol. 3, no. 1, pp. 34-40, 2011.
- [43] H. Bitaraf, S. Rahman, and M. Pipattanasomporn, "Sizing energy storage to mitigate wind power forecast error impacts by signal processing techniques," *IEEE Transactions on Sustainable Energy*, vol. 6, no. 4, pp. 1457-1465, 2015.
- [44] Q. Jiang and H. Hong, "Wavelet-based capacity configuration and coordinated control of hybrid energy storage system for smoothing out wind power fluctuations," *IEEE Transactions on Power Systems*, vol. 28, no. 2, pp. 1363-1372, 2012.
- [45] M. K. Molla, S. Das, E. Hamid, and K. Hirose, "Empirical Mode Decomposition for Advanced Speech Signal Processing," *Journal of Signal Processing*, vol. 17, pp. 215-229, 11/25 2013, doi: 10.2299/jsp.17.215.
- [46] N. E. Huang *et al.*, "The empirical mode decomposition and the Hilbert spectrum for nonlinear and non-stationary time series analysis," *Proceedings of the Royal Society of London. Series A: Mathematical, Physical and Engineering Sciences*, vol. 454, no. 1971, pp. 903-995, 1998.
- [47] N. E. Huang and Z. Wu, "A review on Hilbert-Huang transform: Method and its applications to geophysical studies," *Reviews of geophysics*, vol. 46, no. 2, 2008.

- [48] G. G. Pegram, M. C. Peel, and T. A. McMahon, "Empirical mode decomposition using rational splines: an application to rainfall time series," *Proceedings of the Royal Society A: Mathematical, Physical and Engineering Sciences*, vol. 464, no. 2094, pp. 1483-1501, 2008.
- [49] E. S. Neto *et al.*, "Assessment of cardiovascular autonomic control by the empirical mode decomposition," *Methods of information in medicine*, vol. 43, no. 01, pp. 60-65, 2004.
- [50] B. Barnhart and W. Eichinger, "Empirical mode decomposition applied to solar irradiance, global temperature, sunspot number, and CO2 concentration data," *Journal of Atmospheric and Solar-Terrestrial Physics*, vol. 73, no. 13, pp. 1771-1779, 2011.
- [51] T.-Y. Chu and W.-C. Huang, "Application of Empirical Mode Decomposition Method to Synthesize Flow Data: A Case Study of Hushan Reservoir in Taiwan," *Water*, vol. 12, no. 4, 2020, doi: 10.3390/w12040927.
- [52] H. Ren, Y.-L. Wang, M.-Y. Huang, Y.-L. Chang, and H.-M. Kao, "Ensemble Empirical Mode Decomposition Parameters Optimization for Spectral Distance Measurement in Hyperspectral Remote Sensing Data," *Remote Sensing*, vol. 6, no. 3, pp. 2069-2083, 2014, doi: 10.3390/rs6032069.
- [53] N. Senroy, S. Suryanarayanan, and P. F. Ribeiro, "An Improved Hilbert–Huang Method for Analysis of Time-Varying Waveforms in Power Quality," *IEEE Transactions on Power Systems*, vol. 22, no. 4, pp. 1843-1850, 2007, doi: 10.1109/tpwrs.2007.907542.
- [54] S. Shukla, S. Mishra, and B. Singh, "Empirical-Mode Decomposition With Hilbert Transform for Power-Quality Assessment," *IEEE Transactions on Power Delivery*, vol. 24, no. 4, pp. 2159-2165, 2009, doi: 10.1109/tpwrd.2009.2028792.
- [55] Y. Ren, P. N. Suganthan, and N. Srikanth, "A Comparative Study of Empirical Mode Decomposition-Based Short-Term Wind Speed Forecasting Methods," *IEEE Transactions on Sustainable Energy*, vol. 6, no. 1, pp. 236-244, 2015, doi: 10.1109/tste.2014.2365580.
- [56] Y. Li, M. Vilathgamuwa, S. S. Choi, T. W. Farrell, N. T. Tran, and J. Teague, "Development of a degradation-conscious physics-based lithium-ion battery model for use in power system planning studies," *Applied Energy*, vol. 248, pp. 512-525, 2019/08/15/ 2019, doi: <https://doi.org/10.1016/j.apenergy.2019.04.143>.
- [57] J. Luque, D. Anguita, F. Pérez, and R. Denda, "Spectral Analysis of Electricity Demand Using Hilbert–Huang Transform," *Sensors*, vol. 20, no. 10, 2020, doi: 10.3390/s20102912.
- [58] V. Puliafito, S. Vergura, and M. Carpentieri, "Fourier, Wavelet, and Hilbert-Huang Transforms for Studying Electrical Users in the Time and Frequency Domain," *Energies*, vol. 10, no. 2, p. 188, 2017. [Online]. Available: <https://www.mdpi.com/1996-1073/10/2/188>.
- [59] L. Cohen, *Time-frequency analysis: theory and applications*. Prentice-Hall, Inc., 1995.
- [60] G. Rilling and P. Flandrin, "One or Two Frequencies? The Empirical Mode Decomposition Answers," *IEEE Transactions on Signal Processing*, vol. 56, no. 1, pp. 85-95, 2008, doi: 10.1109/tsp.2007.906771.

- [61] Z. Wu and N. E. Huang, "On the Filtering Properties of the Empirical Mode Decomposition," *Advances in Adaptive Data Analysis*, vol. 02, no. 04, pp. 397-414, 2011, doi: 10.1142/s1793536910000604.
- [62] P. Flandrin, P. Gonçalves, and G. Rilling, "EMD equivalent filter banks, from interpretation to applications," in *Hilbert-Huang transform and its applications*: World Scientific, 2005, pp. 57-74.
- [63] Z. Wu and N. E. Huang, "Ensemble empirical mode decomposition: a noise-assisted data analysis method," *Advances in adaptive data analysis*, vol. 1, no. 01, pp. 1-41, 2009.
- [64] J.-R. Yeh, J.-S. Shieh, and N. E. Huang, "Complementary ensemble empirical mode decomposition: A novel noise enhanced data analysis method," *Advances in adaptive data analysis*, vol. 2, no. 02, pp. 135-156, 2010.
- [65] T. Wang, M. Zhang, Q. Yu, and H. Zhang, "Comparing the applications of EMD and EEMD on time-frequency analysis of seismic signal," *Journal of Applied Geophysics*, vol. 83, pp. 29-34, 2012, doi: 10.1016/j.jappgeo.2012.05.002.
- [66] M. E. Torres, M. A. Colominas, G. Schlotthauer, and P. Flandrin, "A complete ensemble empirical mode decomposition with adaptive noise," in *2011 IEEE international conference on acoustics, speech and signal processing (ICASSP)*, 2011: IEEE, pp. 4144-4147.
- [67] P. Stepien, "Sliding Window Empirical Mode Decomposition -its performance and quality," *EPJ Nonlinear Biomedical Physics*, vol. 2, no. 1, p. 14, 2014/11/22 2014, doi: 10.1140/epjnbp/s40366-014-0014-9.
- [68] C. Song and X. Chen, "Performance Comparison of Machine Learning Models for Annual Precipitation Prediction Using Different Decomposition Methods," *Remote Sensing*, vol. 13, p. 1018, 03/08 2021, doi: 10.3390/rs13051018.
- [69] Empirical Mode Decomposition [Online] Available: <https://au.mathworks.com/help/wavelet/ref/emd.html#description>
- [70] T. Terlouw, T. AlSkaif, C. Bauer, and W. van Sark, "Multi-objective optimization of energy arbitrage in community energy storage systems using different battery technologies," *Applied Energy*, vol. 239, pp. 356-372, 2019/04/01/ 2019, doi: <https://doi.org/10.1016/j.apenergy.2019.01.227>.
- [71] W. Vermeer, G. R. C. Mouli, and P. Bauer, "A comprehensive review on the characteristics and modeling of lithium-ion battery aging," *IEEE Transactions on Transportation Electrification*, vol. 8, no. 2, pp. 2205-2232, 2021.
- [72] R. Xiong, Y. Pan, W. Shen, H. Li, and F. Sun, "Lithium-ion battery aging mechanisms and diagnosis method for automotive applications: Recent advances and perspectives," *Renewable and Sustainable Energy Reviews*, vol. 131, p. 110048, 2020/10/01/ 2020, doi: <https://doi.org/10.1016/j.rser.2020.110048>.
- [73] N. Collath, B. Tepe, S. Englberger, A. Jossen, and H. Hesse, "Aging aware operation of lithium-ion battery energy storage systems: A review," *Journal of Energy Storage*, vol. 55, p. 105634, 2022/11/25/ 2022, doi: <https://doi.org/10.1016/j.est.2022.105634>.
- [74] P. M. Attia, S. Das, S. J. Harris, M. Z. Bazant, and W. C. Chueh, "Electrochemical Kinetics of SEI Growth on Carbon Black: Part I. Experiments," *Journal of The Electrochemical Society*, vol. 166, no. 4, p. E97, 2019/02/23 2019, doi: 10.1149/2.0231904jes.

- [75] B. Xu, A. Oudalov, A. Ulbig, G. Andersson, and D. S. Kirschen, "Modeling of Lithium-Ion Battery Degradation for Cell Life Assessment," *IEEE Transactions on Smart Grid*, vol. 9, no. 2, pp. 1131-1140, 2018, doi: 10.1109/TSG.2016.2578950.
- [76] S. Bashash, S. J. Moura, J. C. Forman, and H. K. Fathy, "Plug-in hybrid electric vehicle charge pattern optimization for energy cost and battery longevity," *Journal of Power Sources*, vol. 196, no. 1, pp. 541-549, 2011/01/01/ 2011, doi: <https://doi.org/10.1016/j.jpowsour.2010.07.001>.
- [77] G. He, Q. Chen, C. Kang, P. Pinson, and Q. Xia, "Optimal Bidding Strategy of Battery Storage in Power Markets Considering Performance-Based Regulation and Battery Cycle Life," *IEEE Transactions on Smart Grid*, vol. 7, no. 5, pp. 2359-2367, 2016, doi: 10.1109/TSG.2015.2424314.
- [78] P. P. Mishra *et al.*, "Analysis of degradation in residential battery energy storage systems for rate-based use-cases," *Applied Energy*, vol. 264, p. 114632, 2020/04/15/ 2020, doi: <https://doi.org/10.1016/j.apenergy.2020.114632>.
- [79] J. M. Reniers, G. Mulder, and D. A. Howey, "Review and Performance Comparison of Mechanical-Chemical Degradation Models for Lithium-Ion Batteries," *Journal of The Electrochemical Society*, vol. 166, no. 14, p. A3189, 2019/09/19 2019, doi: 10.1149/2.0281914jes.
- [80] J. Cai, H. Zhang, and X. Jin, "Aging-aware predictive control of PV-battery assets in buildings," *Applied Energy*, vol. 236, pp. 478-488, 2019/02/15/ 2019, doi: <https://doi.org/10.1016/j.apenergy.2018.12.003>.
- [81] G. Angenendt, S. Zurmühlen, H. Axelsen, and D. U. Sauer, "Comparison of different operation strategies for PV battery home storage systems including forecast-based operation strategies," *Applied Energy*, vol. 229, pp. 884-899, 2018/11/01/ 2018, doi: <https://doi.org/10.1016/j.apenergy.2018.08.058>.
- [82] A. Perez, R. Moreno, R. Moreira, M. Orchard, and G. Strbac, "Effect of Battery Degradation on Multi-Service Portfolios of Energy Storage," *IEEE Transactions on Sustainable Energy*, vol. 7, no. 4, pp. 1718-1729, 2016, doi: 10.1109/TSTE.2016.2589943.
- [83] F. Wankmüller, P. R. Thimmapuram, K. G. Gallagher, and A. Botterud, "Impact of battery degradation on energy arbitrage revenue of grid-level energy storage," *Journal of Energy Storage*, vol. 10, pp. 56-66, 2017/04/01/ 2017, doi: <https://doi.org/10.1016/j.est.2016.12.004>.
- [84] Y. Shi, B. Xu, D. Wang, and B. Zhang, "Using Battery Storage for Peak Shaving and Frequency Regulation: Joint Optimization for Superlinear Gains," *IEEE Transactions on Power Systems*, vol. 33, no. 3, pp. 2882-2894, 2018, doi: 10.1109/TPWRS.2017.2749512.
- [85] A. Maheshwari, N. G. Paterakis, M. Santarelli, and M. Gibescu, "Optimizing the operation of energy storage using a non-linear lithium-ion battery degradation model," *Applied Energy*, vol. 261, p. 114360, 2020/03/01/ 2020, doi: <https://doi.org/10.1016/j.apenergy.2019.114360>.
- [86] T. Weitzel and C. H. Glock, "Energy management for stationary electric energy storage systems: A systematic literature review," *European Journal of Operational Research*, vol. 264, no. 2, pp. 582-606, 2018/01/16/ 2018, doi: <https://doi.org/10.1016/j.ejor.2017.06.052>.

- [87] H. C. Hesse *et al.*, "Ageing and Efficiency Aware Battery Dispatch for Arbitrage Markets Using Mixed Integer Linear Programming †," *Energies*, vol. 12, no. 6, doi: 10.3390/en12060999.
- [88] W.-W. Kim, J.-S. Shin, S.-Y. Kim, and J.-O. Kim, "Operation scheduling for an energy storage system considering reliability and aging," *Energy*, vol. 141, pp. 389-397, 2017/12/15/ 2017, doi: <https://doi.org/10.1016/j.energy.2017.09.091>.
- [89] M. A. Hossain, H. R. Pota, S. Squartini, F. Zaman, and J. M. Guerrero, "Energy scheduling of community microgrid with battery cost using particle swarm optimisation," *Applied Energy*, vol. 254, p. 113723, 2019/11/15/ 2019, doi: <https://doi.org/10.1016/j.apenergy.2019.113723>.
- [90] S. Li, J. Li, C. Su, and Q. Yang, "Optimization of Bi-Directional V2G Behavior With Active Battery Anti-Aging Scheduling," *IEEE Access*, vol. 8, pp. 11186-11196, 2020, doi: 10.1109/ACCESS.2020.2964699.
- [91] K. Liu, X. Hu, Z. Yang, Y. Xie, and S. Feng, "Lithium-ion battery charging management considering economic costs of electrical energy loss and battery degradation," *Energy Conversion and Management*, vol. 195, pp. 167-179, 2019/09/01/ 2019, doi: <https://doi.org/10.1016/j.enconman.2019.04.065>.
- [92] C. Parthasarathy, H. Laaksonen, E. Redondo-Iglesias, and S. Pelissier, "Aging aware adaptive control of Li-ion battery energy storage system for flexibility services provision," *Journal of Energy Storage*, vol. 57, p. 106268, 2023/01/01/ 2023, doi: <https://doi.org/10.1016/j.est.2022.106268>.
- [93] F. Fan, Y. Xu, and X. Feng, "Rule-based health-aware power sharing for a multi-unit battery energy storage system," *International Journal of Electrical Power & Energy Systems*, vol. 132, p. 107208, 2021/11/01/ 2021, doi: <https://doi.org/10.1016/j.ijepes.2021.107208>.
- [94] S. Patel, M. Ahmed, and S. Kamalasadnan, "A Novel Energy Storage-Based Net-Load Smoothing and Shifting Architecture for High Amount of Photovoltaics Integrated Power Distribution System," *IEEE Transactions on Industry Applications*, vol. 56, no. 3, pp. 3090-3099, 2020, doi: 10.1109/TIA.2020.2970380.
- [95] J. Li and M. A. Danzer, "Optimal charge control strategies for stationary photovoltaic battery systems," *Journal of Power Sources*, vol. 258, pp. 365-373, 2014/07/15/ 2014, doi: <https://doi.org/10.1016/j.jpowsour.2014.02.066>.
- [96] N. Padmanabhan, M. Ahmed, and K. Bhattacharya, "Battery Energy Storage Systems in Energy and Reserve Markets," *IEEE Transactions on Power Systems*, vol. 35, no. 1, pp. 215-226, 2020, doi: 10.1109/TPWRS.2019.2936131.
- [97] K. Abdulla *et al.*, "Optimal Operation of Energy Storage Systems Considering Forecasts and Battery Degradation," *IEEE Transactions on Smart Grid*, vol. 9, no. 3, pp. 2086-2096, 2018, doi: 10.1109/TSG.2016.2606490.
- [98] M. Kazemi and H. Zareipour, "Long-Term Scheduling of Battery Storage Systems in Energy and Regulation Markets Considering Battery's Lifespan," *IEEE Transactions on Smart Grid*, vol. 9, no. 6, pp. 6840-6849, 2018, doi: 10.1109/TSG.2017.2724919.
- [99] J.-O. Lee and Y.-S. Kim, "Novel battery degradation cost formulation for optimal scheduling of battery energy storage systems," *International Journal of Electrical Power & Energy Systems*, vol. 137, p. 107795, 2022/05/01/ 2022, doi: <https://doi.org/10.1016/j.ijepes.2021.107795>.



- [100] J. M. Reniers, G. Mulder, S. Ober-Blöbaum, and D. A. Howey, "Improving optimal control of grid-connected lithium-ion batteries through more accurate battery and degradation modelling," *Journal of Power Sources*, vol. 379, pp. 91-102, 2018/03/01/ 2018, doi: <https://doi.org/10.1016/j.jpowsour.2018.01.004>.
- [101] U. R. Nair, M. Sandelic, A. Sangwongwanich, T. Dragičević, R. Costa-Castelló, and F. Blaabjerg, "Grid Congestion Mitigation and Battery Degradation Minimisation Using Model Predictive Control in PV-Based Microgrid," *IEEE Transactions on Energy Conversion*, vol. 36, no. 2, pp. 1500-1509, 2021, doi: 10.1109/TEC.2020.3032534.
- [102] Y. Yang, Q. Ye, L. J. Tung, M. Greenleaf, and H. Li, "Integrated Size and Energy Management Design of Battery Storage to Enhance Grid Integration of Large-Scale PV Power Plants," *IEEE Transactions on Industrial Electronics*, vol. 65, no. 1, pp. 394-402, 2018, doi: 10.1109/tie.2017.2721878.
- [103] R. Manojkumar, C. Kumar, S. Ganguly, and J. P. S. Catalão, "Optimal Peak Shaving Control Using Dynamic Demand and Feed-In Limits for Grid-Connected PV Sources With Batteries," *IEEE Systems Journal*, vol. 15, no. 4, pp. 5560-5570, 2021, doi: 10.1109/JSYST.2020.3045020.
- [104] L. Maeyaert, L. Vandeveld, and T. Döring, "Battery Storage for Ancillary Services in Smart Distribution Grids," *Journal of Energy Storage*, vol. 30, p. 101524, 2020/08/01/ 2020, doi: <https://doi.org/10.1016/j.est.2020.101524>.
- [105] J. Li *et al.*, "Design and real-time test of a hybrid energy storage system in the microgrid with the benefit of improving the battery lifetime," *Applied Energy*, vol. 218, pp. 470-478, 2018/05/15/ 2018, doi: <https://doi.org/10.1016/j.apenergy.2018.01.096>.
- [106] G. de Oliveira e Silva and P. Hendrick, "Photovoltaic self-sufficiency of Belgian households using lithium-ion batteries, and its impact on the grid," *Applied Energy*, vol. 195, pp. 786-799, 2017/06/01/ 2017, doi: <https://doi.org/10.1016/j.apenergy.2017.03.112>.
- [107] T. M. Masaud and E. F. El-Saadany, "Correlating Optimal Size, Cycle Life Estimation, and Technology Selection of Batteries: A Two-Stage Approach for Microgrid Applications," *IEEE Transactions on Sustainable Energy*, vol. 11, no. 3, pp. 1257-1267, 2020, doi: 10.1109/TSTE.2019.2921804.
- [108] M. F. Zia, E. Elbouchikhi, and M. Benbouzid, "Optimal operational planning of scalable DC microgrid with demand response, islanding, and battery degradation cost considerations," *Applied Energy*, vol. 237, pp. 695-707, 2019/03/01/ 2019, doi: <https://doi.org/10.1016/j.apenergy.2019.01.040>.
- [109] F. Hafiz, M. A. Awal, A. R. d. Queiroz, and I. Husain, "Real-Time Stochastic Optimization of Energy Storage Management Using Deep Learning-Based Forecasts for Residential PV Applications," *IEEE Transactions on Industry Applications*, vol. 56, no. 3, pp. 2216-2226, 2020, doi: 10.1109/tia.2020.2968534.
- [110] H. Alharbi and K. Bhattacharya, "Stochastic Optimal Planning of Battery Energy Storage Systems for Isolated Microgrids," *IEEE Transactions on Sustainable Energy*, vol. 9, no. 1, pp. 211-227, 2018, doi: 10.1109/TSTE.2017.2724514.
- [111] I. N. Moghaddam, B. H. Chowdhury, and S. Mohajeryami, "Predictive Operation and Optimal Sizing of Battery Energy Storage With High Wind Energy

- Penetration," *IEEE Transactions on Industrial Electronics*, vol. 65, no. 8, pp. 6686-6695, 2018, doi: 10.1109/TIE.2017.2774732.
- [112] J. Sachs and O. Sawodny, "A Two-Stage Model Predictive Control Strategy for Economic Diesel-PV-Battery Island Microgrid Operation in Rural Areas," *IEEE Transactions on Sustainable Energy*, vol. 7, no. 3, pp. 903-913, 2016, doi: 10.1109/TSTE.2015.2509031.
- [113] F. Zhang *et al.*, "Battery ESS Planning for Wind Smoothing via Variable-Interval Reference Modulation and Self-Adaptive SOC Control Strategy," *IEEE Transactions on Sustainable Energy*, vol. 8, no. 2, pp. 695-707, 2017, doi: 10.1109/TSTE.2016.2615638.
- [114] R. K. Chauhan and K. Chauhan, "Battery monitoring and control system for photovoltaic based DC microgrid," *International Journal of Emerging Electric Power Systems*, vol. 20, no. 6, p. 20190133, 2019.
- [115] F. Conte, S. Massucco, M. Saviozzi, and F. Silvestro, "A Stochastic Optimization Method for Planning and Real-Time Control of Integrated PV-Storage Systems: Design and Experimental Validation," *IEEE Transactions on Sustainable Energy*, vol. 9, no. 3, pp. 1188-1197, 2018, doi: 10.1109/TSTE.2017.2775339.
- [116] M. Cao, Q. Xu, X. Qin, and J. Cai, "Battery energy storage sizing based on a model predictive control strategy with operational constraints to smooth the wind power," *International Journal of Electrical Power & Energy Systems*, vol. 115, p. 105471, 2020/02/01/ 2020, doi: <https://doi.org/10.1016/j.ijepes.2019.105471>.
- [117] G. B. M. A. Litjens, E. Worrell, and W. G. J. H. M. van Sark, "Assessment of forecasting methods on performance of photovoltaic-battery systems," *Applied Energy*, vol. 221, pp. 358-373, 2018/07/01/ 2018, doi: <https://doi.org/10.1016/j.apenergy.2018.03.154>.
- [118] A. Allahham, D. Greenwood, C. Patsios, and P. Taylor, "Adaptive receding horizon control for battery energy storage management with age-and-operation-dependent efficiency and degradation," *Electric Power Systems Research*, vol. 209, p. 107936, 2022/08/01/ 2022, doi: <https://doi.org/10.1016/j.epr.2022.107936>.
- [119] H. Yang, Z. Gong, Y. Ma, L. Wang, and B. Dong, "Optimal two-stage dispatch method of household PV-BESS integrated generation system under time-of-use electricity price," *International Journal of Electrical Power & Energy Systems*, vol. 123, p. 106244, 2020/12/01/ 2020, doi: <https://doi.org/10.1016/j.ijepes.2020.106244>.
- [120] "Sharing energy in White Gum Valley." <https://www.westernpower.com.au/resources-education/network-improvements/network-upgrade-projects/peer-to-peer-energy-sharing/sharing-energy-in-white-gum-valley/> (accessed 05/04/2024).
- [121] M. M. Syed, G. M. Morrison, and J. Darbyshire, "Shared Solar and Battery Storage Configuration Effectiveness for Reducing the Grid Reliance of Apartment Complexes," *Energies*, vol. 13, no. 18, p. 4820, 2020. [Online]. Available: <https://www.mdpi.com/1996-1073/13/18/4820>.
- [122] S. Rajakaruna and S. Islam, "Building a state of the art laboratory for teaching and research in renewable electric energy systems and microgrids," in *2011 IEEE Power and Energy Society General Meeting*, 2011: IEEE, pp. 1-6.

- [123] A. Y. Alani and I. O. Osunmakinde, "Short-Term Multiple Forecasting of Electric Energy Loads for Sustainable Demand Planning in Smart Grids for Smart Homes," *Sustainability*, vol. 9, no. 11, p. 1972, 2017. [Online]. Available: <https://www.mdpi.com/2071-1050/9/11/1972>.
- [124] T. R. Tanim and C. D. Rahn, "Aging formula for lithium ion batteries with solid electrolyte interphase layer growth," *Journal of Power Sources*, vol. 294, pp. 239-247, 2015/10/30/ 2015, doi: <https://doi.org/10.1016/j.jpowsour.2015.06.014>.
- [125] K. Thirugnanam, S. K. Kerk, C. Yuen, N. Liu, and M. Zhang, "Energy Management for Renewable Microgrid in Reducing Diesel Generators Usage With Multiple Types of Battery," *IEEE Transactions on Industrial Electronics*, vol. 65, no. 8, pp. 6772-6786, 2018, doi: 10.1109/tie.2018.2795585.
- [126] S. V. Rajani, V. J. Pandya, and V. A. Shah, "Experimental validation of the ultracapacitor parameters using the method of averaging for photovoltaic applications," *Journal of Energy Storage*, vol. 5, pp. 120-126, 2016/02/01/ 2016, doi: <https://doi.org/10.1016/j.est.2015.12.002>.
- [127] D. Hettiarachchi, S. Rajakaruna, S. S. Choi, and A. Ghosh, "A new approach to identify the optimum frequency ranges of the constituent storage devices of a hybrid energy storage system using the empirical mode decomposition technique," *Journal of Energy Storage*, vol. 51, p. 104285, 2022/07/01/ 2022, doi: <https://doi.org/10.1016/j.est.2022.104285>.
- [128] N. Meddings *et al.*, "Application of electrochemical impedance spectroscopy to commercial Li-ion cells: A review," *Journal of Power Sources*, vol. 480, p. 228742, 2020/12/31/ 2020, doi: <https://doi.org/10.1016/j.jpowsour.2020.228742>.
- [129] S. J. Moura, J. C. Forman, S. Bashash, J. L. Stein, and H. K. Fathy, "Optimal Control of Film Growth in Lithium-Ion Battery Packs via Relay Switches," *IEEE Transactions on Industrial Electronics*, vol. 58, no. 8, pp. 3555-3566, 2011, doi: 10.1109/TIE.2010.2087294.
- [130] C. Quintáns, R. Iglesias, A. Lago, J. M. Acevedo, and C. Martínez-Peñalver, "Methodology to Obtain the Voltage-Dependent Parameters of a Fourth-Order Supercapacitor Model With the Transient Response to Current Pulses," *IEEE Transactions on Power Electronics*, vol. 32, no. 5, pp. 3868-3878, 2017, doi: 10.1109/TPEL.2016.2593102.
- [131] C.-T. Pham and D. Månsson, "On the physical system modelling of energy storages as equivalent circuits with parameter description for variable load demand (Part I)," *Journal of Energy Storage*, vol. 13, pp. 73-84, 2017/10/01/ 2017, doi: <https://doi.org/10.1016/j.est.2017.05.015>.
- [132] N. Mousavi, G. Kothapalli, D. Habibi, M. Khiadani, and C. Das, "An improved mathematical model for a pumped hydro storage system considering electrical, mechanical, and hydraulic losses," *Applied Energy*, vol. 247, pp. 228-236, 08/01 2019, doi: 10.1016/j.apenergy.2019.03.015.
- [133] K. Nováková, A. Pražanová, D.-I. Stroe, and V. Knap, "Second-Life of Lithium-Ion Batteries from Electric Vehicles: Concept, Aging, Testing, and Applications," *Energies*, vol. 16, no. 5, p. 2345, 2023. [Online]. Available: <https://www.mdpi.com/1996-1073/16/5/2345>.

- [134] N. Kachate, D. Sharma, and K. Baidya, "Material recovery in Li-ion battery recycling: Case study," *Materials Today: Proceedings*, vol. 72, pp. 1498-1502, 2023/01/01/ 2023, doi: <https://doi.org/10.1016/j.matpr.2022.09.377>.
- [135] B. Lu, A. Blakers, M. Stocks, and T. N. Do, "Low-cost, low-emission 100% renewable electricity in Southeast Asia supported by pumped hydro storage," *Energy*, vol. 236, p. 121387, 2021/12/01/ 2021, doi: <https://doi.org/10.1016/j.energy.2021.121387>.
- [136] N. Mousavi, G. Kothapalli, D. Habibi, C. K. Das, and A. Baniasadi, "A novel photovoltaic-pumped hydro storage microgrid applicable to rural areas," *Applied Energy*, vol. 262, p. 114284, 2020/03/15/ 2020, doi: <https://doi.org/10.1016/j.apenergy.2019.114284>.
- [137] D. Hettiarachchi, S. Shing Choi, S. Rajakaruna, and A. Ghosh, "Development of control strategy for community battery energy storage system in grid-connected microgrid of high photovoltaic penetration level," *International Journal of Electrical Power & Energy Systems*, vol. 155, p. 109527, 2024/01/01/ 2024, doi: <https://doi.org/10.1016/j.ijepes.2023.109527>.
- [138] S. Y. M. Mousavi, A. Jalilian, M. Savaghebi, and J. M. Guerrero, "Autonomous Control of Current- and Voltage-Controlled DG Interface Inverters for Reactive Power Sharing and Harmonics Compensation in Islanded Microgrids," *IEEE Transactions on Power Electronics*, vol. 33, no. 11, pp. 9375-9386, 2018, doi: 10.1109/TPEL.2018.2792780.
- [139] H. M. Marczinkowski and P. A. Østergaard, "Residential versus communal combination of photovoltaic and battery in smart energy systems," *Energy*, vol. 152, pp. 466-475, 2018/06/01/ 2018, doi: <https://doi.org/10.1016/j.energy.2018.03.153>.
- [140] R. Dai, R. Esmailbeigi, and H. Charkhgard, "The Utilization of Shared Energy Storage in Energy Systems: A Comprehensive Review," *IEEE Transactions on Smart Grid*, vol. 12, no. 4, pp. 3163-3174, 2021, doi: 10.1109/TSG.2021.3061619.
- [141] E. Barbour, D. Parra, Z. Awwad, and M. C. González, "Community energy storage: A smart choice for the smart grid?," *Applied Energy*, vol. 212, pp. 489-497, 2018, doi: 10.1016/j.apenergy.2017.12.056.
- [142] M. M. Syed, P. Hansen, and G. M. Morrison, "Performance of a shared solar and battery storage system in an Australian apartment building," *Energy and Buildings*, vol. 225, 2020, doi: 10.1016/j.enbuild.2020.110321.
- [143] J. Martins, S. Spataru, D. Sera, D.-I. Stroe, and A. Lashab, "Comparative Study of Ramp-Rate Control Algorithms for PV with Energy Storage Systems," *Energies*, vol. 12, no. 7, p. 1342, 2019. [Online]. Available: <https://www.mdpi.com/1996-1073/12/7/1342>.
- [144] Q. Hou, N. Zhang, E. Du, M. Miao, F. Peng, and C. Kang, "Probabilistic duck curve in high PV penetration power system: Concept, modeling, and empirical analysis in China," *Applied Energy*, vol. 242, pp. 205-215, 2019/05/15/ 2019, doi: <https://doi.org/10.1016/j.apenergy.2019.03.067>.
- [145] A. Mamun, I. Narayanan, D. Wang, A. Sivasubramaniam, and H. K. Fathy, "Multi-objective optimization of demand response in a datacenter with lithium-ion battery storage," *Journal of Energy Storage*, vol. 7, pp. 258-269, 2016/08/01/ 2016, doi: <https://doi.org/10.1016/j.est.2016.08.002>.

- [146] A. a. Mamun, I. Narayanan, D. Wang, A. Sivasubramaniam, and H. K. Fathy, "A Stochastic Optimal Control Approach for Exploring Tradeoffs between Cost Savings and Battery Aging in Datacenter Demand Response," *IEEE Transactions on Control Systems Technology*, vol. 26, no. 1, pp. 360-367, 2018, doi: 10.1109/TCST.2016.2643569.
- [147] M. Goldsworthy, T. Moore, M. Peristy, and M. Grimeland, "Cloud-based model-predictive-control of a battery storage system at a commercial site," *Applied Energy*, vol. 327, p. 120038, 2022/12/01/ 2022, doi: <https://doi.org/10.1016/j.apenergy.2022.120038>.
- [148] F. M. Vieira, P. S. Moura, and A. T. de Almeida, "Energy storage system for self-consumption of photovoltaic energy in residential zero energy buildings," *Renewable Energy*, vol. 103, pp. 308-320, 2017, doi: 10.1016/j.renene.2016.11.048.
- [149] W. Tushar *et al.*, "Energy Storage Sharing in Smart Grid: A Modified Auction-Based Approach," *IEEE Transactions on Smart Grid*, vol. 7, no. 3, pp. 1462-1475, 2016, doi: 10.1109/tsg.2015.2512267.
- [150] M. Sheppy, A. Beach, and S. Pless, "Metering Best Practices Applied in the National Renewable Energy Laboratory's Research Support Facility: A Primer to the 2011 Measured and Modeled Energy Consumption Datasets," National Renewable Energy Lab.(NREL), Golden, CO (United States), 2013.
- [151] I. S. Bayram, M. Abdallah, A. Tajer, and K. A. Qaraq, "A Stochastic Sizing Approach for Sharing-Based Energy Storage Applications," *IEEE Transactions on Smart Grid*, vol. 8, no. 3, pp. 1075-1084, 2017, doi: 10.1109/tsg.2015.2466078.
- [152] E. Wilson, "Commercial and residential hourly load profiles for all tmy3 locations in the united states," DOE Open Energy Data Initiative (OEDI); National Renewable Energy Lab.(NREL),Golden, CO (United States), 2014.
- [153] A. L. Bukar, C. W. Tan, L. K. Yiew, R. Ayop, and W.-S. Tan, "A rule-based energy management scheme for long-term optimal capacity planning of grid-independent microgrid optimized by multi-objective grasshopper optimization algorithm," *Energy Conversion and Management*, vol. 221, p. 113161, 2020/10/01/ 2020, doi: <https://doi.org/10.1016/j.enconman.2020.113161>.
- [154] O. Lindberg, D. Lingfors, J. Arnqvist, D. van der Meer, and J. Munkhammar, "Day-ahead probabilistic forecasting at a co-located wind and solar power park in Sweden: Trading and forecast verification," *Advances in Applied Energy*, vol. 9, p. 100120, 2023/02/01/ 2023, doi: <https://doi.org/10.1016/j.adapen.2022.100120>.
- [155] S. J. Moura, "Techniques for battery health conscious power management via electrochemical modeling and optimal control," University of Michigan, 2011.
- [156] Y. Li, D. M. Vilathgamuwa, S. S. Choi, T. W. Farrell, N. T. Tran, and J. Teague, "Optimal control of film growth in dual lithium-ion battery energy storage system," in *2017 IEEE 12th International Conference on Power Electronics and Drive Systems (PEDS)*, 12-15 Dec. 2017 2017, pp. 202-207, doi: 10.1109/PEDS.2017.8289208.
- [157] K. Uddin, A. Picarelli, C. Lyness, N. Taylor, and J. Marco, "An Acausal Li-Ion Battery Pack Model for Automotive Applications," *Energies*, vol. 7, no. 9, pp. 5675-5700, 2014. [Online]. Available: <https://www.mdpi.com/1996-1073/7/9/5675>.

- [158] L. Kolzenberg, J. Stadler, J. P. Fath, M. Ecker, B. Horstmann, and A. Latz, "Towards a Physics-Based Battery Aging Prediction," 2021.
- [159] J. M. Thomas, P. P. Edwards, P. J. Dobson, and G. P. Owen, "Decarbonising energy: The developing international activity in hydrogen technologies and fuel cells," *Journal of Energy Chemistry*, vol. 51, pp. 405-415, 2020/12/01/ 2020, doi: <https://doi.org/10.1016/j.jechem.2020.03.087>.
- [160] S. Wilkinson, M. J. Maticka, Y. Liu, and M. John, "The duck curve in a drying pond: The impact of rooftop PV on the Western Australian electricity market transition," *Utilities Policy*, vol. 71, p. 101232, 2021/08/01/ 2021, doi: <https://doi.org/10.1016/j.jup.2021.101232>.
- [161] J. Dumas, S. Dakir, C. Liu, and B. Cornélusse, "Coordination of operational planning and real-time optimization in microgrids," *Electric Power Systems Research*, vol. 190, p. 106634, 2021/01/01/ 2021, doi: <https://doi.org/10.1016/j.epsr.2020.106634>.
- [162] K. Li and K. J. Tseng, "Energy efficiency of lithium-ion battery used as energy storage devices in micro-grid," in *IECON 2015 - 41st Annual Conference of the IEEE Industrial Electronics Society*, 9-12 Nov. 2015 2015, pp. 005235-005240, doi: 10.1109/IECON.2015.7392923.
- [163] S. Subramanian, M. A. Johny, M. Malamal Neelanchery, and S. Ansari, "Self-Discharge and Voltage Recovery in Graphene Supercapacitors," *IEEE Transactions on Power Electronics*, vol. 33, no. 12, pp. 10410-10418, 2018, doi: 10.1109/tpel.2018.2810889.
- [164] R. L. Spyker and R. M. Nelms, "Classical equivalent circuit parameters for a double-layer capacitor," *IEEE Transactions on Aerospace and Electronic Systems*, vol. 36, no. 3, pp. 829-836, 2000, doi: 10.1109/7.869502.
- [165] V. Sedlakova *et al.*, "Supercapacitor equivalent electrical circuit model based on charges redistribution by diffusion," *Journal of Power Sources*, vol. 286, pp. 58-65, 2015, doi: 10.1016/j.jpowsour.2015.03.122.
- [166] T. Iqbal, M. Asif, and R. Hasan, "Dynamic modeling and analysis of a remote hybrid power system with pumped hydro storage," *International Journal of Energy Science (IJES)*, vol. 3, no. 5, 2013.
- [167] N. Mousavi, G. Kothapalli, D. Habibi, M. Khiadani, and C. K. Das, "An improved mathematical model for a pumped hydro storage system considering electrical, mechanical, and hydraulic losses," *Applied Energy*, vol. 247, pp. 228-236, 2019/08/01/ 2019, doi: <https://doi.org/10.1016/j.apenergy.2019.03.015>.
- [168] C. Nicolet *et al.*, "High-Order Modeling of Hydraulic Power Plant in Islanded Power Network," *IEEE Transactions on Power Systems*, vol. 22, no. 4, pp. 1870-1880, 2007, doi: 10.1109/TPWRS.2007.907348.
- [169] C. Nicolet, "Hydroacoustic modelling and numerical simulation of unsteady operation of hydroelectric systems," Epfl, 2007.
- [170] C.-T. Pham and D. J. J. o. E. S. Månsson, "On the physical system modelling of energy storages as equivalent circuits with parameter description for variable load demand (Part I)," vol. 13, pp. 73-84, 2017.
- [171] S. J. Moura, J. C. Forman, S. Bashash, J. L. Stein, and H. K. Fathy, "Optimal control of film growth in lithium-ion battery packs via relay switches," *IEEE Transactions on Industrial Electronics*, vol. 58, no. 8, pp. 3555-3566, 2010.

Every reasonable effort has been made to acknowledge the owners of copyright material. I would be pleased to hear from any copyright owner who has been omitted or incorrectly acknowledged.